Springer ThesesRecognizing Outstanding Ph.D. Research

Hannsjörg Artur Weber

Search for Supersymmetry in Hadronic Final States

Evolution Studies of the CMS Electromagnetic Calorimeter



Springer Theses

Recognizing Outstanding Ph.D. Research

Aims and Scope

The series "Springer Theses" brings together a selection of the very best Ph.D. theses from around the world and across the physical sciences. Nominated and endorsed by two recognized specialists, each published volume has been selected for its scientific excellence and the high impact of its contents for the pertinent field of research. For greater accessibility to non-specialists, the published versions include an extended introduction, as well as a foreword by the student's supervisor explaining the special relevance of the work for the field. As a whole, the series will provide a valuable resource both for newcomers to the research fields described, and for other scientists seeking detailed background information on special questions. Finally, it provides an accredited documentation of the valuable contributions made by today's younger generation of scientists.

Theses are accepted into the series by invited nomination only and must fulfill all of the following criteria

- They must be written in good English.
- The topic should fall within the confines of Chemistry, Physics, Earth Sciences, Engineering and related interdisciplinary fields such as Materials, Nanoscience, Chemical Engineering, Complex Systems and Biophysics.
- The work reported in the thesis must represent a significant scientific advance.
- If the thesis includes previously published material, permission to reproduce this must be gained from the respective copyright holder.
- They must have been examined and passed during the 12 months prior to nomination.
- Each thesis should include a foreword by the supervisor outlining the significance of its content.
- The theses should have a clearly defined structure including an introduction accessible to scientists not expert in that particular field.

More information about this series at http://www.springer.com/series/8790

Hannsjörg Artur Weber

Search for Supersymmetry in Hadronic Final States

Evolution Studies of the CMS Electromagnetic Calorimeter

Doctoral Thesis accepted by the ETH Zurich, Switzerland



Author
Dr. Hannsjörg Artur Weber
Institute for Particle Physics
ETH Zurich
Zurich
Switzerland

Supervisor
Prof. Günther Dissertori
Institute for Particle Physics
ETH Zurich
Zurich
Switzerland

ISSN 2190-5053 ISSN 2190-5061 (electronic) Springer Theses ISBN 978-3-319-19955-9 ISBN 978-3-319-19956-6 (eBook) DOI 10.1007/978-3-319-19956-6

Library of Congress Control Number: 2015941133

Springer Cham Heidelberg New York Dordrecht London © Springer International Publishing Switzerland 2015

This work is subject to copyright. All rights are reserved by the Publisher, whether the whole or part of the material is concerned, specifically the rights of translation, reprinting, reuse of illustrations, recitation, broadcasting, reproduction on microfilms or in any other physical way, and transmission or information storage and retrieval, electronic adaptation, computer software, or by similar or dissimilar methodology now known or hereafter developed.

The use of general descriptive names, registered names, trademarks, service marks, etc. in this publication does not imply, even in the absence of a specific statement, that such names are exempt from the relevant protective laws and regulations and therefore free for general use.

The publisher, the authors and the editors are safe to assume that the advice and information in this book are believed to be true and accurate at the date of publication. Neither the publisher nor the authors or the editors give a warranty, express or implied, with respect to the material contained herein or for any errors or omissions that may have been made.

Printed on acid-free paper

Springer International Publishing AG Switzerland is part of Springer Science+Business Media (www.springer.com)

Supervisor's Foreword

The Standard Model (SM) of Particle Physics describes very successfully the fundamental building blocks of matter and the interactions among them. It has been tested to extremely high precision in many experiments. However, most likely the SM is only a "low-energy" effective theory of a more general theoretical framework, expected to be valid way beyond the energy scales probed so far. Currently, particular interest is devoted to the electroweak energy scale of about a Tera electronVolt (TeV), which is probed by the LHC accelerator and its experiments at CERN. In fact, during the years 2010–2012 the LHC has delivered proton-proton collisions at the center-of-mass energies of 7 and 8 TeV. The main questions addressed at this high-energy collider setup are the origin of electroweak symmetry breaking and the related question of the existence of one or more scalar Higgs bosons, with the spectacular discovery of a new boson, consistent with the hypothesis of an SM Higgs boson, in 2012. Further important efforts are devoted to the searches for physics beyond the SM, such as the appearance of supersymmetric particles. Supersymmetry (SUSY) is a theory, which introduces a new fundamental symmetry between fermions and bosons, and thus ultimately between matter and force particles. This theory has had enormous theoretical and experimental attention for many years, and can be considered as one of the most studied possibilities for an extension of the SM. The reason for the popularity of this model is its potential to solve a number of problems arising in the SM. For example, the various coupling constants appear to unite at a very high energy scale, and probably most importantly, the model offers a candidate for the dark matter particle, namely weakly interacting massive particles such as the neutralino. If SUSY particles exist with masses accessible at the LHC, typically they would be produced in coloured pairs, such as squarks and gluinos, which then undergo characteristic decay chains to further SUSY or SM particles. In most cases, a decay chain ends with a lightest stable SUSY particle, which is very weakly interacting and thus leaves the experiment undetected. The experimental signature is thus a considerable missing transverse energy, accompanied by a certain number of hadronic jets and/or leptons. Many searches at the LHC have been developed for such signatures or topologies, characterized by different sensitivities to SUSY particles and different amounts of backgrounds to be controlled.

The data sample, which the LHC has already delivered, represents only a small fraction of the total expected dataset to be collected by the experiments during the coming decade(s). Because of the foreseen increase in luminosity, the detectors will have to operate in an ever more challenging environment, with particular attention to be given to the radiation hardness of detector components and their related longevity and continued excellent performance. In order to respond to these challenges, the CMS experiment will be upgraded in several steps. A first important upgrade will consist in the replacement of the current three-layer pixel detector with a new, four-layer detector in the year-end technical stop 2016–2017. Other extensive R&D studies are targeted toward the replacement of the forward-calorimeter elements in a long shutdown, foreseen around 2023–2024. In all of these cases extensive simulation studies had and have to be carried out, in order to evaluate the performance and physics potential of the proposed detector upgrades.

The thesis of Hannsjörg Artur Weber represents an exceptionally complete approach to the above-mentioned issues, since it consists of an analysis of the 8 TeV dataset targeted at the search for SUSY particles, which has led to some of the world's best limits, as well as of simulation and R&D studies related to the pixel and calorimeter upgrades.

Regarding the data analysis, already during his master thesis he contributed to the so-called $M_{\rm T2}$ hadronic SUSY analysis ($M_{\rm T2}$ is a kinematic observable well-suited for SUSY searches), carried out by members of the ETH Zurich group in the CMS experiment. The analysis, which was published in JHEP, resulted in the world's best limits on squarks and gluinos in the context of the constrained minimal SUSY extension of the SM. For the 8 TeV $M_{\rm T2}$ hadronic SUSY analysis, Hannsjörg became one of the two leading members of the analysis team, and, notably, the driving force behind most of the data-driven background predictions which constitute one of the core elements of this analysis and which have gained considerable attention and recognition within the CMS collaboration. Again, the analysis resulted in some of the world's best limits on the production of coloured SUSY particles. The corresponding publication has been submitted to JHEP in February 2015.

The second part of his thesis describes the work carried out in the context of the CMS upgrade efforts. In a first study based on simulations, he evaluated the physics potential of the proposed pixel detector upgrade, by taking a special version of the $M_{\rm T2}$ analysis, which also requires hadronic jets tagged as originating from b-quarks. He showed that the new detector would allow for a substantial improvement in terms of b-jet selection efficiency, and thus improves the performance of analyses, which are based on final states including b-jets. Finally, Hannsjörg has performed an in-depth study of the response evolution of the CMS electromagnetic calorimeter endcaps. The scintillating crystals and light detectors in this part of the calorimeter are expected to suffer from the radiation environment at the LHC. Indeed, changes are revealed by a monitoring system using laser light injection to track the overall response evolution. However, it is difficult to disentangle the contributions of the

different detector components, and to understand their origin: whether they are dependent on the rate of exposure and possibly recovering spontaneously, or whether they are proportional to the cumulated exposure. In order to gain a better understanding, he performed a study of monitoring data taken in-situ, trying to find a correlation with component quality parameters measured during detector construction. The study performed by Hannsjörg has allowed to observe such correlations, and to disentangle the order of magnitude of the various contributions. As such, it represents an important input to the ongoing discussions within CMS for selecting the best possible upgrade solutions.

With this thesis, Hannsjörg Artur Weber has very clearly shown to have a deep understanding of LHC physics, and to be able to carry out very involved data analyses, in an independent manner and using innovative approaches. Furthermore, he has made important contributions to the upgrade activities of the CMS experiment. The amount, quality and impact of the results obtained during his Ph.D. studies, covering a broad spectrum of experimental issues, are rather exceptional. I am very happy and proud that his work has been selected for publication in the Springer Theses Series.

Zurich, Switzerland May 2015 Prof. Günther Dissertori

Abstract

Over the past decades, the standard model of particle physics has been proven to accurately describe the vast majority of the experimental observations within particle physics. The discovery of a boson at a mass of about 125 Gev seems to provide the last missing piece of the standard model, the Higgs boson.

Despite this success, there are some phenomena, for which the description of the standard model is insufficient. In order to surmount these shortcomings, new-physics models have been advanced. One popular model is supersymmetry, which solves several of the deficiencies of the standard model. Supersymmetry extends the description of the standard model by adding a symmetry between fermions and bosons: the elementary particle spectrum is at least doubled.

In this dissertation, a search for supersymmetry in fully hadronic final states is presented. The search analyzes proton–proton collision data, collected at $\sqrt{s} = 8 \text{ TeV}$ with the Compact Muon Solenoid experiment at the Large Hadron Collider. The data correspond to an integrated luminosity of 19.5 fb⁻¹.

The search uses the variable $M_{\rm T2}$ to discriminate between events coming from standard model processes and signal events. The variable is a generalization of the transverse mass for events containing two pair-produced particles, where both particles decay at least to one detected and one undetectable particle. Selecting events with high values of $M_{\rm T2}$ reduces the contribution from standard model processes, in particular multijet events, and enhances the sensitivity for signal events for a large variety of supersymmetric models.

The signal regions of this search are defined by the jet and b-tagged jet multiplicities, the hadronic energy in the event, and the value of M_{T2} . The combined information of multiple signal regions yields a high sensitivity for the production of the partner particles of both gluons and quarks, regardless of the quark flavor, for a wide range of particle masses.

The event yields in the signal regions stemming from standard model processes are estimated by prediction methods that use data from control regions orthogonal to the signal regions definition. No significant excess over the expected numbers of background events is observed. The comparison of data yields and predictions is used to set exclusion limits on various models of supersymmetry.

x Abstract

Beyond this search in hadronic final states, the potential of a search for the pair production of supersymmetric partners of the top quark is assessed using events containing two charged leptons. Several signal discriminating variables have been tested, such as variants of the M_{T2} variable or a discriminant based on the examination of the event kinematics.

The second part of this dissertation contains two studies related to the upgrade program of the Compact Muon Solenoid detector.

The physics performance of the pixel detector upgrade, which is foreseen to happen in 2017, is evaluated in the first study. Based on the event selection of the so-called $M_{\rm T2}b$ search for supersymmetry, performed in 2011, the focus of the study is the improvement of identifying jets, which originate from bottom quark hadronization. For the tested model, an increase of 20 % in the signal selection efficiency is observed for a fixed rate of misidentifying light-quark or gluon jets as bottom-quark jets.

In the final study presented in this dissertation, the long-term evolution of signals produced in the forward part of the electromagnetic calorimeter of the Compact Muon Solenoid experiment is analyzed. The lead–tungstate crystals, which act both as absorber and scintillator, are the heart of the calorimeter. The scintillation light is read out by vacuum phototriodes in the forward part of the detector.

The transparency of the crystals decreases under radiation. In order to measure and correct for these transparency changes, a light monitoring system has been installed within the calorimeter.

Several sources are known to contribute to the transparency decrease. The goal of this study is to disentangle various contributions to the signal change. In order to achieve this, measurements, performed during quality assurance tests prior to the construction of the detector, are correlated with signal changes observed in monitoring data during proton–proton collision data taking. Pseudorapidity-dependent contributions are singled out: ionizing damages to crystals, damages to the vacuum phototriodes, and possible cumulative damages to crystals. The results of this study are compared with predictions, which are based on laboratory and testbeam results and are used in studies for possible detector upgrades. The comparison indicates that the modeling of the predictions is satisfactory.

Preface

Concepts of fundamental states or elements have been developed independently by several ancient civilizations several centuries before the Common Era, such as the concept of indestructible particles, which was devised in Greece and India, for example. However, the scientific discipline of particle physics is rather young. The first elementary particle to our current knowledge, the electron, was only discovered at the end of the nineteenth century. The discovery of quantum mechanics and special relativity, around the same time, allowed for the development of theories of the fundamental interactions. The first successful description of interactions between fundamental particles, quantum electrodynamics, was developed only in the 1940s.

During the past century, huge efforts on both theoretical and experimental sides have led to the current description in particle physics, the standard model (SM) of particle physics. It describes, within the common framework of relativistic quantum field theory, the interactions between elementary particles for three out of the four known fundamental forces: the strong force described by quantum chromodynamics, and the weak and electromagnetic forces, described by the electroweak theory. For gravitation, the "oldest" known fundamental force, no successful description at short distances exists. Up to the time of this writing, 17 elementary particles (not counting the antiparticles) have been observed: six quarks, six leptons, four gauge bosons, and a boson, which is likely the Higgs boson.

The observations of a huge amount of experiments have proven the validity of the SM to an extremely high precision for all accessible energy scales. Despite this unprecedented success of the SM, several theoretical indications and experimental measurements clearly point to physics beyond the SM. The observation of neutrino oscillations or the evidence of dark matter find no explanation within the SM. The missing description of quantum gravity, which is important for energies around the Planck scale, $M_{Planck} \sim 10^{18}$ GeV, requires a new theoretical framework. These and other arguments place the SM as an effective low-energy theory, valid for energies up to the electroweak scale, $\nu \sim 246$ GeV.

In order to overcome some of the shortcomings of the SM, multiple theories have been developed. One very popular theory is supersymmetry (SUSY). The SM

xii Preface

is extended by an additional symmetry between bosons and fermions: for each elementary particle in the SM, there exists a partner particle, which differs in spin by one half. Because of the breaking of the symmetry, these particles are much heavier than their SM counterparts and have not yet been observed. The model of SUSY provides elegant solutions to multiple problems, for example, the problem of dark matter mentioned above: the lightest new particle within the SUSY framework could be a candidate for the dark matter particle.

Yet, no observation of supersymmetric particles or other evidence for SUSY have been found so far.

With the construction of the Large Hadron Collider (LHC), a new energy regime has been made accessible: the energy frontier has been pushed up to the TeV scale. If supersymmetric particles exist, they will likely have masses around this scale. Therefore, the general purpose detectors at the LHC should be able to discover them.

In this dissertation, a search for supersymmetric particles produced in proton-proton (pp) collisions is presented. The search is performed using data collected by the Compact Muon Solenoid (CMS) experiment at a center of mass energy of \sqrt{s} = 8 TeV. The data sample corresponds to an integrated luminosity of 19.5 fb⁻¹. This search uses primarily the kinematic variable M_{T2} for discriminating between new physics candidate events and events from SM processes. This variable is a generalization of the transverse mass to the case of the pair production of two particles, which both decay semi-invisibly.

The variable $M_{\rm T2}$ is also used in a study for evaluating the feasibility of a search for the production of supersymmetric partner particles of the top quark in events containing two charged leptons. In many SUSY scenarios, the supersymmetric top quark partner is the lightest strongly produced supersymmetric particle. Therefore, several dedicated searches for this particle are designed. The study presented here shows the possibility of using various variables to discriminate between the SUSY signal events and events from the main SM background process, $t\bar{t}$ + jets.

It has been decided that the full potential of the LHC will be exploited by an upgrade of the LHC machine around 2022. The upgrade will increase the instantaneous luminosity of the LHC by approximately a factor ten, thus allowing for the collection of *pp* collision data corresponding to about 3000 fb⁻¹. The upgrade will require also the experiments to be upgraded.

Already before the year 2022, the innermost detector of the CMS experiment, the pixel detector, will have to be replaced because of radiation damages. The replacement will be used to change the pixel detector design. In this dissertation, a study of the physics performance of this upgrade is shown with focus on the capability of tagging jets, which come from b-quark hadronization. The study is performed in the context of SUSY using the event selection of the $M_{T2}b$ search, which was performed during 2011 for the analysis of 7 TeV pp collision data.

It is expected that by 2022, the forward part of the electromagnetic calorimeter of the CMS experiment will also need to be replaced due to high radiation damages. A study of the long-term evolution of the signals produced in this forward part is

presented using in-situ data of the light monitoring system of the calorimeter. Comparisons with laboratory measurements preceding the construction of the CMS experiment are discussed. The correlations between these laboratory measurements and the in-situ data are used to disentangle various components that contribute to the change in signal measurements of the calorimeter.

The thesis is organized as follows: in Chap. 1, the theoretical aspects of the SM relevant for high energy physics are reviewed. Then, in Chaps. 2 and 3, SUSY and consequent signatures at the LHC are introduced. In Chap. 4, the LHC accelerator and CMS detector are described, followed by a description of the reconstruction of basic physics objects in Chap. 5. In Part II of the thesis, the search for SUSY is covered: in Chap. 6, the main search variable, M_{T2} , and its kinematical properties are introduced. This chapter contains also a summary of the SUSY search performed at $\sqrt{s} = 7$ TeV. Chapter 7 is dedicated to the search for SUSY in hadronic final states using the M_{T2} variable with pp collision data collected at $\sqrt{s} = 8$ TeV. In Chap. 8, the feasibility study of a search for the pair production of scalar top quark partners is summarized. In Part III, studies related to the upgrade program of the CMS experiment are presented. After a short review of the upgrade program in Chap. 9, the physics performance study for the pixel detector upgrade is discussed in Chap. 10. Finally, Chap. 11 contains the evolution study of the electromagnetic calorimeter endcap signals. In Chap. 12, a summary is given.

Contents

Part I Introduction to Theory and Experiment

Intr	oduction to Physics at the High-Energy Frontier			
1.1	Electroweak Theory			
	1.1.1 The Electroweak Symmetry Breaking			
1.2	Quantum Chromodynamics			
	1.2.1 The Strong Coupling Constant: "Running" of α_s			
	1.2.2 Infrared Divergencies			
	1.2.3 The Structure of the Proton			
	1.2.4 The Physics of Proton-Proton Collisions			
1.3	Summary and Experimental Tests of the Standard Model			
	1.3.1 Experimental Tests of the Standard Model			
1.4	Limitations of the Standard Model			
Refe	rences			
Phys	sics Beyond the Standard Model: Supersymmetry			
2.1	The Minimal Supersymmetric Standard Model			
	2.1.1 Breaking of Supersymmetry			
	2.1.2 The Hidden Sector—The Origin of Supersymmetry			
	Breaking			
	2.1.3 R-parity			
	2.1.4 Unification of Gauge Couplings			
2.2	The Higgs Sector in the Minimal Supersymmetric			
	Standard Model			
2.3	Sparticle Masses in the Minimal Supersymmetric			
	Sparticle Masses in the Minimal Supersymmetric			
	Sparticle Masses in the Minimal Supersymmetric Standard Model			
2.4				

xvi Contents

3	Possible Signatures of Supersymmetry at the Large Hadron Collider								
	3.1								
	3.2	Production of Sparticles at Hadron Colliders							
	3.3								
	3.3	Models for Testing Supersymmetric Signatures							
		Standard Model							
		3.3.2 The Constrained Minimal Supersymmetric							
		Standard Model							
		3.3.3 The Simplified Model Framework							
	Refe	rences							
	11010								
4	Exp	erimental Set-Up4							
	4.1	The Large Hadron Collider							
	4.2	The Compact Muon Solenoid Experiment							
		4.2.1 The Tracking System							
		4.2.2 The Electromagnetic Calorimeter							
		4.2.3 The Hadron Calorimeter							
		4.2.4 The Muon System							
		4.2.5 Trigger and Data Acquisition							
	Refe	rences							
5	Ever	nt Reconstruction for Proton-Proton Collisions							
	5.1	Track Reconstruction							
	0.1	5.1.1 Primary Vertex Reconstruction							
	5.2	The Particle-Flow Algorithm							
	5.3	Muon Reconstruction							
	5.4	Electron Reconstruction							
	5.5	Tau Reconstruction							
	5.6	Photon Reconstruction							
	5.7								
	5.7	Jet Reconstruction.65.7.1B-Quark Jet Tagging.							
	5.8	Reconstruction of the Missing Transverse Momentum							
		rences							
Pai	rt II	The Search for Supersymmetry							
6		The characteristic of the M and M are the M and M are the M are the M are the M are the M and M are the							
	6.1	Definition of the M_{T2} Variable							
	6.2	Definition of the Visible Systems for the M_{T2} Calculation 7							
	6.3	Kinematical Properties of M_{T2}							
		6.3.1 The Influence of the Initial State Radiation							
		in the $M_{\rm T2}$ Calculation							
	6.4	The Search for Supersymmetry at $\sqrt{s} = 7 \text{ TeV}$							
	Refe	rences							

Contents xviii

7	Searc	ch for Supersymmetry in Hadronic Events	
	Using	g M_{T2} at $\sqrt{s} = 8 \text{ TeV} \dots$	89
	7.1	Data Selection and Simulation	90
	7.2	Event Selection and Validation	92
		7.2.1 Validation of the Stability of the M_{T2} Variable	93
		7.2.2 Cleaning Procedure Against Instrumental Effects	94
		7.2.3 Selection Criteria to Reduce the Standard	
		Model Background	96
		7.2.4 Summary of the Event Selection	99
	7.3	Optimization and Search Strategy	99
		7.3.1 The Inclusive M_{T2} Analysis: Distributions	
		and Background Composition	103
	7.4	Prediction of the Background Due to Jet Energy	
		Mismeasurements	105
	7.5	Prediction of the Background Due to Leptonic	
		W Boson Decays	109
	7.6	Prediction of the Background Due to Z Boson Decays	
		into Neutrinos	115
	7.7	Results	125
	7.8	Interpretation of the Results	132
		7.8.1 Statistical Procedure	132
		7.8.2 Exclusion Limits on the Production	
		of Supersymmetric Particles	134
	7.9	Comparison of the Results of the M_{T2} Analysis	
		to Other Searches for Supersymmetry	140
	7.10	Summary of the Hadronic M_{T2} Search for Supersymmetry	141
		7.10.1 Prospects for the Continuation of This Search	142
	Refer	rences	143
8		ssment of a Search for Stop Pair Production	1.47
		leptonic Events	147
8	8.1	Basic Event Selection and Signal Models	148
	8.2	M_{T2} -based Search Variables	148
		8.2.1 Search with $M_{T2}(lb)$	149
		8.2.2 Search with $M_{T2}(b)$	151
		8.2.3 Search with $M_{T2}(l)$	152
		8.2.4 Search Using Multiple Variants of M_{T2}	152
		8.2.5 Comment on the Stop Decays via Sleptons	154
	0.2	or Sneutrinos.	154
	8.3	Distinguishing Direct Stop Pair Production from $t\bar{t}$ +jets	154
	0.4	Production Using the Event Kinematics	154
	8.4	Summary	157 157
	Keler	ences	17/

xviii Contents

Par	t III	Studies for the Upgrade Program of the Compact Muon Solenoid Detector	
9		rade Efforts for the Compact Muon Solenoid Detector	161 163
10	Phys	ics Performance Study for the Pixel Detector	
	Phas	e-I Upgrade	165
	10.1	The Need of a Pixel Detector Upgrade	165
	10.2 10.3	The Design of the Upgraded Phase-1 Pixel Detector The 2011 $M_{T2}b$ Analysis as a Performance Study	166
		of the Pixel Phase-1 Upgrade	167
	Refe	rences	171
11		ution Studies of the CMS Electromagnetic	
	Calo	rimeter Endcap Signals	173
	11.1	Signal Losses Within the Electromagnetic	
		Calorimeter Endcaps	173
	11.2	Characteristic Variables Describing the Radiation	
		Hardness of Detector Components	175
	11.3	The Monitoring System of the Electromagnetic Calorimeter	177
	11.4	Correlation Between Light Monitoring Signals and $\mu_{\rm std}$	179
		11.4.1 Study of the Correlation for a Fixed Time Period	180
		11.4.2 Time Evolution of the Correlations	182
		with Simulation	184
	11.5	Correlations Between Light Monitoring Signals	
		and $\mu_{\rm SIC}$, a Validation	186
	11.6	Correlations Between Light Monitoring Signals	
		and the Burn-In	188
		11.6.1 Time Evolution of the Anti-correlations	189
	11.7	Summary	192
	Refe	rences	193
12	Sum	mary	195
App	endix	A: Alternatives to the Hemisphere Algorithm	
		Used in the 7 and 8 TeV Searches	199
Cur	riculu	um Vitae	209
List	of Pu	ıblications	213

Part I Introduction to Theory and Experiment

Chapter 1 Introduction to Physics at the High-Energy Frontier

Particle physics is the research field among the physics disciplines that explores the fundamental constituents of the universe. The theory describing the properties of those constituents is known as the standard model of particle physics (SM). Within the framework of the SM, three fundamental forces between particles are described: the strong, weak, and electromagnetic interactions.

The strong interaction is described by quantum chromodynamics (QCD) based on a SU(3) gauge group. Due to the self-interaction of the bosons associated to this gauge group, the gluons, the force is very short ranged, up to ranges of order of the proton radius.

The weak and electromagnetic interactions have a common description, called the electroweak theory, which is based on SU(2) and U(1) gauge groups. While the range of the electromagnetic interaction is very long-ranged, the range of the weak force is short due to the masses of the associated gauge bosons. The theory behind the masses of those gauge bosons is called electroweak symmetry breaking, which is mediated by the Higgs field. The recent observation of a new boson [1–3] seems to be, up to this writing, the last missing component of the SM, the Higgs boson.

In Tables 1.1 and 1.2 the properties of the gauge and Higgs bosons and fermions are summarized. These are all the fundamental particles within the SM.

In the following, the SM is reviewed in more detail, focusing on the important aspects for energies much larger than the proton mass equivalent. The electroweak theory and QCD are presented in Sects. 1.1 and 1.2. A short summary and experimental tests of the theory are given in Sect. 1.3 and finally, in Sect. 1.4, several limitations of the SM are discussed, hinting to the conjecture that the SM is only an effective theory, valid up to the electroweak scale.

This chapter follows the notation and argumentation of [6, 7] and is further based on [8-11].

Boson	Gauge group	Interaction	Number	Interacting particle		
Gluon (g)	SU(3) _C	Strong	8	q, g		
W^\pm	SU(2) _L	Weak	2	$\begin{array}{c} q_L, l_L, W^{\pm}, Z, \gamma, \\ h \end{array}$		
Z	$SU(2)_L \times U(1)_Y$	Weak	1	$q, l^{\pm}, \nu_L, W^{\pm}, Z, h$		
Photon (γ)	U(1) _Q	Electromagnetic	1	q, l^{\pm}, W^{\pm}		
Higgs boson (h)	-	Higgs field	1	Massive particles		
Harry (I) decreased and decreased The substitute of the decreased decreased and the decreased decreased the decreased decreased and the decreased						

Table 1.1 Properties of the SM gauge and Higgs bosons

Here, q(l) denotes quarks (leptons). The subscript L denotes left-handed particles, while the \pm signs indicate the sign of the electric charge

Table 1.2 Properties of the SM fermions: C is the color, T the weak isospin, T_3 its third component, Y the hypercharge and Q the electric charge

Type	Generation			C	T	<i>T</i> ₃	Y	Q
	1st	2nd	3rd					
Quarks	$\begin{pmatrix} u \\ d' \end{pmatrix}_L$	(c)	$\begin{pmatrix} t \\ b' \end{pmatrix}_L$	r, g,b	1/2	+1/2 -1/2	+1/3	+2/3 -1/3
		$(s')_L$	$(b')_L$			-1/2		-1/3
	u_R	c_R	t_R	r, g,b	0	0	+4/3	+2/3
	d_R	s_R	b_R	1, 5,0			-2/3	-1/3
Leptons	(ν_e)	$\left(\begin{array}{c} \nu_{\mu} \end{array}\right)$	$\left(\nu_{\mu}\right)$ $\left(\nu_{\tau}\right)$	0	1/2	+1/2 -1/2	-1	0
Leptons	$\left(\begin{array}{c} e \end{array}\right)_L$	$(\mu)_L$	$(\tau)_L$			-1/2	•	-1
	e_R	μ_R	$ au_R$	0	0	0	-2	-1

The weak quark eigenstates (q') refer to the CKM matrix [4, 5] rotated flavor eigenstate (q)

1.1 Electroweak Theory

The electroweak theory $[12-15]^1$ is a unification of the electromagnetic force, which is described by quantum electrodynamics (QED), and the weak force. The theory describes the interaction between leptons, quarks and weak gauge bosons (W^{\pm} , Z) or photons (γ), the gauge boson of QED. Its Lagrangian can be written as

$$\mathcal{L}_{EW} = -\frac{1}{4}W^{i,\mu\nu}W^{i}_{\mu\nu} - \frac{1}{4}B^{\mu\nu}B_{\mu\nu} + \overline{\psi}_{L}\gamma^{\mu}\left(i\partial_{\mu} - g\frac{1}{2}\sigma^{i}\cdot W^{i}_{\mu} - g'\frac{Y}{2}B_{\mu}\right)\psi_{L} + \overline{\psi}_{R}\gamma^{\mu}\left(i\partial_{\mu} - g'\frac{Y}{2}B_{\mu}\right)\psi_{R}$$
(1.1)

with
$$W^i_{\mu\nu} = \partial_\mu W^i_\nu - \partial_\nu W^i_\mu - g \varepsilon_{ijk} W^j_\mu W^k_\nu$$
 and $B_{\mu\nu} = \partial_\mu B_\nu - \partial_\nu B_\mu$.

¹Note, that in these papers quarks were not part of the model. The existence of quarks was suggested by [16–18].

Here, $\psi_{L/R}$ are left/right-handed fermion fields, B_{μ} is the U(1)_Y gauge field, and W_{μ}^{i} are the SU(2)_L gauge fields. The values g and g' are the coupling constants of the two gauge fields to the fermion fields. The hypercharge Y is the generator of the U(1) algebra, while the Pauli matrices fullfil the SU(2) algebra $[\sigma^{k}, \sigma^{l}] = i\varepsilon^{klm}\sigma^{m}$. The B boson couples to the hypercharge, while the W bosons couple to the weak isospin.

Comparing the SU(2) and U(1) currents with the electromagnetic one, the relation

$$Q = \frac{1}{2}Y + T_3,\tag{1.2}$$

is found: The electric charge Q can be derived from T_3 , the third component of the weak isospin, and the hypercharge Y.

The mass eigenstates of the charged and neutral currents are defined as

$$W_{\mu}^{\pm} = \frac{1}{\sqrt{2}} \left(W_{\mu}^{1} \mp i W_{\mu}^{2} \right), \qquad \begin{pmatrix} A_{\mu} \\ Z_{\mu} \end{pmatrix} = \begin{pmatrix} \cos \theta_{w} & \sin \theta_{w} \\ -\sin \theta_{w} & \cos \theta_{w} \end{pmatrix} \begin{pmatrix} B_{\mu} \\ W_{\mu}^{3} \end{pmatrix}, \tag{1.3}$$

where θ_w is called the electroweak mixing angle. The photon field is A_μ . Using again the analogy of the respective currents one can derive the relation

$$e = g\sin\theta_w = g'\cos\theta_w. \tag{1.4}$$

The W^{\pm} bosons couple to the weak isospin, and therefore only to left-handed fermions, while γ and Z bosons couple both to left- and right-handed fermions. This can be appreciated from the corresponding Feynman rules:

The vector and axial-vector couplings \boldsymbol{c}_{V}^{f} and \boldsymbol{c}_{A}^{f} of Z bosons to fermion type f are defined as

$$c_V^f = T_3^f - 2Q_f \sin^2 \theta_w, \ c_A^f = T_3^f.$$
 (1.5)

In the upper rules, one finds the projectors on left- and right-handed particles, $P_{L/R} = \frac{1}{2}(1 \mp \gamma_5)$.

Gauge Invariance and Massive Particles

It has been experimentally observed, that W and Z bosons and fermions carry mass. In principle, those masses can be introduced by hand

$$\mathcal{L}_{m} = M_{Z}^{2} Z_{\mu} Z^{\mu} + M_{W}^{2} W_{\mu}^{+} W^{-,\mu} - \left[\bar{u}_{L} M^{u} u_{R} + \bar{d}_{L} V^{\dagger} M^{d} d_{R} + \bar{e}_{L} M^{e} e_{R} + h.c. \right]. \tag{1.6}$$

The 3×3 unitary CKM matrix is denoted by V.

The mass terms within the Lagrangian as in Eq. (1.6) violate gauge invariance: The fermion mass terms mix left- and right-handed components, but those components carry different quantum numbers for the gauge fields. Also the mass terms of the gauge bosons violate gauge invariance. This can be observed by reviewing gauge transformations:

Defining T^a as the generator of the gauge group and $\alpha^a(x)$ as real numbers, a local infinitesimal SU(n) transformation acts on ψ and A^a_μ as

$$\begin{split} \psi(x) &\to \left[1 + i T^a \alpha^a(x)\right] \psi(x), \\ A^a_\mu(x) T^a &\to A^a_\mu(x) T^a + \frac{1}{g_X} \partial_\mu \alpha^a(x) T^a + f^{abc} T^a A^b_\mu(x) \alpha^c(x), \end{split}$$

with g_X being the considered gauge coupling and f^{abc} the structure constants defined by

$$[T^a, T^b] = if^{abc}T^c. (1.7)$$

For massless gauge bosons, gauge invariance is possible with the covariant derivate

$$D_{\mu} = \partial_{\mu} + ig_X T^a A^a_{\mu} \tag{1.8}$$

and the gauge field strength tensor

$$F_{\mu\nu}^{a} = \partial_{\mu}A_{\nu}^{a} - \partial_{\nu}A_{\mu}^{a} - g_{X}f_{abc}A_{\mu}^{b}A_{\nu}^{c}. \tag{1.9}$$

A Lagrangian with massive gauge bosons cannot be made invariant under these transformations.

"Unrenormalizibility" of a Gauge Theory with Massive Gauge Bosons

The propagator of the massive weak gauge boson behaves for large momentum transfer as

$$\frac{-ig_{\mu\nu} + \frac{p_{\mu}p_{\nu}}{M^2}}{p^2 - M^2 + i\epsilon} \xrightarrow[p^2 \to \infty]{} \frac{p_{\mu}p_{\nu}}{p^2M^2}.$$

Integrating over momentum space for gauge bosons leads to severe divergences. Even for a p^2 cut-off parameter, an infinite number of such parameters would be needed due to higher order diagrams. Thus, the theory would be "unrenormalizable".

Unitarity Violation

Processes contributing to the WW scattering of longitudinal polarized W bosons, W_L , are shown in Fig. 1.1. The scattering amplitude for this process scales as E^2 for high energies E:

$$|\mathcal{M}(W_L^+W_L^- \longrightarrow W_L^+W_L^-)| \underset{F \gg M_W}{\sim} E^2.$$

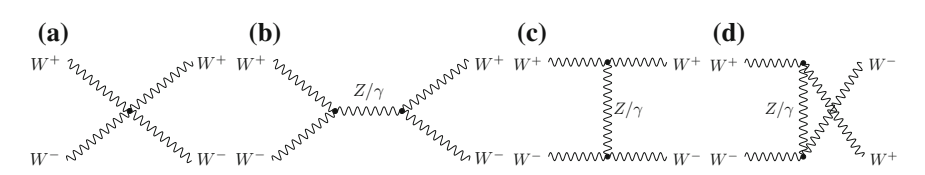


Fig. 1.1 Leading Order diagrams contributing to $W^+W^- \longrightarrow W^+W^-$ scattering. **a** Quartic coupling, **b** s-channel, **c** t-channel

Therefore, the electroweak theory of the Lagrangian in Eq. (1.1) breaks down at high energies.

1.1.1 The Electroweak Symmetry Breaking

At the end of the previous section, three problems within the electroweak theory were shown. The minimal solution to those problems is to retain the gauge symmetry in the Lagrangian, but dropping it for the physical states. This concept is known as electroweak symmetry breaking. In the following, the discussion is restricted to the case of the SM, the Higgs mechanism [19–21], sometimes also called Brout-Englert-Higgs mechanism.

The Higgs mechanism introduces a complex scalar field ϕ with Y=1 and weak isospin T=1/2:

$$\phi = \frac{1}{\sqrt{2}} \begin{pmatrix} \phi_1 + i\phi_2 \\ \phi_3 + i\phi_4 \end{pmatrix} \equiv \begin{pmatrix} \phi^+ \\ \phi^0 \end{pmatrix}$$
 (1.10)

The Lagrangian of the Higgs field can be written as

$$\mathcal{L}_{\text{Higgs}} = \left| \left(i \partial_{\nu} - \frac{g}{2} \sigma^{i} W_{\nu}^{i} - g' \frac{Y}{2} B_{\nu} \right) \phi \right|^{2} - \mu^{2} \phi^{\dagger} \phi - \lambda (\phi^{\dagger} \phi)^{2} + \mathcal{L}_{\text{Yukawa}}.$$
(1.11)

The term $V(\phi) = \mu^2 \phi^\dagger \phi + \lambda (\phi^\dagger \phi)^2$ is referred to as the Higgs potential with μ^2 being the mass parameter, and λ the four-point vertex coupling. The term $\mathcal{L}_{\text{Yukawa}}$ is discussed later in this section. All terms of Eq. (1.11) are invariant under $SU(2)_L \times U(1)_Y$ transformations.

For $\mu^2 < 0$ and $\lambda > 0$, the minimum of the potential will not be for $\phi = (0, 0)^{\top}$, but for

$$\phi^{\dagger}\phi = v^2 = -\frac{\mu^2}{\lambda}.\tag{1.12}$$

By choosing a vacuum configuration, for example

$$\langle \phi \rangle = \frac{1}{\sqrt{2}} \begin{pmatrix} 0 \\ v \end{pmatrix},\tag{1.13}$$

the electroweak symmetry is *spontaneously broken*, as the Lagrangian itself is still invariant under the symmetry, while the expansion of the potential around the vacuum state $\langle \phi \rangle$ is not. Due to the relation (1.2), the scalar field does not carry electric charge, the symmetry of QED is conserved and therefore the photon remains massless.

Inserting the vacuum state $\langle \phi \rangle$ as in Eq. (1.13) into the kinematic term of Eq. (1.11), one obtains mass terms with

$$M_W = \frac{1}{2}vg,$$
 $M_Z = \frac{1}{2}v\sqrt{g^2 + g'^2},$ $M_A = 0.$ (1.14)

Using Eq. (1.4), a relation between the W and Z boson masses is derived:

$$\frac{M_W}{M_Z} = \cos \theta_w. \tag{1.15}$$

Also fermions obtain masses by their couplings to the Higgs field, described in the term $\mathcal{L}_{\text{Yukawa}}$ of Eq.(1.11). For this, one introduces the Yukawa coupling G^f of the Higgs field to the fermion and the charge conjugate of the Higgs doublet, $\phi^c = i \sigma^2 \phi^{\dagger}$. The Lagrangian of the Yukawa coupling can then be written as

$$\mathcal{L}_{\text{Yukawa}} = -G^e \overline{E}_L \cdot \phi e_R - G^d \overline{Q'}_L \cdot \phi d_R - G^u \overline{Q}_L \cdot \phi^c u_R + h.c., \qquad (1.16)$$

where e denotes all lepton flavors, u(d) all up-(down-)type quark flavors, and E_L and Q_L are the corresponding $SU(2)_L$ doublets. Inserting the vacuum state Eq. (1.13) into this formula yields fermion masses

$$M_f = \frac{G^f v}{\sqrt{2}}. (1.17)$$

Higgs Field Self-Coupling and the Higgs Boson Mass

Expanding the scalar field ϕ around the vacuum state leads to four new fields ξ^a and h(x):

$$\phi(x) = \frac{1}{\sqrt{2}} e^{i\sigma^a \xi^a(x)/v} \begin{pmatrix} 0 \\ v + h(x) \end{pmatrix}. \tag{1.18}$$

The fields ξ^a are massless. Those unobserved states are called Goldstone bosons, as predicted by Goldstone's theorem [22, 23]. They are absorbed into the massive gauge fields, and provide the longitudinal polarization of those fields. The field h(x) describes the Higgs boson. Due to the self-coupling of the Higgs field, it acquires a mass of $M_h = \sqrt{2\lambda v^2}$.

Unitarity Violation Revisited

In Fig. 1.1, leading order diagrams contributing to the $W^+W^- \longrightarrow W^+W^-$ scattering were shown. The interaction between the W boson and the Higgs boson leads

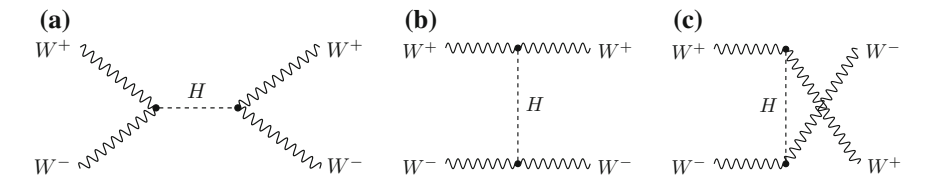


Fig. 1.2 Leading Order diagrams contributing to $W^+W^- \longrightarrow W^+W^-$ scattering via Higgs boson exchange. a s-channel, b t-channel, c u-channel

to additional diagrams as displayed in Fig. 1.2. The contribution of $|\mathcal{M}|^2$ that scaled with E^2 for the gauge boson interactions cancels exactly with the contribution from the Higgs boson exchange for high energies. The unitarity of the WW scattering for longitudinally polarized W bosons is restored.

1.2 Quantum Chromodynamics

The theory of the strong interaction between quarks and gluons, the gauge boson of the theory, is QCD [24–26].² It describes the strongest interaction among the fundamental forces, but the interaction is also short-ranged with typical ranges of order of the proton radius. The symmetry group is SU(3), the corresponding charge is called color.

So far, no free color charges have been experimentally observed. Neutral color states, the formation of hadrons, are a result of the strong interaction. Two kinds of color-neutral hadrons are observed³ (indices are denoting the color):

- Mesons are quark–anti-quark pairs $(q_i\overline{q}_i)$, have integer spins, and are bosons.
- Baryons are (anti-)quark triplets $(\varepsilon_{ijk}q^iq^jq^k, \varepsilon_{ijk}\overline{q}^i\overline{q}^j\overline{q}^k)$, have half-integer spins, and are fermions.

But first, the fundamental interaction between quarks and gluons is introduced. The QCD Lagrangian can be written as⁴

$$\mathcal{L}_{QCD} = \overline{q}_j (i\delta_{jk}\partial_\mu - g_s T^a_{jk} G^a_\mu) \gamma^\mu q_k - \frac{1}{4} G^{\mu\nu}_a G^a_{\mu\nu}, \tag{1.19}$$

where q is the quark field, G^a_μ the gluon field, and g_s the strong coupling. The indices j,k denote the color charge, and $G^a_{\mu\nu}=\partial_\mu G^a_\nu-\partial_\nu G^a_\mu-g_s\,f_{abc}G^b_\mu G^c_\nu$. The SU(3) algebra has eight generators T^a and therefore eight types of gluons exist.

²The mentioned references introduced the gluon or the SU(3) algebra leading to the color charge. Many more people contributed to the development of QCD.

³Recent results of the LHCb experiment show the existence of a state not belonging to these two classes [27].

⁴The quark masses are omitted as they are already explained in Sect. 1.1.1.

In principle, the Lagrangian would additionally have a gauge fixing term in order to properly define the gluon propagator. This term would then be accompanied by a ghost field term. As these ghost fields are not physical, they are not discussed any further.

1.2.1 The Strong Coupling Constant: "Running" of α_s

Any interaction within QCD is proportional to powers of g_s^2 . Therefore we define the strong coupling constant

$$\alpha_s = \frac{g_s^2}{4\pi}.\tag{1.20}$$

In perturbation theory, the calculation of interaction amplitudes will contain loop diagrams for higher order contributions. The integration over those loop momenta can lead to divergencies for the limit of infinite loop momenta. These divergencies are usually called *ultraviolet* (*UV*) divergencies. In particle physics theory, these divergencies are controlled by renormalization techniques: The bare parameters of the theory, like the masses, field strengths, and coupling constants are modified, such that they contain counterterms to absorb these divergencies. In the context of renormalization, an unphysical scale μ_R , the renormalization scale, has to be introduced. As this scale μ_R is not physical, any physical observable does not depend on it. Details about renormalization can be found elsewhere, for example in [10].

The physical observables themselves are not constants, but depend on the momentum transfer Q^2 , at which the observable is probed. The dependency is ruled by the renormalization group equation (RGE) [28]. For α_s , on which several observables depend on, the RGE is

$$\mu^2 \frac{\partial \alpha_s(\mu^2)}{\partial \mu^2} = -\alpha_s \left[\beta_0 \frac{\alpha_s}{4\pi} + \beta_1 \left(\frac{\alpha_s}{4\pi} \right)^2 + \mathcal{O}(\alpha_s^3) \right]$$
 (1.21)

with β_i being constants depending on the gauge group. For example, $\beta_0 = 11 - \frac{2}{3}n_f$, where n_f is the number of quark flavors.

Solving Eq. (1.21) at leading order results in

$$\alpha_s(Q^2) = \frac{\alpha_s(Q_0^2)}{1 + \alpha_s(Q_0^2)\beta_0 \ln(Q^2/Q_0^2)},$$
(1.22)

where α_s has to be determined by measurements for a reference value $\alpha_s(Q_0^2)$.

For high momentum transfer (or short distances), the coupling constant becomes small as $\beta_0 > 0$. Thus, quarks and gluons can be regarded as free at short distances. This behavior is called *asymptotic freedom* [29, 30]. At hadron colliders, the processes of interest occur at large Q^2 . Hence, perturbation theory can be used to calculate observables and get accurate predictions.

If, however, the momentum transfer becomes small ($Q \rightarrow \Lambda_{QCD} = 90.6 \pm 3.4 \,\text{MeV}^5$ [31]), α_s gets very large and perturbation theory breaks down. This is called *confinement*. This effect prohibits the existence of free quarks, hadrons are formed.

1.2.2 Infrared Divergencies

In the last section, the evolution of the strong coupling constant due to the absorption of UV divergencies was presented. There exists also another category of divergencies, classified as *infrared* (*IR*). These occur as virtual corrections for soft loop momenta in loop diagrams, but also as real emission in the soft or collinear limit, meaning that the emitted particle has very low energy or is collinear to the emitting particle. In experiments, these effects are not measureable as a soft particle or two collinear particles are not resolvable. Hence, observables that are predicted by QCD should be invariant (*IR-safe*) under these effects, for example by the cancellation between the virtual and real emissions.

1.2.3 The Structure of the Proton

This thesis is mainly based on data collected in proton-proton (pp) collisions. Therefore, a good understanding about the structure of the proton is required. The proton itself is not a fundamental particle, it is a composite hadron made out of three valence quarks $(|p\rangle = |uud\rangle)$, as well as sea-quark pairs and gluons. The parton model of the proton assumes that each constituent of the proton, further called partons, carries a certain momentum fraction ξ of the proton's momentum.

For pp collisions at the LHC, where large momentum transfers are expected, the partons involved in the hard scatter are approximately free and independent from the proton structure. The long-distance behavior of the proton, described by the parton density function (PDF), $f_a(\xi, \mu_F^2)$, and the hard scatter process factorize:

$$\sigma(pp \to X) = \int_0^1 dx_1 \int_0^1 dx_2 \sum_{a,b} f_a(x_1, \mu_F^2) f_b(x_2, \mu_F^2) \hat{\sigma}^{(ab \to X)}(Q^2, \mu_F^2),$$
(1.23)

where $\hat{\sigma}^{(ab \to X)}$ is the hard-scatter cross section. The new introduced factorization scale μ_F sets the scale between the hard physics and the resolution of the partons a, b. At leading order, the PDF describes the probability of finding a parton a with the momentum fraction ξ within the proton. Collinear and soft emissions below μ_F

⁵The value has been calculated in the \overline{MS} scheme with six quark flavors. Using only five quark flavors, the value is $\Lambda_{\rm OCD}=214\pm7$ MeV.

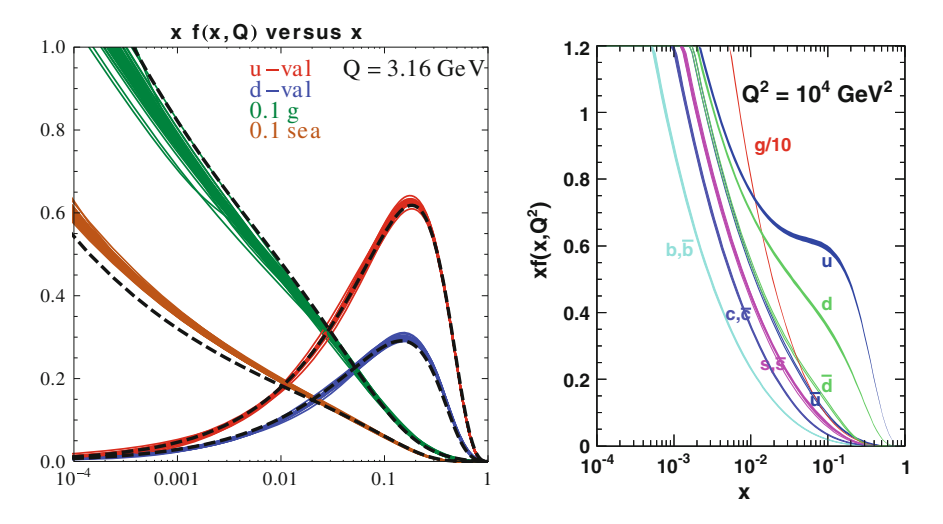


Fig. 1.3 Scale dependence on two sets of PDFs: Left for the CT10 NNLO PDF set at $Q^2 = 10 \text{ GeV}^2$ [35]. The dashed curves are the central fits of the CT10 NLO PDFs. Right for the MSTW2008NLO PDF set at $Q^2 = 10^4 \text{ GeV}^2$ [36]

are unresolvable and thus inside the PDF. As the PDF absorbs the divergencies of those emissions, the leading-order picture of the PDF does not fully apply.

The PDFs themselves cannot be calculated within QCD, they need to be measured experimentally for a given scale. The evolution of PDFs as a function of μ_F^2 is described by the DGLAP equation [32–34]

$$\mu_F^2 \frac{\partial f_a(x, \mu_F^2)}{\partial \mu_F^2} = \sum_b \frac{\alpha_s(\mu_F^2)}{2\pi} \int_x^1 \frac{dz}{z} P_{ab}(z) f_b\left(\frac{x}{z}, \mu_F^2\right)$$
(1.24)

with $P_{ab}(z)$ being the splitting function representing the probability of parton a to split $a \to bc$ with longitudinal momentum $p_b = zp_a$.

In Fig. 1.3, the scale dependence is shown for two sets of PDFs obtained by different analyses.

1.2.4 The Physics of Proton-Proton Collisions

So far, the hard interaction between partons, described by perturbative QCD, and its convolution with the proton structure, from which the partons originate, were discussed.

However, a collision event is far more complicated as illustrated in Fig. 1.4. In this section, the missing parts for describing a full event will be introduced. It is based on the discussion in [11, 37].

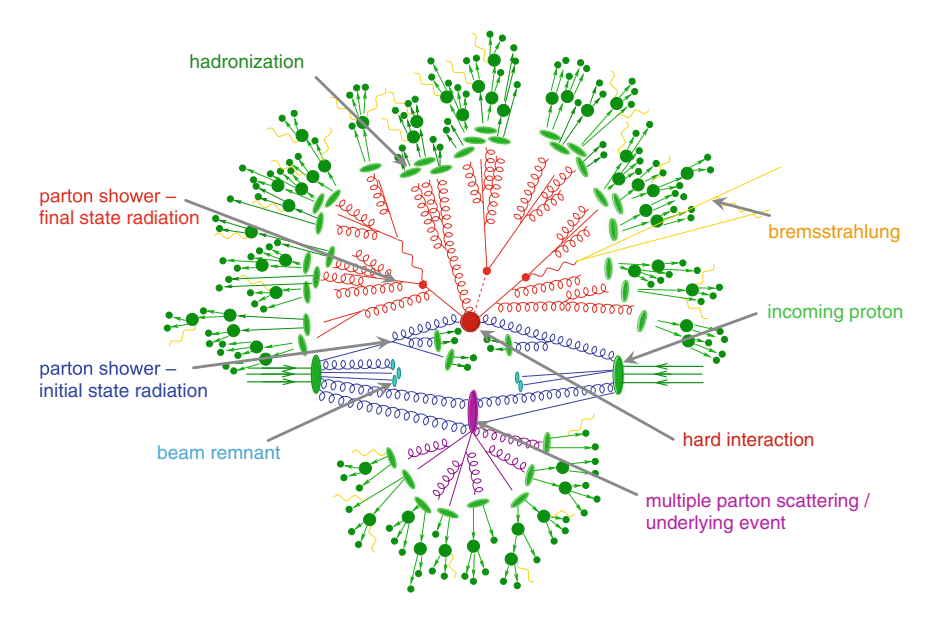


Fig. 1.4 Illustration of a pp collision event. Taken from [38] with added labels

Parton Shower

Before and after the hard scatter, partons emit gluons or split into quarks. This process is called parton shower and is also known as initial (final) state radiation (ISR/FSR), depending if the emission happens before (after) the hard interaction. Emitted photons are also called bremsstrahlung. The idea for the computation of the parton shower is that the matrix element of a parton emission is largest, if the emission is either soft or collinear. In this approximation one can determine the cross section of a n+1 parton final state, $d\sigma_{n+1}$, from the cross section of the n parton final state before the parton emission, $d\sigma_n$, via

$$d\sigma_{n+1} = d\sigma_n \frac{dQ^2}{Q^2} dz \frac{\alpha_s}{2\pi} \hat{P}_{ab}(z), \qquad (1.25)$$

where $\hat{P}_{ab}(z) = P_{ab}(z)$ is the splitting function for z < 1.

The probability of a parton to evolve from momentum scale t to t_c without a splitting $a \to bc$ is given by the Sudakov factor

$$\Delta(t) = \exp\left\{-\int_{t_c}^{t} \frac{dt'}{t'} \int_{\varepsilon(t')}^{1-\varepsilon(t')} dz \frac{\alpha_s}{2\pi} \hat{P}_{ab}(z)\right\}. \tag{1.26}$$

The cutoff t_c is the scale where hadronization becomes important $(t_c \gtrsim \Lambda_{\rm QCD}^2)$.

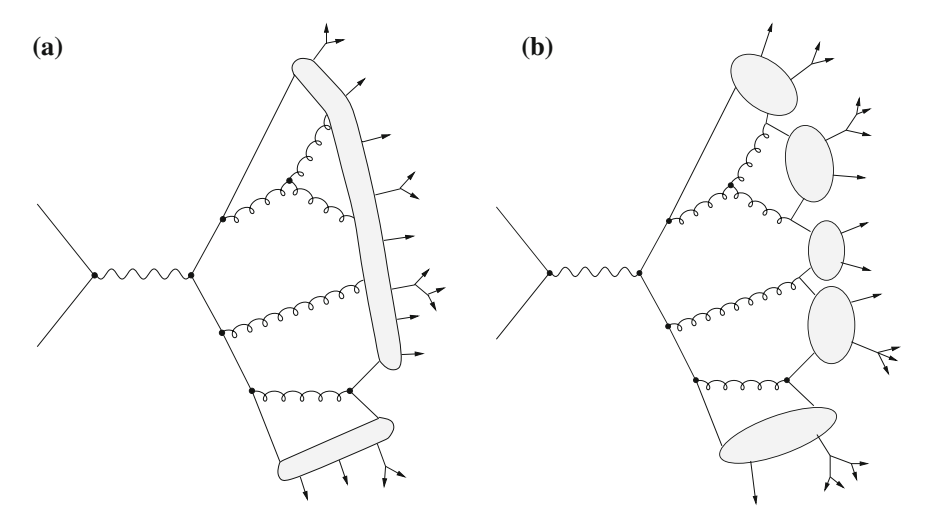


Fig. 1.5 Sketches of hadronization models. a String model, b Cluster model [37]

Hadronization

There exist no free quarks or gluons due to confinement. After the parton shower the existing partons have such low virtualities (Q^2) that the strong coupling constant is very large and the partons begin to build stable hadrons. This process is called hadronization and cannot be described by perturbative QCD. Only phenomenological models are available. The idea is that gluons and quarks build color-neutral hadrons, and unstable hadrons decay into stable hadrons, leptons and photons. In experiments, the cluster of hadrons around the direction of a parton from the hard interaction is called jet, see also Sect. 5.7. Two models of hadronization are commonly used by simulation programs, the *string* model [39–41] and the *cluster* model [42], illustrated in Fig. 1.5.

The string model assumes that the color field between $q\overline{q}$ pairs collapses into a string of uniform energy density at the end of the parton shower. This string is broken up by quarks or antiquarks, while gluons produce 'kinks' in the string. These kinks have local energy equal to the gluon energy. In the model, a string then breaks into hadrons through spontaneous $q\overline{q}$ pair creation. While meson production is explained naturally in this model, baryon creation is more complicated [11].

The second popular model, the cluster model, requires all gluons at the end of the shower to split into $q\overline{q}$ pairs. Then, clusters are formed by connecting neighboring quarks to color-singlets. The clusters decay isotropically into a pair of hadrons. The energy needed for the hadron formation by the $q\overline{q}$ production is extracted from the cluster field. Clusters with too low energy will decay into only one hadron, while heavy clusters can split into lighter daughter clusters [11].

Multiple Parton Interaction and Underlying Event

Besides the hard interaction, there can be secondary interactions of other partons of the protons. These processes are called underlying event (UE). The beam remnants usually have very small momentum transfers that they need to be described by non-perturbative QCD. If the secondary scatter interaction is still hard enough to be described by perturbative QCD, the process is called multiple parton interaction (MPI).

The UE is often modeled by so-called minimum bias events. Minimum bias events is an experimental expression: The decision of recording an event by a detector is usually based on some trigger condition. If minimal trigger conditions are met like requiring a minimal energy deposit in the detector, the recorded event is called minimum bias. These events basically correspond to soft inelastic collision events due to the cross section of hadron-hadron scattering.

1.3 Summary and Experimental Tests of the Standard Model

In Sects. 1.1 and 1.2, the underlying theories of the SM were reviewed. The total description of the SM is the combination of these theories using a $SU(3)_C \times SU(2)_L \times U(1)_Y$ gauge group.

The hard interaction can be described using the total Lagrangian, which is

$$\mathcal{L}_{SM} = \mathcal{L}_{EW} + \mathcal{L}_{Higgs} + \mathcal{L}_{OCD}$$
 (1.27)

with the single terms described by Eqs. (1.1), (1.11), (1.16), and (1.19).

The properties of the bosons and fermions were already summarized in Tables 1.1 and 1.2. As right-handed neutrinos have no quantum numbers at all, they are considered as non-existing in the SM.

1.3.1 Experimental Tests of the Standard Model

The SM leaves several parameters free, they have to be determined by experiments. Among those are the gauge, Higgs and Yukawa couplings and the Higgs mass parameter

$$g, g', g_s, \lambda, \mu, G^f$$
.

All parameters of the SM can be measured in several ways. Usually these measurements are indirect and therefore depend on the underlying theory itself. Thus, measuring several observables with high precision to deduce the same parameter results, on the one hand, on a higher accuracy of the parameter value, but also provides, on the other hand, a test of the theory itself as the measurements should be compatible with each other.

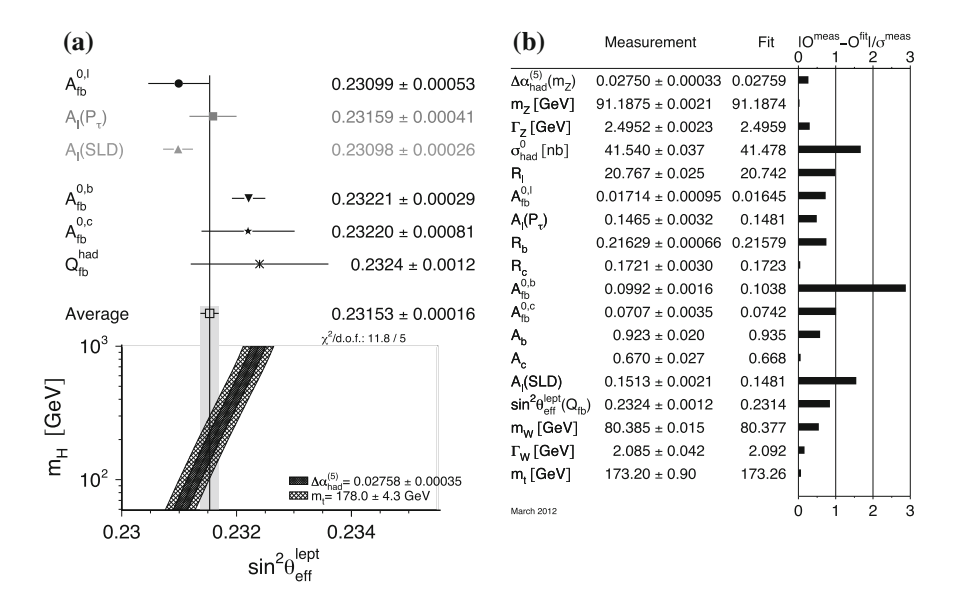


Fig. 1.6 Examples of experimental tests of the SM. **a** Determination of the electroweak mixing angle from several forward-backward asymmetry measurements and its constraint on the Higgs boson mass [43]. **b** Agreement between measured quantities and their values from the global SM fit to electroweak precision data [44]

An example is shown in Fig. 1.6a: Measurements of forward-backward asymmetry parameters for leptonic or quark couplings are combined. These asymmetries depend on c_V^f and c_A^f , Eq. (1.5), and one can deduce the weak mixing angle. The result can be used further, to constrain other parameters. In the example of Fig. 1.6a, the Higgs boson mass dependence on the weak mixing angle can be used to constrain the mass.

Considering several measurements together, the consistency of the SM can be tested. Such a consistency test is the global fit to electroweak precision data by LEP and SLC [43, 44], shown in Fig. 1.6b. The precision of the measurements ranges from 10^{-3} for strong variables like α_s , 10^{-5} – 10^{-4} for weak quantities, up to 10^{-10} for the electromagnetic coupling constant [31].

These studies are continued by present experiments. A measurement of the strong coupling constant α_s using a three-to-two jet ratio is shown in Fig. 1.7a, for example. Some of these studies are the first measurements performed, like tests on the new observed Higgs boson-like particle. For instance, the measurement of the vector boson and fermion couplings to the Higgs boson is shown in Fig. 1.7b.

Newest results from the large LHC experiments can be found in [47], comprehensive summaries and combinations are performed by the Particle Data Group [31].

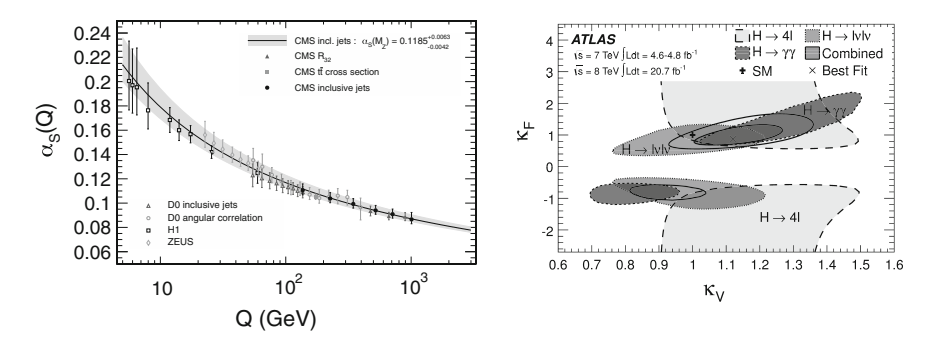


Fig. 1.7 Examples of present studies on the SM physics. a Measurement of α_s and comparison to previous measurements by the CMS experiment [45]. b Measurement of vector boson and fermion coupling factors to the Higgs boson (observed at \sim 126 GeV) by the ATLAS experiment [46]

1.4 Limitations of the Standard Model

In the previous section, experimental tests of the SM showed good agreement between theoretical predictions and experimental measurements. Despite this tremendous success, the SM is not the final theory of particle physics, as several theoretical questions and experimental observations cannot be answered by it. Below is a list of questions, which are not answered by the SM.

• The SM is a theory describing the strong, and electroweak forces. There exists no consistent quantum theory of gravitation between fundamental particles. Gravitational effects are expected to be important at the Planck scale

$$M_P = \sqrt{\frac{\hbar c}{8\pi G}} \approx 2.4 \times 10^{18} \text{ GeV}.$$
 (1.28)

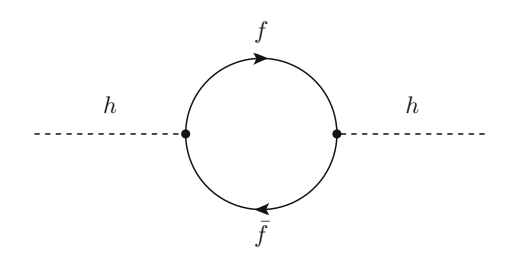
This scale is much larger than the electroweak scale $v \sim 246$ GeV, therefore gravitational effects cannot be observed at accelerators so far.

 The extreme mass scale difference between the electroweak and the Planck scale seems unnatural. The different scales create an unattractiveness called the *hierar-chy problem*. Calculating fermionic loop corrections to the Higgs boson mass, as sketched in Fig. 1.8, yields mass corrections of

$$\delta M_h^2|_f = -\frac{(G^f)^2}{8\pi^2} \left[\Lambda^2 - \mathcal{O}\left(M_f^2 \ln \frac{\Lambda}{M_f}\right) \right]. \tag{1.29}$$

Here, Λ is the UV cutoff scale. For the SM it is usually around M_P , the scale where gravitation becomes important. In order to achieve a small mass of $M_h \sim 125$ GeV, one requires extreme fine-tuning in the renormalization process.

Fig. 1.8 Fermion loop contribution to the Higgs boson mass



- Recent observations of neutrino oscillations have established that at least two
 neutrino generations have mass [48–51] while they are assumed to be massless in
 the SM.
- There are several astrophysical and cosmological observations suggesting the existence of dark matter [52, 53]. The baryonic mass that we can observe makes out only 4% of the energy of the universe. The SM fails to provide a particle candidate for dark matter. Even more obscure is the concept of dark energy.
- During the creation of the universe, there should have been (almost) equal amounts of matter and antimatter, yet we only observe clusters of matter. The SM cannot explain this large matter-antimatter asymmetry observed in the universe.
- The theory of QCD allows for a CP violating phase [54, 55]. Measurements show that this phase must be extremely small or even zero. There is no natural explanation for this.
- The SM has 19 free parameters⁶ needed to be determined by experiments. The question is, if these parameters are fundamentally independent or interconnected.

This list could be extended with several more questions: Why is there such a hierarchy among the quark masses? Why are there three families? Hence, the SM is not the final theory. As the SM explains most of the phenomena observed so far with high accuracy, it is an effective theory valid up to the electroweak scale.

In the following chapter, a possible extension of the SM will be introduced, which will allow to "fix" several of the above problems.

References

- ATLAS Collaboration, Observation of a new particle in the search for the Standard Model Higgs boson with the ATLAS detector at the LHC. Phys. Lett. B 716, 1 (2012). doi:10.1016/j. physletb.2012.08.020, 1207.7214
- 2. CMS Collaboration, Observation of a new boson at a mass of 125 GeV with the CMS experiment at the LHC. Phys. Lett. B 716, 30 (2012). doi:10.1016/j.physletb.2012.08.021. arXiv:1207.7235
- 3. CMS Collaboration, Observation of a new boson with mass near 125 GeV in pp collisions at $\sqrt{s} = 7$ and 8 TeV. JHEP **06**, 081 (2013), doi:10.1007/JHEP06(2013)081, arXiv:1303.4571
- N. Cabibbo, Unitary symmetry and leptonic decays. Phys. Rev. Lett. 10, 531 (1963). doi:10. 1103/PhysRevLett.10.531

⁶This number could be increased, for example by introducing mixing angles in the leptonic sector.

References 19

5. M. Kobayashi, T. Maskawa, CP violation in the renormalizable theory of weak interaction. Prog. Theor. Phys. **49**, 652 (1973). doi:10.1143/PTP.49.652

- 6. V. Chiochia, G. Dissertori, T. Gehrmann, Phenomenology of particle physics 1. Lecture notes (2009)
- 7. V. Chiochia, G. Dissertori, T. Gehrmann, Phenomenology of particle physics 2. Lecture notes (2010)
- 8. F. Halzen, A.D. Martin, Quarks and Leptons—An Introductory Course in Modern Particle Physics (Wiley, 1984)
- 9. I. Aitchison, A. Hey, *Gauge Theories in Particle Physics: A Practical Introduction*, (Institute of Physics Publishing, 1989)
- 10. M.E. Peskin, D.V. Schroeder, *An Introduction to Quantum Field Theory* (Addison-Wesley Advanced Book Program, 1995)
- 11. G. Dissertori, I. Knowles, M. Schmelling, Quantum Chromodynamics—High Energy Experiments and Theory (Oxford university press, 2009)
- S. Glashow, Partial symmetries of weak interactions. Nucl. Phys. 22, 579 (1961). doi:10.1016/ 0029-5582(61)90469-2
- A. Salam, J.C. Ward, Electromagnetic and weak interactions. Phys. Lett. 13, 168 (1964). doi:10. 1016/0031-9163(64)90711-5
- 14. A. Salam, Weak and electromagnetic interactions. Conf. Proc. C **680519**, 367 (1968)
- S. Weinberg, A model of leptons. Phys. Rev. Lett. 19, 1264 (1967). doi:10.1103/PhysRevLett. 19.1264
- M. Gell-Mann, A schematic model of baryons and mesons. Phys. Lett. 8, 214 (1964). doi:10. 1016/S0031-9163(64)92001-3
- G. Zweig, An SU₃ model for strong interaction symmetry and its breaking. Version 1, CERN TH-401 (1964)
- G. Zweig, An SU₃ model for strong interaction symmetry and its breaking. Version 2, CERN TH-412 (1964) in: Developments in the Quark Theory of Hadrons, ed. by D.B. Lichtenberg, S.P. Rosen (Hadronic press, 1980)
- 19. F. Englert, R. Brout, Broken symmetry and the mass of gauge vector mesons. Phys. Rev. Lett. 13, 321 (1964). doi:10.1103/PhysRevLett.13.321
- P.W. Higgs, Broken symmetries, massless particles and gauge fields. Phys. Lett. 12, 132 (1964). doi:10.1016/0031-9163(64)91136-9
- 21. P.W. Higgs, Broken symmetries and the masses of gauge bosons. Phys. Rev. Lett. 13, 508 (1964). doi:10.1103/PhysRevLett.13.508
- 22. J. Goldstone, Field theories with superconductor solutions. Nuovo Cimento 19, 154 (1961). doi:10.1007/BF02812722
- J. Goldstone, A. Salam, S. Weinberg, Broken symmetries. Phys. Rev. 127, 965 (1962). doi:10. 1103/PhysRev.127.965
- M. Gell-Mann, Symmetries of baryons and mesons. Phys. Rev. 125, 1067 (1962). doi:10.1103/ PhysRev.125.1067
- M. Han, Y. Nambu, Three triplet model with double SU(3) symmetry. Phys. Rev. 139, B1006 (1965). doi:10.1103/PhysRev.139.B1006
- O. Greenberg, Spin and unitary spin independence in a paraquark model of baryons and mesons. Phys. Rev. Lett. 13, 598 (1964). doi:10.1103/PhysRevLett.13.598
- LHCb Collaboration, Observation of the resonant character of the Z(4430)⁻ state, Phys. Rev. Lett. 112, 222002 (2014). doi:10.1103/PhysRevLett.112.222002. arXiv:1404.1903. See also BELLE collaboration, Phys. Rev. Lett. 100, 142001 (2008)
- 28. E.C.G. Stückelberg, A. Petermann, Normalization of constants in the quanta theory. Helvetica Physica Acta **26**, 499 (1953)
- H.D. Politzer, Reliable perturbative results for strong interactions? Phys. Rev. Lett. 30, 1346 (1973). doi:10.1103/PhysRevLett.30.1346
- D.J. Gross, F. Wilczek, Ultraviolet behavior of nonabelian gauge theories. Phys. Rev. Lett. 30, 1343 (1973). doi:10.1103/PhysRevLett.30.1343

- Particle Data Group Collaboration, Review of particle physics. Chin. Phys. C 38, 090001 (2014). doi:10.1088/1674-1137/38/9/090001
- G. Altarelli, G. Parisi, Asymptotic freedom in parton language. Nucl. Phys. B 126, 298 (1977). doi:10.1016/0550-3213(77)90384-4
- 33. Y.L. Dokshitzer, Calculation of the structure functions for deep inelastic scattering and e^+e^- annihilation by perturbation theory in quantum chromodynamics. Sov. Phys. JETP **46**, 641 (1977)
- 34. V. Gribov, L. Lipatov, Deep inelastic e p scattering in perturbation theory. Sov. J. Nucl. Phys. **15**, 438 (1972)
- J. Gao et al., The CT10 NNLO global analysis of QCD. Phys. Rev. D 89, 033009 (2014). doi:10.1103/PhysRevD.89.033009. arXiv:1302.6246
- A. Martin et al., Parton distributions for the LHC. Eur. Phys. J. C 63, 189 (2009). doi:10.1140/epjc/s10052-009-1072-5. arXiv:0901.0002
- 37. R.K. Ellis, W.J. Stirling, B. Webber, *QCD and Collider Physics*, Cambridge Monographs on Particle Physics, Nuclear Physics Cosmology, vol.8 1996. (Cambridge University Press, 2003)
- 38. A. Schaelicke et al., Event generator for particle production in high-energy collisions. Prog. Part. Nucl. Phys. **53**, 329 (2004). doi:10.1016/j.ppnp.2004.02.031. arXiv:hep-ph/0311270
- B. Andersson, G. Gustafson, B. Söderberg, A general model for jet fragmentation. Z. Phys. C 20, 317 (1983). doi:10.1007/BF01407824
- B. Andersson et al., Parton fragmentation and string dynamics. Phys. Rept. 97, 31 (1983). doi:10.1016/0370-1573(83)90080-7
- T. Sjöstrand, Jet fragmentation of nearby partons. Nucl. Phys. B 248, 469 (1984). doi:10.1016/ 0550-3213(84)90607-2
- 42. B. Webber, A QCD model for jet fragmentation including soft gluon interference. Nucl. Phys. B 238, 492 (1984). doi:10.1016/0550-3213(84)90333-X
- 43. ALEPH, DELPHI, L3, OPAL, SLD, LEP Electroweak, SLD Electroweak, SLD Heavy Flavour Collaboration, Precision electroweak measurements on the *Z* resonance, Phys. Rept. 427 (2006) 257, doi:10.1016/j.physrep.2005.12.006, arXiv:hep-ex/0509008
- ALEPH, DELPHI, L3, OPAL, LEP Electroweak Collaboration, Electroweak measurements in electron-positron collisions at w-boson-pair energies at LEP. Phys. Rep. 532 (2013) 119, doi:10.1016/j.physrep.2013.07.004, arXiv:1302.3415. Latest plots taken from http://lepewwg. web.cern.ch/LEPEWWG/plots/lep2_2013/
- 45. CMS Collaboration, Constraints on parton distribution functions and extraction of the strong coupling constant from the inclusive jet cross section in pp collisions at $\sqrt{s} = 7$ TeV, arXiv:1410.6765. Submitted to EJPC
- ATLAS Collaboration, Measurements of Higgs boson production and couplings in diboson final states with the ATLAS detector at the LHC. Phys. Lett. B 726 (2013). 88, doi:10.1016/j. physletb.2013.08.010, arXiv:1307.1427
- 47. http://aliceinfo.cern.ch/ArtSubmission/publications, https://twiki.cern.ch/twiki/bin/view/AtlasPublic, https://twiki.cern.ch/twiki/bin/view/CMSPublic/PhysicsResults, http://lhcbproject.web.cern.ch/lhcbproject/CDS/cgi-bin/index.php
- 48. Super-Kamiokande Collaboration, Evidence for oscillation of atmospheric neutrinos. Phys. Rev. Lett. 81, 1562 (1998). doi:10.1103/PhysRevLett.81.1562. arXiv:hep-ex/9807003
- SNO Collaboration, Direct evidence for neutrino flavor transformation from neutral current interactions in the sudbury neutrino observatory. Phys. Rev. Lett. 89, 011301 (2002). doi:10. 1103/PhysRevLett.89.011301. arXiv:nucl-ex/0204008
- MINOS Collaboration, Observation of muon neutrino disappearance with the MINOS detectors and the NuMI neutrino beam. Phys. Rev. Lett. 97, 191801 (2006).doi:10.1103/PhysRevLett. 97.191801, arXiv:hep-ex/0607088
- 51. K2K Collaboration, Measurement of neutrino oscillation by the K2K experiment. Phys. Rev. D 74, 072003 (2006). doi:10.1103/PhysRevD.74.072003, arXiv:hep-ex/0606032
- 52. F. Zwicky, Die Rotverschiebung von extragalaktischen Nebeln, Helvetica Physica Acta 6, 110 (1933). doi:10.1007/s10714-008-0707-4. doi-link redirects to republication in Gen. Relativ. Gravitat. 41(207) 2009, an English translation

References 21

53. Planck Collaboration, Planck 2013 results. XVI. Cosmological parameters. Astron. Astrophys. (2014) doi:10.1051/0004-6361/201321591, arXiv:1303.5076

- 54. C.G. Callan Jr, R.F. Dashen, D.J. Gross, The structure of the gauge theory vacuum. Phys. Lett. B 63, 334 (1976). doi:10.1016/0370-2693(76)90277-X
- 55. R. Jackiw, C. Rebbi, Vacuum periodicity in a yang-mills quantum theory. Phys. Rev. Lett. 37, 172 (1976). doi:10.1103/PhysRevLett.37.172

Chapter 2 Physics Beyond the Standard Model: Supersymmetry

In this chapter, one model for physics beyond the SM is introduced: supersymmetry (SUSY). As it will be shown, this model will "solve" several of the problems mentioned in Sect. 1.4.

The concept behind SUSY is quite simple: There exists a symmetry relating fermions and bosons, or to be more precise: There exists an operator changing the spin of a particle by 1/2. As this operator changes only the spin, all superpartners of the SM particles should already have been observed, as they would have the same masses. This is clearly not the case. However, an escape to this is SUSY breaking, which can lead to larger masses for the superpartners.

The transformation between fermions and bosons can be simply expressed as

$$Q|b\rangle = |f\rangle, \qquad Q|f\rangle = |b\rangle,$$
 (2.1)

where Q is the symmetry operator, $|f\rangle$ a fermionic state, and $|b\rangle$ a bosonic state.

The operator Q itself must carry spin 1/2 and is fermionic. This symmetry operator¹ must satisfy the following algebra [2, 3]:

$$\{Q_{\alpha}, Q_{\beta}^{\dagger}\} = 2\sigma_{\alpha\beta}^{\mu} P_{\mu}, \tag{2.2}$$

$$\{Q_{\alpha}, Q_{\beta}\} = \{Q_{\alpha}^{\dagger}, Q_{\beta}^{\dagger}\} = 0,$$
 (2.3)

$$[P^{\mu}, Q_{\alpha}] = [Q_{\beta}^{\dagger}, P^{\mu}] = 0,$$
 (2.4)

$$[M_{\mu\nu}, Q_{\alpha}] = \frac{1}{2} (\sigma_{\mu\nu})_{\alpha}^{\beta} Q^{\beta}, \qquad (2.5)$$

with $\sigma^{1,2,3}$ being the Pauli matrices, σ^0 the identity matrix, and α , β being spinor indices. The generator of the translation and Lorentz groups are P_{μ} and $M_{\mu\nu}$, respectively, and $(\sigma_{\mu\nu})^{\beta}_{\alpha} = \frac{1}{4}((\sigma_{\mu})_{\alpha\gamma}(\sigma_{\nu})^{\gamma\beta} - (\sigma_{\nu})_{\alpha\gamma}(\sigma_{\mu})^{\gamma\beta})$.

¹The representation here is the so-called N = 1 supersymmetry, see for example [1].

[©] Springer International Publishing Switzerland 2015

²³

Equation (2.5) simply states that Q_1 (Q_2) changes the z component of the spin by $+\frac{1}{2}$ ($-\frac{1}{2}$). Similarly, Q_1^{\dagger} (Q_2^{\dagger}) changes the z component of the spin by $-\frac{1}{2}$ ($+\frac{1}{2}$). As Q has to commute with the Hamiltonian (it is a symmetry operator), so has its anticommutator: the Eq. (2.2) follows, as the anticommutator has to be a conserved spin-1 operator, and therefore $\sim P_{\mu}$. In principle, states with spins between -2 up to 2 are allowed, thus up to eight SUSY operators Q are possible, since an operator cannot be applied twice (follows from Eq. (2.3)). The discussion in this thesis is restricted to SUSY with one such operator. The symmetry operator Q is the only possible extension to the Poincaré group (follows from the commutator relations of Eqs. (2.4) and (2.5) and [2, 3]).

In theory, the fields of the SM particles and their supersymmetric partners can be arranged into supermultiplets. As the symmetry operators commute with the generators of the gauge group, all particles within the same supermultiplet have the same electric, weak, and color charges. An elegant formulation of SUSY can be obtained using the superspace formulation. One displays all fields within a supermultiplet in one object, the superfield [4]. While we do not engage in the discussion of superfields here (for more details, see for instance [5]), we want to mention that the properties of SUSY can be derived directly in this formulation, such as the fact that the numbers of degrees of freedom for a boson field and its fermion partner field have to be identical. This argument will also lead to the introduction of the non-propagating auxiliary fields F and D, as discussed later.

The naming convention of the partner fields, that will be used hereafter, is simply constructed out of the names of the SM partner fields: for fermions, the partners will be called *sfermions*, like squarks for quark partners.² For gauge and Higgs bosons, the partners are denoted with an appended *ino*, like higgsino for the Higgs boson partner. The symbol for the partner particle has the same letter with a tilde, for example the gluino \tilde{g} is the partner particle of the gluon g.

In the following, the basic principles of the supersymmetric theory will be introduced in Sect. 2.1. The consequences on the Higgs sector are reviewed in Sect. 2.2, and on the masses of the supersymmetric particles in Sect. 2.3. Also, the SM problems from Sect. 1.4 are revisited in Sect. 2.4. Possible experimental signatures of SUSY will be discussed in Chap. 3.

This and the following chapters are mainly based on [5-7].

2.1 The Minimal Supersymmetric Standard Model

In its minimal form of adding one supersymmetric operator on top of the SM theory, the extended theory is called the Minimal Supersymmetric Standard Model (MSSM).

The Lagrangian of the unbroken MSSM can be written as

$$\mathcal{L}_{\text{MSSM}}^{\text{unbroken}} = \mathcal{L}_{\text{kin}} + \mathcal{L}_{\text{chiral}} - V. \tag{2.6}$$

²For the name of flavored squarks, we omit the word *quark* (that is *stop* instead of *stop quark* or *top squark*). The same holds for the word *boson*.

The Kinematic Part of the Lagrangian

The kinematic term of Eq. (2.6) can be written as

$$\mathcal{L}_{kin} = -D^{\mu}\phi^{*i}D_{\mu}\phi_{i} - i\psi^{\dagger i}\bar{\sigma}^{\mu}D_{\mu}\psi_{i} - \frac{1}{4}F^{a}_{\mu\nu,j}F^{\mu\nu,a}_{j} - i\lambda^{\dagger a}_{j}\bar{\sigma}^{\mu}\nabla_{\mu}\lambda^{a}_{j} - \sqrt{2}g_{j}\left[(\phi^{*i}T^{a}_{j}\psi_{i})\lambda^{a}_{j} + \lambda^{\dagger a}_{j}(\psi^{\dagger i}T^{a}_{j}\phi_{i})\right]. \tag{2.7}$$

Here, ψ denotes the fermion fields and ϕ its partner fields; the index i runs over all flavors and chiralities. The gauge boson and its partner fields are A^a_μ and λ^a , respectively, with couplings g_j and generators T^a_j . The index j denotes the gauge group. In this and following equations, we apply the Einstein notation for summing over indices appearing twice. The field strength tensors $F^a_{\mu\nu}$ are known from Eq. (1.9) as well as the covariant derivatives D_μ from Eq. (1.8). The covariant derivative for the gaugino fields, ∇_μ , is defined as

$$\nabla_{\mu}\lambda^{a} = \partial_{\mu}\lambda^{a} - gf^{abc}A^{b}_{\mu}\lambda^{c}. \tag{2.8}$$

The gauge couplings are the same for the SM particles and their supersymmetric partner particles.

The Chiral Part of the Lagrangian

In order to obtain the chiral part of Eq. (2.6), the superpotential W, a function leading to the MSSM Lagrangian that is invariant under supersymmetric transformations, is defined:

$$W = \epsilon_{ij} \left[G_{ab}^{l} H_d^{i} (\widetilde{L}_L^{j})_a (\widetilde{\overline{e}}_R)_b + G_{ab}^{d} H_d^{i} (\widetilde{Q}_L^{j})_a (\widetilde{\overline{d}}_R)_b - G_{ab}^{u} H_u^{i} (\widetilde{Q}_L^{j})_a (\widetilde{\overline{u}}_R)_b + \mu H_u^{i} H_d^{j} \right]$$

$$(2.9)$$

with $G^{l,u,d}$ being Yukawa couplings, μ the Higgs mixing parameter, $^3H_{u,d}$ the Higgs doublets, and \widetilde{Q}_L , \widetilde{L}_L , \widetilde{u}_R , \widetilde{d}_R , \widetilde{e}_R the left- and right-handed partner multiplets for all three fermion generations. The antisymmetric tensor $\epsilon_{ij} = -\epsilon_{ji}$ is defined with $\epsilon_{12} = 1$. The superpotential has to be a holomorphic function of the scalar fields. Therefore, terms like HH^* are forbidden, and two Higgs doublets are needed to provide masses for up- and down-type quarks and leptons.

The chiral Lagrangian is then given as

$$\mathcal{L}_{\text{chiral}} = -\frac{1}{2} \frac{\partial^2 W}{\partial \phi_i \partial \phi_j} \psi_i \psi_j + h.c.$$
 (2.10)

Here, ϕ are any of the scalar fields of Eq. (2.9) and ψ their partner fields.

This Lagrangian resembles the well known SM Yukawa coupling of Eq. (1.16), but also describes similar vertices, where the Higgs boson and one fermion are exchanged

³This parameter should not be confused with the Higgs mass parameter from the SM, Eq. (1.11).

by their superpartners. Also vertices with charged Higgs bosons or higgsinos are described by it. The μ -term of Eq. (2.9) leads to masses for the higgsinos.

The Potential of the Lagrangian

The final term in Eq. (2.6), the potential, can be written as

$$V(\phi) = F_i^* F^i + \frac{1}{2} D^a D^a$$
 (2.11)

with

$$F_i = \frac{\partial W}{\partial \phi^i}, \qquad D^a = -g\phi_i^* T_{ij}^a \phi_j.$$

These F and D fields are auxiliary fields. They are needed to match the numbers of degrees of freedom for fermion supermultiplets (F-term) and the gauge supermultiplets (D-term) in the case of off-shell fields.

The F-term can be separated into three types of interactions. First, the Yukawa part of Eq. (2.9), leads to quartic interactions between two Higgs bosons and two sfermions of the same flavor generation. Secondly, there exists a part with interactions between one Higgs boson and two sfermions. The final part is the terms coming from the μ -term of Eq. (2.9):

$$V_{\rm H} = |\mu|^2 \left(|H_u^0|^2 + |H_d^0|^2 + |H_u^+|^2 + |H_d^-|^2 \right).$$

Note, that this potential is similar to the μ^2 term of Eq.(1.11). However, it is positive definite, and thus electroweak symmetry breaking does not occur, if SUSY is unbroken.

The contribution to the Lagrangian, introduced by the D-term of Eq. (2.11) is quadratic in gauge couplings and quartic in scalar fields. Quartic Higgs boson couplings have already been observed in Eq. (1.11). SUSY also adds these couplings to the other type of scalar fields, the sfermion fields. One should note, that in SUSY these quartic couplings are determined by gauge couplings through the definition of D^a .

Summarizing our current findings: So far, we have reproduced the interaction vertices from the SM. The theory doubles the particle spectrum, and the chiral and gauge eigenstates are summarized in Table 2.1. Further interactions are introduced by exchanging two SM particles by their supersymmetric partners at the SM vertices. These interactions happen at the same strength as the ones in the SM, because the coupling constants are equal. It is important to note, that SUSY does not introduce new couplings. Additional interaction vertices emerge like the quartic coupling between sfermion fields, where no analogon in the SM exists.

This extended theory has some problems: First, we have no electroweak symmetry breaking. Also, we introduced a lot of new particles, which only differ in spin from their SM partner particles, but not in mass. However, these particles have not

Name		Spin-0	Spin-1/2	Spin-1	$\begin{array}{c} SU(3)_C \times \\ SU(2)_L \times \\ U(1)_Y \end{array}$
Squarks, quarks	Q_L	$(\widetilde{u}_L,\ \widetilde{d}_L)$	(u_L, d_L)	_	$(3,2,+\frac{1}{6})$
(×3 generations)	u_R	\widetilde{u}_R	u_R	_	$(3,1,+\frac{2}{3})$
	d_R	\widetilde{d}_R	d_R	_	$(3, 1, -\frac{1}{3})$
Sleptons, leptons	L_L	$(\widetilde{\nu}_L,\ \widetilde{e}_L)$	(ν_L, e_L)	_	$(1,2,-\frac{1}{2})$
(×3 generations)	e_R	\tilde{e}_R	e_R	_	(1, 1, -1)
Gauginos,	g	_	\widetilde{g}	g	(8, 1, 0)
gauge bosons	W	-	\widetilde{W}	W	(1, 3, 0)
	В	-	\widetilde{B}	В	(1, 1, 0)
Higgs boson,	H_u	(H_u^+, H_u^0)	$(\widetilde{H}_u^+,\ \widetilde{H}_u^0)$	_	$(1,2,+\frac{1}{2})$
higgsino	H_d	(H_d^0, H_d^-)	$(\widetilde{H}_d^0,\ \widetilde{H}_d^-)$	_	$(1, 2, -\frac{1}{2})$

Table 2.1 The particle content of the MSSM in terms of the chiral and gauge eigenstates and the representation in the SM gauge groups

been observed. In order to obtain a SUSY model with realistic phenomenological observations, SUSY needs to be broken.

2.1.1 Breaking of Supersymmetry

SUSY should be broken in such a way that the symmetry itself is preserved, but the vacuum state is not symmetric under supersymmetric transformations.

Unlike the Higgs mechanism, the underlying mechanism to break SUSY is not yet fully understood, and only a parameterization of the breaking terms can be written down. The way SUSY is broken should not introduce new "problems" like the ones mentioned in Sect. 1.4. For example, dimensionless couplings lead to quadratic divergencies as observed in the hierarchy problem [5]. Thus, only *soft* SUSY breaking terms are allowed. A possible parameterization can be

$$\mathcal{L}_{\text{MSSM}}^{\text{soft}} = -\frac{1}{2} \left(M_1 \widetilde{B} \widetilde{B} + M_2 \widetilde{W} \widetilde{W} + M_3 \widetilde{g} \widetilde{g} + c.c. \right)$$

$$- \left(\widetilde{\overline{u}}_R A_u \widetilde{Q}_L H_u - \widetilde{\overline{d}}_R A_d \widetilde{Q}_L H_d - \widetilde{\overline{e}}_R A_e \widetilde{L}_L H_u + c.c. \right)$$

$$- \widetilde{Q}_L^{\dagger} m_Q^2 \widetilde{Q}_L - \widetilde{L}_L^{\dagger} m_L^2 \widetilde{L}_L - \widetilde{u}_R^{\dagger} m_u^2 \widetilde{u}_R - \widetilde{d}_R^{\dagger} m_d^2 \widetilde{d}_R - \widetilde{e}_R^{\dagger} m_e^2 \widetilde{e}_R$$

$$- M_{H_u}^2 |H_u|^2 - M_{H_d}^2 |H_d|^2 + (B\mu H_u H_d + c.c.).$$
(2.12)

In total, 105 new parameters are introduced: the gaugino mass terms M_1 , M_2 , M_3 , the sfermion 3 \times 3 mass matrices m_Q^2 , m_L^2 , m_u^2 , m_d^2 , m_e^2 , the Higgs mass terms $M_{H_u}^2$, $M_{H_d}^2$, trilinear sfermion-sfermion-Higgs coupling 3 \times 3 matrices A_u , A_d , A_e , and off-diagonal Higgs mass term $B\mu$. These terms should be roughly of the SUSY breaking scale $M_{\rm soft}$.

This new Lagrangian introduces flavor-changing neutral currents and CP-violating effects that have been excluded experimentally. One potential way out is diagonalizing the newly introduced 3×3 mass matrices, $m_X^2 = m_{X0}^2 \mathbb{I}$, making the trilinear couplings proportional to the Yukawa couplings, $A_x = A_{x0}G^x$, and removing new complex phases, $\text{Im}(M_{1,2,3}) = \text{Im}(A_{u0,d0,e0}) = 0$.

2.1.2 The Hidden Sector—The Origin of Supersymmetry Breaking

If global SUSY is broken, the potential of Eq. (2.11) is required to have a non-zero vacuum expectation value, and thus $\langle F \rangle \neq 0$ or $\langle D \rangle \neq 0$. As none of the MSSM fields can obtain a non-zero vacuum expectation value without spoiling gauge invariance, this breaking must occur in the "hidden sector". It is assumed that this hidden sector either couples extremely weakly or only indirectly via messenger particles to the "visible sector". One consequence of SUSY breaking is the existence of a neutral and massless fermion, the goldstino. Two popular models of spontaneous SUSY breaking are discussed here. Other SUSY breaking scenarios have been developed, for instance anomaly mediated breaking [8, 9], but are not discussed.

In supergravity mediated models (SUGRA), the hidden sector is around the Planck scale, M_P , and interacts with the visible sector via gravitation. When gravitation is taken into account, SUSY becomes a local symmetry, supergravity, with the addition of the spin-2 graviton and its spin-3/2 partner, the gravitino. The gravitino absorbs the goldstino, acquiring the mass $M_{3/2} \sim \langle F \rangle / M_P$. The scale requested for the soft breaking terms is at the TeV scale,

$$M_{\rm soft} \sim \frac{\langle F \rangle}{M_P} \sim 1 \, {\rm TeV},$$

hence one estimates $\sqrt{\langle F \rangle} \sim 10^{11}\,\mathrm{GeV}$. In this scenario the gravitino is heavy. For collider physics, typically it does not play a role due to the weakness of the gravitational interaction.

Another popular model of SUSY breaking is the gauge-mediated SUSY breaking (GMSB). Instead of coupling directly to the hidden sector, GMSB introduces messenger fields with SM gauge quantum numbers: gauge interactions with these messenger fields mediate the breaking by quantum fluctuations. Hence, the soft breaking scale can be estimated as

$$M_{
m soft} \sim rac{lpha}{2\pi} rac{\langle F \rangle}{M_{
m mess}} \sim 1 \, {
m TeV}$$

with α being the gauge couplings involved in the loop interaction. Assuming that $M_{\rm mess}^2$ is of the same scale as $\langle F \rangle$, one concludes that $\sqrt{\langle F \rangle} \sim 10^4 - 10^5$ GeV. A direct consequence of this is that the gravitino is extremely light: $M_{3/2} \ll v \approx 246$ GeV.

2.1.3 *R-parity*

The Lagrangian introduced in Eqs. (2.6) and (2.12) conserves the discrete quantum number

$$R = (-1)^{3B+L+2S}, (2.13)$$

with B being the baryon number, L the lepton number, and S the spin. This quantum number has values R = +1 for all the SM particles and R = -1 for their supersymmetric partners.

Requiring *R*-parity conservation has several phenomenological consequences:

- both the baryon and lepton numbers are conserved,
- sparticles can only be produced in pairs,
- sparticles can only decay into an odd number of other sparticles, thus requiring that the lightest supersymmetric particle (LSP) is stable,
- due to cosmological constraints, the LSP must be electrically neutral and interact only very weakly.

Previously, *R*-parity conservation was assumed without mentioning. In fact, more terms in Eq. (2.9) are allowed:

$$W_{RPV} = \lambda_{ijk}(\widetilde{L}_L)_i(\widetilde{L}_L)_j(\widetilde{\overline{e}}_R)_k + \lambda'_{ijk}(\widetilde{L}_L)_i(\widetilde{Q}_L)_j(\widetilde{\overline{d}}_R)_k + \lambda''_{ijk}(\widetilde{\overline{u}}_R)_i(\widetilde{\overline{d}}_R)_j(\widetilde{\overline{d}}_R)_k + \mu'_i(\widetilde{L}_L)_i H_d$$
 (2.14)

The first, second and fourth term violate lepton number conservation, while the third term violates baryon number conservation. The coupling λ_{ijk} permits slepton-lepton-lepton interactions, the second coupling, λ'_{ijk} , slepton-quark-quark or lepton-squark-quark interactions, while the third coupling, λ''_{ijk} , corresponds to a squark-quark-quark vertex.

Allowing for *R*-parity violation (RPV) has severe consequences: sparticles can be produced as single particle and also decay into an even number (including zero) of other sparticles: the LSP does neither have to be stable nor to be neutral. Besides direct SUSY phenomenology, RPV allows for several interactions forbidden by the SM. For example, protons can decay at strength $\lambda'\lambda''$ via squark exchange, like $p \to e^+\pi^0$. A very concise review of RPV can be found in [10]. Indirect measurements put strong limits on the couplings of Eq. (2.14). Taking the example of the proton decay $p \to e^+\pi^0$, experiments have limited the proton lifetime $\gtrsim 10^{33}$ years. This yields a stringent limit of $\lambda'_{11k}\lambda''_{11k} \lesssim \frac{1}{2} \cdot 10^{-27} (\widetilde{M}_k/100\,\text{GeV})^2$.

For the rest of this writing, *R*-parity conservation is assumed, unless stated otherwise.

2.1.4 Unification of Gauge Couplings

In Sect. 1.2.1, the evolution of the strong coupling constant α_s as a function of Q^2 was shown. The β_i coefficients of Eq. (1.21) depend on the particles entering the loops. If this evolution is considered for all three coupling constants, no scale Q^2 is found, for which the three coupling constants intersect within the SM, see Fig. 2.1, left.

The framework of MSSM introduces new particles at a scale of the order of 1 TeV. These particles alter the coefficients β_i and all three gauge couplings meet at a scale $M_{\rm GUT} \sim 10^{15} - 10^{16}$ GeV below the Planck scale M_P , allowing for a unification, see Fig. 2.1, right. The unified coupling $\alpha_{\rm GUT} \simeq 1/25$ is well within the perturbative regime. Such a theory is known as Grand Unification Theory (GUT).

If unification occurs, the three SM gauge groups unify into one group. Consequences depend on the unification group. Some of them are phenomenologically interesting: A SU(5) unification can predict the electroweak mixing angle compatible with measurements, or explain the quantization of charge $q(e) = -3q(\overline{d})$. On the other hand, also new phenomena open up, like the introduction of leptoquarks (couple to lq) and diquarks (couple to qq). These can be derived from the representations for quarks and leptons, which are, for SU(5), $\bar{\bf 5} = \{d_R, L_L\}$ and ${\bf 10} = \{Q_L, u_R, e_R\}$. The interactions with leptoquarks or diquarks lead to tree-level contributions to the

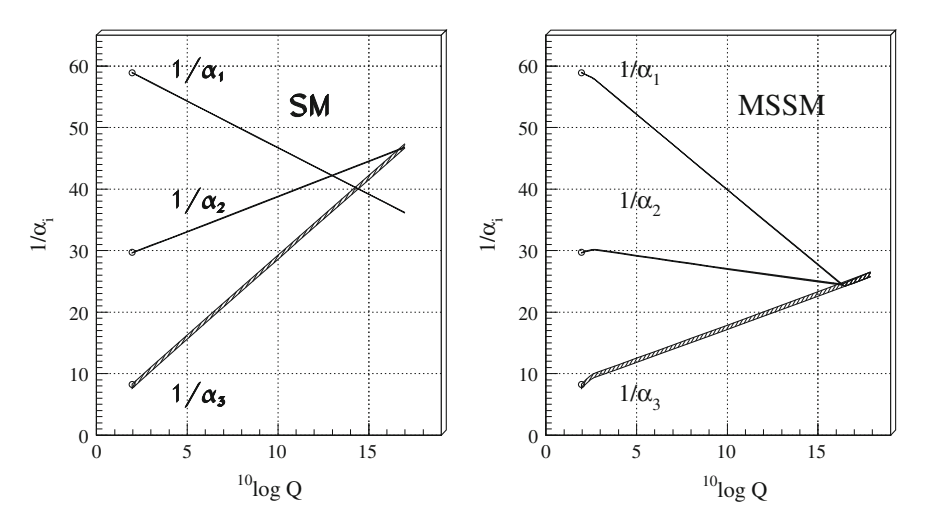


Fig. 2.1 Evolution of the inverse of the gauge coupling constants with energy Q [GeV]. *Left* for SM, *right* for MSSM with sparticle masses of \sim 1 TeV. Based on [11] and taken from [12]

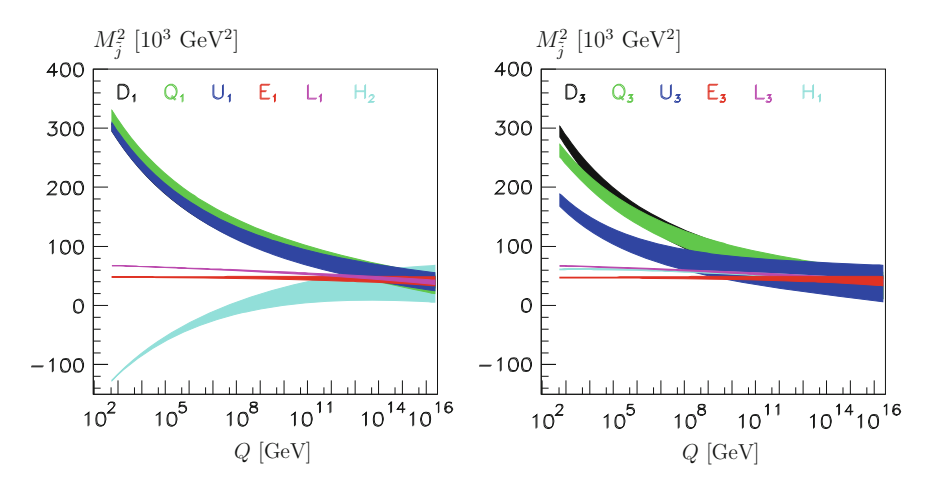


Fig. 2.2 Example of a mass spectrum: *left* for sfermions of the first and second generations and the Higgs boson mass parameter M_{H_u} (here M_{H_2}), *right* for sfermions of the third generation and M_{H_1} . The parameter $M_{H_u}^2$ becomes negative for $Q \ll M_{\rm GUT}$. Taken from [15]

proton decay. However, the contributions are surpressed compared to GUT scenarios within the SM alone. Another popular group is SO(10). In this model, all SM leptons of a given generation, including ν_R , are unified in one supermultiplet within the representation $\mathbf{16} = \{Q_L, u_R, d_R, L_L, e_R, \nu_R\}$. A review on the popular SU(5), SO(10), and other unification groups can be found in [13].

One possible result of gauge unification is discussed here: The positive Higgs boson mass parameter $M_{H_u}^2$ (at $M_{\rm GUT}$) becomes negative at the electroweak scale, v, due to the influence of the strong top quark Yukawa coupling in the RGE. This natural explanation of electroweak symmetry breaking via quantum corrections is called *radiative electroweak symmetry breaking* [14]. An example of a mass spectrum is shown in Fig. 2.2.

2.2 The Higgs Sector in the Minimal Supersymmetric Standard Model

In the MSSM, two Higgs doublets $H_u = (H_u^+, H_u^0)$ and $H_d = (H_d^0, H_d^-)$ are required, as anomaly cancellation involving chiral fermions requires the existence of two fermionic partners in the Higgs sector with $Y = \pm 1/2$. Minimizing the Higgs potential for H_u^0 and H_d^0 , obtained from all relevant terms of Eqs. (2.6) and (2.12), one arrives at the conditions

$$2B\mu < 2|\mu|^2 + M_{H_u}^2 + M_{H_d}^2$$
 and $(B\mu)^2 > (|\mu|^2 + M_{H_u}^2)(|\mu|^2 + M_{H_d}^2)$.

Due to the running of $M_{H_u}^2$ described in Sect. 2.1.4, these conditions can be met easily. Defining the vacuum expectation values $v_{u/d} = \langle H_{u/d}^0 \rangle / \sqrt{2}$, one finds the relation

$$v^2 = v_u^2 + v_d^2 = \frac{4M_Z^2}{g^2 + g^2}. (2.15)$$

The two Higgs doublets have eight degrees of freedom. As described in Sect. 1.1.1, three of them are absorbed by the massive gauge bosons (W^{\pm} and Z), leaving five degrees of freedom, forming five Higgs bosons: h, H, A, and H^{\pm} . Two of them (h, H) are scalar bosons with convention $M_h \leq M_H$, A is a pseudoscalar boson, while H^{\pm} are two charged bosons.

Calculating the pseudoscalar boson mass

$$M_A^2 = B\mu \frac{v_u^2 + v_d^2}{v_u v_d} \tag{2.16}$$

and defining the ratios $(-\pi/2 < \alpha < 0)$

$$\tan \beta = \frac{v_u}{v_d}, \quad \tan(2\alpha) = \tan(2\beta) \frac{M_A^2 + M_Z^2}{M_A^2 - M_Z^2}, \tag{2.17}$$

one can obtain the Higgs boson masses at leading order

$$M_{H^{\pm}}^{2} = M_{W}^{2} + M_{A}^{2}, \quad M_{H,h}^{2} = \frac{1}{2} \left(M_{A}^{2} + M_{Z}^{2} \pm \sqrt{(M_{A}^{2} + M_{Z}^{2})^{2} - 4M_{A}^{2}M_{Z}^{2}\cos^{2}(2\beta)} \right). \tag{2.18}$$

It is interesting to note, that at tree-level $M_h \le M_Z |\cos(2\beta)|$. However, including radiative corrections from stop- and top-quark loops,

$$\Delta(M_h) \approx \frac{3}{4\pi} \cos^2 \alpha (G^t)^2 M_t^2 \ln \left(\frac{M_{\tilde{t}_1} M_{\tilde{t}_2}}{M_t^2} \right)$$
 (2.19)

an upper limit of $M_h \lesssim 135\,\text{GeV}$ is obtained. The newly found Higgs-like boson at a mass of $M_h \sim 125\,\text{GeV}$ fulfills this requirement.

The relative coupling strengths of the neutral MSSM Higgs bosons compared to the ones of the SM Higgs boson are expressed in Table 2.2.

The case of $M_A^2 \gg M_Z^2$, that is for $M_A \gtrsim 300$ GeV, is known as the decoupling limit. In this limit, A, H, and H^\pm have the same mass scale ($M_A \sim M_H \sim M_{H^\pm}$) and decouple from h. As $\beta - \alpha \approx \pi/2$, the couplings of the light MSSM Higgs boson h become identical to the ones of the SM Higgs boson and the discovery potential for the heavier MSSM Higgs bosons might be challenging [16].

Higgs state

SMh

 h_V

1

1

51.17	1 *	*	1 *	*			
MSSM h	$\sin(\beta - \alpha)$	$\cos(\beta - \alpha)$	$\cos \alpha / \sin \beta$	$-\sin\alpha/\cos\beta$			
MSSM H	$\cos(\beta - \alpha)$	$-\sin(\beta-\alpha)$	$\sin \alpha / \sin \beta$	$\cos \alpha / \cos \beta$			
MSSM A	0	0	$\cot \beta$	$\tan \beta$			
The relative coupling strength h_V denotes couplings to vector bosons, h_A couplings to AZ , and $h_{u/d}$ couplings to up- or down-type quarks and leptons							
2.3 Sparticle Masses in the Minimal Supersymmetric Standard Model							
-			-	ne soft SUSY breakers mix among each			

Table 2.2 The MSSM Higgs couplings relative to the SM Higgs couplings expressed in α and β

1

other. The mass eigenstates are obtained by diagonalizing the mass matrices in the Lagrangian.

Gluinos do not share quantum numbers with any other sparticle and therefore do not mix. The other neutral gauginos and higgsinos form four mass eigenstates, called neutralinos, $\tilde{\chi}^0$, while their charged counterparts form two mass eigenstates, called charginos, $\tilde{\chi}^{\pm}$.

Mixing also appears in the sfermion sector. However, the diagonalization of the mass matrices and trilinear couplings, as mentioned in Sect. 2.1.1, leads to negligible mixing among the flavors. Because of the Yukawa coupling strengths, mixing is usually assumed only for third generation sfermions. The amount of the mixing also depends on tan β : for small tan β , the sbottom and staus mixing is small, and the stop mixing is large, while it is the opposite for large tan β .

In Table 2.3, the gauge and mass eigenstates of the sparticles are summarized. It is conventional that $M(\widetilde{X}_i) \geq M(\widetilde{X}_i)$ if j > i for the mixed mass eigenstates $X = \widetilde{\chi}^0$,

Туре	Gauge eigenstate	Mass eigenstate
Neutralinos	$\widetilde{B},\ \widetilde{W}^0,\ \widetilde{H}_u^0,\ \widetilde{H}_d^0$	$\widetilde{\chi}_1^0, \widetilde{\chi}_2^0, \widetilde{\chi}_3^0, \widetilde{\chi}_4^0$
Charginos	$\widetilde{W}^{\pm},\ \widetilde{H}_{u}^{+},\widetilde{H}_{d}^{-}$	$\widetilde{\chi}_1^{\pm},\widetilde{\chi}_2^{\pm}$
Gluinos	\widetilde{g}	\widetilde{g}
Squarks	$\widetilde{u}_L, \widetilde{u}_R, \widetilde{d}_L, \widetilde{d}_R$	$\widetilde{u}_L, \widetilde{u}_R, \widetilde{d}_L, \widetilde{d}_R$
	$\widetilde{c}_L, \widetilde{c}_R, \widetilde{s}_L, \widetilde{s}_R$	$\widetilde{c}_L, \widetilde{c}_R, \widetilde{s}_L, \widetilde{s}_R$
	$\widetilde{t}_L, \widetilde{t}_R, \widetilde{b}_L, \widetilde{b}_R$	$ \widetilde{t}_1, \widetilde{t}_2, \widetilde{b}_1, \widetilde{b}_2 $
Sleptons	$\widetilde{e}_L,\widetilde{e}_R,\widetilde{ u}_e$	$\widetilde{e}_L,\widetilde{e}_R,\widetilde{ u}_e$
	$\widetilde{\mu}_L,\widetilde{\mu}_R,\widetilde{ u}_\mu$	$\widetilde{\mu}_L$, $\widetilde{\mu}_R$, $\widetilde{\nu}_{\mu}$
	$\widetilde{ au}_L,\widetilde{ au}_R,\widetilde{ u}_{ au}$	$\widetilde{ au}_2,\ \widetilde{ au}_1,\ \widetilde{ au}_{ au}$

Table 2.3 The gauge and mass eigenstates of the MSSM sparticles

 $\widetilde{\chi}^{\pm}, \widetilde{t}, \widetilde{b}, \text{ or } \widetilde{\tau}$. For displaying purposes, hereafter, all anti-particles of supersymmetric particle states will be denoted like $\tilde{q}^* \equiv \frac{\tilde{q}}{\tilde{q}}$. We also will denote the mass of particle X as M(X) instead of M_X from here on.

The mass spectrum depends strongly on the SUSY parameters of the soft-breaking Lagrangian, Eq. (2.12), as well as the breaking scenario. Some limiting scenarios are worth mentioning.

One limit considers the electroweak symmetry breaking effects to be small compared to the MSSM parameters: $M(Z) \ll |\mu \pm M_1|, |\mu \pm M_2|$. Three hierarchies can be distinguished:

- $|\mu| \gg M_2 > M_1$: The $\tilde{\chi}_1^0$ is bino-like, $\tilde{\chi}_2^0$ and $\tilde{\chi}_1^{\pm}$ are wino-like, and $\tilde{\chi}_{3,4}^0$ and $\tilde{\chi}_2^{\pm}$
- are higgsino-like. Furthermore, $M(\widetilde{\chi}_1^{\pm}) \simeq M(\widetilde{\chi}_2^0)$.

 $|\mu| \gg M_1 > M_2$: The $\widetilde{\chi}_1^0$ is wino-like, $\widetilde{\chi}_2^0$ is bino-like, while the other states behave as in the previous case. Furthermore, $M(\widetilde{\chi}_1^{\pm}) \simeq M(\widetilde{\chi}_1^0)$.

 $|\mu| \ll M_1, M_2$: Here, both the $\widetilde{\chi}_1^{\pm}$ and $\widetilde{\chi}_{1,2}^0$ are higgsino-like with $M(\widetilde{\chi}_1^{\pm}) \simeq M(\widetilde{\chi}_1^0)$.
- $M(\widetilde{\chi}_{1,2}^0)$, while $\widetilde{\chi}_2^{\pm}$ and $\widetilde{\chi}_{3,4}^0$ are gaugino-like.

As for the gauginos and higgsinos, the sfermion masses are obtained from the running of the corresponding soft-term parameters at the SUSY breaking scale down to the electroweak scale. From the D-term contribution of the potential, Eq. (2.11), general sum rules can be stated:

$$M^{2}(\tilde{e}_{L}) - M^{2}(\tilde{\nu}_{eL}) = M^{2}(\tilde{u}_{L}) - M^{2}(\tilde{d}_{L}) = g^{2} \frac{v_{u}^{2} - v_{d}^{2}}{2} = -M^{2}(W)\cos(2\beta).$$
(2.20)

Since $\cos(2\beta) < 0$, it follows that $M(\tilde{e}_L) > M(\tilde{\nu}_{eL})$, and similar for the other cases. If it is further assumed that the sfermion masses unify at the GUT scale, another sum rule holds:

$$2(M^{2}(\tilde{u}_{R}) - M^{2}(\tilde{d}_{R})) + M^{2}(\tilde{d}_{R}) - M^{2}(\tilde{d}_{L}) + M^{2}(\tilde{e}_{L}) - M^{2}(\tilde{e}_{R}) = \frac{10}{3}M^{2}(Z)\sin^{2}\theta_{w}\cos(2\beta).$$
(2.21)

These rules also apply to the second generation.

For third generation sfermions, the strong Yukawa couplings introduce a mixing of the left- and right-handed scalars and reduce the effect of the RGE evolution. Therefore, in many scenarios, \tilde{t}_1 or \tilde{b}_1 are the lightest squarks, and $\tilde{\tau}_1$ the lightest slepton.

The explicit mass formula for the mentioned cases can be found in [5], for example. In R-parity conserving models, the LSP is stable, and thus its content is important to study.

From cosmological considerations, charged sparticles as LSP are excluded, natural candidates are the neutralino $\tilde{\chi}_1^0$, the lightest sneutrino $\tilde{\nu}$, or the gravitino \tilde{G} .

In GMSB models, the LSP is \widetilde{G} . The next-to-LSP (NLSP) can be charged, most likely being the $\widetilde{ au}_1$, or neutral, usually being the $\widetilde{\chi}_1^0$. In SUGRA models, all three candidates can have masses of few hundreds GeV. The most likely candidate for the LSP is the lightest neutralino $\tilde{\chi}_1^0$, which is assumed to be the LSP from now on.

2.4 Revisiting the Limitations of the Standard Model

The theory of SUSY has been introduced in its minimal version, the MSSM. For each SM particle, there exists one partner particle. They are connected via an operator Q that changes the spin quantum number by 1/2. The doubled particle spectrum requires the presence of two Higgs doublets, leading to the existence of five Higgs bosons.

Having introduced the most important aspects of the theory, the SM limitations of Sect. 1.4 are revisited: How does the MSSM change the picture?

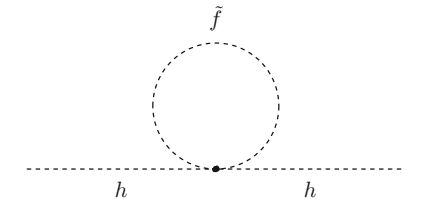
• Solving the hierarchy problem is one of the key motivations for SUSY. Each fermion has a scalar supersymmetric partner particle, coupling to the Higgs boson as sketched in Fig. 2.3. The correction to the Higgs boson mass is:

$$\delta M^{2}(h)|_{\widetilde{f}} = +\frac{(G^{f})^{2}}{8\pi^{2}} \left[\Lambda^{2} - \mathcal{O}\left(M^{2}(\widetilde{f}) \ln \frac{\Lambda}{M^{2}(\widetilde{f})}\right) \right]. \tag{2.22}$$

The coupling strength is equal to Eq. (1.29), but the mass correction has opposite sign due to the scalar nature of the sfermion: the quadratic divergencies cancel exactly with those of Eq. (1.29). The remaining correction is only logarithmic in Λ . If the differences between the squared masses of the fermions and sfermions are not too large, small Higgs boson masses can be achieved naturally.⁴

- The electroweak symmetry breaking is not constructed adhoc as in the SM (by choosing $\mu^2 < 0$ and $\lambda > 0$), but can be naturally explained via quantum corrections (radiative electroweak symmetry breaking). The observed mass of the Higgs-like boson, $M(h) \simeq 125 \, \text{GeV}$ fits well within the bound set by the radiative corrections $M(h) \lesssim 135 \, \text{GeV}$.
- Grand unification is not a limitation of the SM. However, SUSY allowing for unification of the gauge couplings is more than just a coincidence: some free parameters in the SM are determined at the unification scale. For example, SUSY can explain that the proton charge is equal to the positron charge. Also, the electroweak mixing angle is fixed, and agrees with measurements.
- The MSSM is still a theory of the strong, weak, and electromagnetic interactions. Gravitation is not included in SUSY, with the exception of being a possible source

Fig. 2.3 Sfermion loop contribution to the Higgs boson mass



⁴The observation of a Higgs-like boson with $M(h) \simeq 125$ GeV raises the so-called *little hierarchy problem*, as large stop masses are required for the Higgs boson acquiring this mass. A fine-tuning of 1–10 % is needed [17, 18].

- of SUSY breaking in the hidden sector. However, local SUSY requires the existence of a spin-3/2 particle, the gravitino, and its partner, the graviton. This theory is called supergravity. It might be a step to a more inclusive theory like superstring theory, describing all fundamental interactions.
- There exists no particle candidate within the SM, that could explain the amount of dark matter observed in the universe. In *R*-parity conserving SUSY models, the $\tilde{\chi}_1^0$ is a good particle candidate for dark matter.

The principles of SUSY, a symmetry relating fermions and bosons, provide elegant solutions to several of the limitations in the SM. It is therefore a very well motivated and appealing theory. As of this writing, no direct evidence, especially none of the SM superpartners, has been observed.

References

- 1. A. Bilal, Introduction to supersymmetry. arXiv:hep-th/0101055
- S.R. Coleman, J. Mandula, All possible symmetries of the S matrix, Phys. Rev. 159, 1251 (1967). doi:10.1103/PhysRev.159.1251
- 3. R. Haag, J. T. Lopuszanski, M. Sohnius, All possible generators of supersymmetries of the S-matrix, Nucl. Phys. B 88, 257 (1975). doi:10.1016/0550-3213(75)90279-5
- A. Salam, J. Strathdee, Super-gauge transformations, Nucl. Phys. B 76, 477 (1974). doi:10. 1016/0550-3213(74)90537-9
- S. P. Martin, A Supersymmetry primer, Adv. Ser. Direct. High Energy Phys. 21, 1 (2010). doi:10.1142/9789814307505_0001. arXiv:hep-ph/9709356
- M. Spira, F. Moortgat, Phänomenologie der Physik jenseits des Standardmodells (2010). Lecture notes
- L. Pape, D. Treille, Supersymmetry facing experiment: much ado (already) about nothing (yet), Rept. Prog. Phys. 69, 2843 (2006). doi:10.1088/0034-4885/69/11/R01
- G.F. Giudice et al., Gaugino mass without singlets, JHEP 12, 027 (1998). doi:10.1088/1126-6708/1998/12/027. arXiv:hep-ph/9810442
- L. Randall, R. Sundrum, Out of this world supersymmetry breaking, Nucl. Phys. B 557, 79 (1999). doi:10.1016/S0550-3213(99)00359-4. arXiv:hep-th/9810155
- G. Bhattacharyya, R-parity violating supersymmetric Yukawa couplings: A Minireview, Nucl. Phys. Proc. Suppl. 52A, 83 (1997). doi:10.1016/S0920-5632(96)00539-7. arXiv:hep-ph/9608415
- U. Amaldi, W. de Boer, H. Fürstenau, Comparison of grand unified theories with electroweak and strong coupling constants measured at LEP, Phys. Lett. B 260 447 (1991). doi:10.1016/ 0370-2693(91)91641-8
- Particle Data Group Collaboration, Review of particle physics, Chin. Phys. C 38, 090001 (2014). doi:10.1088/1674-1137/38/9/090001
- R.N. Mohapatra, Supersymmetric grand unification: an update, particle physics 1999, in Proceedings of the ICTP Summer School in Particle Physics (World Scientific) 336 (1999). arXiv:hep-ph/9911272
- 14. L.E. Ibáñez, G.G. Ross, $SU(2)_L \times U(1)$ symmetry breaking as a radiative effect of supersymmetry breaking in GUTs. Phys. Lett. B **110**, 215 (1982). doi:10.1016/0370-2693(82)91239-4
- G. Blair, W. Porod, P. Zerwas, The reconstruction of supersymmetric theories at high-energy scales, Eur. Phys. J. C 27, 263 (2003). doi:10.1140/epjc/s2002-01117-y. arXiv:hep-ph/0210058

References 37

16. H.E. Haber, Challenges for nonminimal Higgs searches at future colliders, Perspectives for Electroweak Interactions in e^+e^- Collisions: Proceedings of the Ringberg Workshop (World Scientific, Singapore) 219 (1995). arXiv:hep-ph/9505240

- L.J. Hall, D. Pinner, J.T. Ruderman, A natural SUSY higgs near 126 GeV. JHEP 04, 131 (2012). doi:10.1007/JHEP04(2012)131. arXiv:1112.2703
- H. Baer et al., Radiative natural supersymmetry: Reconciling electroweak fine-tuning and the Higgs boson mass, Phys. Rev. D 87, 115028 (2013). doi:10.1103/PhysRevD.87.115028. arXiv:1212.2655

Chapter 3 Possible Signatures of Supersymmetry at the Large Hadron Collider

Following the motivation and introduction of SUSY in Chap. 2, this chapter is devoted to possible signatures of SUSY that could be observed at hadron colliders. A special focus is set on hadronic signatures for SUGRA models with *R*-parity conservation, relevant to this dissertation. Other models, such as models with RPV or models with GMSB scenarios, will not be mentioned. For more details on such models, see for instance [1].

3.1 Production of Sparticles at Hadron Colliders

In this section, the sparticle production for models with *R*-parity conservation is presented. Sparticles are produced in pairs, as mentioned in Sect. 2.1.3. For similar masses, strong production dominates over electroweak processes because of the couplings. Strong processes involve

$$gg, q\overline{q} \to \widetilde{g}\widetilde{g},$$
 $gq/g\overline{q} \to \widetilde{g}\widetilde{q}/\widetilde{g}\widetilde{q}^*,$ $qq' \to \widetilde{q}\widetilde{q}',$ $gg/q\overline{q}' \to \widetilde{q}\widetilde{q}'*/\widetilde{q}\widetilde{q}'^*.$

As exemplified in Fig. 3.1, the relative strength of the production heavily depends on the averaged produced mass, as well as the relative mass relation between the \tilde{q} and the \tilde{g} . The exclusive pair production cross section of a given particle is largely independent on other sparticles.

Production processes for charginos, neutralinos, and sleptons involve

$$\begin{split} q\overline{q} &\to \widetilde{\chi}_i^+ \widetilde{\chi}_j^-, \ \widetilde{\chi}_i^0 \widetilde{\chi}_j^0, \\ u\overline{d}/\overline{u}d &\to \widetilde{\chi}_i^+ \widetilde{\chi}_j^0/\widetilde{\chi}_i^- \widetilde{\chi}_j^0, \\ \end{split} \qquad \begin{split} q\overline{q} &\to \widetilde{l}^+ \widetilde{l}^-, \ \widetilde{\nu}\overline{\widetilde{\nu}}, \\ u\overline{d}/\overline{u}d &\to \widetilde{l}^+ \widetilde{\nu}_l/\widetilde{l}^- \overline{\widetilde{\nu}}_l. \end{split}$$

The production cross section for these processes is much lower due to the weaker couplings involved, and due to the $qq/q\overline{q}$ initial state. Of course, also mixed processes

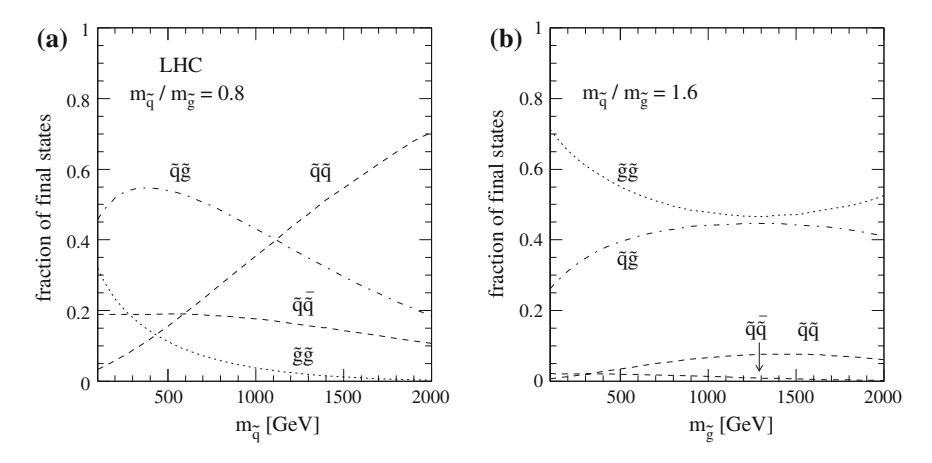
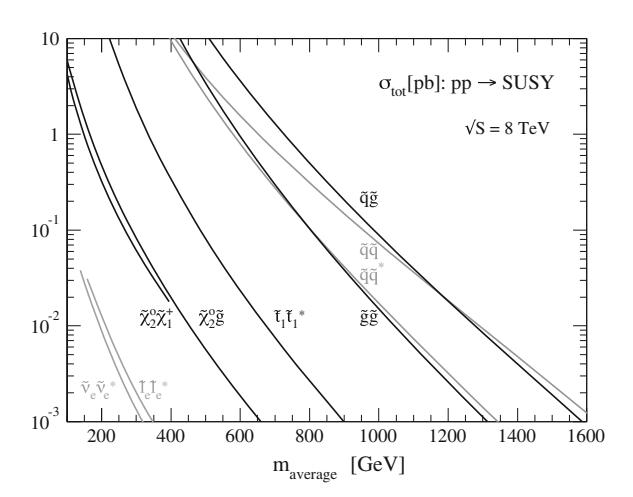


Fig. 3.1 Relative fractions of final states containing squarks and gluinos for pp collisions at $\sqrt{s} = 14$ TeV as a function of $M(\widetilde{q}), M(\widetilde{g})$: **a** for $M(\widetilde{q})/M(\widetilde{g}) = 0.8$, **b** for $M(\widetilde{q})/M(\widetilde{g}) = 1.6$ [2, 3]

Fig. 3.2 Cross section for sparticle pair production at pp collisions with $\sqrt{s} = 8$ TeV, calculated with PROSPINO [2–5]. Plot taken from [6]



are possible, like $q\overline{q} \to \widetilde{g}\widetilde{\chi}^0$. Figure 3.2 shows the sparticle pair production cross section for pp collisions at $\sqrt{s}=8\,\text{TeV}$.

3.2 Sparticle Decays

Decay chains of sparticles can be long with several intermediate sparticle states. It is very dependent on the mass hierarchy of the involved particles. All sparticle decays will end up in final states containing a number of SM particles plus an odd number of LSPs (usually one). The LSPs cannot be detected with collider experiments. Thus,

for *R*-parity conserving models, events usually contain some amount of missing transverse momentum, 1 $E_{\rm T}^{\rm miss}$.

Gluino decays

Gluinos can only decay via squark exchange, as they do not couple to other particles. If the gluino is heavier than at least one squark, it will decay via

$$\widetilde{g} \to \widetilde{q}\overline{q} \ (\widetilde{q}^*q).$$

Hereafter, the expression \widetilde{ff}' will include \widetilde{f}^*f' with f and f' denoting fermions. The decay happens democratically to all squarks accessible, unless one squark is much lighter than the other ones. If the gluino is lighter than any squark, three-body decays will be mediated by a virtual squark,

$$\widetilde{g} \to \widetilde{\chi}_i^{\pm} q \overline{q}' \text{ or } \widetilde{g} \to \widetilde{\chi}_i^0 q \overline{q}.$$

The mass hierarchy of the squarks is important: if one squark type is much lighter than all other squarks, the mediating virtual squark will be dominantly of that type.

A phenomenological possibility is the formation of R-hadrons [7]. If the lifetime of the gluino is long enough because of extremely heavy squark, it will build bound states like $\tilde{q}q\bar{q}$, $\tilde{q}qqq$ or $\tilde{q}q$.

Squark decays

Squarks couple both via the strong and electroweak forces. In the phase space of gluinos being lighter than the squark, the dominant decay mode is

$$\widetilde{q} \to \widetilde{g} q$$

Otherwise, the usual decays are

$$\widetilde{q} \to \widetilde{\chi}_i^0 q$$
 and $\widetilde{q} \to \widetilde{\chi}_i^{\pm} q'$.

The relative decay fraction depends on the mass hierarchy and the chirality: for binolike LSP, the \tilde{q}_R will decay to $\tilde{\chi}_1^0 q$ with ~100%, while the \tilde{q}_L decays to $\tilde{\chi}_i^{\pm} q'$ and $\tilde{\chi}_i^0 q$ with a ratio of about 2:1. Furthermore, decays to lighter squarks happen if the mass difference is large enough:

$$\widetilde{q} \to \widetilde{q}' W^{\pm}, \ \widetilde{q}' H^{\pm} \ \text{and} \ \widetilde{q}_2 \to \widetilde{q}_1 Z, \ \widetilde{q}_1 H.$$

In this section, H is used as a representative for all neutral Higgs bosons. There are cases, for which the upper rules might not be applicable. The stop decay is discussed as an example. Processes like $\widetilde{t} \to t\widetilde{g}$ or $\widetilde{t} \to b\widetilde{\chi}_1^+$, $t\widetilde{\chi}_1^0$ might not be allowed if the mass splitting is too small. In that case, the stop undergoes multi-body decays, for

 $^{^{\}mathrm{l}}\mathrm{The}$ historical term "missing transverse energy" is not used, but its symbol $E_{\mathrm{T}}^{\mathrm{miss}}.$

example $\widetilde{t} \to bW^+\widetilde{\chi}_1^0$, $b\widetilde{l}^+\nu$, $bl^+\widetilde{\nu}$, or even $\widetilde{t} \to bf\overline{f}'\widetilde{\chi}_1^0$. In the case of extremely compressed spectra $(M(\tilde{t}) < M(\tilde{\chi}_1^0) + M(b))$, the flavor-changing process $\tilde{t} \to c\tilde{\chi}_1^0$ will open up, involving a loop and the CKM matrix element V_{bc} .

Chargino, neutralino, and slepton decays

Charginos can decay into sfermions or neutralinos via

$$\widetilde{\chi}_i^{\pm} \to \widetilde{q} q$$
, $\widetilde{\nu} l$, $\widetilde{l} \nu$, $\widetilde{\chi}_i^0 W^{\pm}$, or $\widetilde{\chi}_i^0 H^{\pm}$.

Neutral decays can only happen between $\tilde{\chi}_2^{\pm}$ and $\tilde{\chi}_1^{\pm}$. In case of compressed spectra with respect to the LSP, decays can involve virtual W, Z, or Higgs bosons or threebody decays $\widetilde{\chi}_i^{\pm} \to f \overline{f}' \widetilde{\chi}_1^0$. Possible neutralino decay modes are

$$\widetilde{\chi}_i^0 \to \widetilde{q} \overline{q}, \ \widetilde{l} \overline{l}, \ \widetilde{\nu} \overline{\nu}, \ \widetilde{\chi}_j^{\pm} W^{\mp}, \ \widetilde{\chi}_j^{\pm} H^{\mp}, \ \widetilde{\chi}_j^0 Z, \ \text{or} \ \widetilde{\chi}_j^0 H.$$

Decays might involve virtual sparticles or bosons, or three-body decays for some regions of the phase space. In regions of nearly degenerated $\tilde{\chi}_2^0$ and $\tilde{\chi}_1^0$, the one-loop decay via $\widetilde{\chi}_2^0 \to \widetilde{\chi}_1^0 \gamma$ might be important.

Sleptons usually decay to neutralinos, charginos, or to the partner slepton:

$$\widetilde{l} \to l \widetilde{\chi}_{j}^{0}, \ \nu \widetilde{\chi}_{j}^{-}, \ \widetilde{\nu} W^{-}, \ \text{or} \ \widetilde{\nu} H^{-};$$

 $\widetilde{\nu} \to \nu \widetilde{\chi}_{j}^{0}, \ l \widetilde{\chi}_{j}^{+}, \ \widetilde{l} W^{+}, \ \text{or} \ \widetilde{l} H^{+}.$

The last two decays $\widetilde{\nu} \to \widetilde{l}W^+$, $\widetilde{l}H^+$ might not be open for all sneutrinos, see Eq. (2.20). As for the squark decays, the relative branching fraction depends on the chirality of the lepton. Decays into Higgs bosons usually are not important for \tilde{e} or $\widetilde{\mu}$ due to the weak Yukawa couplings. If the difference between $\widetilde{\tau}_2$ and $\widetilde{\tau}_1$ is large enough, decays via Z or Higgs bosons are allowed.

Other interesting phenomenological signatures might also involve SM particle decays. For example, Higgs boson decays such as $h \to \tilde{\chi}_1^0 \tilde{\chi}_1^0$ are not fully excluded by experiments.

3.3 Models for Testing Supersymmetric Signatures

In the MSSM, there are over 100 parameters unconstrained by theory. The amount of parameters allows for arbitrarily many variations. From an experimentalist's point of view, only the phenomenology of the theory is important in order to design a search. On the other hand, models for interpretations should be general enough, such that they can be used for wider interpretations in different models. They should contain only small numbers of parameters or sample the parameter space appropriately. Three variations of sampling the MSSM are introduced.

3.3.1 The Phenomenological Minimal Supersymmetric Standard Model

The phenomenological MSSM, or short pMSSM [8], contains only 19 parameters in addition to the SM parameters. The assumptions for this models are:

- *R*-parity conservation: based on the non-observation of baryon- and lepton-number violation,
- no new source of *CP* violation or flavor changing neutral currents,
- and first and second generation universality: based, for example, on data from $K^0\overline{K}{}^0$ mixing.

The 19 parameters can be chosen as:

```
\tan \beta, \ M_A, \ \mu: parameters of the MSSM Higgs sector, M_1, M_2, M_3: gaugino mass parameters, m_Q, m_u, m_d, m_L, m_e \ (\times 2): sfermion mass parameters of all three generations, A_t, A_b, A_\tau: third generation trilinear couplings.
```

Further assumptions can be made, for example requiring that the LSP is the $\tilde{\chi}_1^0$ or that sparticle decays happen promptly. This model captures largely the phenomenology of the R-parity conserving MSSM supported by experimental (non-)observations.

3.3.2 The Constrained Minimal Supersymmetric Standard Model

The constrained MSSM (cMSSM) [9–12], also known as minimal supergravity (mSUGRA), considers more constraints. In this model, the SUSY breaking is mediated by gravity, and gauge unification happens at the scale $M_{\rm GUT}$. Further constraints are derived at the unification scale:

```
common gaugino masses: M_1 = M_2 = M_3 = m_{1/2}, common scalar masses: m_Q = m_u = m_d = m_L = m_e = m_0 \mathbb{1}, M_{H_u} = M_{H_d} = m_0, common trilinear couplings: A_u = A_0 G^u, A_d = A_0 G^d, A_e = A_0 G^e.
```

The number of parameters is thus reduced to five²:

$$m_{1/2}$$
, m_0 , A_0 , $\tan \beta$, $\operatorname{sign}(\mu)$.

 $^{^2}$ More precisely, to four parameters and a sign, as the value of μ^2 is determined by the radiative electroweak symmetry breaking.

The constraints at the unification scale have several consequences for the sparticle spectrum at the TeV scale. For example, the running of the gaugino masses is connected to the gauge coupling evolution via $M_i/g_i^2 = m_{1/2}/g_U^2$ with g_U being the unified gauge coupling. It thus follows that

$$M_3: M_2: M_1 \approx 6:2:1.$$
 (3.1)

This means that the gluino is significantly heavier than the lighter neutralinos and charginos. Squark masses are a factor 2–3 larger than slepton masses, following from the formula [13]:

$$M^{2}(\widetilde{f}_{L,R}) = M^{2}(f) + m_{0}^{2} + b(\widetilde{f}_{L,R})m_{1/2}^{2} \pm M^{2}(Z)\cos(2\beta)[T_{3}^{f_{L,R}} - Q_{f_{L,R}}\sin^{2}\theta_{w}].$$
(3.2)

The coefficients b are determined by the RGE equations. For third generation sfermions, where mixing is important, the masses of the mixed states $\tilde{f}_{1,2}$ are at leading order

$$M^{2}(\tilde{f}_{1,2}) = \frac{1}{2} \left[M^{2}(\tilde{f}_{L}) + M^{2}(\tilde{f}_{R}) + \sqrt{\left(M^{2}(\tilde{f}_{L}) - M^{2}(\tilde{f}_{R})\right)^{2} + 4M^{2}(f)\left(A_{0} - \mu r_{f}\right)^{2}} \right]$$
(3.3)

with r_f being $\cot \beta$ for stops, and $\tan \beta$ for sbottoms or staus. Because of the mixing, \widetilde{t}_1 and \widetilde{b}_1 are expected to be the lightest squarks, and $\widetilde{\tau}_1$ the lightest slepton.

The recent observation of a Higgs-like boson can be used to further constrain the model parameters. If this boson is the lightest MSSM Higgs boson h, its mass $M(h) \sim 125$ GeV can be used to eliminate another parameter. It has been suggested in [14, 15], that the observed Higgs boson mass can be achieved by requiring maximal stop mixing. A choice for a model could be

$$A_0 = -2\max(m_0, m_{1/2}). \tag{3.4}$$

3.3.3 The Simplified Model Framework

The Simplified Model Spectra (SMS) [16, 17] are the most restricted models available. The approach of providing a full SUSY model is given up, instead only one sparticle production and decay process is considered. In its simplest form, one sparticle gets produced and decays directly, under emission of SM particles, to the LSP in a multi-body decay. At most, there are one or two intermediate steps in the decay chain. The branching ratio is set to 100% for the considered production and decay

of the sparticle. All involved SM particles decay with their measured SM branching ratios.

The SMS cannot fully describe the underlying physics behind the MSSM. However, they can be used to identify the sensitivity of a search to a given class of processes and give a rough characterization of the new physics signals, if observed. Furthermore, the results of the SMS interpretations can be recast for the interpretation in the context of other, more complete models, see for example [18]. However, one should also be aware that the interpretations in the SMS framework do not cover the phenomenology of the MSSM, and limits set on SMS parameters cannot be translated into limits on corresponding parameters in the full MSSM, see for example [19].

For this work, the production of squarks and gluinos is of particular interest. Hence, generic SMS models considered are

$$\begin{split} \mathrm{pp} &\to \widetilde{g}\widetilde{g} \to q\overline{q}\widetilde{\chi}_1^0 q\overline{q}\widetilde{\chi}_1^0, \qquad \mathrm{pp} \to \widetilde{g}\widetilde{g} \to b\overline{b}\widetilde{\chi}_1^0 b\overline{b}\widetilde{\chi}_1^0, \qquad \mathrm{pp} \to \widetilde{g}\widetilde{g} \to t\overline{t}\widetilde{\chi}_1^0 t\overline{t}\widetilde{\chi}_1^0, \\ \mathrm{pp} &\to \widetilde{q}\widetilde{q}^* \to q\widetilde{\chi}_1^0\overline{q}\widetilde{\chi}_1^0, \qquad \mathrm{pp} \to \widetilde{b}_1\widetilde{b}_1^* \to b\widetilde{\chi}_1^0\overline{b}\widetilde{\chi}_1^0, \qquad \mathrm{pp} \to \widetilde{t}_1\widetilde{t}_1^* \to t\widetilde{\chi}_1^0\overline{t}\widetilde{\chi}_1^0. \end{split}$$

The corresponding diagrams are displayed in Fig. 3.3.

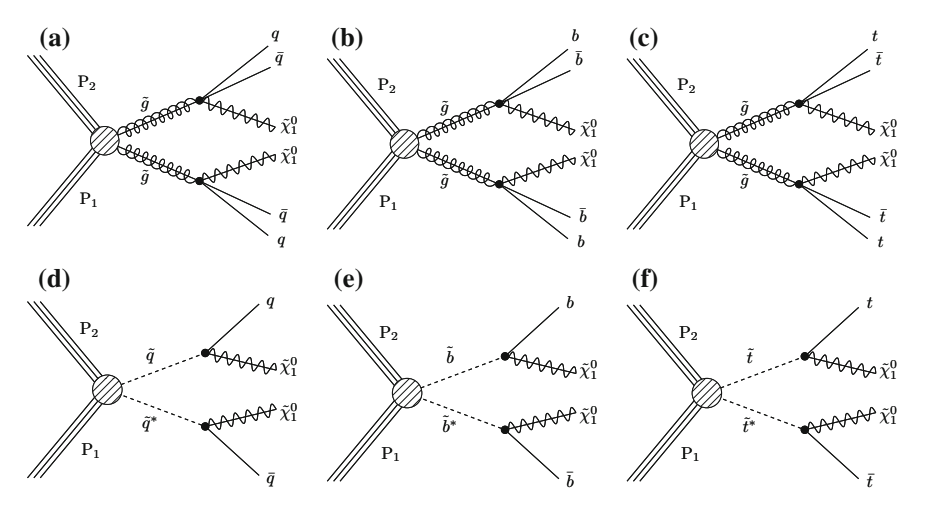


Fig. 3.3 Diagrams for the processes of different SMS models. **a** pp $\rightarrow \widetilde{g}\widetilde{g} \rightarrow q\overline{q}\widetilde{\chi}_1^0q\overline{q}\widetilde{\chi}_1^0$, **b** pp $\rightarrow \widetilde{g}\widetilde{g} \rightarrow b\overline{b}\widetilde{\chi}_1^0b\overline{b}\widetilde{\chi}_1^0$, **c** pp $\rightarrow \widetilde{g}\widetilde{g} \rightarrow t\overline{t}\widetilde{\chi}_1^0t\overline{t}\widetilde{\chi}_1^0$, **d** pp $\rightarrow \widetilde{q}\widetilde{q}^* \rightarrow q\widetilde{\chi}_1^0\overline{q}\widetilde{\chi}_1^0$, **e** $\rightarrow \widetilde{b}_1\widetilde{b}_1^* \rightarrow b\widetilde{\chi}_1^0\overline{b}\widetilde{\chi}_1^0$, **f** pp $\rightarrow \widetilde{t}_1\widetilde{t}_1^* \rightarrow t\widetilde{\chi}_1^0\overline{t}\widetilde{\chi}_1^0$

References

- L. Pape, D. Treille, Supersymmetry facing experiment: Much ado (already) about nothing (yet). Rep. Prog. Phys. 69, 2843 (2006). doi:10.1088/0034-4885/69/11/R01
- W. Beenakker, R. Höpker, M. Spira, PROSPINO: A program for the production of supersymmetric particles in next-to-leading order QCD. arXiv:hep-ph/9611232
- W. Beenakker et al., Squark and gluino production at hadron colliders. Nucl. Phys. B 492, 51 (1997). doi:10.1016/S0550-3213(97)80027-2. arXiv:hep-ph/9610490
- W. Beenakker et al., Stop production at hadron colliders. Nucl. Phys. B 515, 3 (1998). doi:10. 1016/S0550-3213(98)00014-5.arXiv:hep-ph/9710451
- W. Beenakker et al., The Production of charginos / neutralinos and sleptons at hadron colliders. Phys. Rev. Lett. 83, 3780 (1999). doi:10.1103/PhysRevLett.83.3780. arXiv:hep-ph/9906298. An erratum was published under Phys. Rev. Lett. 100, 029901 (2008)
- 6. http://www.thphys.uni-heidelberg.de/plehn/index.php?show=prospino
- G.R. Farrar, P. Fayet, Phenomenology of the production, decay, and detection of new hadronic states associated with supersymmetry. Phys. Lett.B 76, 575 (1978). doi:10.1016/ 0370-2693(78)90858-4
- MSSM Working Group Collaboration, The Minimal supersymmetric standard model: group summary report. arXiv:hep-ph/9901246
- A.H. Chamseddine, R.L. Arnowitt, P. Nath, Locally supersymmetric grand unification. Phys. Rev. Lett. 49, 970 (1982). doi:10.1103/PhysRevLett.49.970
- R. Barbieri, S. Ferrara, C.A. Savoy, Gauge models with spontaneously broken local supersymmetry. Phys. Lett. B 119, 343 (1982). doi:10.1016/0370-2693(82)90685-2
- L.J. Hall, J.D. Lykken, S. Weinberg, Supergravity as the messenger of supersymmetry breaking. Phys. Rev. D 27, 2359 (1983). doi:10.1103/PhysRevD.27.2359
- 12. G.L. Kane et al., Study of constrained minimal supersymmetry. Phys. Rev. D 49, 6173 (1994). doi:10.1103/PhysRevD.49.6173. arXiv:hep-ph/9312272. This paper mentions explicitly the restriction to six parameters (including the top mass) for the first time
- J.R. Ellis, L. Roszkowski, Supergravity dark matter. Phys. Lett. B 283, 252 (1992). doi:10. 1016/0370-2693(92)90016-W. This paper is based on a constrained model that has additionally the pseudoscalar mass as free parameter
- H. Baer et al., Implications of a high mass light MSSM Higgs scalar for supersymmetry searches at the LHC. Phys. Rev. D84, 091701 (2011). doi:10.1103/PhysRevD.84.091701. arXiv:1109.3197
- F. Brümmer, S. Kraml, S. Kulkarni, Anatomy of maximal stop mixing in the MSSM. JHEP 08, 089 (2012). doi:10.1007/JHEP08(2012)089. arXiv:1204.5977
- J. Alwall, P. Schuster, N. Toro, Simplified models for a first characterization of new physics at the LHC. Phys. Rev. D 79, 075020 (2009). doi:10.1103/PhysRevD.79.075020. arXiv:0810.3921
- LHC New Physics Working Group Collaboration, Simplified models for LHC new physics searches. J. Phys. G 39, 105005 (2012). doi:10.1088/0954-3899/39/10/105005. arXiv:1105.2838
- S. Kraml et al., SModelS: a tool for interpreting simplified-model results from the LHC and its application to supersymmetry. Eur. Phys. J. C 74, 2868 (2014). doi:10.1140/epjc/s10052-014-2868-5. arXiv:1312.4175
- M. Cahill-Rowley et al., Lessons and Prospects from the pMSSM after LHC Run I: Neutralino LSP. arXiv:1407.4130

Chapter 4 Experimental Set-Up

4.1 The Large Hadron Collider

The LHC [1–4] is a particle ring accelerator and collider located at the border between Switzerland and France near Geneva, Switzerland at the European Organization for Nuclear Research (CERN). The purpose of the LHC is to provide high energy particle collisions between protons and/or heavy ions to experiments so that the SM, including the Higgs sector, can be probed and studied at these energies, and searches for physics beyond the SM can be performed.

The LHC is built inside a 26.7 km long tunnel, roughly 100 m underground, that had been constructed for the Large Electron Positron collider (LEP) [5]. Besides the tunnel, also the injector chain of LEP has been largely reused, with upgrades for proton and ion injections.

The CERN accelerator complex is shown in Fig. 4.1. Protons are extracted from a duoplasmatron source (an apparatus that ionizes hydrogen). The protons are accelerated by the linear accelerator Linac2 to energies of 50 MeV. The proton beam is then successively accelerated by the Proton Synchrotron Booster (PSB) (50 MeV \rightarrow 1.4 GeV), the Proton Synchrotron (PS) (1.4 GeV \rightarrow 26 GeV), and finally by the Super Proton Synchrotron (SPS) (26 GeV \rightarrow 450 GeV) before it is injected into the LHC main ring. During the PS acceleration, the proton beam is also split into short bunches of protons with nominal 25 ns bunch spacing. In case of heavy ion acceleration, the ions are first accelerated by Linac3 instead of Linac2.

The LHC is used as the final step of acceleration. In 2010 and 2011, protons had been accelerated up to energies of 3.5 TeV. For 2012, the energy had been increased to 4 TeV. The design energy for proton beams is 7 TeV. Ions are accelerated to 2.76 TeV per nucleon. The acceleration is performed by radiofrequency (RF) cavities running at 400 MHz with a field of 5.5 MV/m. Besides their primary purpose of acceleration, they also keep the proton beam separated in short and dense bunches. The beams are bent to a circular orbit by 1232 superconducting dipole magnets. The maximal magnetic field of 8.33 T is the limiting factor in the proton beam energy. As two equally charged proton beams run counter-clockwise in the LHC ring, all structures

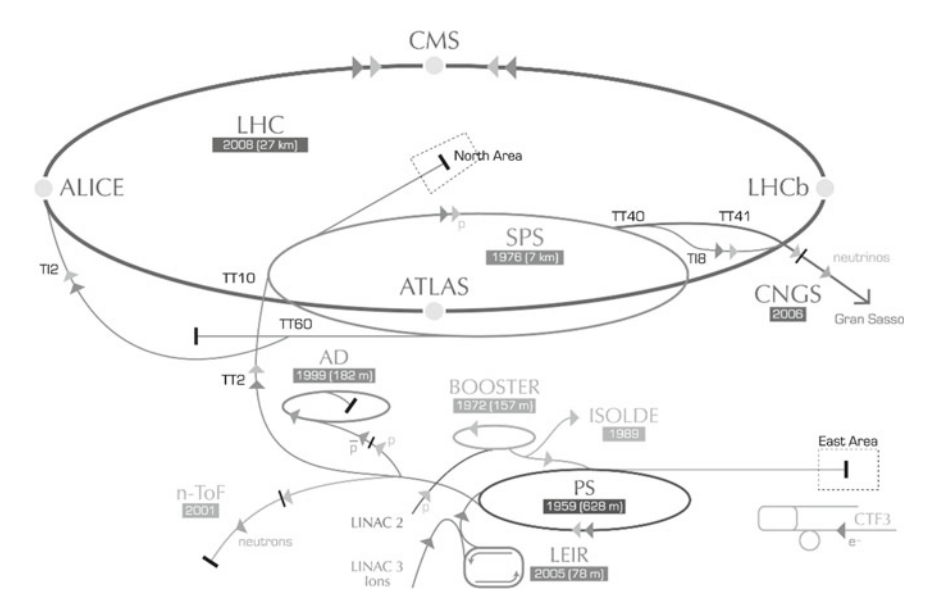


Fig. 4.1 The CERN accelerator complex with the LHC. Illustrative sketch taken from [6] and modified

need to have two beam lines with separate bending coils and RF cavities for each single beam.

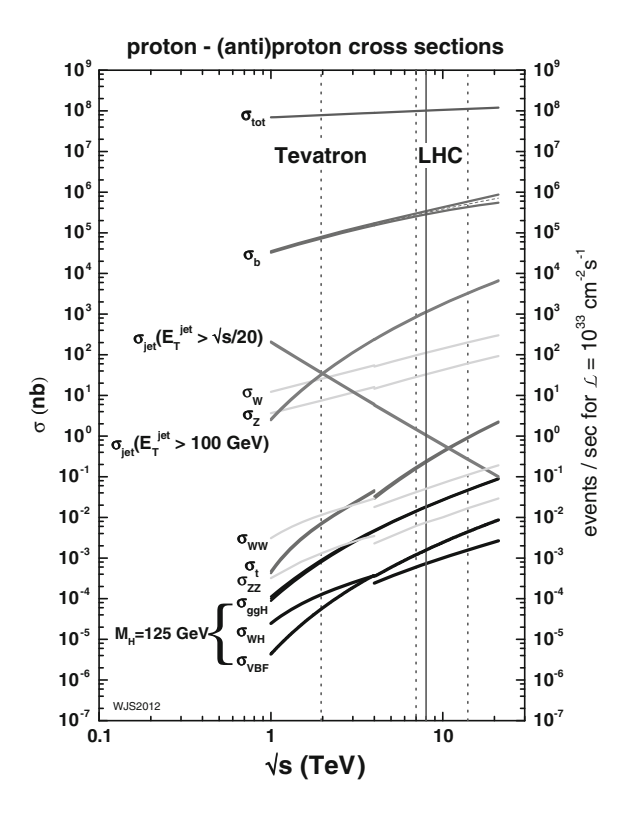
In order to perform physics studies with high precision, experiments at the LHC need high rates of particle collisions. This can be appreciated from Fig. 4.2: Several processes of interest (like Higgs boson production) happen with a rate more than ten orders of magnitude smaller than the total rate of pp interactions. The rate of a process is given as $R = \sigma \mathcal{L}$, the cross section σ multiplied by the instantaneous luminosity \mathcal{L} , which can be expressed as

$$\mathcal{L} = f_{\text{rev}} n_B \frac{N_1 N_2 \gamma}{4\pi \varepsilon_n \beta^*} F. \tag{4.1}$$

It depends on the revolution frequency, f_{rev} , the number of bunches, n_B , the numbers of protons per bunch, N_1 and N_2 , for the two colliding beams, a geometry factor F arising from the crossing angle between the colliding beams, and the transverse beam profile, usually parameterized by the normalized beam emittance, ε_n , the relativistic γ , and the beta function at the interaction point, β^* . For a high rate, large n_B , N_1 , N_2 , and small β^* are required.

A high number of dense bunches are obtained prior to the LHC injection, the bunching is mainly performed by the PS. Nominally, up to 2808 proton bunches with 1.2×10^{11} protons per bunch are kept in the LHC, leading to a bunch crossing rate of 40 MHz. A small transverse beam profile is achieved by the beam focussing of 392 quadrupole magnets. Both the bending dipole magnets, as well as the focussing

Fig. 4.2 SM cross section for $pp(\overline{p}p)$ collisions as a function of \sqrt{s} . The steps are due to differences between the pp and $\overline{p}p$ initial state. Plot taken from [7]



quadrupole magnets are superconductive and need to be cooled down to 1.9 K using pressurized superfluid helium. Additional multipole magnets are used for beam corrections in order to keep the beams stable.

The number of protons per bunch is very high at the LHC, the chances of having multiple pp collisions at the same bunch-crossing are high. In interesting physics events (a collision at high Q^2), additional collisions at the same or neighboring bunch-crossings feeding into detector signatures are usually called *pileup interactions* or just *pileup*. These pileup interactions happen at low Q^2 , and are treated as minimum bias interactions.

In Table 4.1, the design parameters for LHC *pp* collisions are listed and compared to the conditions during 2010, 2011, and 2012 operation.

The LHC provides proton and heavy ion collisions to four experiments:

- ALICE (A Large Ion Collider Experiment) [9] is dedicated to heavy-ion physics.
- ATLAS (A Toroidal LHC ApparatuS) [10] is one of the two general-purpose detectors
- CMS (Compact Muon Solenoid) [11] is the other general-purpose detector. It will be discussed in Sect. 4.2.
- LHCb (LHC beauty) [12] is specialized for heavy-flavor physics.

Parameter	2010	2011	2012	Design
Beam energy [TeV]	3.5	3.5	4	7
β^* for ATLAS/CMS [m]	2.0/3.5	1.5/1.0	0.6	0.55
Bunch spacing [ns]	150	75/50	50	25
Number of bunches	368	1380	1380	2808
Maximal number of protons per bunch	1.2×10^{11}	1.45×10^{11}	1.7×10^{11}	1.2×10^{11}
ε_n at start of a fill [mm·mrad]	≈2.0	≈2.4	≈2.5	3.75
Peak luminosity [cm ⁻² s ⁻¹]	2.1×10^{32}	3.7×10^{33}	7.7×10^{33}	10 ³⁴
Maximal mean number of pileup events	3	16	36	18
Stored beam energy [MJ]	≈28	≈110	≈140	362
m.i. 0. 503				

Table 4.1 LHC parameters during 2010, 2011, and 2012 operation for *pp* collisions compared with the design parameters

Taken from [8]

The LHC also hosts three smaller experiments: LHCf [13], MoEDAL [14, 15], and TOTEM [16].

4.2 The Compact Muon Solenoid Experiment

The CMS experiment is a general-purpose detector located at the LHC. The physics goals of the experiment are:

- discover and study the properties of the Higgs boson to understand the nature of the electroweak symmetry breaking,
- search for physics beyond the SM, such as SUSY or extra dimensions,
- perform high precision measurements of the SM to probe its validity at the TeV scale.
- observe and study rare processes in the heavy-flavor sector,
- and study the quark-gluon plasma in heavy-ion collisions.

To achieve these goals the focus of the CMS detector construction was set to have

- a muon system that provides good momentum resolution and high muon identification efficiency,
- a compact inner system with good track momentum resolution and high precision electromagnetic energy measurements,
- and a hermetic hadron calorimeter allowing for a reliable reconstruction of the $E_{\mathrm{T}}^{\mathrm{miss}}$.

The CMS detector is constructed out of many subdetectors. In the innermost part are the silicon pixel and strip detectors for measuring the tracks and momenta of charged particles, followed by the electromagnetic crystal and hadron sampling calorimeters, measuring the energies of electrons, photons, and hadrons.

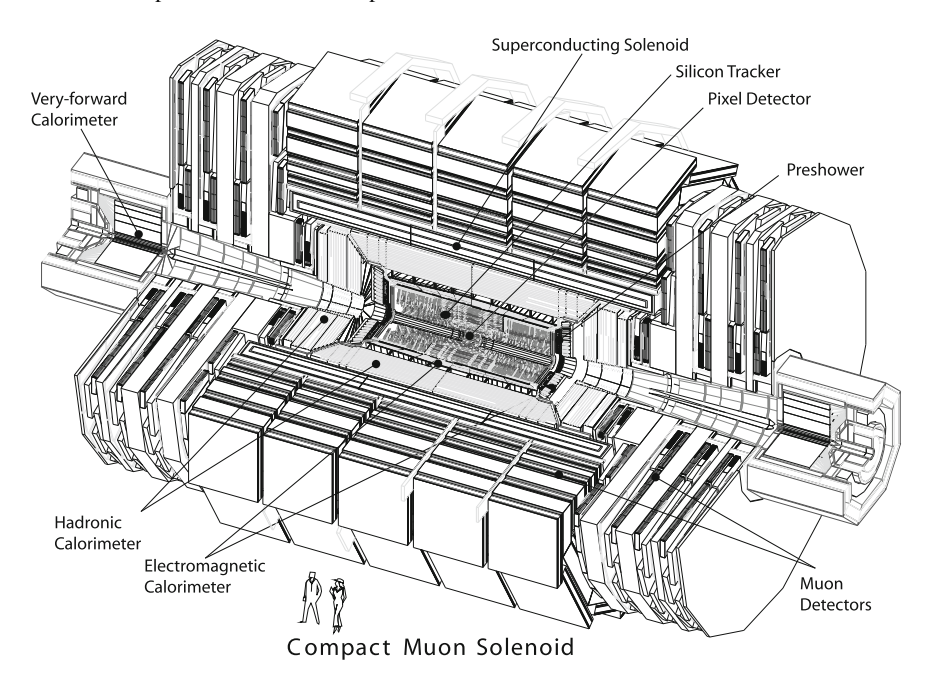


Fig. 4.3 Schematic view of the CMS detector [11]

The heart of the CMS experiment is the superconducting magnet. The 6 m-in-diameter and 12.5 m-long solenoid produces a magnetic field of 3.8 T. This strong field bends the tracks of charged particles, allowing the tracking system to precisely measure the momenta of charged particles, but also to build the detector in a compact way. Around the solenoid, a steel yoke, made out of five wheels and two endcaps, has been built to return the magnetic flux.

Within the steel return yoke, the muon system is built, providing additional track measurements for muons. Additional hadron calorimeters complement the energy measurement in the very forward region. The architecture of the detector can be decomposed in three parts: a cylindrical, onion-shaped part at the center around the beamline, the barrel, as well as two endcaps at the forward ends of the detector, allowing for a nearly 4π coverage around the interaction point. A schematic view of CMS is shown in Fig. 4.3.

The coordinate system used in CMS and throughout this dissertation is defined as follows: the origin is set to the nominal interaction point in the middle of the experiment. The x axis points upwards, the y axis to the center of the LHC ring, and the z-axis is along the counter-clockwise beam direction. The azimuthal angle ϕ is defined as the angle in the transverse xy plane starting at the x axis. The polar angle θ is measured from the z axis. Furthermore, the radius r is defined as the distance to the beam axis z, and the pseudorapidity η is defined as $\eta = -\ln\tan(\theta/2)$.

In the next sections, the design of each subdetector is reviewed. A more detailed overview is given [11], which is the basis to this chapter. Section 4.2.5 is based on [17].

4.2.1 The Tracking System

The tracking system is the innermost subdetector of the CMS experiment. It measures accurately the position of charged particles, leading to precise measurements of the track momenta and efficient vertex reconstruction. The system is built out of a pixel detector surrounded by a strip detector. The full tracker volume has a length of 5.8 m and is 2.5 m in diameter, covering a region up to $|\eta| < 2.5$. The layout of the tracking system is shown in Fig. 4.4.

The pixel detector is made out of 1440 modules with 66 million silicon pixels. They are located in three cylindrical barrel layers at radii r = 4.4, 7.3, and 10.2 cm, and two disks in each endcap at |z| = 34.5 and 46.5 cm. The pixel dimension is $100 \times 150 \,\mu\text{m}^2$. The total active area is about $1 \,\text{m}^2$. The pixel detector has high resolutions in the $r\phi$ - and z-direction of 10 and $20 \,\mu\text{m}$, respectively.

The strip detector is made out of 9.3 million silicon micro-strips with an active area of about $198 \, \mathrm{m}^2$. The detector has a dense inner part (TIB/TID, see Fig. 4.4) consisting of four cylindrical layers and three disks on each end within the radii of $20-55 \, \mathrm{cm}$, and a less dense outer part (TOB/TEC region, see Fig. 4.4) covering a region with radii up to $116 \, \mathrm{cm}$ and a z range up to $|z| < 282 \, \mathrm{cm}$. The outer part is arranged in six barrel layers and nine disks per endcap. The strip detector provides up to nine ϕ measurements along r. The two innermost layers and rings of both the inner and outer parts, as well as the fifth ring for the outer disks are equipped with

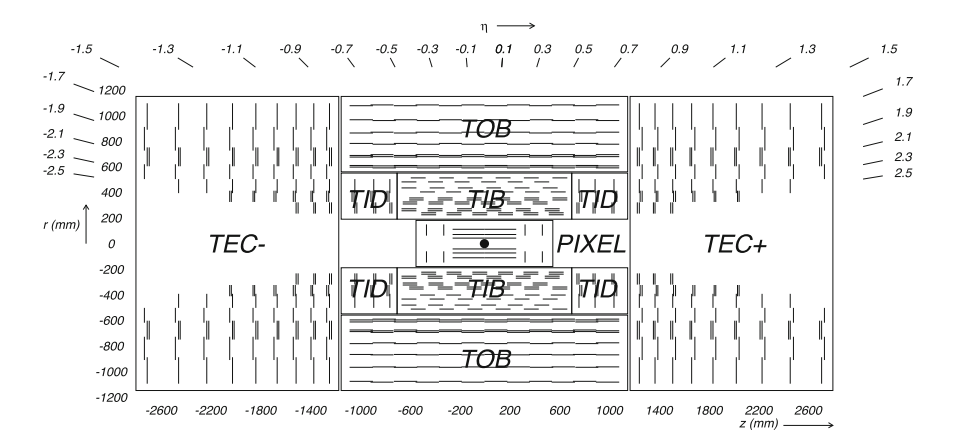


Fig. 4.4 Layout of the CMS tracking system in the rz view [11]

secondary strip modules allowing also measurements along r in the barrel, and z in the endcaps.

The track momentum resolution in CMS is $\lesssim 2\%$ in the barrel ($|\eta| < 1.6$) for a charged particle with transverse momentum ($p_{\rm T}$) less than 100 GeV and deteriorates to $\approx 7\%$ at $|\eta| = 2.4$ for $p_{\rm T} = 100$ GeV. The resolution on the transverse impact parameter is below 20–30 μ m for tracks of $p_{\rm T} > 10$ GeV and degrades to 90–200 μ m for $p_{\rm T} = 1$ GeV.

4.2.2 The Electromagnetic Calorimeter

The electromagnetic calorimeter (ECAL) is a homogeneous crystal calorimeter surrounding the tracker volume. The main component are the 75'848 lead tungstate (PbWO₄) crystals. They act as both absorber and scintillator, and therefore provide an excellent energy resolution.

The crystals have a high density of $\rho = 8.28 \, \text{g/cm}^3$ resulting in a small Molière radius (2.2 cm) and a short radiation length (0.89 cm). Thus, the calorimeter can be made compact with high granularity. In the ECAL barrel (EB), covering $|\eta| < 1.479$, the crystals have a front-face size of $22 \times 22 \text{ mm}^2$ and a length of 23 cm. For the ECAL endcaps (EE), extending the coverage up to $|\eta|$ < 3.0, the front-face cross section of the crystals is $28.62 \times 28.62 \text{ mm}^2$ and their length is 22 cm. Another advantage of PbWO₄ is that it is radiation-hard and fast: about 80 % of the light is emitted within 25 ns. The discussion of sources of radiation damages is postponed to Sect. 11.1. The limitations of PbWO₄ is its low light output of \approx 6–10 photoelectrons/MeV [18, 19]. The reason of the spread in light yield is found in the production mechanism: Two producers were chosen for providing the PbWO₄ crystals to CMS: The Bogoroditsk Techno-Chemical Plant (BTCP) in Russia and the Shanghai Institute of Ceramics (SIC) from China used different crystal growing techniques and different doping. This results in a 50% higher light yield for SIC crystals [19]. Therefore, it has been chosen to use only SIC crystals for the most inner part (high $|\eta|$ region) in the ECAL endcaps.

The scintillation light produced by the crystals is collected by two silicon avalanche photodiodes (APDs) per crystal in the barrel. In the endcaps, vacuum phototriodes (VPTs) are used as they are radiation-harder. Their lower gain times quantum efficiency compared to the APDs is partially compensated by the larger coverage of the back-face crystal surface. Both the light yield of the crystals as well as the amplification factor of the APDs are highly temperature dependent: a stability of $18 \pm 0.05\,^{\circ}\mathrm{C}$ is required.

The ECAL has been built to measure precisely the energy of electrons and photons. One of the physics goals is to provide a very good $\gamma\gamma$ mass resolution, needed for Higgs boson physics. In order to distinguish photons from neutral pion decays into $\gamma\gamma$, the preshower detector has been built in front of the ECAL endcaps, covering the region $1.653 < |\eta| < 2.6$. The preshower has two layers of lead absorbers, each layer followed by a plane of silicon strip sensors.

A schematic view of the CMS ECAL components is shown in Fig. 4.5.

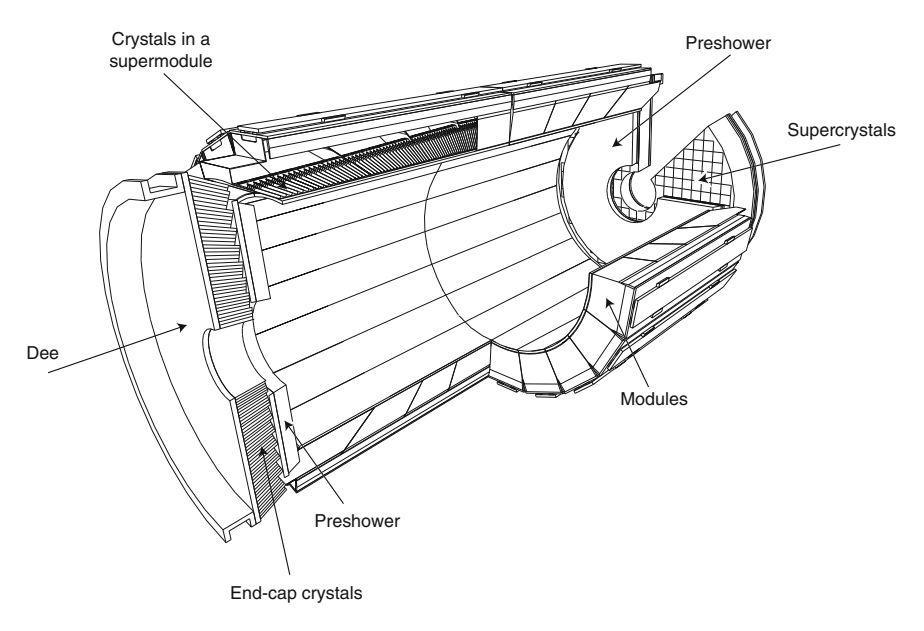


Fig. 4.5 Layout of the ECAL subdetector. Taken from [11]

The energy resolution has been measured to be [11]

$$\frac{\sigma(E)}{E} = \frac{2.8\%}{\sqrt{E/\text{GeV}}} \oplus \frac{12\%}{E/\text{GeV}} \oplus 0.3\%$$
 (4.2)

for a 3×3 crystal matrix using testbeam data. The first term is the *stochastic* contribution due to fluctuations in photostatistics and due to the preshower. The second term comes from *noise* of the detector electronics and digitization. The third term is *constant* and arises from non-uniformity of the light collection, intercalibration errors, and back-end energy leakage.

4.2.3 The Hadron Calorimeter

The hadron calorimeter (HCAL) is located between the ECAL and the magnet, complementing the energy measurement for hadrons. It is particularly important for jet energy and $E_{\rm T}^{\rm miss}$ measurements. The HCAL, illustrated in Fig. 4.6, is divided into four components: the HCAL barrel (HB) and HCAL endcaps (HE), enclosed in the magnet volume, the HCAL outer (HO) outside the magnet, and the HCAL forward (HF) in the very forward region close to the beam line.

The HCAL is an absorber/scintillator sampling calorimeter. In the HB, covering $|\eta| < 1.3$, it has 16 absorber plates, the first and last being out of steel, while the

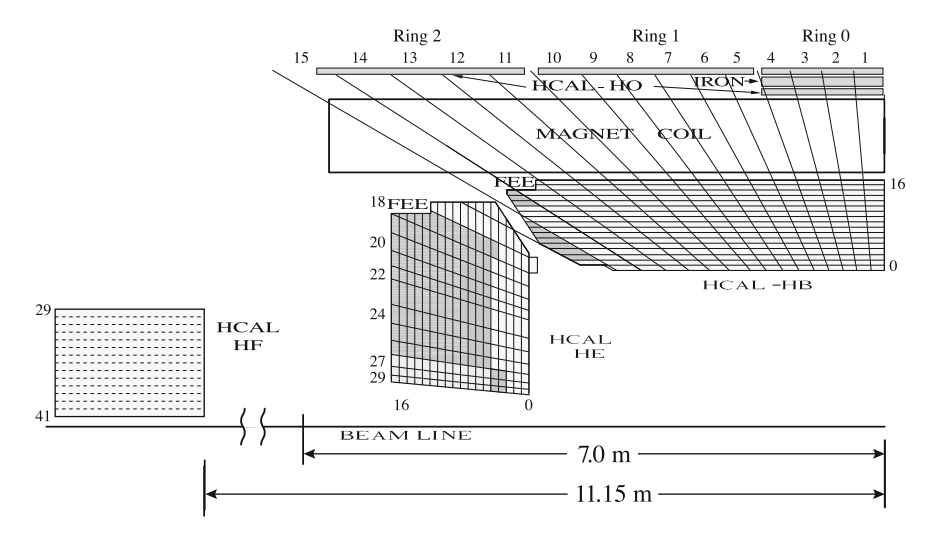


Fig. 4.6 Illustration of the segmentation of the CMS HCAL [20]

others are made out of brass. The thickness of these plates varies between 50.5–56.5 mm for the brass plates, and is 40 (70) mm for the inner (outer) steel plate. The active material between these absorber plates is a radiation-hard plastic scintillator of 3.7 mm thickness, except for the first and last layers, which are 9 mm thick. This sampling corresponds to 5.82 (10.6) interaction lengths (λ_I) for $|\eta| = 0.0$ (1.3). The channel segmentation in the HB is $\Delta \eta \times \Delta \phi = 0.087 \times 0.087$.

At central rapidities, the hadronic shower is not fully contained within the HB. Therefore, the HCAL is extended outside the magnet with the HO. The solenoid is used as additional absorber material. The HO has two scintillator layers interleaved with a 19.5 cm thick iron plate for the most inner ring, and one scintillation layer for the outer rings. The effective absorber length of the HCAL is extended beyond $10 \, \lambda_I$ in the barrel. The coverage of the HO is $|\eta| < 1.262$.

The HE covers 1.3 < $|\eta|$ < 3.0. The sampling is done with 79 mm thick brass absorber plates and 3.7–9 mm thick plastic scintillation layers. The granularity of the HE is $\Delta\eta \times \Delta\phi \approx 0.17 \times 0.17$.

These inner HCAL components (HB, HE, and HO) are read out by multichannel hybrid photodetectors (HPDs) with a gain of \approx 2000.

The HF extends the coverage of the HCAL to the very forward region of 3.0 < $|\eta| < 5.0$. It has to sustain extremely high particle fluxes and must be very radiation-hard. Two sets of quartz fibers are used as active material: long fibers, running over the full depth of the detector, and short fibers, starting at a depth of 22 cm from the front of the detector. They are interleaved with steel absorber. The Cherenkov light captured by the quartz fibers is read out by conventional photomultiplier tubes (PMTs). The segmentation of the HF is $\Delta \eta \times \Delta \phi \approx 0.175 \times 0.175$.

The energy resolution for hadrons of the combined calorimeter (ECAL and HCAL) has been determined for the barrel as

$$\frac{\sigma(E)}{E} = \frac{84.7\%}{\sqrt{E/\text{GeV}}} \oplus 7.4\%,$$
 (4.3)

and for the HF as

$$\frac{\sigma(E)}{E} = \frac{198\%}{\sqrt{E/\text{GeV}}} \oplus 9\% \text{ [20]}.$$
 (4.4)

4.2.4 The Muon System

The radial most outer subsystem of the CMS detector is the muon system, which is embedded in the steel return yoke. The muon system complements the inner tracker for the measurements of muons. It ensures a high identification efficiency and very precise momentum measurements. The muon system is comprised of three different detector technologies: drift tube (DT) chambers in the barrel ($|\eta| < 1.2$), cathode strip chambers (CSCs) in the endcaps (0.9 < $|\eta| < 2.4$), and resistive plate chambers (RPCs) in both the barrel region and a fraction of the endcap region ($|\eta| < 1.6$). A sketch of the muon system can be found in Fig. 4.7.

The DTs are segmented in four cylindrical stations with a total number of 172'000 sensitive wires. The wires are arranged into groups of four layers. In the three inner stations two groups are aligned with the beamline, providing a $r\phi$ measurement, and

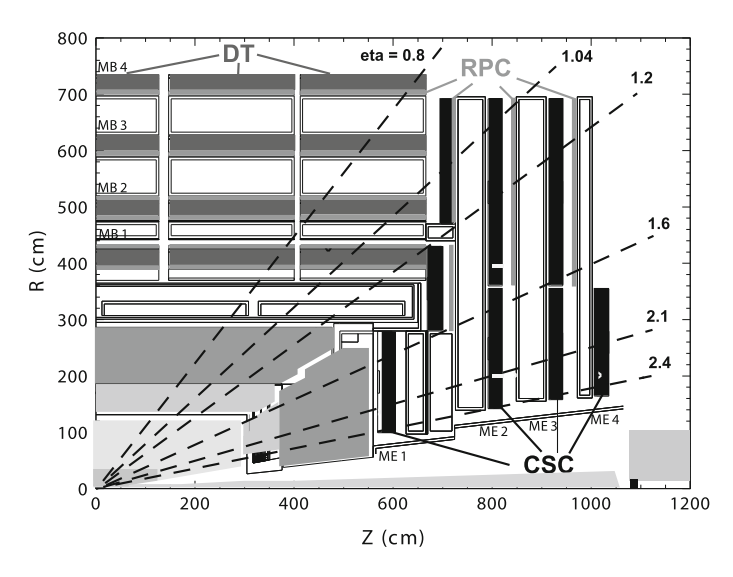


Fig. 4.7 Illustration of the CMS muon system [17]

one group is orthogonal to the beamline to provide an additional rz measurement. The outer stations have two groups for the $r\phi$ measurement. The wires are made out of gold-plated stainless steel and have a length of 2.4 m, one drift cell has a transverse dimension of 21 mm. The cathode is made out of aluminium tape. The drift gas is a mixture of 85 % Ar + 15 % CO₂.

In each endcap, 234 CSCs are deployed, stationed in four layers. The CSCs are multiproportional wire chambers with anode wires made out of gold-plated tungsten, and cathode strips perpendicular to the wires. The gase mixture for the CSCs is $40\% \text{ Ar} + 50\% \text{ CO}_2 + 10\% \text{ CF}_4$.

The RPCs provide a very fast muon measurement, important for efficiently triggering an event containing a muon. The RPCs are parallel-plate detectors with a gas-filled gap between them. The plates are bakelite-based, the gas mixture of 95.2 % $C_2H_2F_4 + 4.5$ % $C_4H_10 + 0.3$ % SF₆ is kept at ~45 % humidity to keep the bakelite resistivity constant. The RPCs are divided into 109'608 strips with widths of 1.95–4.10 cm [21].

The resolution for muons, reconstructed only by the muon system, is about 9% for low $p_{\rm T}$ muons ($p_{\rm T} \lesssim 200~{\rm GeV}$) and up to 15–40% for $p_{\rm T}=1~{\rm TeV}$. Combining tracker and muon system information yields a momentum resolution of 0.8–2% for $p_{\rm T} \lesssim 200~{\rm GeV}$ and 5–10% at $p_{\rm T}=1~{\rm TeV}$.

During the long shutdown of the LHC in 2014, the muon system has been upgraded [22]: the fourth layer for both the CSC and RPC systems is completed for the outer rings, enhancing the muon identification efficiency by $\sim 2\%$ for $1.2 < |\eta| < 1.8$.

4.2.5 Trigger and Data Acquisition

At the LHC, pp collisions happened at a bunch-crossing rate of 20 MHz, the design rate is 40 MHz. The amount of data accumulated is so large that it cannot be stored, an immense reduction of a factor 10^6 is needed. The CMS trigger system is a two stage trigger: the Level-1 (L1) trigger is a hardware-based system, consisting of programmable electronics, with a design output rate of $30-100\,\text{kHz}$. The second step, the High-Level trigger (HLT), is software-based, and reduces further the rate to about 100 events per second.

The L1 trigger is based on the information of the calorimeter and muon system only. It analyzes each bunch-crossing with a maximum latency between the bunch-crossing and the trigger decision of 3.2 μ s, requiring pipelining of the event processing. The local trigger tower for the calorimeters is formed by 5 × 5 ECAL crystals and one HCAL cell. This local trigger information is sent to regional triggers of 4 × 4 trigger towers. The regional trigger selects e, γ , and τ_{had} candidates, and determines isolation bits for muons. The global trigger determines jets, transverse energy, E_{T}^{miss} , jet counts, and H_{T} (the scalar sum of the transverse momenta of jets above a programmable threshold). Both the DTs and CSCs form the local trigger from each single chamber. The RPCs form a muon candidate if the pattern logic is

consistent with a possible muon track. The global muon trigger combines the information of all three subsystems using the four best muon candidates of the DT and CSC substystems and all RPCs candidates.

The HLT farm processes all events with positive L1 decision and uses the full detector information including the tracker and the full granularity of the calorimeter. The HLT allows to compute sophisticated objects and to use combinations of objects for the final trigger decision: the trigger paths can be based on two or more objects, like jets and $E_{\rm T}^{\rm miss}$, and can contain complex objects like b-quark or $\tau_{\rm had}$ tagging information. The HLT is very flexible, but the general idea is to use as few information as possible and discard events as soon as possible.

The data acquisition (DAQ) system must be able to cope with the high data rates produced by the L1 trigger, which is of order of 100 GB/s. The DAQ system is responsible for reading out the information from the subdetectors of about 500 sources, process the events in the HLT farm, send the data to the CERN computing center (called Tier-0), where the data is stored with a rate of several hundred MB/s. The data is further distributed and duplicated to few national computing centers (Tier-1's), and also regional or institutional computing centers (Tier-2's).

References

- L. Evans, P. Bryant, LHC machine. JINST 3, S08001 (2008). doi:10.1088/1748-0221/3/08/ S08001
- O.S. Brüning et al., LHC design report 1, the LHC main ring.CERN (2004). doi:10.5170/ CERN-2004-003-V-1
- O.S. Brüning et al., LHC design report 2, the LHC infrastructure and general services. CERN (2004). doi:10.5170/CERN-2004-003-V-2
- M. Benedikt et al., LHC design report 3, the LHC injector chain. CERN (2004). doi:10.5170/ CERN-2004-003-V-3
- 5. S. Myers, E. Picasso, The design, construction and commissioning of the CERN large electron positron collider. Contemp. Phys. **31**, 387 (1990). doi:10.1080/00107519008213789
- C. Lefèvre, The CERN accelerator complex. Complexe des acclrateurs du CERN (2008).
 Available on the CERN document server: https://cds.cern.ch/record/1260465
- J.M. Campbell, J. Huston, W. Stirling, Hard interactions of quarks and gluons: A primer for LHC physics. Rep. Prog. Phys. 70, 89 (2007). doi:10.1088/0034-4885/70/1/R02. arXiv:hep-ph/0611148. Updated plot taken from http://www.hep.ph.ic.ac.uk/wstirlin/plots/ plots.html
- 8. M. Lamont, LHC, HL-LHC and beyond. PoS, EPS-HEP2013, 149 (2014)
- ALICE Collaboration, The ALICE experiment at the CERN LHC. JINST, 3, S08002 (2008). doi:10.1088/1748-0221/3/08/S08002
- ATLAS Collaboration, The ATLAS experiment at the CERN large hadron collider. JINST, 3, S08003 (2008). doi:10.1088/1748-0221/3/08/S08003
- CMS Collaboration, The CMS experiment at the CERN LHC. JINST, 3, S08004, (2008). doi:10.1088/1748-0221/3/08/S08004
- LHCb Collaboration, The LHCb detector at the LHC. JINST, 3, S08005, (2008). doi:10.1088/ 1748-0221/3/08/S08005
- LHCf Collaboration, The LHCf detector at the CERN large Hadron Collider. JINST, 3, S08006, (2008). doi:10.1088/1748-0221/3/08/S08006

14. MOEDAL Collaboration, Searching for exotic particles at the LHC with dedicated detectors. Nucl. Phys. Proc. Suppl. **78**, 52 (1999). doi:10.1016/S0920-5632(99)00522-8

- MoEDAL Collaboration, Technical design report of the MoEDAL experiment. CERN, LHCC-2009-006 (2009). http://cds.cern.ch/record/1181486
- G. Franzoni on behalf of the CMS Collaboration, Performance of CMS ECAL with first LHC data. Nucl. Instrum. Methods A, 628, 90 (2011). doi:10.1016/j.nima.2010.06.291
- CMS Collaboration, CMS physics technical design report, volume I: Detector performance and software. CERN, LHCC-2006-001 (2006). http://cds.cern.ch/record/922757
- E. Auffray et al., Status on PWO crystals from Bogoroditsk after one year of preproduction for CMS-ECAL. Nucl. Instrum. Methods A 453, 218 (2000). doi:10.1016/S0168-9002(00)00633-1
- R. Mao, L. Zhang, R. Zhu, Quality of mass produced lead tungstate crystals. IEEE Trans. Nucl. Sci. 51, 1777 (2004). doi:10.1109/TNS.2004.832561
- CMS Collaboration, Performance of the CMS Hadron calorimeter with cosmic ray muons and LHC beam data. JINST, 5, T03012, (2010). doi:10.1088/1748-0221/5/03/T03012. arXiv:0911.4991
- P. Paolucci et al., CMS resistive plate chamber overview, from the present system to the upgrade phase I. PoS, RPC2012, 004 (2012). doi:10.1088/1748-0221/8/04/P04005. arXiv:1209.1941
- 22. M.S. Kim, The CMS RPC system—detector performance and upgrade, PoS EPS-HEP2013, 123 (2014). For more details on CSCs see also I. Suarez, Cathode Strip Chamber Upgrade for the CMS Endcap at the HL-LHC, talk given at 2013 Meeting of the APS Division of Particles and Fields

Chapter 5 Event Reconstruction for Proton-Proton Collisions

In this chapter, the event reconstruction of the CMS experiment is introduced. First, the basic ingredient of track and vertex reconstruction is discussed, then the particle flow algorithm and object definitions are reviewed. A special focus is set on the definitions used in this dissertation.

5.1 Track Reconstruction

Before reconstructing a track, local signals above a threshold in the pixel and strip detectors (for muons also in the muon chambers) have to be clustered into so-called *hits*. The threshold is defined for noise suppression. Local signals in adjacent detector units (like pixels) are combined, the hit center is estimated and corrected for the drift of the collected charge in the magnetic field [1].

Tracks are reconstructed from hits using a combinatorial track finder algorithm based on an adapted Kalman filter [2]. The idea is to perform the tracking iteratively: first, the "simple" tracks (for example high- $p_{\rm T}$ and high purity tracks) are reconstructed. The associated hits are removed, before the next iteration is started. Thus, combinatorics are reduced for the more difficult classes such as low- $p_{\rm T}$ tracks. In total, six iterations take place.

Each iteration is performed in four steps: First, a seed is defined. Each seed is extracted out of two or three hits. For example, the first iteration requires three hits in the pixel detector. These hits must be compatible for a track and define its initial trajectory. The second step is the track finding based on a Kalman filter: The trajectory is extrapolated and compatible hits are added to the track. Then, the track is fitted to provide the best estimate of its properties (like its momentum). The reconstructed track quality is examined and tracks failing quality criteria are removed.

A detailed description of the combinatorial track finder algorithm can be found in [1].

5.1.1 Primary Vertex Reconstruction

A vertex is called primary if it comes from a hard scattering. This includes both the vertex of the hard interaction of interest as well as vertices of additional pileup interactions.

Tracks used for primary vertex (PV) reconstruction [1] have to be compatible with the beamspot, contain at least two pixel and five pixel+strip hits, and must be of high quality.

The vertices are then found by a deterministic annealing algorithm [3]. The trackvertex assignment is soft: a track i has a probability p_{ik} to come from vertex k. The number of vertices and vertex positions are found in the iterative minimization procedure for the possible vertex position z_k^V . The algorithm starts with one vertex. During the iterations, a vertex is split if tracks associated to it are compatible to come from two distinct vertices. The algorithm stops at a critical scale, set to have a possibly large vertex finding efficiency, but low fraction of incorrect vertices. To reduce the number of fake vertices, a vertex is kept if at least two tracks are compatible only with that vertex. A track must have a probability of at least 0.5 to be assigned to a vertex.

In the final step, an adaptive vertex fitter is used to obtain the best estimate of the vertex properties, such as its position. The vertex resolution is about $20 \,\mu$ m for the x and y directions, and around $25 \,\mu$ m for the z direction for vertices with at least 50 associated tracks.

The hard scatter vertex is usually chosen as the PV, which has the largest $\sum_{i} (p_{T,i})^2$ of tracks i associated to it. Below, if the PV is not specified, it is assumed to be that vertex.

5.2 The Particle-Flow Algorithm

The particle-flow (PF) event reconstruction [4] aims to identify each particle in a collision by using information of all subdetectors. Input to this algorithm are tracks from the tracker and muon systems as well as calorimeter clusters. These clusters are seeded by calorimeter cells having local energy maxima, and adjacent cells are clustered if they exceed the noise signal threshold. For the HF, no clustering is performed. Then, the signals of tracks, calorimeter clusters, and muon tracks are linked together to form PF blocks. For example, the track trajectory is extrapolated to the ECAL system, and if a compatible ECAL cluster is found, these two measurements are linked together. In this linking, also effects like bremsstrahlung photons along the track are considered to recover their energies. Similar linkings happen between the ECAL and HCAL systems, and inner and muon tracks. Additional information, like the calorimeter shower shapes, are taken into account to discriminate between the different particle types and noise signals. The particle types reconstructed by the PF algorithm are electrons, muons, photons, charged and neutral hadrons.

In the following, the reconstruction of important objects are described. At the end of each section, the identification criteria are stated as used in this dissertation.

5.3 Muon Reconstruction

Muons can be measured by the tracker only (tracker muons), the muon system only (stand-alone muons) or their combination (global muons). Similar to the track finding, stand-alone muon tracks are obtained by a Kalman filter. These tracks are extrapolated to the tracker, and its measurement with the best-compatible track is combined to form a global muon. Furthermore, vertex constraints are required. The PF algorithm for muons is based on this global muon reconstruction [5, 6]. As muons are minimizing ionizing particles, they leave little deposits in the ECAL and HCAL. This information can be used to identify prompt muons and discriminate against charged hadrons. However, the PF algorithm also exploits the reconstruction of non-prompt muons, for example from heavy-flavor decays. These muons are inside a jet and therefore not isolated. Their measurements are important to correct the energy of the jet measured by the calorimeter. The identification efficiency for PF muons has been measured to be \approx 99 % for muons with $p_{\rm T} < 20\,{\rm GeV}$ and close to $100\,$ % for muons above $p_{\rm T} > 20\,{\rm GeV}$ [5].

In the analysis described in this thesis, muons with $p_T > 10 \,\text{GeV}$ and $|\eta| < 2.4$ are selected. They are required to be global PF muons, must be compatible with the PV and must fulfill identification criteria to distinguish them from charged hadrons. These criteria are stated in [5] as *tight* muon selection. Muons are required to be isolated as the interest is in prompt muons from W or Z boson decays. The isolation [5] is defined using the transverse momentum sum of charged hadrons from the PV, neutral hadrons and photons in a cone of $\Delta R = \sqrt{(\Delta \phi)^2 + (\Delta \eta)^2} = 0.3$ around the muon axis. This momentum sum is corrected for the effect of additional energy in the cone due to neutral particles coming from pileup interactions as described in [7]. The ratio between this corrected momentum sum and the muon- p_T , called relative isolation, is required to be less than 0.2.

5.4 Electron Reconstruction

Electrons produce a track in the inner tracking system and leave their energy completely in the ECAL. Therefore, the electron reconstruction [8] is either seeded by a track (for low- p_T electrons) or an ECAL supercluster (for isolated high- p_T electrons). A supercluster is a group of ECAL cells, 35×5 crystals wide in $\phi \times \eta$, taking into account the characteristics of the energy deposits due to bremsstrahlung photons. For the ECAL endcaps, superclusters are a group of 5×5 crystals. The combination of track and ECAL deposit and the trajectory reconstruction are performed by

a Gaussian sum filter (GSF). Due to the large material budget of the tracker, many electrons undergo bremsstrahlung before reaching the calorimeter. The GSF takes into account the bremsstrahlung photon emissions, the subsequent loss of the electron momentum, and the influence on the electron trajectory. Compatibility between the track trajectory and ECAL deposit location as well as track momentum and ECAL energy is required. In addition, to discriminate electrons against charged hadrons, requirements on the HCAL deposit with respect to the ECAL deposit, and on the shower shape along η within the ECAL are set. The identification efficiency for electrons is measured to be between 96–99 %, but can go as low as 80 % if tight identification criteria are required [8].

For this work, electrons with $p_T > 10 \, \text{GeV}$ and $|\eta| < 2.4$ are selected, unless the electron candidate enters the EB-EE transition region (1.442 < $|\eta| < 1.566$). The interest is to select electrons from W or Z boson decays with high efficiency. Therefore, selected electrons are required to pass loose identification and be isolated. The isolation is defined similar to the one for muons (see Sect. 5.3), however, pileup contributions in the isolation cone are treated differently: the transverse momentum sum of neutral particles is corrected using the energy density of pileup interactions and the effective area of the isolation cone, as motivated by [9]. The relative isolation is required to be less than 0.15.

5.5 Tau Reconstruction

About 63% of all taus decay hadronically to one or three charged hadrons plus several neutral hadrons and a tau-neutrino, else a tau decays into one electron or muon and two neutrinos. For simplicity, hadronically-decaying taus are called taus further on. The tau reconstruction [10] is based on the collection of jets, described in Sect. 5.7. Taus are identified via the hadron-plus-strips algorithm. The algorithm uses PF to identify one or three reconstructed charged hadrons, and uses the silicon strip detector to identify photon conversions from neutral hadron decays. PF photons and electrons within the jet, compatible with a silicon strip signal, and the charged hadron candidates are combined to a tau candidate if they are in a narrow cone around the tau candidate axis. In order to reduce the misidentification rate of jets as taus, the tau decay products need to be isolated.

Taus used in this dissertation are selected with $p_T > 20\,\text{GeV}$ and $|\eta| < 2.3$. They are required to pass loose isolation criteria on PF charged and neutral candidates. The isolation is corrected for contribution of pileup interactions similar to the case of muons, see Sect. 5.3. For this isolation, a tau identification efficiency of $\approx 50\,\%$ is achieved for a misidentification rate for jets of about 1 % [10]. Further rejection criteria are applied to discriminate taus against muons or electrons.

5.6 Photon Reconstruction

As for electrons, photons are not directly reconstructed by the PF algorithm. The main reason is, that PF is not fully efficient in the electron-photon disambiguation. The photon reconstruction [11] is based on the ECAL supercluster signal. Due to the large material budget of the tracker, a significant fraction of photons converts into e^+e^- pairs before reaching the calorimeter. These conversions are recovered by finding a pair of oppositely charged tracks inside a supercluster compatible with a conversion signal. Photon candidates compatible with an electron signature are rejected. A narrow shower shape is required to discriminate against isolated neutral hadron decays into photons (like $\pi^0 \to \gamma \gamma$). The shower shape in η is independent of the magnetic field. Therefore, a good discriminator is the energy-weighted variance, σ_{inin} , of the position in η of the crystal with maximum energy within the 5 × 5 crystal array around it. It expresses the extent of the cluster in η . Another discriminant against neutral hadrons is the requirement of low energy deposit in a single HCAL tower with respect to the corresponding ECAL signal. Prompt photons are required to be isolated. The isolation is based on PF using particles in a cone of $\Delta R < 0.3$ around the photon candidate and including pileup corrections similar to the electron case, see Sect. 5.4.

For this work, photons with $p_T > 20 \, \text{GeV}$, $|\eta| < 2.4$ are selected, unless the photon candidate is pointing to the EB-EE transition region (1.442 $< |\eta| < 1.566$). The photon candidate must fulfill loose identification and isolation criteria. The selection efficiency for these criteria is $\gtrsim 90 \%$ (85 %) for photons reconstructed in the ECAL barrel (endcaps) [12].

5.7 Jet Reconstruction

As already described in Sect. 1.2.4, quarks and gluons create showers and hadronize and form clusters of hadrons, called jets. A jet represents the properties of the initial parton, for example its four-momentum. The clustering method used in this dissertation is the anti- $k_{\rm T}$ algorithm [13]. For each pair of particles i and j, three distance parameters, d_i (d_j) and d_{ij} , are defined as

$$d_{i} = p_{T,i}^{-2},$$

$$d_{ij} = \min(p_{T,i}^{-2}, p_{T,j}^{-2}) \frac{(\phi_{i} - \phi_{j})^{2} + (y_{i} - y_{j})^{2}}{R^{2}},$$
(5.1)

where $y = \frac{1}{2} \ln \left(\frac{E + p_z}{E - p_z} \right)$ is the rapidity, and R a distance parameter. In this analysis, as for most CMS analyses, R = 0.5 is chosen. The algorithm starts with a list of all particles. In each clustering step, all distances d_i and d_{ij} are calculated and the minimum is found. If the minimum is any d_{ij} , objects i and j are clustered to a new object k and removed from the object list, the new object k is added to the list. If any

 d_i is the minimum, this object is removed from the list and called a jet. The algorithm is performed until no object is left in the list. This algorithm is both collinear and infrared safe. All PF particles are clustered into jets using this algorithm [4, 14].

In this work, two exceptions are made: Charged particles not originating from the PV are removed from a jet, the so-called charged-hardon subtraction (CHS) [15]. This reduces the influence of pileup interactions on the jet energy measurement. The second exception is that jets, which axes are within $\Delta R = 0.4$ of the direction of selected electrons, muons, or photons, are not considered.

Any measured object within the detector, including artificial detector signatures such as noise signals from readout electronics or the calorimeter, is taken into account in the jet clustering. To avoid jets arising from such noise signatures, identification criteria are applied on the hadronic, electromagnetic and charged energy fractions [14]. These retain almost all jets truly originating from a quark or gluon hadronization, but reject most jets due to noise and other spurious signals.

In this dissertation, jets are reconstructed as PF jets with $p_{\rm T} > 40\,{\rm GeV}$ and $|\eta| < 2.4$. For some variables, jet candidates with $p_{\rm T} > 20\,{\rm GeV}$ are used if specified. The jet- $p_{\rm T}$ is corrected for non-uniform jet energy response as described in the next section. Additionally, loose identification criteria are applied.

Jet Energy Corrections

A reconstructed jet should resemble the property of the initial parton, especially its direction and energy. While the energy is measured with high precision for single particles, energy measurements of jets are not perfect due to effects of the UE, pileup, noise, hadronization products being outside the jet cone, or non-uniformities in η and $p_{\rm T}$. Therefore, the measured ("raw") jet momenta $p_{\rm raw}^{\mu}$ have to be corrected for these effects [16]. As jets are an important ingredient in the analyses presented in this work, the jet energy corrections are reviewed in greater detail.

The calibrated jet momenta are obtained via

$$p^{\mu} \equiv p_{\text{calib}}^{\mu} = \mathcal{C}p_{\text{raw}}^{\mu}. \tag{5.2}$$

The correction factor C is factorized via

$$C = C_{\text{offset}}(p_{\text{T,raw}}) \cdot C_{\text{MC}}(p_{\text{T}}', \eta) \cdot C_{\text{rel}}(\eta) \cdot C_{\text{abs}}(p_{\text{T}}''), \tag{5.3}$$

where $p_{\mathrm{T}}'(p_{\mathrm{T}}'')$ denotes the jet- p_{T} after applying the offset (all previous) corrections. The offset correction, $\mathcal{C}_{\mathrm{offset}}$, removes energy from pileup interactions. As charged particles not coming from the PV are already removed, this correction is only applied to the neutral part of the jet momentum. The correction uses a hybrid FastJet pileup subtraction scheme [9, 17]: the average p_{T} -density ρ is defined as the median $\left(\frac{p_{\mathrm{T},j}}{A_j}\right)$, where A_j is the area of jet j. The calculation of ρ is performed with jets clustered by the k_{T} algorithm [18, 19] with R=0.6 so that ρ is insensitive to jets from the hard interaction. In the offset correction, ρ is adjusted for the contribution from the UE,

5.7 Jet Reconstruction 67

and an additional factor $\beta(\eta)$ is used to correct for non-uniformities of the energy response along η . The correction $\mathcal{C}_{\text{offset}}$ is expressed as

$$C_{\text{offset}}(\rho, p_{\text{T,raw}}, A, \eta) = 1 - \beta(\eta)\rho_{\text{corr}(\text{UE})} \frac{A}{p_{\text{T,raw}}}.$$
 (5.4)

The second factor, C_{MC} , corrects for the difference between generated jet energies and reconstructed jet energies using simulation. The reconstructed particles are processed through the simulation of the CMS detector based on GEANT4 [20].

The goal of the relative correction, $C_{\rm rel}$, is to obtain a uniform jet energy response as a function of η . The relative response, $\mathcal{R}_{\rm rel}$, is calibrated to jets with $|\eta| < 1.3$ using dijet balancing with one jet (tag) being within $|\eta| < 1.3$ and the second jet (probe) at any arbitrary η :

$$\mathcal{R}_{\text{rel}} = \frac{2 + \langle \mathcal{B} \rangle}{2 - \langle \mathcal{B} \rangle} \text{ with } \mathcal{B} = \frac{p_{\text{T}}^{\text{probe}} - p_{\text{T}}^{\text{tag}}}{(p_{\text{T}}^{\text{probe}} + p_{\text{T}}^{\text{tag}})/2}.$$
 (5.5)

The factor C_{rel} is the relative response \mathcal{R}_{rel} with additional small residual corrections absorbing the radiation bias (due to the presence of a soft third jet) and asymmetries in η .

The absolute correction, \mathcal{C}_{abs} , provides uniformity of the jet energy response in p_T . It is measured for jets within $|\eta|<1.3$ using the E_T^{miss} -projection-fraction method in $\gamma+{\rm jets}$ and $Z+{\rm jets}$ events with $Z\to e^+e^-$ or $\mu^+\mu^-$. The idea is that a balanced event has no E_T^{miss} (thus $\vec{p}_T^{\gamma,Z}=-\vec{p}_T^{\rm recoil}$), while if the responses R are not one,

$$R_{\gamma,Z}\vec{p}_{\mathrm{T}}^{\gamma,Z} + R_{\mathrm{recoil}}\vec{p}_{\mathrm{T}}^{\mathrm{recoil}} = -\vec{E}_{\mathrm{T}}^{\mathrm{miss}}.$$
 (5.6)

Photons, electrons, and muons can be measured with high precision and therefore $R_{\gamma,Z} \approx 1$. If one requires the γ or Z boson to recoil against one hard jet, the measurement of R_{recoil} can be used for the absolute response calibration. The bias of additional jet activity is corrected for.

In Fig. 5.1, the jet energy correction factor for PF jets in simulation is shown on the left, the uncertainty on the correction, as measured in data, is shown on the right.

5.7.1 B-Quark Jet Tagging

The identification of jets from b-quark hadronization (also called b-quark jets) is of particular interest, because third generation squarks are expected to be lighter than those of the first and second generations in many SUSY scenarios, see Sect. 2.3.

Jets originating from heavy-flavor quark hadronization (mostly b-quarks) can be discriminated against light-flavor quark and gluon jets, further called light jets. The reason is that B hadrons (and to a lesser extent D hadrons 1) have relatively large

¹Mesons containing a c quark are called *D* hadrons.

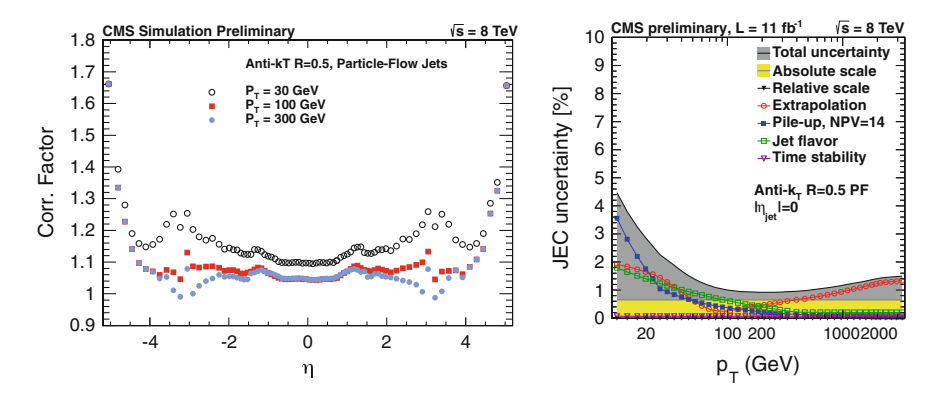


Fig. 5.1 Jet energy corrections in simulation as a function of η^{jet} (*left*) and jet energy correction uncertainty measured in data for $\eta^{\text{jet}} \approx 0$ as a function of $p_{\text{T}}^{\text{jet}}$ (*right*). Taken from [21]

masses and long lifetimes, they fly a short distance before decaying. The tracks of the daughter particles from that decay point to a secondary vertex close to the PV, from which the *B* hadron originated. In CMS, several methods are used to identify b-quark jets [22, 23]. Here, the combined secondary vertex (CSV) tagger is described. The tagger uses a sample of high-purity tracks and is based on secondary vertex and track-based lifetime information.

Secondary vertices are reconstructed by the adaptive vertex fitter [24]. A high purity is obtained by requiring that the majority of tracks associated to the secondary vertex are not pointing to the PV, and the two vertices are significantly separated. Vertices compatible with K^0 decays are rejected. Although the tracking system of CMS is very performant, a secondary vertex cannot always be reconstructed. Even though, information on the tracks inside the jet can be used to discriminate B-hadron decays: For example, tracks pointing to a secondary vertex are expected to have high impact parameters. The CSV tagger therefore builds a likelihood using vertex information, and track information like the 3D impact parameter of all tracks inside a jet. This likelihood yields a high discrimination power: For a light-jet rejection of $\approx 99\,\%$, a b-quark jet tagging efficiency of 65–75% is achieved. As D hadrons also have a significantly long lifetime, the c-quark jet tagging rate is about 15–20%. This working point is usually called medium operating point [22, 23] and is used throughout this dissertation. A jet tagged with this working point will be called b jet.

In Fig. 5.2, the b-quark jet tagging efficiency as a function of the CSV discriminant is shown.

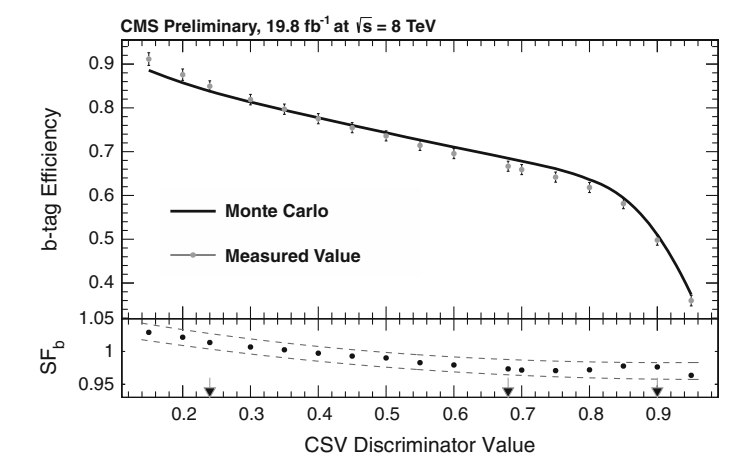


Fig. 5.2 The b-quark jet tagging efficiency as a function of the CSV tagger discriminant [23]. The medium operation point is indicated by the second arrow at 0.679

5.8 Reconstruction of the Missing Transverse Momentum

The $E_{\mathrm{T}}^{\mathrm{miss}}$ [25] is the magnitude of the momentum imbalance observed in the detector. In its simplest form, the vector $\vec{E}_{\mathrm{T,raw}}^{\mathrm{miss}}$ is the transverse projection of the negative momentum sum of all PF particles. It also can be calculated using only calorimeter information, $\vec{E}_{\mathrm{T,calo}}^{\mathrm{miss}}$.

The magnitude of $E_{\rm T,raw}^{\rm miss}$ is often underestimated. The reasons are similar to the ones for the jet energy reconstruction: Non-uniform response in the calorimeters, but also inefficiencies in tracking or minimal energy thresholds in calorimeter cells [25].

As a lot of the energy inside an event is contained in jets, one can use the jet energy corrections, as described in Sect. 5.7 and defined as "type-1" corrections, to reduce this underestimation:

$$\vec{E}_{\mathrm{T}}^{\mathrm{miss}} = \vec{E}_{\mathrm{T,raw}}^{\mathrm{miss}} - \sum_{\mathrm{jets}} \left(\vec{p}_{\mathrm{T,calib}}^{\mathrm{jet}} - \vec{p}_{\mathrm{T,raw}}^{\mathrm{jet}} \right). \tag{5.7}$$

The response and resolution of $E_{\rm T}^{\rm miss}$ are shown in Fig. 5.3. There exist further methods to improve the $E_{\rm T}^{\rm miss}$ resolution, but those usually come at the expense of a non-uniform response [25].

In this dissertation, type-1 corrected $E_{\rm T}^{\rm miss}$ is used.

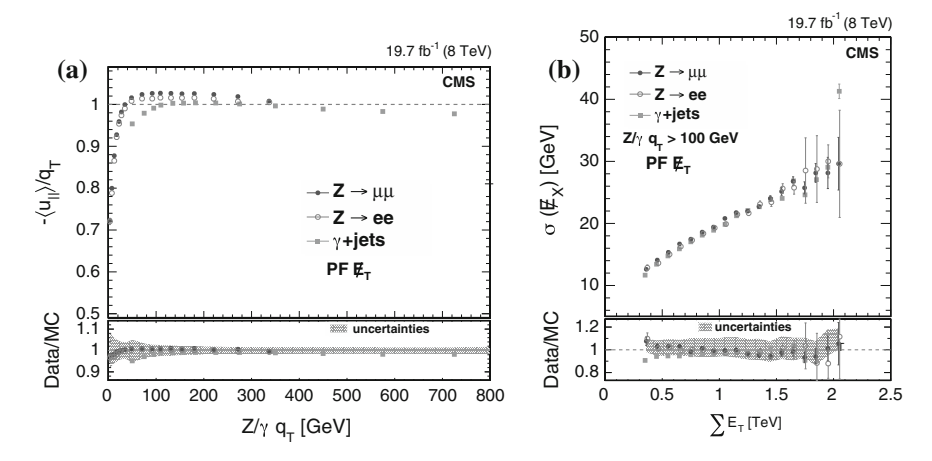


Fig. 5.3 Response and resolution of E_T^{miss} [25]. a \vec{E}_T^{miss} response as measured with $Z \to \mu\mu$, ee, and γ data as a function of the boson- p_T (= q_T). Here, $u_{||}$ is the projection of transverse momentum of the hadronic recoil parallel to the axis set by \vec{q}_T . The scalar quantity $-\langle u_{||} \rangle/q_T$ is referred to as the \vec{E}_T^{miss} response. b Resolution of the \vec{E}_T^{miss} projection along the x axis as a function of the scalar sum of the transverse momenta of all PF particles. The resolution along the y axis is comparable

References

- CMS Collaboration, Description and performance of track and primary-vertex reconstruction with the CMS tracker. JINST 9, P10009 (2014). doi:10.1088/1748-0221/9/10/P10009. arXiv:1405.6569
- R. Frühwirth, Application of Kalman filtering to track and vertex fitting. Nucl. Instrum. Methods A 262, 444 (1987). doi:10.1016/0168-9002(87)90887-4
- K. Rose, Deterministic annealing for clustering, compression, classification, regression, and related optimization problems. Proc. IEEE 86, 2210 (1998). doi:10.1109/5.726788
- CMS Collaboration, Particle-flow event reconstruction in CMS and performance for Jets, Taus, and E_T^{miss}. CMS-PAS PFT-09-001 (2009)
- 5. CMS Collaboration, Performance of CMS muon reconstruction in pp collision events at $\sqrt{s} = 7$ TeV. JINST 7, P10002 (2012). doi:10.1088/1748-0221/7/10/P10002. arXiv:1206.4071
- CMS Collaboration, Particle-flow commissioning with muons and electrons from J/Psi and W events at 7 TeV. CMS-PAS PFT-10-003 (2010)
- 7. CMS Collaboration, Search for neutral Higgs bosons decaying to tau pairs in pp collisions at $\sqrt{s}=7$ TeV. Phys. Lett. B **713**, 68 (2012). doi:10.1016/j.physletb.2012.05.028. arXiv:1202.4083
- 8. CMS Collaboration, Electron reconstruction and identification at $\sqrt{s}=7$ TeV. CMS-PAS EGM-10-004 (2010)
- M. Cacciari, G.P. Salam, Pileup subtraction using jet areas. Phys. Lett. B 659, 119 (2008). doi:10.1016/j.physletb.2007.09.077. arXiv:0707.1378
- 10. CMS Collaboration, Performance of τ -lepton reconstruction and identification in CMS. JINST 7, P01001 (2012). doi:10.1088/1748-0221/7/01/P01001. arXiv:1109.6034
- 11. CMS Collaboration, Isolated photon reconstruction and identification at $\sqrt{s}=7$ TeV. CMS-PAS EGM-10-006 (2011)
- 12. CMS Collaboration, Photon ID performance with 19.6 fb⁻¹ of data collected at $\sqrt{s} = 8$ TeV with the CMS detector. CMS DP-2013-010 (2013)

References 71

13. M. Cacciari, G.P. Salam, G. Soyez, The anti- k_t jet clustering algorithm. JHEP **04**, 063 (2008). doi:10.1088/1126-6708/2008/04/063. arXiv:0802.1189

- 14. CMS Collaboration, Jet performance in pp collisions at $\sqrt{s}=7$ TeV. CMS-PAS JME-10-003 (2010)
- A. Perloff on behalf of the CMS Collaboration, Pileup measurement and mitigation techniques in CMS. J. Phys. Conf. Ser. 404, 012 (2012). doi:10.1088/1742-6596/404/1/012045
- CMS Collaboration, Determination of jet energy calibration and transverse momentum resolution in CMS. JINST 6, P11002 (2011). doi:10.1088/1748-0221/6/11/P11002. arXiv:1107.4277
- M. Cacciari, G.P. Salam, G. Soyez, The catchment area of jets. JHEP 04, 005 (2008). doi:10. 1088/1126-6708/2008/04/005. arXiv:0802.1188
- 18. S. Catani et al., New clustering algorithm for multijet cross sections in e⁺e⁻ annihilation. Phys. Lett. B **269**, 432 (1991). doi:10.1016/0370-2693(91)90196-W
- S.D. Ellis, D.E. Soper, Successive combination jet algorithm for hadron collisions. Phys. Rev. D 48, 3160 (1993). doi:10.1103/PhysRevD.48.3160. arXiv:hep-ph/9305266
- Nucl. Instrum. Methods A GEANT4—A Simulation toolkit. 506, 250 (2003). doi:10.1016/ S0168-9002(03)01368-8
- CMS Collaboration, Status of the 8 TeV jet energy corrections and uncertainties based on 11 fb⁻¹ of data in CMS. CMS DP-2013-011 (2013)
- CMS Collaboration, Identification of b-quark jets with the CMS experiment. JINST 8, P04013 (2013). doi:10.1088/1748-0221/8/04/P04013. arXiv:1211.4462
- 23. CMS Collaboration, Performance of b tagging at $\sqrt{s} = 8$ TeV in multijet, $t\bar{t}$ and boosted topology events. CMS-PAS BTV-13-001 (2013)
- R. Frühwirth, W. Waltenberger, P. Vanlaer, Adaptive vertex fitting. J. Phys. G 34, N343 (2007). doi:10.1088/0954-3899/34/12/N01
- 25. CMS Collaboration, Performance of the missing transverse energy reconstruction by the CMS experiment in $\sqrt{s} = 8$ TeV pp data. arXiv:1411.0511. Submitted to JINST

Part II The Search for Supersymmetry

Chapter 6 Search for Supersymmetry: Using M_{T2} as Discovery Variable

The M_{T2} variable [1, 2], sometimes called *stransverse mass*, has been proven to be very sensitive to events emerging from SUSY production processes, while strongly suppressing the background due to SM processes. This chapter is devoted to the introduction and discussion of this variable.

In Sects. 6.1–6.3, I will review its definition and kinematical properties. Furthermore, in Sect. 6.4, I will summarize the SUSY search that used the M_{T2} variable in a hadronic environment and was performed at $\sqrt{s} = 7$ TeV. Since this analysis and the review of the kinematical properties had been part of another thesis [3], it will not be discussed in detail here.

The review of both the $M_{\rm T2}$ variable and the 7 TeV search can be seen as an introduction to the main body of this part of the dissertation, the search for SUSY with the $M_{\rm T2}$ variable at $\sqrt{s}=8$ TeV, which will be presented in Chap. 7.

6.1 Definition of the M_{T2} Variable

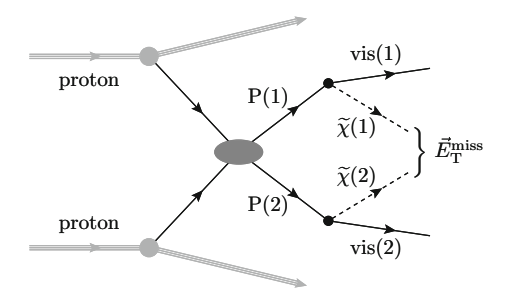
For the discovery of the W boson in 1983 [4, 5], the UA1 collaboration introduced the transverse mass M_T [4] to give a first estimate of the W boson mass. In events of a single produced particle, P, that decays semi-invisibly, the transverse momenta of the unobserved particle, $\vec{p}_T^{\tilde{\chi}}$, and the sum of the observed decay products, \vec{p}_T^{vis} , can be combined to form

$$(M_{\rm T})^2 = (M_{\rm vis})^2 + (M_{\tilde{\chi}})^2 + 2\left(E_{\rm T}^{\rm vis}E_{\rm T}^{\tilde{\chi}} - \vec{p}_{\rm T}^{\rm vis} \cdot \vec{p}_{\rm T}^{\tilde{\chi}}\right)$$

$$\approx 2p_{\rm T}^{\rm vis}p_{\rm T}^{\tilde{\chi}}\left(1 - \cos\Delta\phi\right).$$
(6.1)

Here, the visible (invisible) systems are denoted by vis $(\widetilde{\chi})$. The approximation in the second line holds for the massless case, $M_{\text{vis}} = M_{\widetilde{\chi}} = 0$, and $\Delta \phi$ is the angle between $\vec{p}_{\text{T}}^{\text{vis}}$ and $\vec{p}_{\text{T}}^{\widetilde{\chi}}$. This variable has an endpoint at the parent mass: $M_{\text{T}} \leq M(P)$.

Fig. 6.1 Illustration of a particle pair-production for particles *P* decaying semi-invisibly



For the case of leptonic W boson decays, $\widetilde{\chi}$ is a neutrino with $M_{\widetilde{\chi}}=M(\nu)=0$, and the mass of the charged lepton is negligible compared to the W boson mass. Therefore, the approximation holds.

In R-parity conserving SUSY models, sparticles are produced in pairs. Both sparticles decay into several SM particles and at least one LSP, which is not detectable. As at least two LSPs are present in the event, their momenta are not directly accessible. Only the transverse momentum sum of the LSPs is known by measuring $\vec{p}_{\rm T}^{\rm miss} \equiv \vec{E}_{\rm T}^{\rm miss}$. Hence, it is not straight-forward to form $M_{\rm T}$ for a single decay chain. A way out is the definition of the *stransverse mass* variable, $M_{\rm T2}$:

$$M_{\rm T2}(M_{\tilde{\chi}}) = \min_{\vec{p}_{\rm T}^{\tilde{\chi}(1)} + \vec{p}_{\rm T}^{\tilde{\chi}(2)} = \vec{p}_{\rm T}^{\rm miss}} \left[\max \left(M_{\rm T}^{(1)}, M_{\rm T}^{(2)} \right) \right]$$
(6.2)

with the free parameter¹ $M_{\tilde{\chi}}$. The index i=1,2 denotes the two decay chains. The $M_{\rm T2}$ variable is the extension of the $M_{\rm T}$ variable to the case of pair-produced particles, each decaying semi-invisibly, as illustrated in Fig. 6.1.

The idea behind this definition is that for correct transverse masses $M_{\rm T}^{(1,2)}$, the larger of the two is still smaller than or equal to the parent mass. The minimization over all possible splittings of $\vec{p}_{\rm T}^{\rm miss}$ to the transverse momenta of the unseen particles, $\vec{p}_{\rm T}^{\tilde{\chi}(1,2)}$, ensures that each transverse mass is not exceeding the parent mass. The mass of the unseen particle cannot be determined with this formula and is kept as a free parameter. If this testmass is smaller (larger) than the true mass, the endpoint of the $M_{\rm T2}$ distribution will be below (above) the parent mass.

In this work, the testmass in the $M_{\rm T2}$ calculation is set to zero: $M_{\rm T2} \equiv M_{\rm T2}(0)$.

Let us, for a moment, assume that all visible particles are correctly assigned and there is no transverse boost due to ISR. Then, an exact solution to Eq. (6.2) exists [2, 6]. There are two cases to consider: In the first case, the $\vec{p}_{\rm T}^{\rm miss}$ splitting yields a minimal $M_{\rm T}$ of one system, for which the $M_{\rm T}$ of the other system is smaller, as sketched in Fig. 6.2, left. This solution is called *unbalanced*, and

$$M_{\rm T2} = M_{\rm vis}^{(1)} + M_{\tilde{\gamma}}.\tag{6.3}$$

¹As $M_{\tilde{\chi}}$ is a parameter, the symbol $M_{\tilde{\chi}}$ is chosen over $M(\tilde{\chi})$ in the equations of this section.

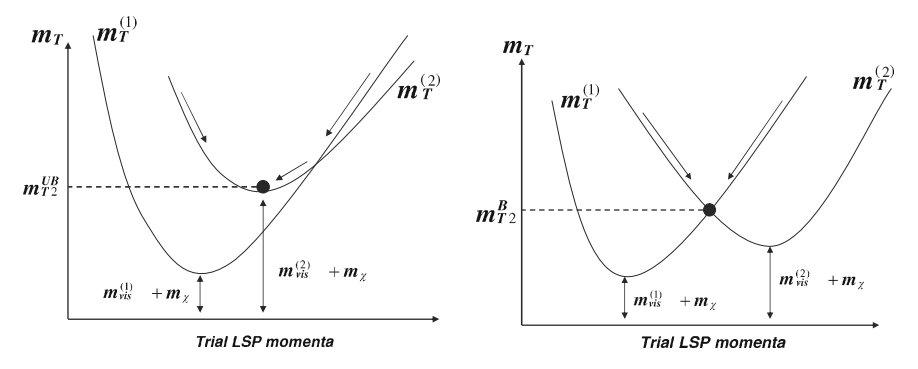


Fig. 6.2 Illustration of the unbalanced (left) and balanced (right) solutions of M_{T2} [6]

The second case is the *balanced* solution, where M_{T2} is the intersection between the two M_T curves along the \vec{p}_T^{miss} splitting, illustrated in Fig. 6.2, right. Using the definition

$$A_{\rm T} = E_{\rm T}^{\rm vis(1)} E_{\rm T}^{\rm vis(2)} + \vec{p}_{\rm T}^{\rm vis(1)} \cdot \vec{p}_{\rm T}^{\rm vis(2)}$$
(6.4)

one finds [6]

$$M_{\rm T2}^2 = M_{\tilde{\chi}} + A_{\rm T} + \sqrt{\left(1 + \frac{4M_{\tilde{\chi}}^2}{2A_{\rm T} - (M_{\rm vis}^{(1)})^2 - (M_{\rm vis}^{(2)})^2}\right) \left(A_{\rm T}^2 - (M_{\rm vis}^{(1)}M_{\rm vis}^{(2)})^2\right)}.$$
(6.5)

The system can be boosted by upstream transverse momentum (UTM). This boost comes from particles, upstream the parent particle decay, like ISR. If there is such a boost, only numerical solutions to the $M_{\rm T2}$ computation exist. The calculation of $M_{\rm T2}$ can be done, for example, by the bisection method using the code of [7]. This method has been used in this dissertation.

The initial idea of M_{T2} was to measure masses [1]. However, the variable can be used to discriminate SUSY signals against the SM background, as first proposed in [8]. The analysis presented in this dissertation follows this approach, with the difference of using *pseudojets* for the definition of the visible systems, as described in Sect. 6.2, instead of the two leading jets.

6.2 Definition of the Visible Systems for the $M_{\rm T2}$ Calculation

In an event with exactly two visible objects (leptons or jets), the definition of M_{T2} is unambiguous. However, as soon as three visible objects are reconstructed, multiple combinations exist, and the question is how to group these objects into the two visible systems, needed for the M_{T2} calculation.

In this section, the hemisphere algorithm [9] is introduced, which will be used to form the two visible systems that will be used for the M_{T2} calculation.

The idea of the hemisphere algorithm is to cluster all observed particles into two groups, such that each group correctly represents the momentum sum of the visible decay products of the parent particle. The algorithm has three steps: First, two seeds are chosen, forming the initial axes. Then all other objects are assigned to one of the two hemispheres (in the first step to the seeds) given a certain association criterion. In the last step, the momenta of all objects in a group are summed up, and the hemisphere axes are recomputed. This algorithm is iterated, until no object switches from one hemisphere to the other one during an iteration. The final two hemispheres will be called pseudojets throughout this dissertation.

In this work, the seeding of the hemisphere algorithm is performed with the two (massless) jets, for which the invariant dijet mass M_{jj} is the largest. The association method uses energy-weighted hemisphere masses, the so-called *Lund distance measure* [9], inspired by Eq. (15.15) of [10]: an object k is associated to hemisphere i rather than j if:

$$(E_i - p_i \cos \theta_{ik}) \frac{E_i}{(E_i + E_k)} \le (E_j - p_j \cos \theta_{jk}) \frac{E_j}{(E_j + E_k)},$$
 (6.6)

where θ_{ik} is the angle between hemisphere i and object k.

In [9], the efficiency to correctly assign a jet to the parent hemisphere has been measured in several SUSY benchmark models. For squarks, the association efficiency is of order 85%, while for gluinos it is of order 70–75%. The reason for the weaker efficiency in the gluino case is that the jets, for the tested models, are softer with respect to the ones from squark decays.

The hemisphere algorithm allows for some flexibility, both in the input to the algorithm as well as for the choice of seeding and clustering. Furthermore, one can replace the algorithm by another clustering algorithm like a $k_{\rm T}$ -type algorithm. This flexibility has been studied after the searches, presented in Sect. 6.4 and Chap. 7, had been performed. In order to not interrupt the line of argument here, these studies are presented in Appendix A.

Hemisphere Masses in the M_{T2} Calculation

The formula of M_{T2} includes masses of both the visible systems and the unseen LSP, see Eq. (6.1). It has been argued before (Sect. 6.1) that the LSP testmass in the calculation of Eq. (6.2) cannot be constrained by the M_{T2} variable itself, and is set to zero.

In order to better understand the influence of the masses of the visible systems (pseudojets), we approximate the formula (6.5) for the case of $M_{\text{vis}}^{(i)} \ll p_{\text{T}}^{\text{vis}(i)}$:

$$(M_{\rm T2})^2 \simeq p_{\rm T}^{\rm vis(1)} p_{\rm T}^{\rm vis(2)} \left[2 \left(1 + \cos \Delta \phi_{12} \right) + \left(\frac{M_{\rm vis}^{(1)}}{p_{\rm T}^{\rm vis(1)}} \right)^2 + \left(\frac{M_{\rm vis}^{(2)}}{p_{\rm T}^{\rm vis(2)}} \right)^2 \right], \tag{6.7}$$

where $\Delta \phi_{12}$ is the angle between the two pseudojets in the transverse plane.

It is evident that using pseudojets in the $M_{\rm T2}$ calculation over the two leading jets, as proposed in [8], has a significant influence on the $M_{\rm T2}$ variable: While the mass of a single jet is usually small compared to its $p_{\rm T}$, the invariant mass of a pseudojet, involving multiple jets, can be large. For the case of the $M_{\rm T2}$ calculation with the two leading jets, the $M_{\rm T2}$ variable is mostly dominated by the angular term. Let us inspect the case of massive pseudojets: The $M_{\rm T2}$ variable is bounded from below by the larger mass of the two pseudojets, due to the maximum requirement in Eq. (6.2) and the inherited mass dependence of Eq. (6.1). This means that events with no $E_{\rm T}^{\rm miss}$ from unseen particles, such as the LSPs, can have large $M_{\rm T2}$ if one pseudojet mass is large.

The variable M_{T2} can be used as a signal-discriminating variable, as will be discussed in the next section. For a hadronic search, the QCD multijet production is extremely important due to the huge cross section. Having the masses of pseudojets in the M_{T2} calculation will lead to a dramatic enhancement of multijet events in the tail of the M_{T2} distribution, and any signal will be covered by a huge multijet background. Hence, it is important for a search to enforce zero masses on the visible systems (in practice, set $E_{\rm T}^{{\rm vis}(i)} = p_{\rm T}^{{\rm vis}(i)}$) in order to suppress the multijet background with no $E_{\rm T}^{{\rm miss}}$. This argument is supported by comparing the distributions of $M_{\rm T2}$ using massless pseudojets and $M_{\rm T2}$ with massive pseudojets, as done in Fig. 6.3. For the hadronic searches presented in this dissertation, the $M_{\rm T2}$ variable is calculated using massless pseudojets.

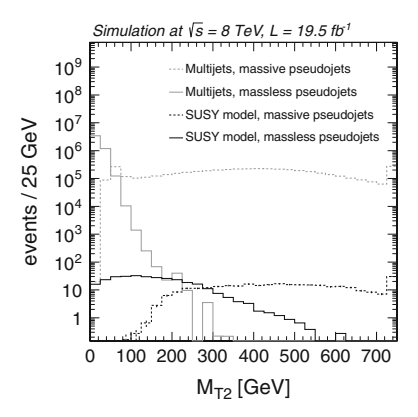


Fig. 6.3 Comparison between the M_{T2} distributions using massive (*dashed lines*) and massless pseudojets (*solid lines*) for QCD multijet production (*gray*) and a SUSY model (*black*) of direct stop pair production with $\tilde{t} \to t \tilde{\chi}_1^0$, $M(\tilde{t}) = 400$ GeV, $M(\tilde{\chi}_1^0) = 0$ GeV. While the SUSY signal becomes dominant over the multijet background for $M_{T2} \gtrsim 200$ GeV when using massless pseudojets, it is hidden under the multijet background for M_{T2} with massive pseudojets

6.3 Kinematical Properties of M_{T2}

In this section, the properties of M_{T2} are discussed. The discussion is limited to the most important aspects for SUSY searches, as a detailed study was subject to another dissertation [3].

As we just discussed in Sect. 6.2, pseudojets have to be defined massless so that $M_{\rm T2}$ has discrimination power between multijet events and SUSY signal events. An interesting approximation of Eq. (6.5) is the case of zero masses, $M_{\tilde{\chi}} = M_{\rm vis}^{(1,2)} = 0$:

$$M_{\rm T2}^2 = 2A_{\rm T} = 2p_{\rm T}^{\rm vis(1)}p_{\rm T}^{\rm vis(2)}(1+\cos\Delta\phi_{12}),$$
 (6.8)

where $\Delta \phi_{12}$ is the angle between the two pseudojets in the transverse plane.

Correlation Between $M_{\rm T2}$ and $E_{\rm T}^{\rm miss}$

In Eq. (6.8), we found a simple expression for M_{T2} in the case of zero masses and no UTM. Three conclusions can be drawn from this result:

For back-to-back systems ($\Delta\phi_{12}\approx\pi$), M_{T2} will be close to zero. This observation is important for constraining QCD multijet production: In dijet events, even for strong mismeasurement of the energy of one jet, $M_{T2}=0$. For multijet events, if one of the leading jets is mismeasured, M_{T2} will still have small values. In a spherical multijet event with several equally hard jets, jet energy mismeasurements can result in two pseudojets not being back-to-back. Further handles are needed to suppress the multijet background in the M_{T2} tail.

Next, let us inspect the $E_{\rm T}^{\rm miss}$: Using $\vec{E}_{\rm T}^{\rm miss} + \vec{p}_{\rm T}^{\rm vis(1)} + \vec{p}_{\rm T}^{\rm vis(2)} = \overrightarrow{0}$, one can easily find

$$(E_{\rm T}^{\rm miss})^2 = (p_{\rm T}^{\rm vis(1)} - p_{\rm T}^{\rm vis(2)})^2 + 2p_{\rm T}^{\rm vis(1)}p_{\rm T}^{\rm vis(2)}(1 + \cos\Delta\phi_{12}). \tag{6.9}$$

Comparing Eqs. (6.8) and (6.9), we get $M_{T2} \approx E_T^{\text{miss}}$ if $p_T^{\text{vis}(1)} \approx p_T^{\text{vis}(2)}$. Typical SUSY signal events will have large E_T^{miss} due to the presence of the two LSPs. As the pseudojets are not back-to-back, SUSY signal events will populate the tail of the M_{T2} distribution. The same argument holds for events of SM processes involving true E_T^{miss} due to the presence of neutrinos, such as $Z(\nu \overline{\nu}) + \text{jets}$, $W(l\nu) + \text{jets}$, and $t\bar{t} + \text{jets}$ with leptonic W boson decays.

Another conclusion can be drawn for very asymmetric events, where $p_{\rm T}^{{\rm vis}(1)}\gg p_{\rm T}^{{\rm vis}(2)}$. The $E_{\rm T}^{{\rm miss}}$ can be quite large, while the $M_{\rm T2}$ will be small ($M_{\rm T2}\ll E_{\rm T}^{{\rm miss}}$), even for $\Delta\phi_{12}\ll\pi$. For a small asymmetry between the transverse momenta of the pseudojets, $M_{\rm T2}\lesssim E_{\rm T}^{{\rm miss}}$.

As Eq. (6.8) is a simplification of the full M_{T2} calculation, let us inspect the correlation of M_{T2} and E_{T}^{miss} for a SUSY signal model and various SM processes. Fig. 6.4 shows the correlation for events of the SUSY signal model LM6 [9], as well

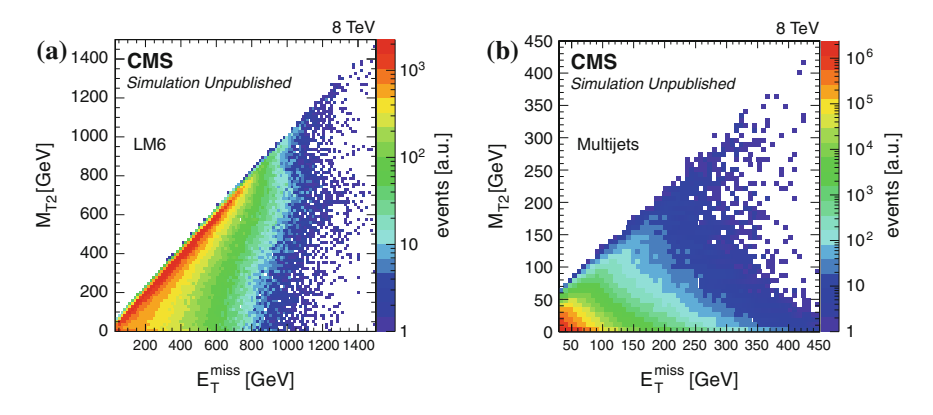


Fig. 6.4 Correlations between $E_{\rm T}^{\rm miss}$ and $M_{\rm T2}$ for LM6 SUSY signal events (a) and QCD multijet events (b). The normalization is arbitrary. For multijet events, most events accumulate at $M_{\rm T2} \lesssim 125$ GeV, while for the LM6 SUSY signal events $M_{\rm T2}$ values over 1000 GeV can be reached

as for QCD multijet events. We observe that for SUSY, most events are around the diagonal $E_{\rm T}^{\rm miss}=M_{\rm T2}$, while for QCD multijet production, events are located at $M_{\rm T2}\approx 0$ even for larger $E_{\rm T}^{\rm miss}$. Figure 6.5 shows the $E_{\rm T}^{\rm miss}$ - $M_{\rm T2}$ correlation also for other SM components, such as $Z(\nu\overline{\nu})$ +jets, $W(l\nu)$ +jets, and semileptonic $t\overline{t}$ +jets events. All three components have $E_{\rm T}^{\rm miss}$ due to the presence of neutrinos. The $t\overline{t}$ production is a pair-production, similar to the case of SUSY. Therefore, $M_{\rm T2}$ can constrain² this component to $M_{\rm T2} \leq M(t)$. However, the presence of additional jets, such as ISR jets, can dilute the endpoint. For W and Z boson production, no such constraint exists, and high values of $M_{\rm T2}$ are possible.

Both figures show, that our conclusions, drawn from the simplified expression of M_{T2} , Eq. (6.8), hold also for the full calculation of M_{T2} .

The Influence of the Upstream Transverse Momentum in the M_{T2} Calculation

Both the full calculation of the balanced solution of M_{T2} , Eq. (6.5), as well as the massless version, Eq. (6.8), assumed that there is no UTM or ISR.

In experiments, however, there is generally some contribution of UTM, for example soft or very forward jets. In the analysis presented in this dissertation, the upstream transverse momentum, $\vec{p}_{\rm T}^{\rm upstream}$, is identified with the momentum imbalance

$$\vec{p}_{\mathrm{T}}^{\mathrm{upstream}} = -\left(\vec{E}_{\mathrm{T}}^{\mathrm{miss}} + \vec{p}_{\mathrm{T}}^{\mathrm{vis}(1)} + \vec{p}_{\mathrm{T}}^{\mathrm{vis}(2)}\right). \tag{6.10}$$

²This argument holds also for the asymmetric decay (one W boson decaying leptonically, the other one hadronically), as reasoned in [3].

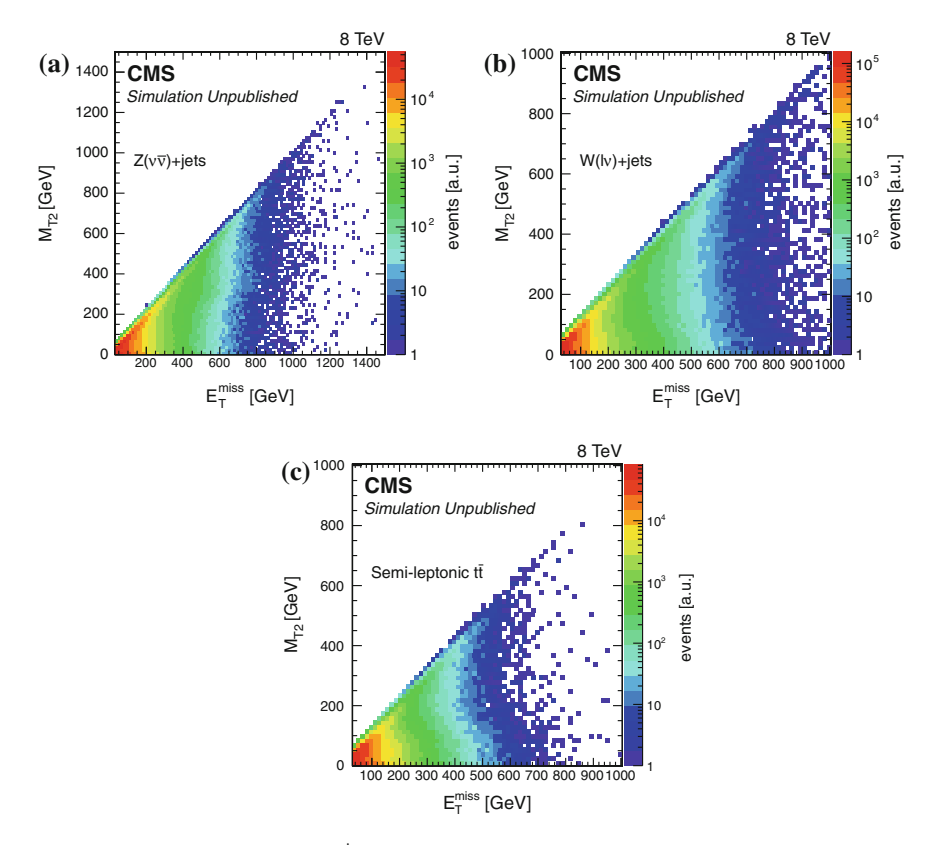


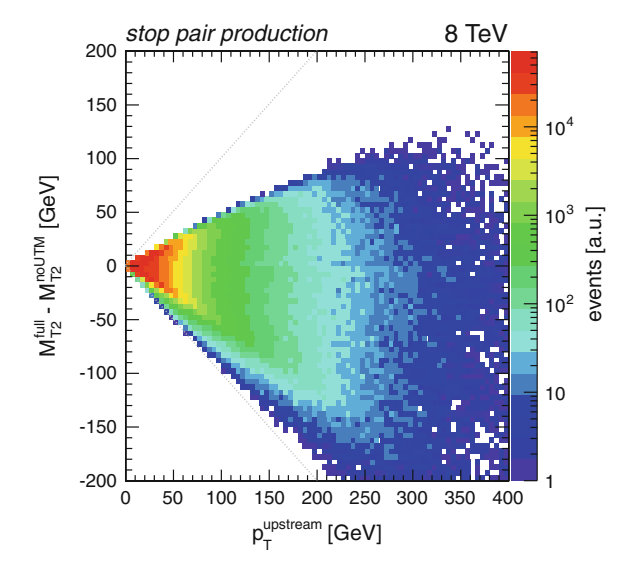
Fig. 6.5 Correlations between $E_{\rm T}^{\rm miss}$ and $M_{\rm T2}$ for $Z(\nu\overline{\nu})+{\rm jets}$ (a), $W(l\nu)+{\rm jets}$ (b), and semileptonic $t\overline{t}+{\rm jets}$ events (c). The normalization is arbitrary

This momentum imbalance is due to reconstructed particle energies not clustered into jets: low momentum, unclustered particles and particles pointing to the forward part of the detector.

There is no analytical expression for M_{T2} for $p_{T}^{\rm upstream} \neq 0$. We, therefore, estimate the influence of UTM by comparing the full calculation of M_{T2} in the massless case, Eq. (6.2), in this section called $M_{T2}^{\rm full}$, with the simplified version of M_{T2} in the massless limit, Eq. (6.8), for this section called $M_{T2}^{\rm noUTM}$. Inspecting the difference $M_{T2}^{\rm full} - M_{T2}^{\rm noUTM}$ as a function of $p_{T}^{\rm upstream}$ for a SUSY signal, we observe that this difference is limited by $p_{T}^{\rm upstream}$, see Fig. 6.6.

It is shown in [3] that the difference $M_{\rm T2}^{\rm full}-M_{\rm T2}^{\rm noUTM}$ is the largest positive (negative) if $\vec{p}_{\rm T}^{\rm upstream}$ is parallel (antiparallel) to $\vec{p}_{\rm T}^{\rm vis(1)}+\vec{p}_{\rm T}^{\rm vis(2)}$ and antiparallel (parallel) to $\vec{E}_{\rm T}^{\rm miss}$.

Fig. 6.6 Correlation between $M_{\rm T2}^{\rm full} - M_{\rm T2}^{\rm noUTM}$ and $p_{\rm T}^{\rm upstream}$ for a stop pair production signal



6.3.1 The Influence of the Initial State Radiation in the M_{T2} Calculation

If jets from ISR are not clustered into one of the pseudojets, they are part of the UTM, which just has been discussed. However, it is not (easily) possible to distinguish between jets from the hard interaction and jets from ISR in a reconstructed event. Usually, ISR jets are clustered into the pseudojets if they are not too soft or forward. In the presence of ISR, there is no analytical solution of Eq. (6.2), and the endpoint of the M_{T2} distribution is diluted, as already observed in Fig. 6.5c, for example. A method to reduce the influence is the definition M_{T2}^{sub} [11], where the visible systems in the M_{T2} calculation are constructed only out of a subset of the reconstructed objects in the event. In [12], a version of M_{T2}^{sub} is proposed that should strongly reduce the influence of ISR in the M_{T2} calculation:

$$M_{\rm T2}^{\rm min} = \min_{i \in \{\text{visible objects}\}} M_{\rm T2}(i), \tag{6.11}$$

where $M_{T2}(i)$ is the M_{T2} variable, for which object i is not clustered into any of the two pseudojets. The idea behind this formula is, that the largest disturbance to the M_{T2} endpoint is due to one hard ISR jet. This variable is tested for a stop pair production model with $M(\tilde{t}) = 400 \,\text{GeV}$, $M(\tilde{\chi}_1^0) = 0 \,\text{GeV}$, and SM processes. In Fig. 6.7, the M_{T2}^{min} variable is shown and compared to M_{T2} for events of electroweak production (left) and signal (right). The M_{T2}^{min} endpoints for both the signal and the SM processes are shifted by $\approx 200 \,\text{GeV}$ compared to the endpoint of M_{T2} . Since it does not improve the sensitivity for a SUSY search, it will not be used further on. Anyhow, this variable is supposed to improve the mass measurement. For this, one

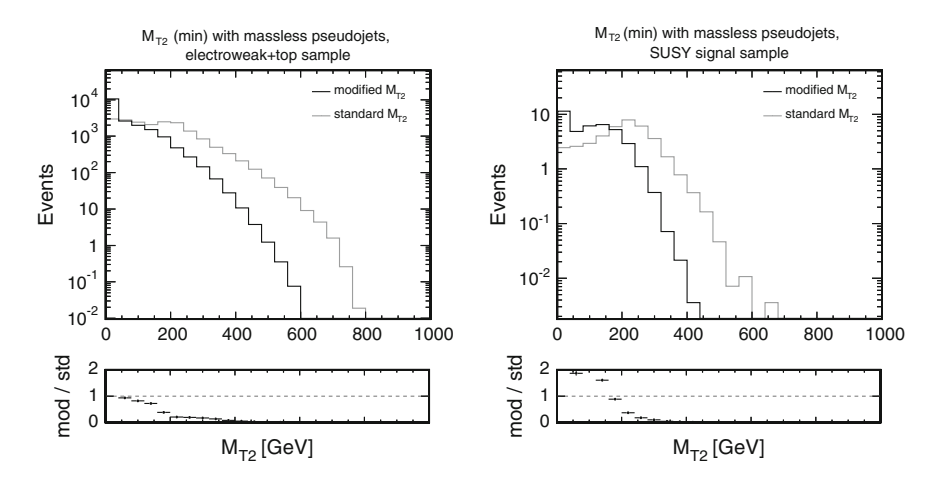


Fig. 6.7 Comparison and ratio between the M_{T2} distribution, where all objects are clustered into the pseudojets ("standard M_{T2} "), and the M_{T2}^{min} distribution ("modified M_{T2} ") for electroweak SM processes (*left*) and stop pair production (*right*) with $M(\widetilde{t}) = 400 \text{ GeV}$, $M(\widetilde{\chi}_1^0) = 0 \text{ GeV}$

should compute M_{T2} with massive pseudojets. Figure 6.8 shows the massive M_{T2}^{\min} variable compared to massive M_{T2} for events of electroweak production (left) and signal (right). The endpoint is sharpened and shifted close to $M(\tilde{t}) = 400 \,\text{GeV}$, the effect of the ISR is reduced. It might, however, be difficult to find the endpoint on top of the electroweak background. Also one should note, that the massive M_{T2}^{\min} cannot be used for a search variable, see discussion in Sect. 6.2.

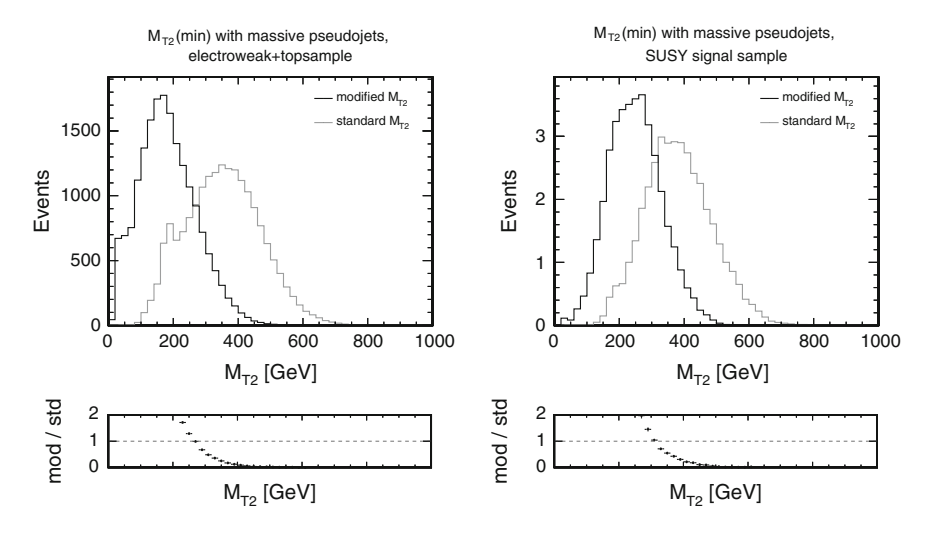


Fig. 6.8 Comparison and ratio between the massive M_{T2} distribution ("standard M_{T2} ") and the M_{T2}^{\min} distribution ("modified M_{T2} ") for electroweak SM processes (*left*) and stop pair production (*right*) with $M(\tilde{t}) = 400 \,\text{GeV}$, $M(\tilde{\chi}_1^0) = 0 \,\text{GeV}$

6.4 The Search for Supersymmetry at $\sqrt{s} = 7 \text{ TeV}$

The $M_{\rm T2}$ variable has been used to perform a search for SUSY with CMS pp collision data, selected during 2011 at $\sqrt{s} = 7 \, {\rm TeV}$, and corresponding to an integrated luminosity of 4.73 fb⁻¹. The $M_{\rm T2}$ variable was calculated using two pseudojets, as described in Sect. 6.2, and raw $E_{\rm T}^{\rm miss}$ (see Sect. 5.8). This search is published [13] and has been the subject of another dissertation [3]; this section contains only a summary.

The 7 TeV search was based on two non-exclusive analyses, the $M_{\rm T2}$ analysis and the $M_{\rm T2}b$ analysis. Both analyses selected events based on the $H_{\rm T}$ variable:

$$H_{\rm T} = \sum_{\rm jets} p_{\rm T},\tag{6.12}$$

where the jets³ are required to have $p_{\rm T} > 50\,{\rm GeV}$ and $|\eta| < 3.0$. These requirements are driven by the jet selection of the trigger. At trigger level, $H_{\rm T} > 650\,{\rm GeV}$ was required for the runs with highest instantaneous luminosity. Offline, events with $H_{\rm T} > 750\,{\rm GeV}$ were selected. Furthermore, events were rejected if they contained electrons, muons, if they were tagged by noise filters, or if the event had $|\vec{E}_{\rm T}^{\rm miss}| = 70\,{\rm GeV}$. Here,

$$\vec{H}_{\rm T}^{\rm miss} = -\sum_{\rm jets} \vec{p}_{\rm T} \tag{6.13}$$

with jets satisfying $p_T > 20 \,\text{GeV}$ and $|\eta| < 2.4$.

For the $M_{\rm T2}$ analysis, at least three jets were required, and $\Delta\phi({\rm all~jets}, E_{\rm T}^{\rm miss}) > 0.3$. The $M_{\rm T2}b$ analysis selected events with at least four jets, $\Delta\phi({\rm four~leading~jets}, E_{\rm T}^{\rm miss}) > 0.3$, and at least one b jet.⁴ As these criteria are similar for the 8TeV search (Sect. 7.2), they are not discussed here.

The signal regions were defined by $H_{\rm T}$ and $M_{\rm T2}$. Two $H_{\rm T}$ regions had been defined (750 $\leq H_{\rm T} < 950\,{\rm GeV}$ and $H_{\rm T} \geq 950\,{\rm GeV}$) and up to five bins in $M_{\rm T2}$ per $H_{\rm T}$ region: for the $M_{\rm T2}$ ($M_{\rm T2}b$) analysis the lowest bin started at $M_{\rm T2} = 150\,(125)\,{\rm GeV}$.

The backgrounds were predicted by the means of data-driven methods.

The results for the $M_{\rm T2}$ and $M_{\rm T2}b$ analyses can be found in Figs. 6.9 and 6.10.

Both analyses did not see a significant excess over the background prediction. Interpretations in several SUSY models had been performed, and the observed limits in the respective model parameter space were among the strongest observed limits of all analyses performed at $\sqrt{s} = 7 \text{ TeV}$.

³For the 7 TeV search, no CHS was applied.

⁴In the $M_{T2}b$ analysis, b jets were selected by a simple secondary vertex tagger with an efficiency of about 40 % and a light-jet mistagging rate of \sim 0.1 %.

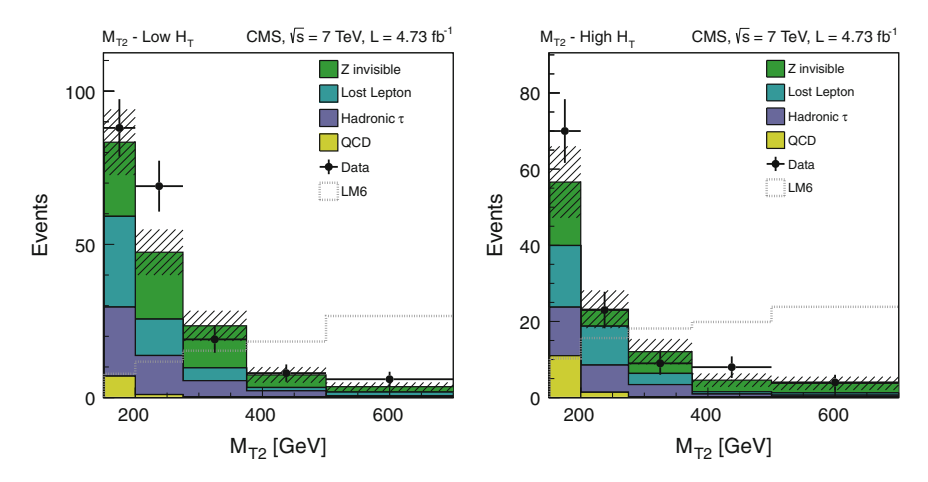


Fig. 6.9 Data yields for the signal regions of the M_{T2} analysis, corresponding to 4.73 fb⁻¹ at $\sqrt{s} = 7$ TeV, compared to the background prediction and a possible SUSY signal. *Left* for the lower H_T region, *right* for the higher H_T region. Taken from [13]

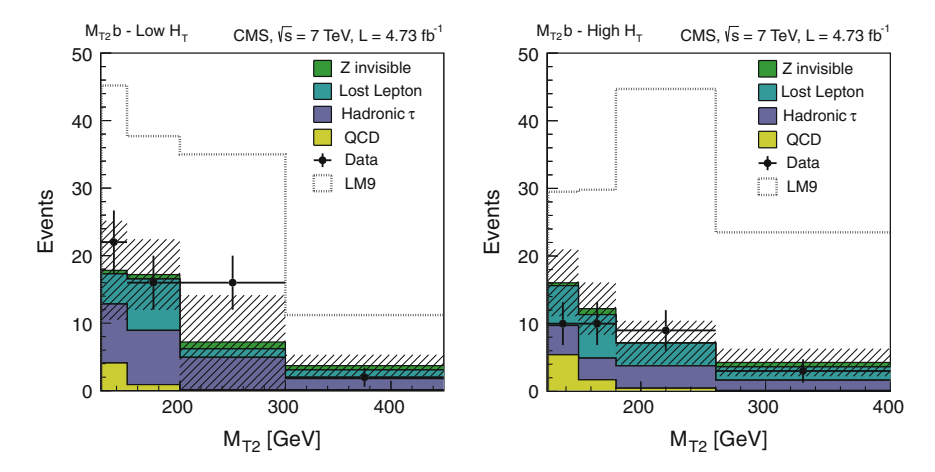


Fig. 6.10 Data yields for the signal regions of the $M_{T2}b$ analysis, corresponding to 4.73 fb⁻¹ at $\sqrt{s} = 7$ TeV, compared to the background prediction and a possible SUSY signal. *Left* for the lower H_T region, *right* for the higher H_T region. Taken from [13]

References

- C. Lester, D. Summers, Measuring masses of semi-invisibly decaying particle pairs produced at hadron colliders. Phys. Lett. B 463, 99 (1999). doi:10.1016/S0370-2693(99)00945-4. arXiv:hep-ph/9906349
- A. Barr, C. Lester, P. Stephens, A variable for measuring masses at hadron colliders when missing energy is expected; m_{T2}: the truth behind the glamour. J. Phys. G 29, 2343 (2003). doi:10.1088/0954-3899/29/10/304. arXiv:hep-ph/0304226

References 87

3. P. Nef, Search for supersymmetry in hadronic final states using M_2 in pp collisions at at $\sqrt{s} = 7$ TeV and discovery potential of top partners in composite Higgs models. Dissertation. ETH Zurich (2013). doi:10.3929/ethz-a-007635937

- 4. UA1 Collaboration, Experimental observation of isolated large transverse energy electrons with associated missing energy at $\sqrt{s} = 540$ GeV. Phys. Lett. B **122**, 103 (1983). doi:10.1016/0370-2693(83)91177-2
- UA2 Collaboration, Observation of single isolated electrons of high transverse momentum in events with missing transverse energy at the CERN pp collider. Phys. Lett. 122, 476 (1983). doi:10.1016/0370-2693(83)91605-2
- W.S. Cho et al., Measuring superparticle masses at hadron collider using the transverse mass kink, JHEP 02, 035 (2008). doi:10.1088/1126-6708/2008/02/035. arXiv:0711.4526
- H.-C. Cheng, Z. Han, Minimal kinematic constraints and m_{T2}. JHEP 12, 063 (2008). doi:10. 1088/1126-6708/2008/12/063. arXiv:0810.5178
- 8. A.J. Barr, C. Gwenlan, The race for supersymmetry: using m_{T2} for discovery. Phys. Rev. D 80, 074007 (2009). doi:10.1103/PhysRevD.80.074007. arXiv:0907.2713
- CMS Collaboration, CMS physics technical design report, volume II: physics performance. J. Phys. G 34, 995 (2007). doi:10.1088/0954-3899/34/6/S01
- T. Sjöstrand, S. Mrenna, P.Z. Skands, PYTHIA 6.4 physics and manual. JHEP 05, 026 (2006). doi:10.1088/1126-6708/2006/05/026. arXiv:hep-ph/0603175
- 11. M. Burns et al., Using subsystem M_{T2} for complete mass determinations in decay chains with missing energy at hadron colliders. JHEP **03**, 143 (2009). doi:10.1088/1126-6708/2009/03/143. arXiv:0810.5576
- 12. M.M. Nojiri, K. Sakurai, Controlling initial state radiation in sparticle mass reconstruction. Phys. Rev. D 82, 115026 (2010). doi:10.1103/PhysRevD.82.115026. arXiv:1008.1813
- 13. CMS Collaboration, Search for supersymmetry in hadronic final states using M_{T2} in pp collisions at $\sqrt{s} = 7$ TeV. JHEP 10, 018 (2012). doi:10.1007/JHEP10(2012)018. arXiv:1207.1798

Chapter 7 Search for Supersymmetry in Hadronic Events Using M_{T2} at $\sqrt{s} = 8 \text{ TeV}$

This chapter is dedicated to the SUSY search using a pp collision data sample collected by the CMS experiment at $\sqrt{s}=8\,\mathrm{TeV}$. The data sample corresponds to an integrated luminosity of $19.5\,\mathrm{fb^{-1}}$. The search selects hadronic events using the H_{T} and $E_{\mathrm{T}}^{\mathrm{miss}}$ variables. The main variable to discriminate SUSY signal events against events from SM processes is the M_{T2} variable, which has been discussed in great detail in Sects. 6.1–6.3. The data are analyzed in separate regions defined by the H_{T} and M_{T2} variables as well as the jet and b-jet multiplicities, N_{j} and N_{b} , respectively.

This search is a continuation of the 7 TeV search [1], which has been presented in Sect. 6.4. As no hint of new physics was observed in 7 TeV *pp* collision data, there was a strong focus on the optimization and improvement of this analysis, both in the strategy as well as the background predictions. In addition, all objects needed to be redefined to handle the harsh environment expected for the high instantaneous luminosity during 2012 data taking.

The analysis presented here is the *inclusive* M_{T2} analysis. The aim of this analysis is to cover a large phase space within SUSY, and to be sensitive to a wide variety of signatures, possibly also outside SUSY. In fact, the analysis is sensitive to any physics beyond the SM if the new physics events contain large $E_{\rm T}^{\rm miss}$ and $H_{\rm T}$, and the new physics particles are produced in pairs.

The event selection criteria are designed to strongly suppress the background due to instrumental noises and jet energy mismeasurements, while keeping a high efficiency for a potential SUSY signal. It is shown in simulation and data, that the main SM background stems from electroweak processes, $Z(\nu\overline{\nu})$ +jets and $W(l\nu)$ +jets events, as well as top quark production, mainly semi-leptonic $t\overline{t}$ +jets events. The background is predicted by the means of data-driven estimation methods.

Alternative inclusive SUSY searches in the hadronic final states at $\sqrt{s} = 8 \text{ TeV}$ have been performed by the CMS [2–4] and ATLAS [5, 6] collaborations. The M_{T2} variable has been used previously for measurements and searches by the CDF, ATLAS, and CMS collaborations [1, 7–16].

This chapter is structured as follows: in Sect. 7.1, the data selection and simulation are discussed. In Sect. 7.2, the event selection and validation are reviewed, followed

by the search optimization and strategy in Sect. 7.3. In Sects. 7.4–7.6, the background predictions are described. In Sect. 7.7, the results are shown, followed by their interpretations in Sect. 7.8. In Sect. 7.9, the results are put into context with respect to other hadronic searches. Finally, Sect. 7.10 contains the summary, including an outlook for the future of this analysis.

This analysis has been published [17], and this chapter is based on that work. Note, that the publication contains a further analysis, the M_{T2} Higgs analysis. That analysis is a spin-off of the inclusive M_{T2} analysis, but is subject to another, future thesis, and is not discussed in this thesis.

7.1 Data Selection and Simulation

Data Selection

Events are selected by three different trigger paths, based on $E_{\rm T}^{\rm miss}$ and/or $H_{\rm T}$. In the 7 TeV analysis, only $H_{\rm T}$ -based triggers had been used. This path is also used in this search. The trigger selected events online with $H_{\rm T} \geq 650\,{\rm GeV}$. The variable $H_{\rm T}$ is defined in Eq. (6.12). This trigger is based on PF jets. For a large fraction of the data taking, pileup corrections for jets were applied online at trigger level, allowing to keep this threshold throughout 2012. This trigger is fully efficient for an offline selection of $H_{\rm T} \geq 750\,{\rm GeV}$, as shown in Fig. 7.1a.

Besides this $H_{\rm T}$ -only trigger, two further trigger streams are used: the first path is purely based on $E_{\rm T}^{\rm miss}$. The selection at trigger level was $E_{\rm T}^{\rm miss} \geq 150\,{\rm GeV}$ throughout 2012. The second path is a cross-trigger based on both $H_{\rm T}$ and $E_{\rm T}^{\rm miss}$. The threshold for this trigger has been $H_{\rm T} \geq 350\,{\rm GeV}$ and $E_{\rm T}^{\rm miss} \geq 100\,{\rm GeV}$. The $E_{\rm T}^{\rm miss}$ -only trigger has been measured to reach an efficiency of $\sim 90\,\%$ for an offline selection of $E_{\rm T}^{\rm miss} \geq 200\,{\rm GeV}$, see Fig. 7.1b. As this trigger does not reach full efficiency, it was decided to select events at lower $H_{\rm T}$ (that is below $H_{\rm T} = 750\,{\rm GeV}$) by combining the

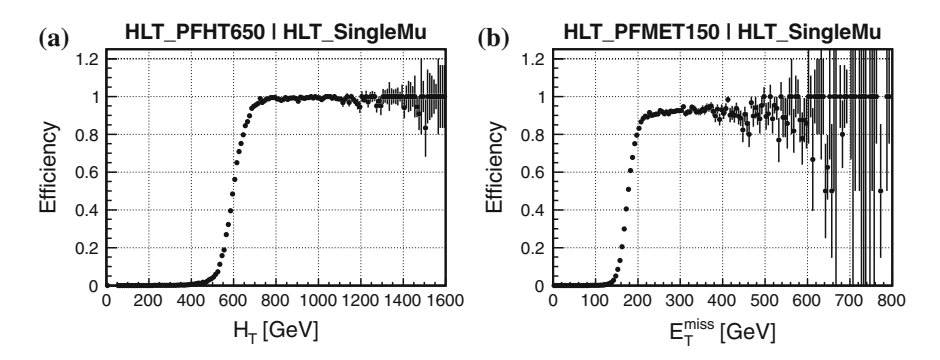
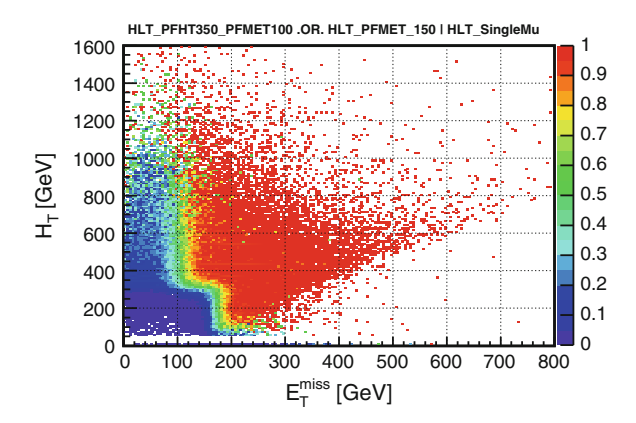


Fig. 7.1 Trigger efficiency of the H_T -only (**a**) and E_T^{miss} -only (**b**) trigger measured with respect to a single muon trigger

Fig. 7.2 Efficiency of the combined trigger of the $E_{\rm T}^{\rm miss}$ -only and the $H_{\rm T}$ - $E_{\rm T}^{\rm miss}$ triggers, measured as a function of (offline) $E_{\rm T}^{\rm miss}$ (x axis) and $H_{\rm T}$ (y axis) using a single muon trigger



 $E_{\rm T}^{\rm miss}$ -only and the $H_{\rm T}$ - $E_{\rm T}^{\rm miss}$ cross trigger via a logical OR. The combined trigger has been measured to be fully efficient for an offline selection of $H_{\rm T} \geq 450\,{\rm GeV}$ and $E_{\rm T}^{\rm miss} \geq 200\,{\rm GeV}$, shown in Fig. 7.2. The selection efficiency of both the combined trigger and the $H_{\rm T}$ -only trigger have been measured in a data sample selected by a single muon trigger.

The selection efficiencies of the triggers have been also measured against other kinematical variables, like the jet or b-jet multiplicities. No dependence on these variables has been found.

For background estimation methods, further triggers have been used. In the estimation of the background due to jet energy mismeasurements (Sect. 7.4), H_T -only triggers with a lower threshold of $H_T \geq 350$ GeV have been used. These triggers were *prescaled*, meaning that only a defined small fraction of events passing the trigger threshold were actually stored. Which events are stored, is random. For the estimation of the $Z(\nu\overline{\nu})$ +jets background, a single photon trigger has been used, selecting photons with $p_T^{\gamma} \geq 150$ GeV. The trigger reached full efficiency for an offline selection with $p_T^{\gamma} \geq 180$ GeV. Further, photon data were selected via a photon- H_T cross trigger with $p_T^{\gamma} \geq 70$ GeV and $H_T \geq 400$ GeV, which was found to be efficient at $p_T^{\gamma} \geq 80$ GeV and $H_T \geq 450$ GeV offline. Also, events containing an e^+e^- or $\mu^+\mu^-$ pair were selected using triggers with an online selection of $p_T \geq 17$ (8) GeV for the leading (trailing) lepton. For an offline selection of $p_T \geq 20$ GeV for both leptons, these triggers have reached the efficiency plateau.

Simulation

The analysis strategy and event selection have been decided using only simulated events. The simulation is further used in the background estimations and the result interpretations. The SM processes are simulated using several generators: PYTHIA 6.4 [18] for the multijet background, POWHEG [19, 20] for single top production, and MADGRAPH 5 [21] for all other processes. Signal samples are produced

¹ For the $Z(\nu \bar{\nu})$ +jets estimation method, also the multijet background is modelled by MADGRAPH 5.

by MADGRAPH 5 for the SMS models (see Sect. 3.3.3) and PYTHIA 6.4 for the cMSSM/mSUGRA model (see Sect. 3.3.2).

The parton shower and hadronization is modeled by the PYTHIA 6.4 generator. All generators use CTEQ6L1 [22] PDFs, and apply the Z2* tune [23, 24] for the modeling of the UE. Tau decays are modeled using TAUOLA [25]. All generated events for SM processes are passed through a detailed simulation of the CMS detector based on GEANT4, [26], generated signal events are processed using the "fast simulation" [27] of the CMS detector response.

The signal mass spectra are calculated with SOFTSUSY [28]. The sparticle decay branching fractions are calculated with SDECAY [29]. For the cMSSM/mSUGRA model, SUSY- HIT [30] is used to interface SDECAY with HDECAY [31], which calculates the decay branching fractions of the MSSM Higgs bosons.

For SM processes, the most accurate cross sections available in literature, usually next-to-leading order (NLO) in α_s , are used. The cross sections for SUSY processes are calculated at NLO using Prospino [32–35] and, additionally for the SMS models, using the calculations of [36–39]. For the cMSSM models, process dependent k-factors were derived using Prospino to reweight the leading-order cross sections to NLO.

7.2 Event Selection and Validation

In the following, I will describe the event selection and validation of the selected events. The selection contains noise cleaning criteria, as well as selection criteria to suppress the SM background contribution in the signal regions. The exact definition of the signal regions will not be discussed in this section, but in Sect. 7.3.

The physics objects, which the selection is based on, have been described in detail in Chap. 5. The selection starts with a minimal set of criteria:

At least one good vertex (Sect. 5.1.1) needs to be reconstructed. The PV, which has the largest $\sum_i (p_{\mathrm{T},i})^2$ of tracks i associated to it, is chosen to be the hard interaction vertex. Next, the events have to pass the trigger requirements (Sect. 7.1): an event must have either $H_{\mathrm{T}} \geq 750\,\mathrm{GeV}$, or $H_{\mathrm{T}} \geq 450\,\mathrm{GeV}$ and $E_{\mathrm{T}}^{\mathrm{miss}} \geq 200\,\mathrm{GeV}$ to be selected. The third primary requirement is the selection of at least two jets: The M_{T2} variable needs as input at least two detected objects and $E_{\mathrm{T}}^{\mathrm{miss}}$. In this analysis, the visible systems in the M_{T2} calculation are defined by two pseudojets, as described in Sect. 6.2. The input to the pseudojet calculation are all jets candidates with $p_{\mathrm{T}} > 20\,\mathrm{GeV}$ and $|\eta| < 2.4$ and all charged leptons. In addition, the two leading jets are required to have $p_{\mathrm{T}} \geq 100\,\mathrm{GeV}$, and $E_{\mathrm{T}}^{\mathrm{miss}}$ must exceed 30 GeV. These requirements make sure, that the momenta of the visible systems and $\vec{E}_{\mathrm{T}}^{\mathrm{miss}}$ have meaningful magnitudes and directions.

7.2.1 Validation of the Stability of the M_{T2} Variable

The experimental environment in the CMS experiment during 2012 data taking has been very harsh, the mean number of pileup interactions per colliding bunch has been 20 [40]. In Fig. 7.3, the number of reconstructed primary vertices is shown. The distributions of pileup interactions in simulation is reweighted to match the one measured in data.

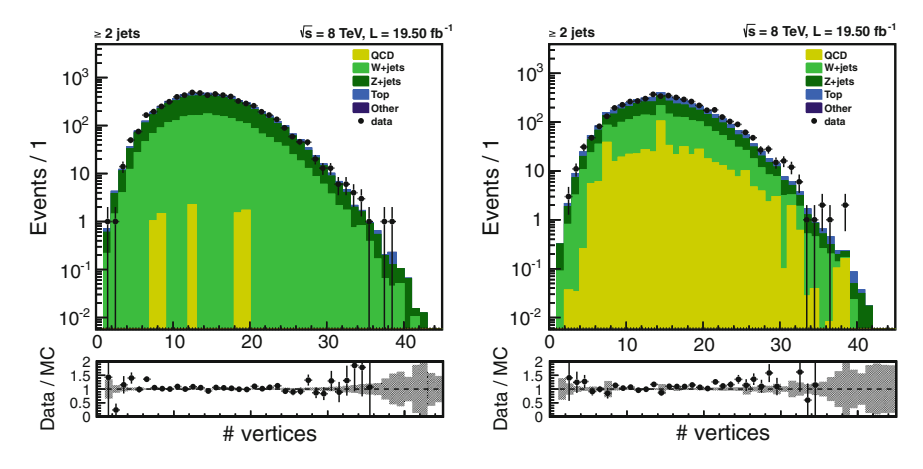


Fig. 7.3 Distribution of the number of vertices. Left for $450 \le H_{\rm T} < 750$ GeV, $E_{\rm T}^{\rm miss} \ge 200$ GeV, and $M_{\rm T2} \ge 200$ GeV. Right for $H_{\rm T} \ge 750$ GeV and $M_{\rm T2} \ge 125$ GeV

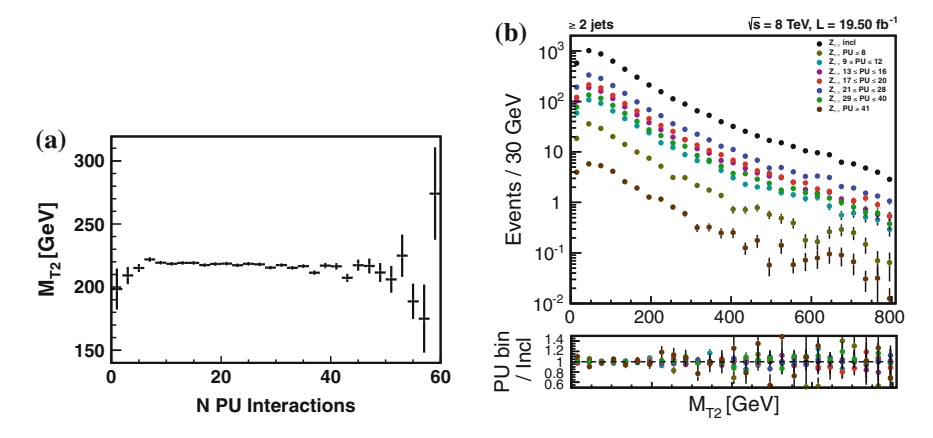


Fig. 7.4 Pileup dependence of the M_{T2} variable. a Profile of the M_{T2} distribution as a function of the number of pileup interactions for simulated $Z(\nu\overline{\nu})$ +jets events, for $450 \le H_T < 750\,\text{GeV}$, $E_T^{\text{miss}} \ge 200\,\text{GeV}$. b M_{T2} distribution for simulated $Z(\nu\overline{\nu})$ +jets events in various selections of the number of pileup interactions, for $H_T \ge 750\,\text{GeV}$. The bottom ratios are between the normalized distribution for a given selection of number of pileup interactions and the inclusive normalized distribution

The main signal discriminant should not depend on the number of pileup interactions. We apply energy corrections to jets (see Sect. 5.7), and thus also to $E_{\rm T}^{\rm miss}$, so that the influence of additional energy due to pileup is largely reduced. These corrections provide also stability for the $M_{\rm T2}$ variable as a function of pileup: in Fig. 7.4a, we see the profile of the $M_{\rm T2}$ distribution as a function of the number of pileup interactions in simulated $Z(\nu\bar{\nu})$ +jets events. The average value of $M_{\rm T2}$ is completely stable, even for scenarios with extremely high numbers of pileup interactions. We also prove that the shape of the $M_{\rm T2}$ distribution is stable as a function of the number of pileup interactions, see Fig. 7.4b. Hence, we conclude that the pileup dependence is very small, and the $M_{\rm T2}$ variable does not depend on the pileup condition.

7.2.2 Cleaning Procedure Against Instrumental Effects

The $M_{\rm T2}$ variable strongly correlates with $E_{\rm T}^{\rm miss}$. The $E_{\rm T}^{\rm miss}$ reconstruction can be affected by instrumental effects like noise signals in the calorimeter and tracker systems, dead detector regions like ECAL cells, misreconstructions, or environmental noise like interactions of protons with residual gas inside the beam pipe.

All these effects can lead to signatures with large reconstructed $E_{\rm T}^{\rm miss}$ and $M_{\rm T2}$, although the physics process does not contain a source of $E_{\rm T}^{\rm miss}$, like neutrinos or LSPs.

Therefore, events with anomalous signatures need to be filtered out. A lot of sources have been studied within the CMS collaboration, and filters have been developed for events affected by those sources [41]. Figure 7.5 shows the $E_{\rm T}^{\rm miss}$ distribution before and after event noise cleaning for events triggered by the $H_{\rm T}$ -only trigger. It is evident that the far tail of the $E_{\rm T}^{\rm miss}$ distribution would be dominated by events with fake $E_{\rm T}^{\rm miss}$ if no cleaning was applied.

During the analysis of the 2012 pp collision data, three noise categories had been identified in studies of the $E_{\rm T}^{\rm miss}$ distributions that are not tagged by filters provided by the CMS collaboration.

One source are deposits in the CMS detector due to *beam halo* particles [42]. The filter provided by the CMS collaboration is about 87% efficient [43]. Some events in the tail of the M_{T2} distribution are due to beam halo particles that were efficiently rejected by requiring the leading jet to pass tighter identification criteria if $\Delta \phi$ between the two leading jets is smaller than 0.2.

Another source of noise are anomalous signals in the HO component of the HCAL (see Sect. 4.2.3). As the HO signals have been part of the PF reconstruction, but were not used for the computation of the calorimeter-based $E_{\rm T,calo}^{\rm miss}$ (see Sect. 5.8), an efficient way to reject these signals has been found by requiring $E_{\rm T}^{\rm miss}/E_{\rm T,calo}^{\rm miss} \leq 2$.

Examples for data events tagged by those two filters are given in Fig. 7.6.

The third source of noise, not tagged by filters provided by the CMS collaboration, is due to fake TOB/TEC tracking seeds (see Sects. 4.2.1 and 5.1). These fake tracking seeds can lead to a huge number of fake tracks resulting sometimes in large $E_{\rm T}^{\rm miss}$.

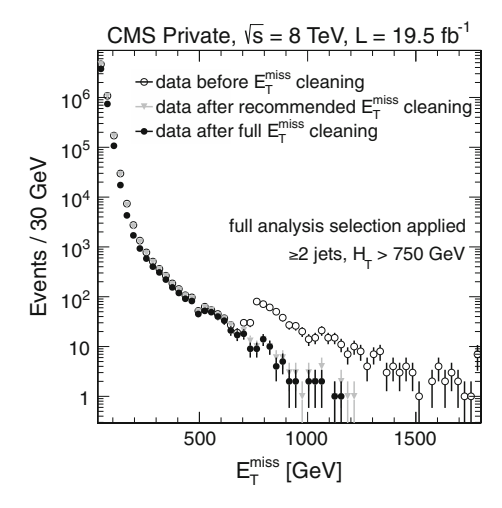


Fig. 7.5 The $E_{\rm T}^{\rm miss}$ distribution for $H_{\rm T} > 750\,{\rm GeV}$ after an event selection without the noise filters. The *open circles* identify data without noise cleaning, the *gray triangles* show data after recommended noise cleaning, and the *solid circles* show the data after full event noise cleaning. The step in the uncleaned data at $E_{\rm T}^{\rm miss} = 750\,{\rm GeV}$ is due to noise sources creating a large local signal in soft events (small true $H_{\rm T}$ and $E_{\rm T}^{\rm miss}$). This noise signal creates $H_{\rm T} > 750\,{\rm GeV}$ and $E_{\rm T}^{\rm miss} \approx H_{\rm T}$

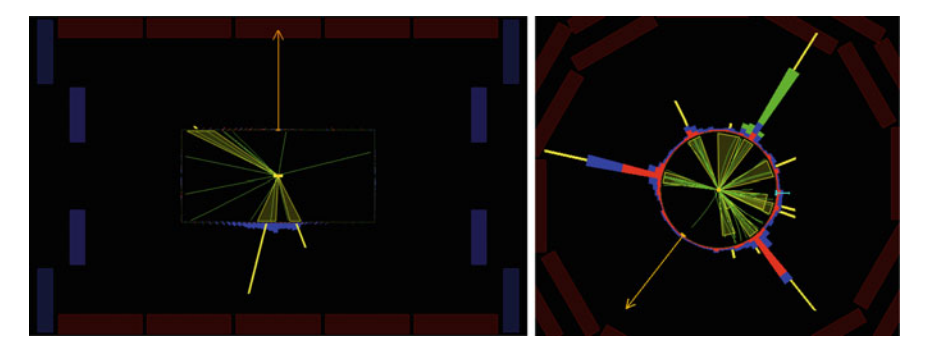


Fig. 7.6 Left Event tagged by the beam halo filter in the rz view: a beam halo signal in the HCAL (blue signal) results in two energetic jets (yellow bars) pointing opposite to $\vec{E}_{\rm T}^{\rm miss}$ (orange arrow). Right Event tagged by the anomalous HO noise filter in the $r\phi$ view: the HO signal is shown in green, the $\vec{E}_{\rm T}^{\rm miss}$ in orange, and the $\vec{E}_{\rm T,calo}^{\rm miss}$ in light blue

Figure 7.7a shows a data event, where correctly reconstructed tracks (green) and possibly fake tracks (yellow) are overlaid.

In order to remove those events from the selection, we require

$$R = \max_{\eta, \phi} \left\{ \frac{\text{number of tracks from last iteration}}{\text{number of tracks from first iteration}} \right\} \le 8, \tag{7.1}$$

where the $\eta\phi$ plane is sampled in 0.1 × 0.1 bins.

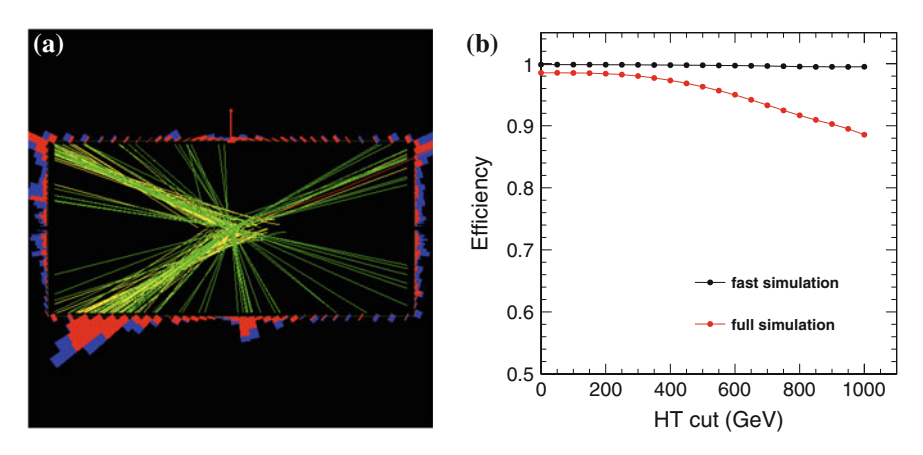


Fig. 7.7 a Data event in the rz view, where correctly reconstructed tracks (*green*) and possibly fake tracks (*yellow*) are overlaid. **b** The overall event passing efficiency of the TOB/TEC noise tagger as a function of H_T for simulated events of stop production processed with detailed (*red dots*) and fast (*black dots*) simulation of the CMS detector

The fast simulation of the CMS detector response includes a simplified version of the tracker, the noise due to TOB/TEC fake seeds is not present in the fast simulation, see Fig. 7.7b. The overall tagging efficiency for signal events, which are processed with the fast simulation, is emulated by parameterizing the TOB/TEC tagger passing efficiency in data as a function of jet- p_T and $|\eta|$. This parameterization has been found to model best the overall event tagging efficiency. The jet used in the parameterization is found as follows: We define a search window around the barrel-endcap transition region: $|\eta| = 1.5 \pm 0.2$, and the highest- p_T jet within that window is selected. If no jet is in that range, the search window is increased by 0.4 in η . For example, in the second iteration, it is $|\eta| = 1.5 \pm 0.4$. This is repeated, until a jet is found. The efficiency map is shown in Fig. 7.8.

7.2.3 Selection Criteria to Reduce the Standard Model Background

In order to enhance the signal sensitivity, we want to reject as much SM background in our signal region as possible while keeping a high signal event selection efficiency. For this, we study the reasons for SM processes to have high values of our signal discriminant M_{T2} .

One reason is the bias to the $M_{\rm T2}$ shape introduced by UTM. As we saw in Sect. 6.3, the difference between the analytical version of $M_{\rm T2}$, Eq. (6.5), and the full expression, Eq. (6.2), is limited to the magnitude of UTM. For this search, the UTM is expressed as $|\vec{p}_{\rm T}^{\rm upstream}| = |\vec{E}_{\rm T}^{\rm miss} - \vec{H}_{\rm T}^{\rm miss}|$ with $\vec{H}_{\rm T}^{\rm miss}$ defined by Eq. (6.13). The

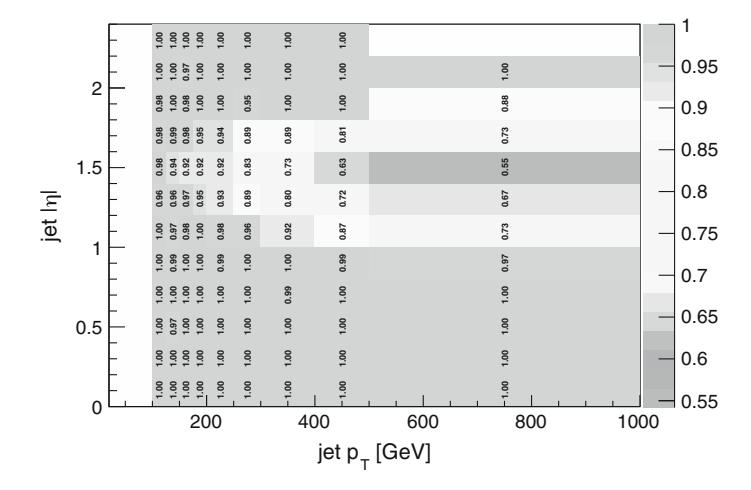


Fig. 7.8 Event passing efficiency of the TOB/TEC noise tagger as a function of jet- p_T (x axis) and jet- $|\eta|$ (y axis) in data

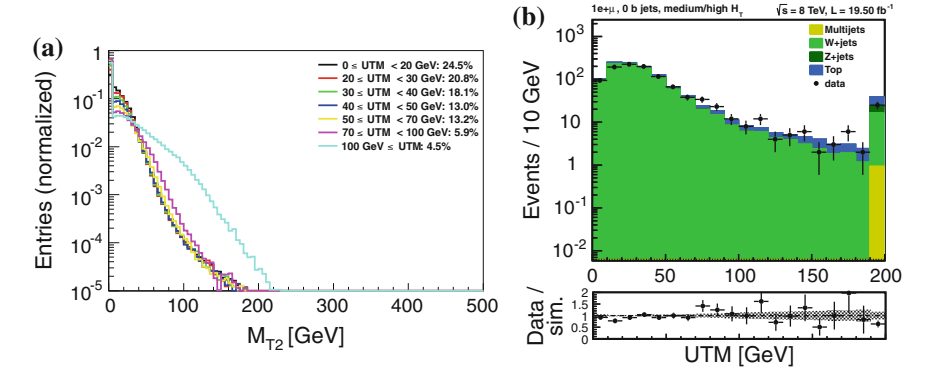


Fig. 7.9 a Normalized $M_{\rm T2}$ distributions in simulated QCD multijet events for $H_{\rm T} \geq 750$ GeV and for various selections on UTM = $|\vec{E}_{\rm T}^{\rm miss} - \vec{H}_{\rm T}^{\rm miss}|$. b Distribution of the UTM = $|\vec{E}_{\rm T}^{\rm miss} - \vec{H}_{\rm T}^{\rm miss}|$ variable in $W(l\nu)$ +jets enriched data, selecting one electron or muon, zero b jets, $H_{\rm T} \geq 750$ GeV, and $M_{\rm T2} \geq 150$ GeV

value of the M_{T2} variable can be driven by the amount of UTM for multijet production with no source of $E_{\rm T}^{\rm miss}$. The normalized $M_{\rm T2}$ distributions for various selections of UTM $\equiv |\vec{p}_{\rm T}^{\rm upstream}|$ are shown in Fig. 7.9a for simulated QCD multijet events. We observe that the distortion of the $M_{\rm T2}$ shape becomes significant for $|\vec{E}_{\rm T}^{\rm miss}-\vec{H}_{\rm T}^{\rm miss}|\gtrsim 70~{\rm GeV}$. We, therefore, require all selected events to pass $|\vec{E}_{\rm T}^{\rm miss}-\vec{H}_{\rm T}^{\rm miss}|<70~{\rm GeV}$. The shape of the $|\vec{E}_{\rm T}^{\rm miss}-\vec{H}_{\rm T}^{\rm miss}|$ distribution at high $M_{\rm T2}$ is reasonably well modelled, as validated in a $W(l\nu)$ +jets data control region, selecting one electron or muon and zero b jets, see Fig. 7.9b.

As we discussed in Sect. 6.3, QCD multijet events enter the tail of the M_{T2} distribution, if one jet is severely mismeasured and the pseudojets are not back-to-back anymore. However, in these cases the \vec{p}_T of the mismeasured jet is aligned with the \vec{E}_T^{miss} . A good variable to reject those events is the minimal azimuthal angle between the \vec{p}_T of jets and \vec{E}_T^{miss} , min $\Delta\phi$ (jets, E_T^{miss}). In order to keep a high signal efficiency for models with multiple jets in the final states (like pp $\to gg \to t\bar{t}\chi_1^0 t\bar{t}\chi_1^0$), min $\Delta\phi$ (jets, E_T^{miss}) is computed using only the four leading jets.

Figure 7.10a shows the min $\Delta\phi(\text{jets}, E_{\text{T}}^{\text{miss}})$ variable in data and simulation for events with $H_{\text{T}} \geq 750\,\text{GeV}$ and $M_{\text{T}2} \geq 125\,\text{GeV}$. We can see, that the min $\Delta\phi(\text{jets}, E_{\text{T}}^{\text{miss}})$ distribution is peaked at min $\Delta\phi(\text{jets}, E_{\text{T}}^{\text{miss}}) = 0$ for QCD multijet production, while it is relatively flat for the electroweak backgrounds and the SUSY signal (here, the LM6 model). The profile of the min $\Delta\phi(\text{jets}, E_{\text{T}}^{\text{miss}})$ distribution as a function of $M_{\text{T}2}$, Fig. 7.10b, illustrates that multijet events in the tail of the $M_{\text{T}2}$ distribution dominantly have small min $\Delta\phi(\text{jets}, E_{\text{T}}^{\text{miss}})$.

For rejecting events due to multijet production, we require min $\Delta \phi$ (jets, $E_{\rm T}^{\rm miss}$) \geq 0.3.

All SM backgrounds except the multijet production contain true $E_{\rm T}^{\rm miss}$ inside the event due to the presence of one or more neutrinos. One background is from events containing a Z boson decaying into two neutrinos and is irreducible. The other source of neutrinos are W boson decays. Events containing a leptonically decaying W boson together with several hard jets can naturally lead to high values of $M_{\rm T2}$. The contribution of such events is reduced by rejecting events containing a charged lepton $(e, \mu, \text{ or } \tau, \text{ where } \tau \text{ means hadronically decaying taus})$. This requirement leaves hadronic SUSY signals nearly unchanged, while the $W(l\nu)$ +jets and $t\bar{t}$ +jets backgrounds are strongly reduced.

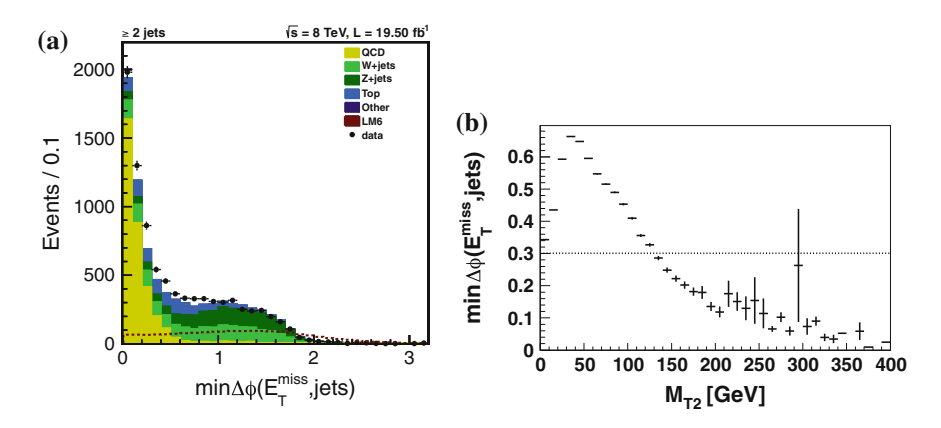


Fig. 7.10 Studies of the min $\Delta\phi(\text{jets}, E_{\text{T}}^{\text{miss}})$ variable. a Distribution of the min $\Delta\phi(\text{jets}, E_{\text{T}}^{\text{miss}})$ variable for data and simulation after a selection of $H_{\text{T}} \geq 750\,\text{GeV}$ and $M_{\text{T2}} \geq 125\,\text{GeV}$. b Profile of the min $\Delta\phi(\text{jets}, E_{\text{T}}^{\text{miss}})$ distribution as a function of M_{T2} for multijet events after a selection of $H_{\text{T}} > 750\,\text{GeV}$

7.2.4 Summary of the Event Selection

In this section, the basic selection was shown. It is:

- at least one good PV,
- pass either $H_T \ge 750 \,\text{GeV}$, or $H_T \ge 450 \,\text{GeV}$ and $E_T^{\text{miss}} \ge 200 \,\text{GeV}$,
- at least two jets, the two leading jets are required to pass $p_T > 100 \,\text{GeV}$,
- $E_{\rm T}^{\rm miss} > 30 \,{\rm GeV}$,
- reject events tagged by one of the noise filters,
- $|\vec{E}_{\mathrm{T}}^{\mathrm{miss}} \vec{H}_{\mathrm{T}}^{\mathrm{miss}}| < 70 \,\mathrm{GeV},$
- min $\Delta \phi$ (jets, $E_{\rm T}^{\rm miss}$) ≥ 0.3 , and
- reject events containing at least one charged lepton.

On top of this selection, further selections are applied on M_{T2} , H_T , and the jet and b-jet multiplicities. These variables are the main signal discriminants and define the signal regions. The selection criteria on them are discussed in Sect. 7.3.

7.3 Optimization and Search Strategy

Now, I will outline the search strategy for the inclusive M_{T2} analysis.

In this analysis, a large phase space is selected and then divided in several mutually exclusive signal regions. This division is optimized for a search for a large variety of possible new physics models, especially in the context of SUSY. The signal regions are defined by both the event topology and kinematical variables. The search strategy is:

- 1. Data are selected with three trigger paths based on $H_{\rm T}$ and $E_{\rm T}^{\rm miss}$, see Sect. 7.1, and are required to pass the event selection from Sect. 7.2.4.
- 2. Three regions along $H_{\rm T}$ are defined as sketched in Fig. 7.11, left: a low $H_{\rm T}$ region requiring $E_{\rm T}^{\rm miss} \geq 200\,{\rm GeV}$ and $450 \leq H_{\rm T} < 750\,{\rm GeV}$, a medium $H_{\rm T}$ region for $750 \leq H_{\rm T} < 1200\,{\rm GeV}$, and a high $H_{\rm T}$ region, going beyond $H_{\rm T} \geq 1200\,{\rm GeV}$. The thresholds on $H_{\rm T}$ and $E_{\rm T}^{\rm miss}$ for the low $H_{\rm T}$ region, and on $H_{\rm T}$ for the medium $H_{\rm T}$ region are driven by the trigger selection.
- 3. Nine different event topologies are selected along the jet and b-jet multiplicities (N_j and N_b, respectively), see Fig. 7.11, right: The regions with 0 b jets are sensitive to SUSY models involving first and second generation squarks, while regions with higher b-jet multiplicity increase the sensitivity to third generation squark production. The signal regions with ≥3 b jets have high sensitivity for gluino decays via third generation squarks.
 - A dijet selection is sensitive to direct squark production, while the 3-5 jet and \geq 6 jet regions increase the sensitivity to gluino and stop pair productions.
- 4. On top of the signal region selection based on H_T and the number of (b-)jets, several adjacent bins along M_{T2} , up to nine, are defined. The sparticle masses determine the average values of H_T and M_{T2} , and therefore having various bins

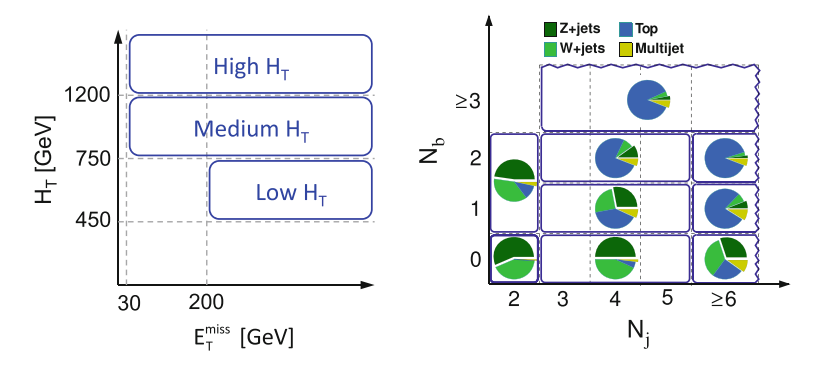


Fig. 7.11 Left Binning in H_T and E_T^{miss} . Right Definition of the topological regions in numbers of jets and b jets, N_j and N_b , respectively. The pie charts show the relative expected contribution from different SM processes to the signal regions for each topological region

in these variables results in a sensitivity for a wide mass range for sparticle production. The number of bins depends on the topological and $H_{\rm T}$ regions. In each of these regions, the lower boundary on $M_{\rm T2}$ has been chosen, such that the expected contribution of the multijet background to the total SM background is of order 1–10% or less. The lowest selection on $M_{\rm T2}$ for all regions is $M_{\rm T2} \geq 100\,{\rm GeV}$. The exact definition of all signal regions is given in Table 7.1.

- 5. The SM background in each signal region is predicted by data-driven background estimation methods. For each source of SM background, a separate method is used. The results of the background predictions are compared to the observed data.
- 6. The results of the analysis are interpreted in several models of SUSY and exclusions on the model parameters are obtained.

The outlined strategy was defined as the result of an optimization exercise, which I want to sketch here: The optimization was based on the expected mass exclusion reach for various simplified models (in the absence of a signal) using the method and models presented in Sect. 7.8. These studies were performed with simplified systematics, and sometimes with enhanced signal cross-section. Therefore, one has to consider all numbers and figures of the optimization as relative.

The first step of optimization had already been presented in Sect. 7.1: Besides the H_T -only trigger that had been used for the 7 TeV search, a combination of a H_T - E_T^{miss} cross trigger and a E_T^{miss} -only trigger is used to access a phase space with lower H_T . The new added low H_T region is sensitive to SUSY models, where the difference between the mass of the initially produced sparticle and the mass of the LSP is relatively small. An example is shown in Fig. 7.12a: The low H_T region (in plot $met_combined$) allows to increase the exclusion reach for higher LSP mass at a fixed sbottom mass. The model in this figure is direct sbottom production with $\widetilde{b} \to b \widetilde{\chi}_1^0$.

Table 7.1 Signal region definitions of the inclusive $M_{\rm T2}$ analysis

	Low H _T	region		Medium	H _T region		High H _T	region
	$M_{\rm T2}$ bin	(GeV)		M _{T2} bin	(GeV)		M _{T2} bin	(GeV)
2 jets, 0 b jets	200–240	350–420	570–650	125–150	220–270	425–580	120–150	260–350
	240-290	420-490	≥650	150-180	270–325	580-780	150-200	350–550
	290–350	490–570		180-220	325–425	≥780	200–260	≥550
2 jets, ≥1 b jets	200–250	310–380	450–550	100–135	170–260	≥450	100-180	
	250-310	380–450	≥550	135–170	260–450		≥180	
3-5 jets, 0 b jets	200–240	420–490		160–185	300–370	≥800	160–185	350–450
	240–290	490–570		185–215	370–480		185–220	450–650
	290–350	570–650		215–250	480–640		220–270	≥650
	350-420	≥650		250-300	640-800		270–350	
3-5 jets, 1 b jets	200–250	310–380	460–550	150–175	210–270	380–600	150–180	230–350
	250-310	380-460	≥550	175–210	270–380	≥600	180-230	≥350
3-5 jets, 2 b jets	200–250	325–425		130–160	200–270	≥370	130–200	
	250–325	≥425		160-200	270–370		≥200	
\geq 6 jets, 0 b jets	200–280	≥380		160–200	250–325	≥425	160–200	≥300
	280–380			200-250	325–425		200-300	
\geq 6 jets, 1 b jets	200–250	≥325		150–190	250–350		150–200	≥300
	250–325			190-250	≥350		200-300	
≥6 jets, 2 b jets	200–250	≥300		130–170	220–300		130–200	
	250-300			170-220	≥300		≥200	
≥3 jets, ≥3 b jets	200–280	≥280		125–175	175–275	≥275	≥125	

The phase space is further increased by the inclusion of dijet events (the 7 TeV search selected events with ≥ 3 jets). This increases the sensitivity for various models dominated by direct squark production. An example is shown in Fig. 7.12b, again for the sbottom production model: the explicit dijet region (here met_2j_ge1b , that is with the requirement of ≥ 1 b jets), has high sensitivity for high sbottom mass, while for a low mass splitting between the sbottom and LSP, signal regions with ≥ 3 jets become important. The reason is, that the selected events often contain ISR jets. These jets boost the $b\widetilde{\chi}_1^0\overline{b}\widetilde{\chi}_1^0$ system such that the event passes the M_{T2} and H_T requirements.

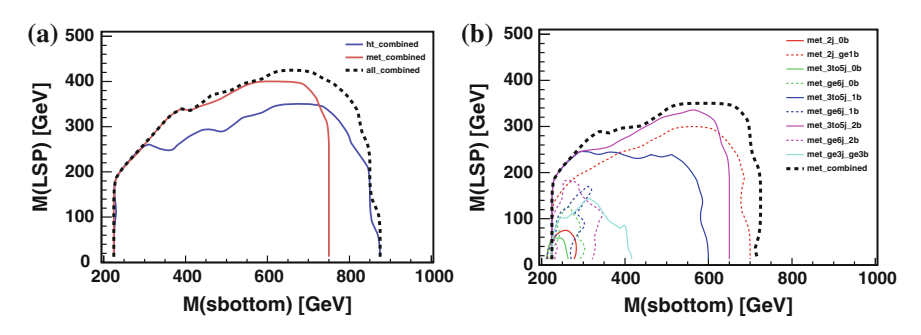


Fig. 7.12 Simplified expected exclusion limits on direct sbottom production. a Simplified expected exclusion limit on direct sbottom production. b Simplified expected exclusion limit on direct sbottom production for $E_T^{miss} \geq 200 \, \text{GeV}$, and $450 \leq H_T < 750 \, \text{GeV}$

In many SUSY models, third generation squarks are expected to be lighter than those of the first two generations, see Sect. 2.3. The division of the phase space along the b-jet multiplicity is designed for a better reach for events involving third generation squarks. An example of exclusion limits on a model of gluino pair production with $\tilde{g} \to b\bar{b}\tilde{\chi}_1^0$ via a virtual sbottom is shown in Fig. 7.13a. Having search regions with multiple b jets, like ht_ge3j_ge3b with ≥ 3 b jets, strongly increases the exclusion and discovery reach of this analysis.

It is also important that the information of multiple signal regions is combined. In Fig. 7.13b, the expected mass exclusion reach for the process of direct stop production with $\tilde{t} \to t \tilde{\chi}_1^0$ for various signal regions in $H_T \times N_j \times N_b$ have the same reach on their own. Using the multibin approach and combining them, strongly enhances the reach.

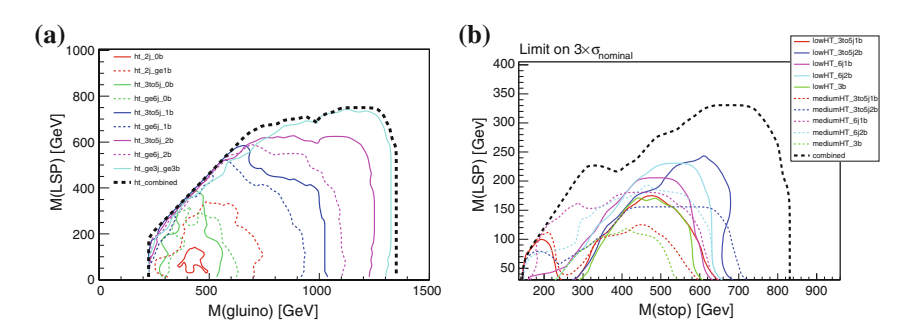


Fig. 7.13 Simplified expected exclusion limits on direct gluino production with gluino decays via a virtual sbottom (a) and on direct stop production (b)

7.3.1 The Inclusive M_{T2} Analysis: Distributions and Background Composition

The $M_{\rm T2}$ distributions for the low, medium, and high $H_{\rm T}$ selections, inclusively in all nine topological regions, are shown in Fig. 7.14. We observed that the events with $M_{\rm T2} \lesssim 80\,{\rm GeV}$ basically stem only from multijet production. We require the expected contribution of multijet events to the total SM background to be of order

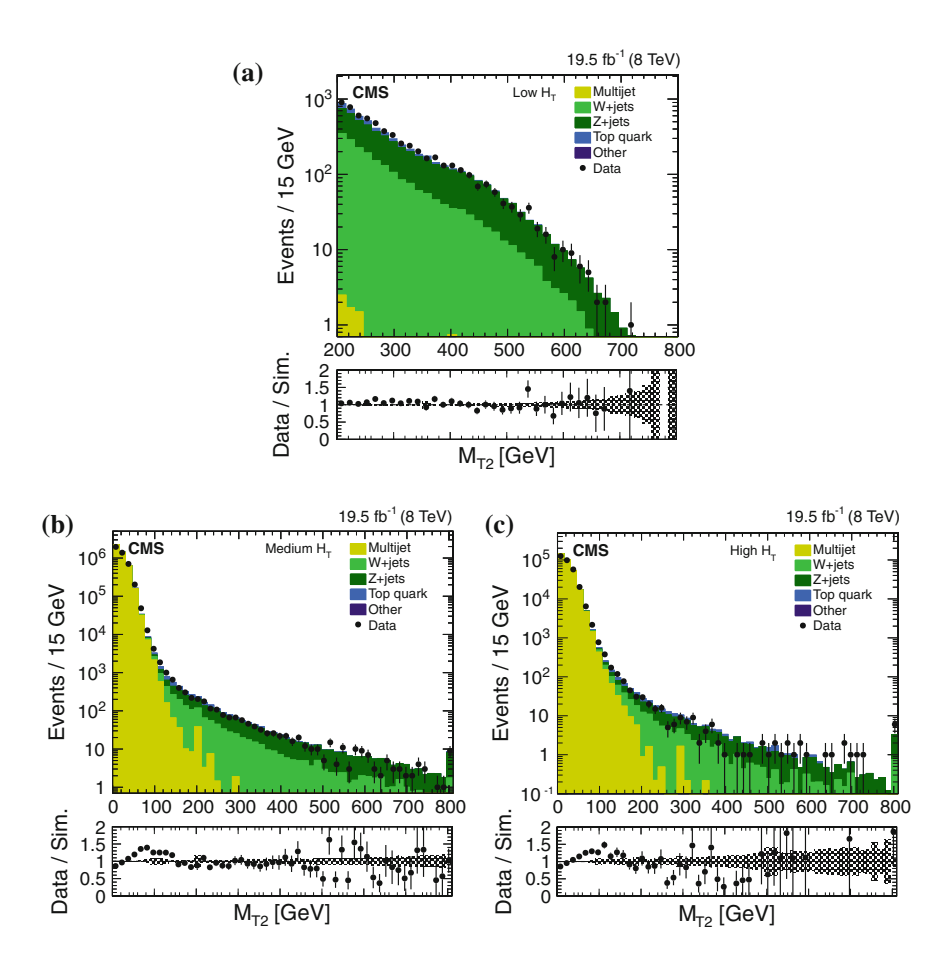


Fig. 7.14 The M_{T2} distributions in data and simulation for the low (a), medium (b), and high (c) H_T selections and for ≥ 2 jets, ≥ 0 b jets. All selection criteria, Sect. 7.2.4, are applied. The data, selected at $\sqrt{s}=8$ TeV, correspond to 19.5 fb⁻¹ integrated luminosity. The simulation is normalized to the integrated luminosity. The last bin contains the overflow. The ratios of the number of data events versus the number of simulated events show some disagreement. However, the final estimation of the SM background event yields is not obtained from simulation, but using data-driven background prediction methods

 \lesssim 10 %. Hence, regions with $M_{T2} < 100\,\mathrm{GeV}$ are not selected. For the low H_{T} region, the M_{T2} distribution below $M_{T2} = 200\,\mathrm{GeV}$ is not used because of the trigger requirement $E_{T}^{\mathrm{miss}} > 200\,\mathrm{GeV}$. The SM background in the signal regions consists mainly out of $Z(\nu\overline{\nu})$ +jets, $W(l\nu)$ +jets, and semileptonic $t\overline{t}$ +jets events. The $t\overline{t}$ +jets background decreases for higher M_{T2} with respect to the $Z(\nu\overline{\nu})$ +jets and $W(l\nu)$ +jets background because of the kinematical properties of the M_{T2} variable, explained in Sect. 6.3.

The dominant background for the low jet and/or zero b-jet regions is $Z(\nu\bar{\nu})$ +jets, followed by $W(l\nu)$ +jets. The production of $t\bar{t}$ +jets is unimportant in these regions. All three processes are of equal importance in the one b-jet region. For increasing b-jet multiplicity, the $t\bar{t}$ +jets background becomes more and more important, and is the dominant component for all regions with at least two b jets. Also in regions with at least six jets, the $t\bar{t}$ +jets background is always important. These observations are independent of the H_T selection, and the features are illustrated in the M_{T2} distributions of Fig. 7.15, where 8 TeV collision data, corresponding to 19.5 fb⁻¹ integrated luminosity, are compared to the yields in simulation for a selection of at least two b jets (left) or at least six jets (right), as well as in the M_{T2} distributions of the previous Fig. 7.14 for an inclusive selection of at least two jets, but different H_T selections.

Other contributions, such as γ +jets, $Z(l^+l^-)$ +jets, or di-/tribosons+jets production are negligible with respect to the three main components, $Z(\nu\overline{\nu})$ +jets, $W(l\nu)$ +jets, and $t\overline{t}$ +jets events.

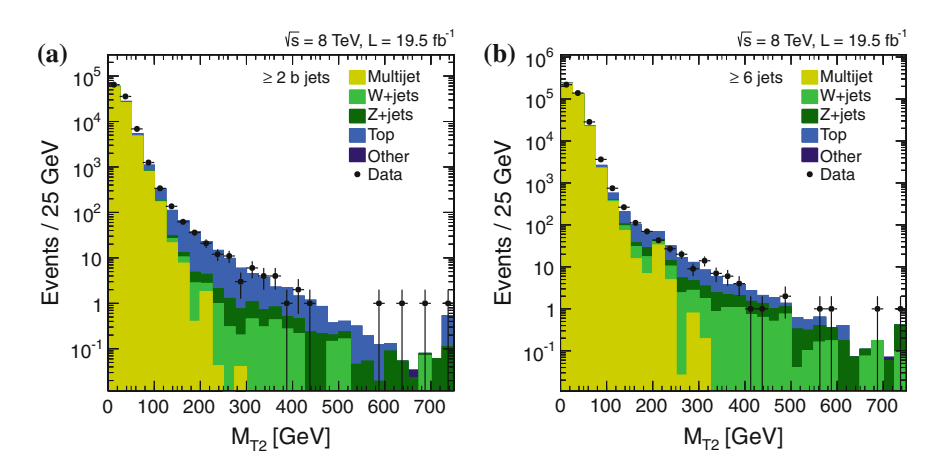


Fig. 7.15 M_{T2} distribution in data and simulation for medium + high H_T selection, for ≥ 2 jets, ≥ 2 b jets (a), and for ≥ 6 jets, ≥ 0 b jets (b). All selection criteria, Sect. 7.2.4, are applied. The data, selected at $\sqrt{s} = 8$ TeV, correspond to 19.5 fb⁻¹ integrated luminosity. The simulation is normalized to the integrated luminosity. The last bin contains the overflow

7.4 Prediction of the Background Due to Jet Energy Mismeasurements

The initially largest background is the one of multijet events, where the energy of at least one jet is mismeasured. Although dramatic jet energy mismeasurements are rare, the overwhelming cross section of multijet production makes this process dominant over the electroweak processes or $t\bar{t}$ +jets production. However, the properties of the M_{T2} variable allow to reduce the multijet background to a negligible level in our signal regions.

The remaining multijet contribution is estimated by a data-driven prediction method. The method also predicts fully hadronic $t\bar{t}$ +jets production and the production of hadronically decaying bosons, which are negligible. As we have seen in Fig.7.10b, the M_{T2} and the min $\Delta\phi(\text{jets}, E_T^{\text{miss}})$ variables are strongly correlated for multijet events. We also know, that multijet events tend to populate the low min $\Delta\phi(\text{jets}, E_T^{\text{miss}})$ region, Fig.7.10a. We will use these two observations to construct a prediction method for multijet events.

We form the ratio $r(M_{T2}) = N(\min \Delta \phi(\text{jets}, E_T^{\text{miss}}) \geq 0.3)/N(\min \Delta \phi(\text{jets}, E_T^{\text{miss}}) \leq 0.2)$. Here, N(X) means the number of events for a given M_{T2} passing the selection of X and the selection of Sect. 7.2.4 but $\min \Delta \phi(\text{jets}, E_T^{\text{miss}}) \geq 0.3$. For the prediction, we use data from a control region with $\min \Delta \phi(\text{jets}, E_T^{\text{miss}}) \leq 0.2$ and high M_{T2} , and scale it with $r(M_{T2})$ to predict the yield of multijet events in the various signal regions.

The ratio $r(M_{T2})$ for simulated multijet events is shown in Fig. 7.16 for all three H_T selections and the high statistics region with 3-5 jets, 0 b jets.

We find in simulation that the ratio falls exponentially for $M_{\rm T2} > 50\,{\rm GeV}$ and reaches a constant value at high $M_{\rm T2}$. This has been confirmed in 7 and 8 TeV data. The ratio can be parameterized for $M_{\rm T2} > 50\,{\rm GeV}$ as

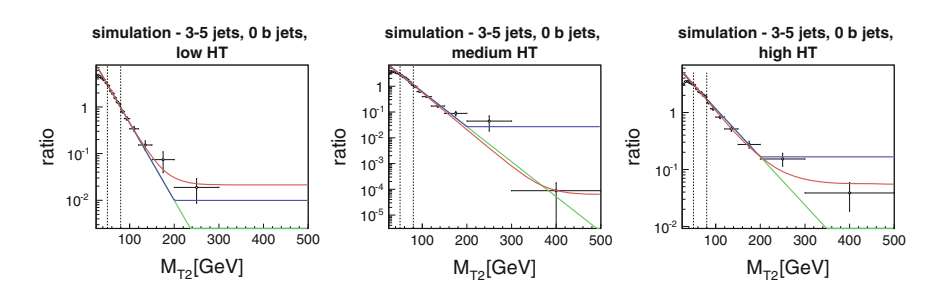


Fig. 7.16 Ratio $r(M_{T2})$ as a function of M_{T2} for simulated events for the low (*left*), medium (*center*), and high (*right*) H_T selections and 3-5 jets, 0 b jets. The simulated data points are overlaid with three fit functions. The *red curve* is a full parameterization fit, the *green curve* is a purely exponential fit, and the *blue curve* is the analysis fit. The *dashed vertical lines* indicate the fit region. More information about the three fit models is given in the text

$$r(M_{\rm T2}) = \frac{N(\min \Delta \phi(\text{jets}, E_{\rm T}^{\rm miss}) \ge 0.3)}{N(\min \Delta \phi(\text{jets}, E_{\rm T}^{\rm miss}) \le 0.2)} = e^{a-b \cdot M_{\rm T2}} + c, \tag{7.2}$$

where a,b, and c are fit parameters. This parameterization is the *full* parameterization. If we set c=0, it is a purely *exponential* parameterization. The parameterization can be understood as follows: The exponential part is modelling the "core" of the jet energy resolution [44]. This core is driven by the detector resolutions of the tracking, ECAL and HCAL systems, see Sects. 4.2.1–4.2.3. Besides this core, the distribution of the jet energy resolution has a long tail due to severe jet energy mismeasurements. In multijet events, the larger the value of $E_{\rm T}^{\rm miss}$ (and $M_{\rm T2}$) is, the larger is the probability of an alignment between the $\vec{E}_{\rm T}^{\rm miss}$ and the $\vec{p}_{\rm T}$ of the mismeasured jet. Thus, the ratio $r(M_{\rm T2})$ decreases as a function of $M_{\rm T2}$. For very large $M_{\rm T2}$, the strongly mismeasured jet and the $\vec{E}_{\rm T}^{\rm miss}$ are always aligned. However, for a certain fraction of events, the mismeasured jet becomes that soft, such that it is too soft and not among the four leading jets anymore. This acceptance fraction determines the constant value.

We have seen before that the event composition in the region of $M_{\rm T2}$ < 80 GeV is dominated by multijet events. Thus, we can obtain the parameters a and b from Eq. (7.2) by fitting the data ratio $r(M_{\rm T2})$ in the region 50 < $M_{\rm T2}$ < 80 GeV. The full fit, including parameter c, can only be obtained using the full range of $M_{\rm T2}$ > 50 GeV (red curves in Fig. 7.16). However, at high $M_{\rm T2}$, the multijet production is small compared to electroweak and top production, and the data cannot be used for fitting. On the other hand, the purely exponential fit (green curves in Fig. 7.16) will underpredict the multijet background for very high values of $M_{\rm T2}$.

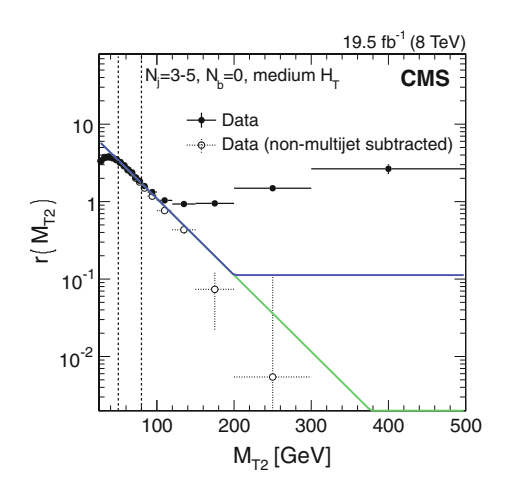
Therefore, a pseudoparameter c' is determined from data in such a way that the multijet background is not underpredicted for high M_{T2} , but one also does not depend on simulation for extreme jet energy mismeasurements. We change the parameterization of Eq. (7.2) to

$$r(M_{\rm T2}) = \frac{N(\min\Delta\phi({\rm jets},\,E_{\rm T}^{\rm miss})\geq 0.3)}{N(\min\Delta\phi({\rm jets},\,E_{\rm T}^{\rm miss})\leq 0.2)} = \begin{cases} e^{a-b\cdot M_{\rm T2}} & \text{if } M_{\rm T2}\leq 200\,{\rm GeV}, \\ c'=e^{a-b\cdot 200\,{\rm GeV}} & \text{if } M_{\rm T2}>200\,{\rm GeV}. \end{cases}$$
 (7.3

This is the *analysis* parameterization (blue curves in Fig. 7.16). It depends only on parameters a and b, which are determined in data as described above. We choose to fix c' at $M_{T2} = 200$ GeV, because we can show that the data follow the exponential fit up to that point. Usually, the analysis parameterization overpredicts the multijet contribution for $M_{T2} > 200$ GeV. However, we will find that in this region the multijet background is negligible compared to the background coming from electroweak and top processes. It should also be noted that for $M_{T2} \le 200$ GeV, the analysis parameterization leads to an accurate prediction of the multijet backgrounds.

The ratio $r(M_{T2})$ is shown for the full range in M_{T2} in Fig. 7.17 for the selection of 3-5 jets, 0 b jets, and medium H_T . We observe that the data, after the subtraction of electroweak and top contributions from simulation, follow the exponential fit. For

Fig. 7.17 The ratio $r(M_{\rm T2})$ in data, before and after subtracting the electroweak and top contribution from simulation, for the selection of 3-5 jets, 0 b jets, and medium $H_{\rm T}$. The fit region, $50 < M_{\rm T2} < 80 \, {\rm GeV}$, is indicated by *two vertical*, *dashed lines*. The data is fitted with an exponential fit (*green line*). The analysis parameterization (*blue line*) is also shown



 $M_{\rm T2} > 200\,{\rm GeV}$, the statistical uncertainty on the ratio is so large that the data are compatible with both fits using the exponential and analysis parameterization.

The data of the low $H_{\rm T}$ regions are triggered by the $E_{\rm T}^{\rm miss}$ and $E_{\rm T}^{\rm miss}$ - $H_{\rm T}$ triggers. The $E_{\rm T}^{\rm miss}$ requirement in the triggers biases the $M_{\rm T2}$ distribution at low $H_{\rm T}$, and strongly reduces the multijet contribution for low $M_{\rm T2}$. Therefore, we need other triggers for determining parameters a and b in the low $H_{\rm T}$ region. We use the prescaled $H_{\rm T}$ triggers with a threshold of $H_{\rm T} \geq 350\,{\rm GeV}$, see Sect. 7.1. We measure the effective prescale factor by comparing the yields in data selected by the prescaled and the analysis $H_{\rm T}$ trigger in the region $H_{\rm T} \geq 750\,{\rm GeV}$. We find a factor 353 \pm 1.9, see Fig. 7.18. The ratio $r(M_{\rm T2})$ is obtained from data selected by the prescaled $H_{\rm T}$ triggers: the yield of the electroweak and top contributions from simulation is downscaled by the prescale factor, and subtracted from the data ratio. Then, the ratio is fitted to obtain parameters a and b.

After finding the parameters a and b for the ratio $r(M_{T2})$ as listed in Table 7.2, the prediction is obtained by selecting the data in a control region with min $\Delta \phi$ (jets, $E_{\rm T}^{\rm miss}$) ≤ 0.2 for each $M_{\rm T2}$, $H_{\rm T}$, and topological region, subtracting the contamination from electroweak and top processes using simulation, and scaling the data yields with the fitted $r(M_{\rm T2})$ ratio.

The systematic uncertainties on the background prediction are obtained by studying the effect of the subtraction of the electroweak and top contribution, and by studying the stability of the fit of $r(M_{T2})$: The fit conditions are varied, such as variations in the borders of the fit window, or changing the selection criterium of min $\Delta \phi$ (jets, E_T^{miss}) for the control region. The fit is robust against these variations, and the uncertainties are mainly driven by the statistical power of the fit. The uncertainties are quoted as the uncertainties on parameters a and b in Table 7.2. For $M_{T2} > 200 \,\text{GeV}$, we require the systematic uncertainty to be at least 50 %. This is done, because there is an intrinsic uncertainty due to the choice of $M_{T2} = 200 \,\text{GeV}$

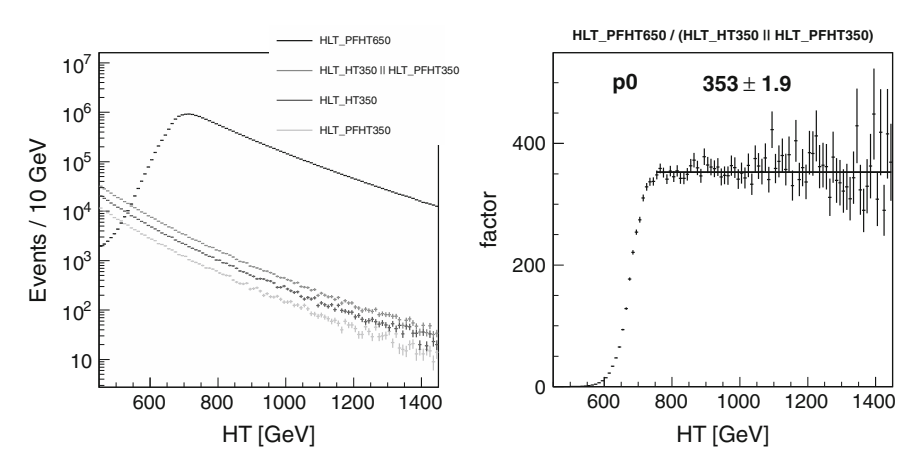


Fig. 7.18 Left H_T distribution for the analysis H_T triggers, and two prescaled H_T triggers with threshold $H_T \ge 350 \text{ GeV}$. Ratio of the data yields selected between the analysis H_T trigger and the prescaled H_T triggers. The ratio is fitted with a constant p0 for $H_T \ge 750 \text{ GeV}$

Table 7.2 Fit results of parameters a and b using the analysis parameterization

	Low H _T		Medium H _T	•	High H _T	
$(N_{\rm j},\ N_{\rm b})$	а	$b \times 10^2$	a	$b \times 10^2$	a	$b \times 10^2$
		(GeV^{-1})		(GeV^{-1})		(GeV^{-1})
(2,0)	3.09 ± 0.94	3.66 ± 1.59	3.12 ± 0.27	2.67 ± 0.46	2.41 ± 0.94	1.91 ± 1.64
(2,≥1)	_	_	2.24 ± 0.66	1.83 ± 1.13	_	_
(3-5,0)	2.99 ± 0.32	3.33 ± 0.54	2.36 ± 0.05	2.27 ± 0.08	1.95 ± 0.14	1.53 ± 0.23
(3-5, 1)	2.36 ± 0.59	3.09 ± 0.98	2.39 ± 0.09	2.57 ± 0.14	1.31 ± 0.23	1.22 ± 0.38
(3-5, 2)	2.79 ± 1.90	3.98 ± 3.18	1.77 ± 0.18	2.36 ± 0.30	1.60 ± 0.57	1.89 ± 0.92
$(\ge 6, 0)$	1.66 ± 1.13	1.63 ± 1.86	1.94 ± 0.10	1.46 ± 0.17	1.08 ± 0.21	0.71 ± 0.34
(≥6,1)	3.60 ± 2.56	4.91 ± 4.46	1.85 ± 0.15	2.00 ± 0.25	2.35 ± 0.37	2.88 ± 0.61
(≥6,2)	4.58 ± 6.91	5.34 ± 10.26	1.65 ± 0.30	1.79 ± 0.50	1.13 ± 0.91	0.99 ± 1.50
(≥3,≥3)	_	_	1.48 ± 0.50	1.72 ± 0.82	_	_

The parameters are obtained separately for each H_T region and topological region, (N_j, N_b) . In regions denoted by "–", no stable fit can be performed. In these regions, the simulation is taken to predict the background. However, the multijet yield is extremely small in these regions (which is the reason why no stable fits can be performed)

for the evaluation of the parameter c'. In addition, uncertainties due to the statistical power of the data control sample are taken into account.

We can see from the example in Fig. 7.19 that the prediction from simulation is not good enough. On the other hand, the data-driven estimation method accurately predicts the yield of the multijet backgrounds.

The results of the multijet background prediction can be found in Sect. 7.7, together with the results of the other estimation methods.

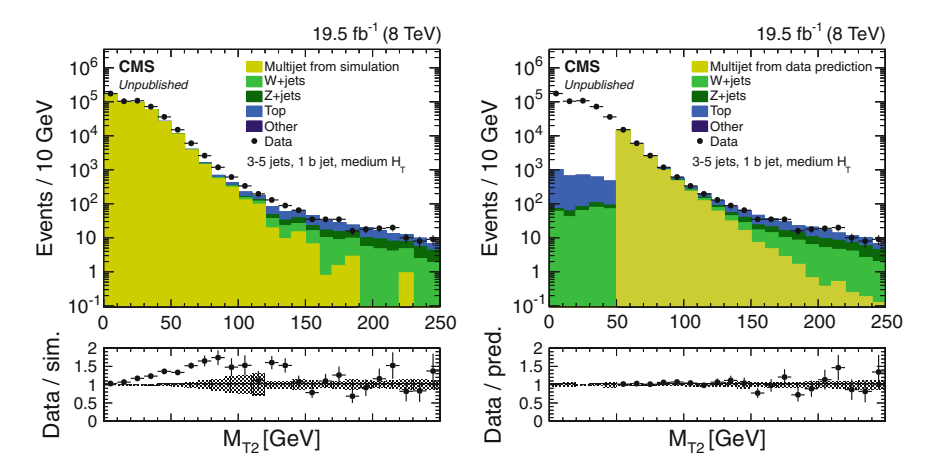


Fig. 7.19 The M_{T2} distributions in simulation and 8 TeV data, corresponding to an integrated luminosity of 19.5 fb⁻¹, for the medium H_T selection, 3-5 jets, and 1 b jet. The multijet background is either obtained from simulation (*left*) or the data-driven estimation method (*right*). The ratio "Data/sim." shows that the simulation does not predict the multijet background precisely enough, but the data-driven prediction is accurate ("Data/pred."). By definition of the estimate, there is no prediction for $M_{T2} < 50$ GeV. However, that region is not part of any signal region

7.5 Prediction of the Background Due to Leptonic W Boson Decays

From Figs. 7.14 and 7.15 and the previous discussion in Sect. 7.3.1, we expect events containing leptonic W boson decays, such as $W(l\nu)$ +jets, $t\bar{t}$ +jets or single top+jets, to be one of the dominant SM background contributions to the signal regions of the M_{T2} analysis. The contribution of hadronic W boson decays to the signal regions is negligible, as the event does not contain any source of E_T^{miss} , except for jet energy mismeasurements. It is estimated with the method presented in Sect. 7.4. In leptonic events, the neutrino is the source of E_T^{miss} . In our selection criteria, Sect. 7.2.4, we reject any event containing at least one charged lepton in order to reduce this type of SM background. The background remaining after rejecting those events has two sources: either the charged lepton is outside the detector acceptance because it is very soft (low p_T) or pointing to the very forward region of the detector (high $|\eta|$), or the lepton fails to pass the identification or isolation criteria, see Sects. 5.3–5.5. We call these leptons lost.

For both sources, we expect the contribution of events with taus to be slightly higher compared to events with muons or electrons, as the reconstruction efficiency is smaller, and the acceptance requirements are more stringent. The contribution of events with muons and electrons to the lost lepton background are comparable. Note,

that leptonic tau decays are assigned to the electron or muon category, depending on the flavor of the tau decay products.

The amount of events with lost leptons is estimated from a data sample with events containing exactly one charged lepton. For the estimation, we need the lepton reconstruction efficiency ε .

In Fig. 7.20, we see two examples, which show that the shape of the M_{T2} distribution for events with leptonic W boson decays is invariant under the requirement of the lepton to be within acceptance or reconstructed. We, therefore, can define one efficiency ε , describing the probability to reconstruct a lepton within acceptance for an event with leptonic W boson decays. This efficiency combines the identification, isolation and acceptance efficiencies of that lepton.

To first order, the number of all events containing a leptonically decaying W boson, $N_{\rm all}$, can be decomposed into the number of events with the lepton being reconstructed, $N_{\rm all}^{\rm reco} = \varepsilon N_{\rm all}$, and the number of events with the lepton being lost, $N_{\rm all}^{\rm lost} = (1 - \varepsilon) N_{\rm all}$.

There are three points to consider beyond this picture.

The efficiency ε depends on the lepton flavor. For example, the tau identification, as well as the acceptance efficiencies result in a lower efficiency compared to muons or electrons: The total reconstruction efficiency is of order 50–60% for electrons, 60–70% for muons, and 15–30% for taus. These numbers contain the acceptance, which is around 70–75% for electrons and muons, and 45–60% for taus. The efficiencies also depend on the jet multiplicity.

The second point is that there can be non-prompt leptons from heavy-flavor hadron decays, or even fake leptons like a jet faking a hadronic tau signature. The component of non-prompt leptons is usually small, as these leptons are not isolated. However, the contribution of jets faking taus is roughly 20% in the one tau data sample.

Finally, SUSY signals might also have signatures with one lepton. We want as little signal contamination to our data control region as possible. For events, where

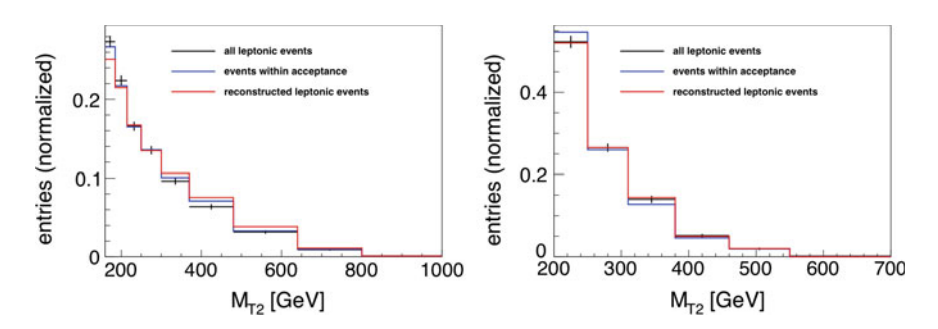


Fig. 7.20 Normalized $M_{\rm T2}$ distribution for simulated events containing a leptonic W boson decay (black), events where the charged lepton is within acceptance (blue), and events where the charged lepton is reconstructed (red). Left for events with one muon, 3-5 jets, 0 b jets, medium $H_{\rm T}$. Right for events with one electron, 3-5 jets, 1 b jet, low $H_{\rm T}$. The black distribution shows the statistical power of the simulation sample

the lepton and the $E_{\rm T}^{\rm miss}$ (coming from a neutrino) originate from a W boson decay, $M_{\rm T} \lesssim M(W)$ with $M_{\rm T}$ constructed out of the lepton- $E_{\rm T}^{\rm miss}$ system, see Eq. (6.1). For SUSY events, this bound does not exist because of the presence of the LSPs. We, therefore, require $M_{\rm T} < 100\,{\rm GeV}$, in order to reduce potential signal contamination to the one lepton data control region.

Figure 7.21 illustrates the $M_{\rm T2}$ distributions in events with one electron, muon, or tau, in data and simulation, for the low and medium + high $H_{\rm T}$ regions and inclusively in all topological regions.

The formula for estimating the lost lepton background from a one lepton data sample is given as

$$N_l^{\text{lost}} = (N_l^{\text{reco}} - N_l^{\text{bg}}) R_{LL} \quad \text{where} \quad R_{LL} = \frac{1 - \varepsilon_l}{\varepsilon_l \varepsilon_{M_T}}.$$
 (7.4)

This formula has to be applied for each lepton flavor separately: $l = e, \mu, \tau$. As we predict the number of lost lepton events, $N_l^{\rm lost}$, from a sample of events with a reconstructed lepton, $N_l^{\rm reco}$, we have to subtract the number of events with non-prompt or fake leptons, $N_l^{\rm bg}$. In addition, the formula has an extra factor $\varepsilon_{M_{\rm T}}$, which is the selection efficiency of the $M_{\rm T} < 100$ GeV criteria applied to the sample with one reconstructed lepton. For events with one electron or muon, $\varepsilon_{M_{\rm T}}$ is of order of

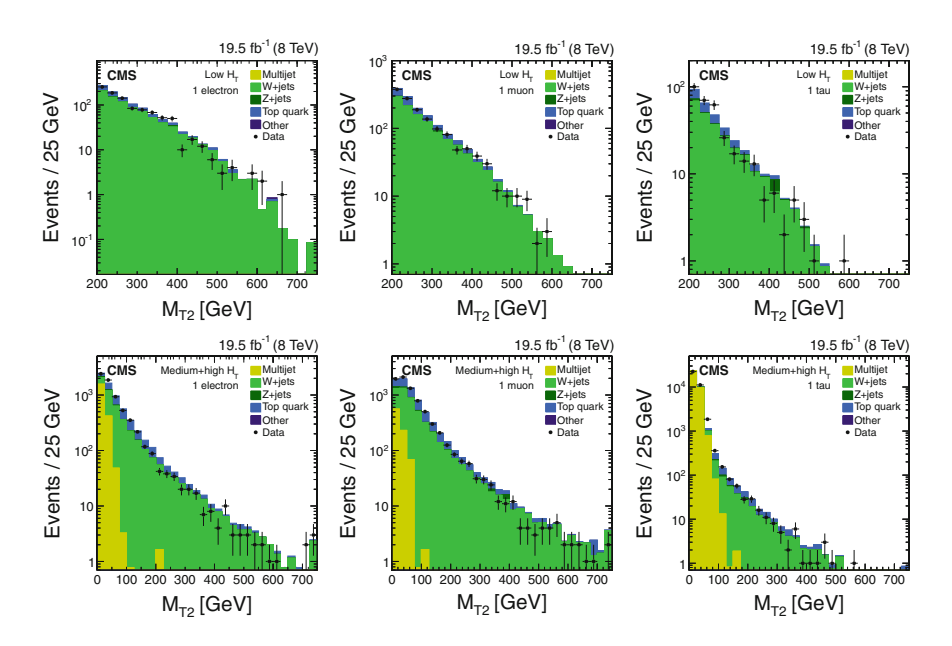


Fig. 7.21 The M_{T2} distributions for events with one reconstructed electron (left), muon (middle), or tau (right) in data and simulation for the low H_T ($top\ row$) and medium + high H_T ($bottom\ row$) selections and ≥ 2 jets. The events are required to pass $M_T < 100\ {\rm GeV}$, where M_T is constructed out of the lepton- \vec{p}_T and $\vec{E}_T^{\rm miss}$. The data correspond to an integrated luminosity of 19.5 fb⁻¹

95%, while for taus it is about 90%. The lower efficiency for taus is expected due to the presence of two tau-neutrinos.

The efficiency ε_{M_T} is taken from simulation: if there is signal contamination to the high M_T region in the one lepton control region, the efficiency measured from data would be too low, leading to an overprediction of this background. Also, the acceptance can be determined only from theory and thus simulation. Besides, a lost lepton can be reconstructed as a jet (if not isolated) or be not clustered (if not passing identification). This leads to a dependency of the event kinematics on how the lepton is lost, which is difficult to determine from data. Therefore, we take ε_l from simulation.

The $\varepsilon_{M_{\mathrm{T}}}$ efficiency is measured in data in a loose selection and compared to simulation. From this study, we assign a relative 5% systematic uncertainty for $\varepsilon_{M_{\mathrm{T}}}$. The reconstruction efficiency ε_{l} has been measured in an orthogonal sample (mainly events containing Z(ll) decays). From this data versus simulation comparison we assign also a relative 5% systematic uncertainty on ε_{l} . The statistical uncertainty on ε because of the limited size of the simulation sample, that has been used to determine ε , is added quadratically to the systematic uncertainty. The systematic uncertainty on the background subtraction has been assessed to be 50% for events with electrons or muons [45], while the mistagging tau rate is known with 20% precision [46].

In the estimate, we have a small contribution of events where two leptons have been lost (that is two leptonic W boson decays, mainly from dileptonic $t\bar{t}$ +jets). These events amount to about 3% of the total lost lepton background. Also, the one lepton data control sample contains events with two leptons, but where one of them has been lost. The lost lepton events in our data control regions (dileptonic $t\bar{t}$ +jets with one lost lepton), to some extent, predict the double lost lepton contribution to the signal regions (dileptonic $t\bar{t}$ +jets with two lost leptons). However, the efficiency ε_{M_T} is expected to be lower in the dileptonic case, as there are two neutrinos present, and efficiency ε_l can be different as the efficiencies of the two leptons are usually correlated. We choose the difference between our estimation of the double lost lepton events and the prediction from simulation as systematic uncertainty.

In principle, this method can be applied in every signal region. However, we see in Fig. 7.21 that the data yield at high M_{T2} is very scarce. A reliable estimate for signal regions with high M_{T2} is not possible. We modify the estimation strategy as follows:

- The data event yields for all signal regions along M_{T2} in a given $H_T \times N_j \times N_b$ region are summed up. The estimate, using Eq. (7.4), is performed in these summed regions.
- The shape of all M_{T2} distributions is extracted from simulation. These shapes are used to split the estimated lost lepton yields in order to obtain the prediction for all individual signal regions in $M_{T2} \times H_T \times N_j \times N_b$.

In Fig. 7.22, the values R_{LL} are reported for all lepton flavors, H_T and topological regions.

The modified approach leads to robust estimates in all signal regions, even for high M_{T2} . But it comes at the expense of an additional modeling uncertainty. We

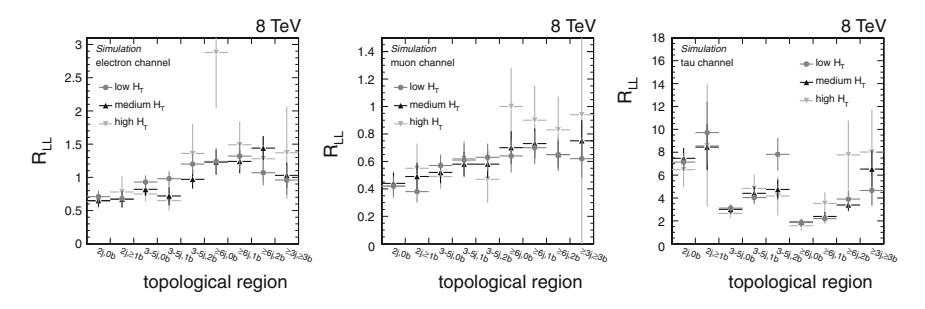


Fig. 7.22 Values of R_{LL} for all topological regions and the three H_T regions. Left for electrons, center for muons, and right for taus

assign the uncertainty on the modeling of the M_{T2} distributions by varying several modeling parameters, namely:

- System recoil [47]: It has been observed that the p_T of the hard process (such as the W boson- p_T or $t\bar{t}$ pair- p_T) is not correctly modeled in simulation, likely due to NLO effects such as ISR. The simulation is corrected for this mismodeling, and the method from [47] is used to assign the uncertainty.
- W+jets and $t\bar{t}$ +jets cross section: The associated uncertainty changes the relative contribution between the two processes; the total combined cross section is determined from the data in the control regions. For $t\bar{t}$ +jets, the cross section is varied by 7% [48], for W+jets by 5% [49]. For events containing b jets, the W+jets cross section is less well known, and the cross section is varied by 50%.
- Renormalization and factorization scale: These two scales are varied by a factor 2 using dedicated simulation samples.
- Matching scale: This scale is varied by a factor 2 using dedicated simulation samples.
- Top mass: The top mass is varied by 5 GeV within the simulation using dedicated samples.
- B-tagging efficiency: It is known that the simulation does not perfectly model the b-tagging discriminator values. The efficiency in simulation is corrected to match the one observed in data [50]. The uncertainty on this scale factor is taken into account.
- Pileup interactions: The number of pileup interactions within a bunch crossing in simulation is reweighted to match the one in data. The number of pileup interactions depends on the instantaneous luminosity and the total cross sections. The uncertainty is obtained by varying the minimum bias cross section by 5%. This leads to different event weights for the simulation.
- Jet energy scale: The jet energy scale is varied by its uncertainty [51]. All variables affected by the change in the transverse momenta of the jets, such as H_T or M_{T2} , are recomputed.

• Unclustered $E_{\rm T}^{\rm miss}$ scale: The energy, which is not clustered into jets, still contributes to the determination of $E_{\rm T}^{\rm miss}$. The unclustered energy is varied by 10%, and all event variables are recomputed.

Out of these parameters, the dominating uncertainty sources are the renormalization, factorization, matching, and jet energy scales and the system recoil. An example of a shape uncertainty is shown in Fig. 7.23, varying the system recoil in events with 2 jets, 0 b jets, and medium H_T .

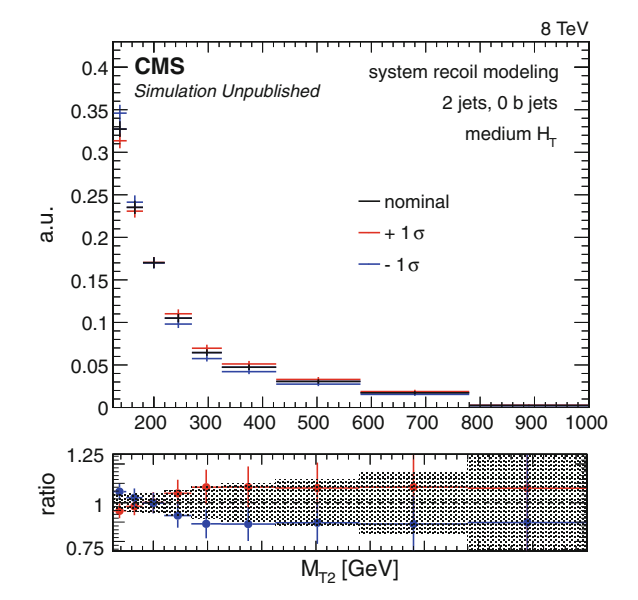
We want to verify the correct modeling of the M_{T2} shape in simulation using data. We apply two relaxed selections:

- First, we combine all $H_{\rm T}$ and jet multiplicity regions together (≥ 2 jets as well as $H_{\rm T} \geq 450\,{\rm GeV}$, $E_{\rm T}^{\rm miss} \geq 200\,{\rm GeV}$ or $H_{\rm T} \geq 750\,{\rm GeV}$), but we keep three b-jet multiplicity regions (0, 1, or ≥ 2 b jets). These three regions are binned in $M_{\rm T2}$ using the $M_{\rm T2}$ signal region definition of the corresponding 3-5 jets, medium $H_{\rm T}$ regions, see Table 7.1.
- For the second selection, we combine the $H_{\rm T}$ and b-jet multiplicity regions, but keep the three jet multiplicity regions. We bin the $M_{\rm T2}$ distributions according to the corresponding 0 b jet, medium $H_{\rm T}$ regions, see Table 7.1.

We apply the lost lepton prediction method to these validation regions and examine the agreement between the data estimations and the predictions from simulation. The agreement is quantified by defining the *Pull* for each validation region in $M_{T2} \times N_i(N_b) \times \text{lepton flavor}$:

$$Pull = \frac{N_{\text{obs}} - N_{\text{pred}}}{\sqrt{\sigma_{\text{obs}}^2 + \sigma_{\text{pred}}^2}},$$
(7.5)

Fig. 7.23 Normalized M_{T2} distribution for 2 jets, 0 b jets, medium H_T , together with the M_{T2} distributions after reweighting the hard process recoil by its uncertainty ($\pm 1\sigma$). These distributions are used, among others, to assess the uncertainty on the shape of the M_{T2} distributions for the lost lepton background estimation



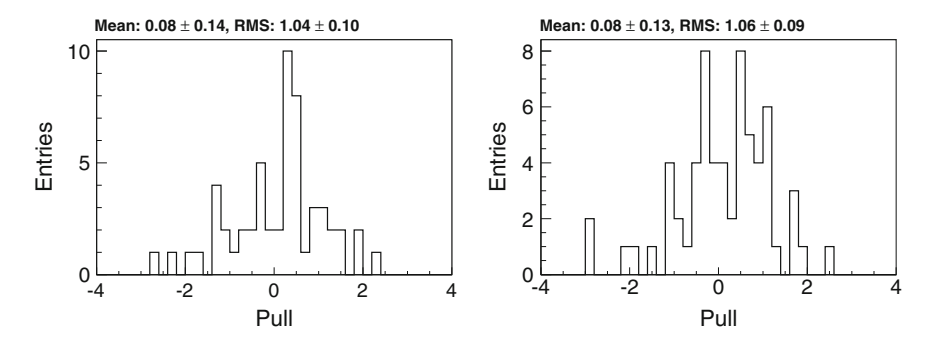


Fig. 7.24 Pull distribution for the first (left) and second (right) validation region selection

where $N_{\rm obs}$ is the estimated yield using the (*observed*) data with its uncertainty $\sigma_{\rm obs}$, and $N_{\rm pred}$ is the prediction using simulation with its uncertainty $\sigma_{\rm pred}$. For a correct modeling, we expect the mean of the pull distribution to be at zero, and its spread (*RMS*) to be one. Figure 7.24 shows the pull distributions for the two selections. We verified, that the $M_{\rm T2}$ shape is reasonably well modeled in simulation.

The results of the lost background prediction can be found in Sect. 7.7, together with the results of the other estimation methods.

7.6 Prediction of the Background Due to Z Boson Decays into Neutrinos

The SM background of events involving Z boson decays into neutrinos is irreducible. Among the main three background categories, this one results in the most SUSY-like event signature. A robust and precise estimation method is crucial.

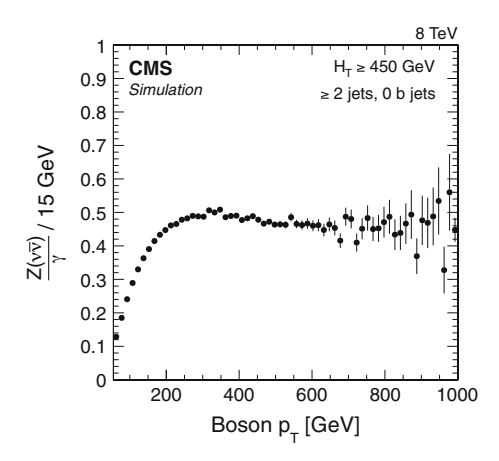
We use a method that is based on a $\gamma+{\rm jets}$ data control sample. The basic idea of the background estimation method is the following: If we treat the photon as if it was not in the event, the event will have the same signature as if there was a Z boson that decayed into two neutrinos. Therefore, we will select $\gamma+{\rm jets}$ events, substitute the $\vec{E}_{\rm T}^{\rm miss}$ by $\vec{E}_{\rm T}^{\rm miss}+\vec{p}_{\rm T}^{\gamma}$, remove the photon from the visible object list, and recompute all event quantities such as $M_{\rm T2}$. Then, the event yields in the $\gamma+{\rm jets}$ control regions are scaled to predict the $Z(\nu\overline{\nu})+{\rm jets}$ event yields in our signal regions.

First, I restrict the discussion to the case of 0 b jets. For events with ≥ 1 b jets, the method is slightly modified.

Prediction of the $Z(\nu \overline{\nu})$ +Jets Background in the 0 b-Jet Signal Regions

The production processes of Z+jets and γ +jets events are similar, they involve the same diagrams. But differences occur because of different coupling factors (see diagrams on p. 5) and the Z boson mass. If the boson- p_T is much larger than the Z boson mass, the ratio of the number of Z+jets events versus the number of γ +jets events

Fig. 7.25 Ratio of the number of $Z(\nu\overline{\nu})+{\rm jets}$ events versus the number of $\gamma+{\rm jets}$ events as a function of the boson- $p_{\rm T}$, obtained from simulation. Events passing $H_{\rm T} \geq 450\,{\rm GeV}, \geq 2$ jets, and 0 b jets are selected. The $Z(\nu\overline{\nu})/\gamma$ ratio is basically flat for boson- $p_{\rm T} > 350\,{\rm GeV}$



will be essentially flat, as it is only determined by the boson-quark couplings [52]. This is illustrated in Fig. 7.25, where only Z boson decays into neutrinos are considered. Therefore, one can predict the $Z(\nu\bar{\nu})+$ jets background in the signal regions using $\gamma+$ jets data.

The selection of photons, see Sect. 5.6, includes prompt photon production via direct production as well as parton-to-photon fragmentation, which is small for large $p_{\rm T}^{\gamma}$ [53]. Also non-prompt photons, mainly from neutral meson decays (like $\pi^0 \to \gamma \gamma$), are part of the photon selection. These mesons are produced in jets. If their boost is high enough, the two photons are so close to each other that they are reconstructed as a single photon. While the isolation criteria of the photon selection strongly reduces the non-prompt photon contribution, the purity of prompt photons within the reconstructed photon selection needs to be determined.

The background prediction method can be described as

$$N_{Z(\nu\overline{\nu})} = N_{\gamma}^{\text{data}} \cdot R(Z(\nu\overline{\nu})/\gamma) \cdot P, \tag{7.6}$$

where $N_{Z(\nu\overline{\nu})}$ is the estimated number of $Z(\nu\overline{\nu})$ +jets events in the respective signal region, N_{γ}^{data} the number of γ +jets events in data, $R(Z(\nu\overline{\nu})/\gamma)$ is the $Z(\nu\overline{\nu})/\gamma$ ratio from simulation, and P is the purity factor of prompt photons within the reconstructed photon selection.

This equation can also be restated as

$$N_{Z(\nu\overline{\nu})} = \left(N_{\gamma}^{\text{data}} - N_{\gamma}^{\text{non-prompt}}\right) R(Z(\nu\overline{\nu})/\gamma) \tag{7.7}$$

with $N_{\gamma}^{\text{non-prompt}}$ being the number of events containing a non-prompt photon.

The data need to be selected by triggers, which are not based on a $E_{\rm T}^{\rm miss}$ selection, as $p_{\rm T}^{\gamma}$ plays the role of $E_{\rm T}^{\rm miss}$ for the $\gamma+{\rm jets}$ event selection. For the medium and high $H_{\rm T}$ selection, one can use the signal trigger. For the low $H_{\rm T}$ region, we use a trigger

based on a selection of one high- $p_{\rm T}$ photon, as described in Sect. 7.1. The photon needs to pass $p_{\rm T}^{\gamma} > 180\,{\rm GeV}$ in this $H_{\rm T}$ region.

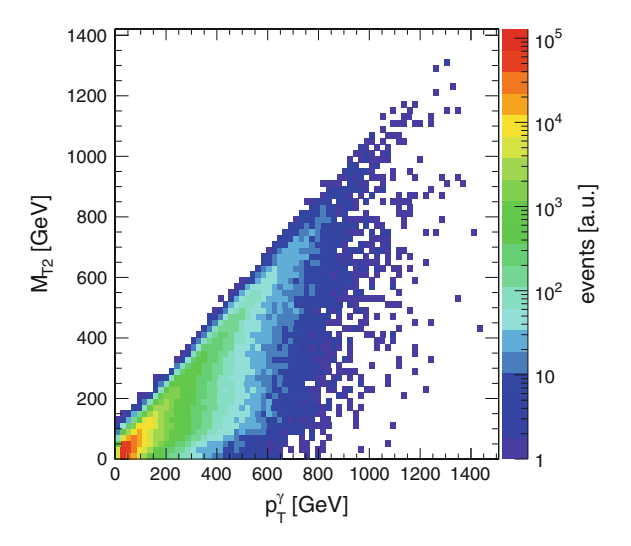
For events in the γ +jets control region, we require $E_{\rm T}^{\rm miss}<100\,{\rm GeV}$ before adding $\vec{p}_{\rm T}^{\gamma}$ to $\vec{E}_{\rm T}^{\rm miss}$. With this requirement we limit potential signal contamination to the data control sample.

After selecting the γ +jets events, we need to determine the prompt photon purity within the data control sample. In simulation, prompt photons are modeled by the γ +jets simulation samples, while non-prompt photons are modeled by the multijet simulation sample. For the latter sample, we need an additional requirement: through the parton shower, this sample includes prompt photon production from ISR and FSR. Events containing such a photon, namely a photon radiated of a parton, are rejected in the multijet simulation sample for this estimation.

In data, we estimate the purity using the distribution of the $\sigma_{i\eta i\eta}$ variable of all photon candidates. As stated in Sect. 5.6, the $\sigma_{i\eta i\eta}$ variable describes the shape of the electromagnetic shower: We expect a narrow shower for a single prompt photon, and therefore low values of $\sigma_{i\eta i\eta}$, while for two close-by photons from a neutral meson decay, which are reconstructed as a single photon, we expect high values of $\sigma_{i\eta i\eta}$ as the shower is wider.

In order to estimate the prompt photon purity, we select photons without any requirement on $\sigma_{i\eta i\eta}$. We build two templates of the $\sigma_{i\eta i\eta}$ distribution: one for prompt photons, the other for non-prompt photons. Both templates are created using simulation. As the non-prompt photon component rapidly decreases with $p_{\rm T}^{\gamma}$, the $\sigma_{i\eta i\eta}$ templates are done inclusively for all $p_{\rm T}^{\gamma}$, but separately for each $H_{\rm T}$ and topological region. The value of $M_{\rm T2}$ is driven by $p_{\rm T}^{\gamma}$ because of the correlation between $M_{\rm T2}$ and $E_{\rm T}^{\rm miss} \sim p_{\rm T}^{\gamma}$, see Sect. 6.3. This can also be appreciated from Fig. 7.26. Therefore, the purity is determined also inclusively in $M_{\rm T2}$.

Fig. 7.26 Correlation between M_{T2} and p_T^{γ} in simulated γ +jets events



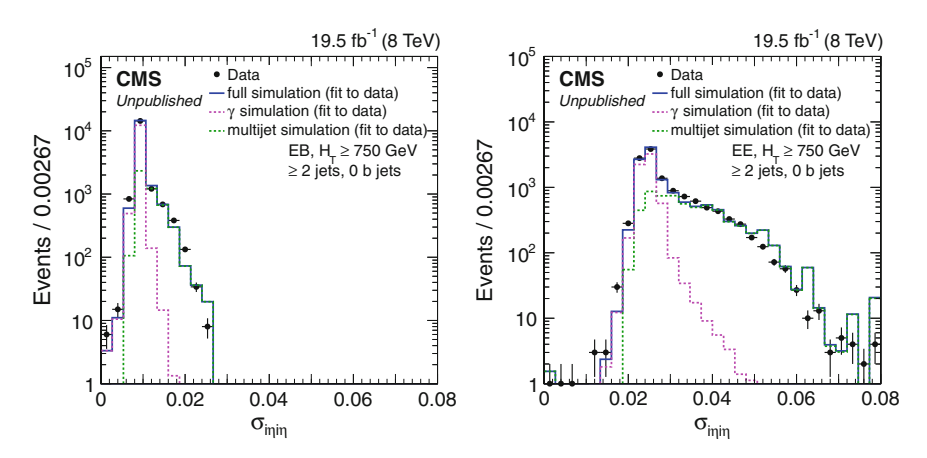


Fig. 7.27 Illustration of the purity fit. The prompt photon template (dashed pink line) and non-prompt photon template (dashed green line) are fitted to the $\gamma+$ jets data (black points) in the $\sigma_{i\eta i\eta}$ variable. The combined fitted template distribution is the blue line. The fit is performed separately for photons measured by the ECAL barrel (left) and by the ECAL endcaps (right). The selection for these plots is $H_T \geq 750\,\text{GeV}, \geq 2\,\text{jets}$, and 0 b jets

The templates are fitted to the $\sigma_{i\eta i\eta}$ distribution observed in data using an extended maximum likelihood fit. The purity fits are performed separately for photons measured by the ECAL barrel and photons measured by the ECAL endcaps, as the prompt photon discrimination power is different for the two detector regions. In Fig. 7.27, the fit is illustrated for an inclusive selection of $H_T \geq 750 \, \text{GeV}$, $\geq 2 \, \text{jets}$, 0 b jets. We observe an overall purity, combined for photons measured by the ECAL endcaps and barrel, of order 75 %.

For the low $H_{\rm T}$ region, we need to require $p_{\rm T}^{\gamma} \ge 180\,{\rm GeV}$ because of the trigger selection. In this boosted regime, the non-prompt photons from neutral meson decays are so collimated that they are indistinguishable from prompt photons. We use the fit results of the medium and high $H_{\rm T}$ regions and extrapolate in $p_{\rm T}^{\gamma}$ to obtain the purity in the low $H_{\rm T}$ region.

The M_{T2} distribution for $\gamma+$ jets events are compared between data and simulation in Fig. 7.28. The \vec{p}_T^{γ} is added to the \vec{E}_T^{miss} , and all event variables are recomputed. The simulated events are reweighted by factors obtained from the purity fits. We observe that the purity increases with M_{T2} : For example, the prompt photon purity is about 95% for $M_{T2} > 100$ GeV. We use simulation to model the purity dependence on M_{T2} : We perform the background prediction using Eq. (7.7), and take $N_{\gamma}^{\text{non-prompt}}$ from simulation after scaling the simulation according to the results of the prompt photon purity fits.

Besides $N_{\gamma}^{\text{non-prompt}}$, we need to determine $R(Z(\nu\overline{\nu})/\gamma)$.

We previously argued that the $Z(\nu\overline{\nu})/\gamma$ ratio can be calculated by theory. We use simulation to obtain $R(Z(\nu\overline{\nu})/\gamma)$ within our selection. The advantage of using simulation is that we also correct for the photon acceptance and reconstruction efficiency.

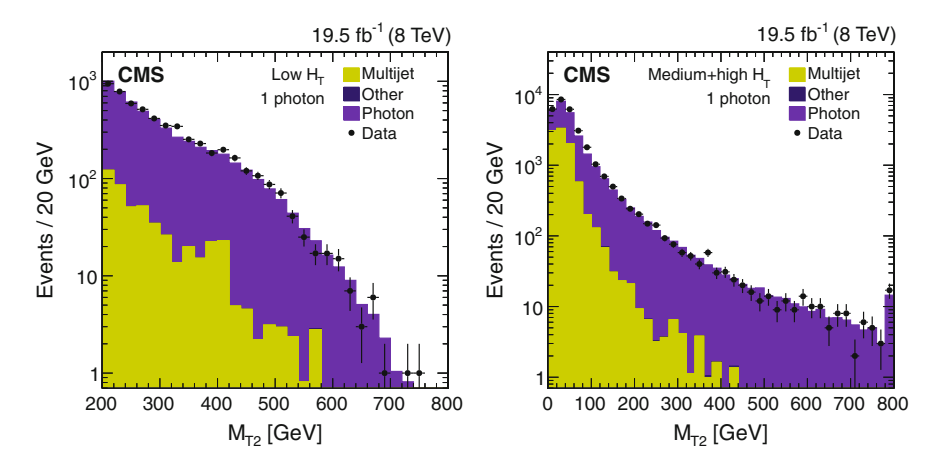


Fig. 7.28 The M_{T2} distribution for γ +jets events in data and simulation after adding \vec{p}_T^{γ} to \vec{E}_T^{miss} and recomputing all event variables. Left for the low H_T selection, ≥ 2 jets, and 0 b jets. Right for the medium + high H_T selection, ≥ 2 jets, and 0 b jets

If we use simulation, we need to verify the modeling of $R(Z(\nu\overline{\nu})/\gamma)$ in simulation. We actually can access the properties of the Z boson in data using $Z \to l^+ l^-$ decays. We select events containing one e^+e^- or $\mu^+\mu^-$ pair using the dileptonic triggers described in Sect. 7.1. We require the invariant mass of the two leptons to be $76 \le M_{ll} \le 106\,\text{GeV}$ in order to select events containing Z boson decays. We add the transverse momenta of the two leptons to $E_{\mathrm{T}}^{\mathrm{miss}}$ in order to mimick a Z boson decay into neutrinos. For this study, we also select photons with the photon- H_{T} trigger, described in Sect. 7.1.

The modeling of the Z/γ ratio is independent of the Z boson decay except for the rate difference due to the branching ratios of the Z boson decay. Therefore, we can use the $Z(ll)/\gamma$ ratio to compare simulation and data, and assign uncertainties on the $Z(\nu\bar{\nu})/\gamma$ ratio. However, one should realize that the selected dileptonic events contain also a contribution from $\gamma^* \to l^+ l^-$. No corresponding contribution of γ^* decays into neutrinos exists. We use the dileptonic data events only for assigning uncertainties to $R(Z(\nu\bar{\nu})/\gamma)$, and not for correcting the value of $R(Z(\nu\bar{\nu})/\gamma)$ in simulation.

We study the $Z(ll)/\gamma$ ratio for different kinematic selections and as a function of our search variables $M_{\rm T2}$, $H_{\rm T}$, number of jets, as well as the boson- $p_{\rm T}$. In Fig. 7.29, the $M_{\rm T2}$ distributions of Z(ll)+jets events and γ +jets events in data and simulation are shown for $H_{\rm T} \geq 450~{\rm GeV}$, $\geq 2~{\rm jets}$, 0 b jets, and boson- $p_{\rm T} \geq 80~{\rm GeV}$. The figure also contains the $Z(ll)/\gamma$ ratios in data and simulation.

²This rate difference is the reason, why Z(ll)+jets data are not used directly to predict the $Z(\nu \overline{\nu})$ +jets yield.

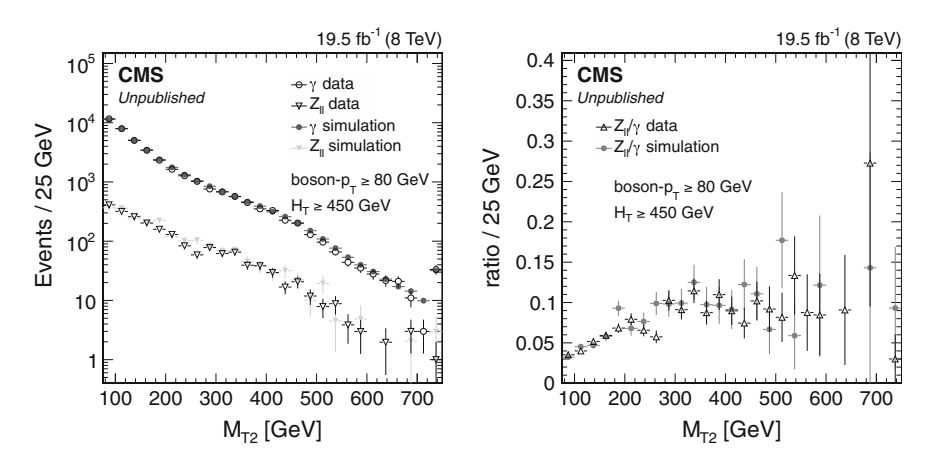


Fig. 7.29 Left The $M_{\rm T2}$ distributions of Z(ll)+jets events and γ +jets events in data and simulation for $H_{\rm T} \geq 450~{\rm GeV}, \geq 2~{\rm jets}, 0~{\rm b}$ jets, and boson- $p_{\rm T} \geq 80~{\rm GeV}$. Right The corresponding $Z(ll)/\gamma$ ratios in data and simulation

The result of these studies is, that we can verify the agreement between data and simulation $Z(ll)/\gamma$ within 20%.³

Let me summarize the methodology for the $Z(\nu\overline{\nu})+$ jets background prediction for the signal regions with 0 b jets. We obtain the prompt photon purity (or the number of events containing non-prompt photons) by performing a template fit in the $\sigma_{i\eta i\eta}$ distribution. The ratio $R(Z(\nu\overline{\nu})/\gamma)$ is obtained in simulation and verified in data comparing the event yields of Z(ll)+jets and $\gamma+$ jets. The number of $Z(\nu\overline{\nu})+$ jets events in each signal region is predicted by using the yields of $\gamma+$ jets data in the corresponding control region, and scale them as stated in Eq. (7.7).

Besides the statistical uncertainty of the $\gamma+{
m jets}$ data sample, the systematic uncertainties are:

- A 20% uncertainty on $R(Z(\nu\overline{\nu})/\gamma)$ from the studies of the $Z(ll)/\gamma$ ratio in data and simulation. As the statistical size of the Z(ll)+jets data sample is limited at high M_{T2} , this uncertainty is increased to 30% for $M_{T2} \geq 350 \,\text{GeV}$.
- Uncertainty on $R(Z(\nu\overline{\nu})/\gamma)$ due to the statistical limitations of the $Z(\nu\overline{\nu})$ +jets and γ +jets simulation samples. This uncertainty is negligible compared to the previous one for most signal regions.
- Uncertainty on the prompt photon purity fits, which results in a 5–10 % uncertainty for subtraction of the non-prompt photon contribution to the γ +jets sample.
- Uncertainty on the non-prompt photon subtraction because of the statistical limitation of the multijet simulation sample.

³Note, that CMS has measured the ratio $Z(ll)/\gamma$ in a looser selection [54]. The ratio in simulation differs with respect to the ratio in data by roughly 15 %. This measurement was performed in parallel to this search, and the authors of both analyses had been in contact.

Prediction of the $Z(\nu \overline{\nu})$ +Jets Background in b-Jet Enriched Signal Regions

It has been pointed out, for example in [55, 56], that there are differences observed between data and simulation in Z+jets events, where at least one jet has been identified as a b jet. The authors speculate that the reason for this difference might be in the treatment of b quarks in the simulation, such as assuming b quarks to be massless quarks, or the choice of the number of quark flavors considered in the parton densities of the proton. A similar study is missing for photon data. However, we conclude that it is not safe to apply the previous method directly for the b-jet enriched case.

Other common data-driven methods, used to predict the $Z(\nu\overline{\nu})+$ jets background, are not practicable either: A data-driven method using $W(l\nu)+$ jets data and the $Z\leftrightarrow W$ correspondence cannot be used as the b-jet enriched data have a too large contribution of $t\overline{t}+$ jets. Also, the data-driven method using Z(ll)+ jets events cannot be used because of statistical limitations of the Z(ll)+ jets data sample.

We use instead a hybrid method, which is applied to all signal regions containing one b jet.

- We apply the previous method using γ +jets data for the signal region definitions with one b jet. However, we revert the b-jet requirement and select 0 b jets.
- Then, we construct the ratio $Z_{ll}(1b)/Z_{ll}(0b)$, the ratio between the numbers of events containing Z boson decays to e^+e^- or $\mu^+\mu^-$, and 1 b jet or 0 b jets, respectively. This ratio is used to scale the estimate, obtained from events containing no b jets, to predict the number of $Z(\nu\overline{\nu})$ +jets events in the one b-jet region.

Z(ll)+jets events are kinematically not different from the $Z(\nu\overline{\nu})$ +jets events. Therefore, the scaling will result in the correct prediction for the one b-jet region without a bias. No theoretical uncertainties are introduced, as the Z(ll)+jets event sample is obtained in data.

This hybrid method has the advantage of using a high statistics sample, the γ +jets data sample, but also keeping the theoretical uncertainties under control, since $R(Z(\nu \overline{\nu})/\gamma)$ is obtained within a 0 b-jet selection. We avoid the statistical limitation of the Z(ll)+jets control sample by constructing the ratio $Z_{ll}(1b)/Z_{ll}(0b)$ inclusively for multiple signal regions instead of separately for every signal region. For this, we need to show that the ratio is stable against our signal region definitions.

The ratio $Z_{ll}(1b)/Z_{ll}(0b)$ as a function of M_{T2} is shown in Fig. 7.30 for events with $H_T \ge 450 \,\text{GeV}$, Z boson- $p_T \ge 80 \,\text{GeV}$, and at least two jets. It is observed that the ratio is flat as a function of M_{T2} . The $Z_{ll}(1b)/Z_{ll}(0b)$ ratio is also flat as a function of H_T , but not as a function of N_i , see Fig. 7.31.

The stability is also tested for more exclusive selections on H_T , M_{T2} , jet multiplicity, and for different requirements on the Z boson- p_T . For all tested selections, we find that the ratio is flat as a function of H_T and M_{T2} , but scales linearly as a function of N_j . The increase with the jet multiplicity is expected, as the phase space for b-quark jets increases with N_j . Therefore, we can extract the $Z_{ll}(1b)/Z_{ll}(0b)$ ratio for an inclusive selection on M_{T2} and H_T , but separately for the different jet multiplicity selections. The $Z_{ll}(1b)/Z_{ll}(0b)$ ratio, as a function of M_{T2} , is fitted with a constant for an inclusive selection on H_T and boson- $p_T \ge 20$ GeV. The estimate

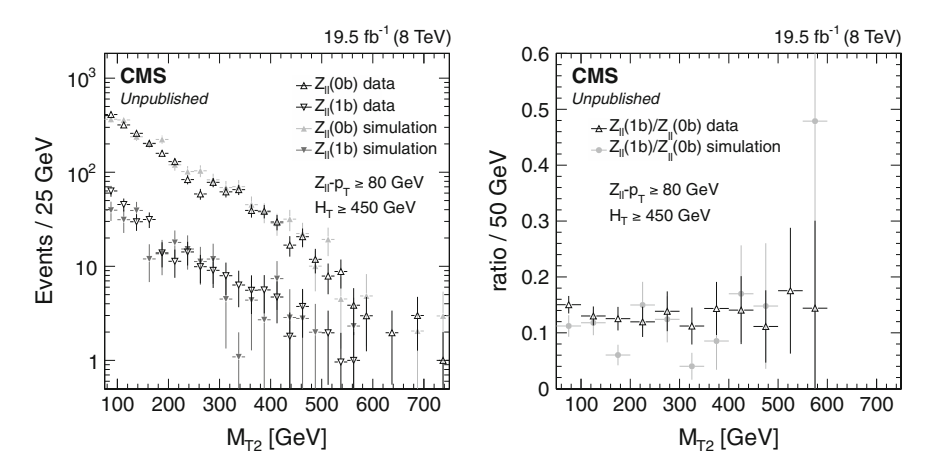


Fig. 7.30 Left Distribution of M_{T2} for Z(ll)+jets events in data and simulation with $H_T \ge 450 \,\text{GeV}$, $Z \,\text{boson-}p_T \ge 80 \,\text{GeV}$ and 0 b jets or 1 b jet, respectively. Right Corresponding ratio $Z_{ll}(1b)/Z_{ll}(0b)$

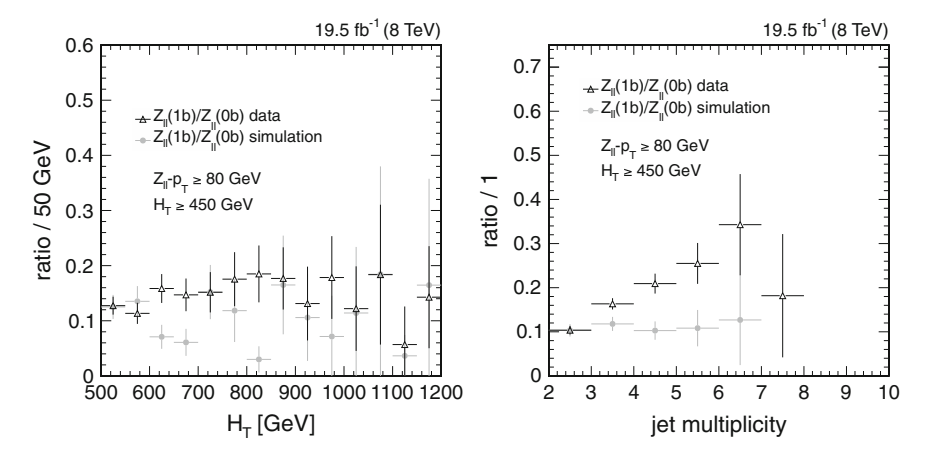


Fig. 7.31 The ratio $Z_{ll}(1b)/Z_{ll}(0b)$ for Z(ll)+jets events in data and simulation with $H_T \ge 450 \, \text{GeV}$, Z boson- $p_T \ge 80 \, \text{GeV}$. Left Ratio $Z_{ll}(1b)/Z_{ll}(0b)$ as a function of H_T , Right Ratio $Z_{ll}(1b)/Z_{ll}(0b)$ as a function of the jet multiplicity. The different behavior of the ratio for data and simulated events in the right plot is not fully understood, see also the discussion at Fig. 7.32

of the γ +jets data for 0 b jets is scaled with this constant in order to obtain the prediction for the 1 b-jet region.

For low N_j (2 jets and 3-5 jets), there is enough data to obtain the ratio $Z_{ll}(1b)/Z_{ll}(0b)$ separately, but not for the high N_j selection (≥ 6 jets). We extrapolate the $Z_{ll}(1b)/Z_{ll}(0b)$ ratio from the low jet multiplicities by fitting the $Z_{ll}(1b)/Z_{ll}(0b)$ ratio as a function of the jet multiplicity with a linear function, as exemplified in Fig. 7.32.

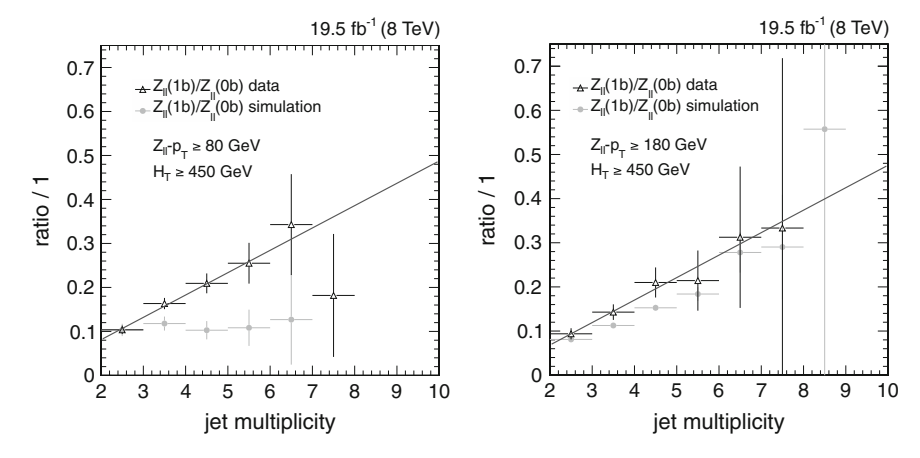


Fig. 7.32 The ratio $Z_{ll}(1b)/Z_{ll}(0b)$ for Z(ll)+jets events as a function of the jet multiplicity in data and simulation with $H_T \geq 450$ GeV, together with a linear fit (*solid line*). Left for Z boson- $p_T \geq 80$ GeV, Right for Z boson- $p_T \geq 80$ GeV. The flat behavior in the simulation for Z boson- $p_T \geq 80$ GeV is not fully understood. Defining the ratio $Z_{ll}(1b)/Z_{ll}(0b)$ using all b-quark jets, as created by the generator program, results in a linear (non-flat) behavior of the ratio as a function of the jet multiplicity. Also, using the high statistics simulation sample for boson- $p_T \geq 180$ GeV (right figure) does not show a flat behavior in the ratio using simulated events

The uncertainties on the $Z_{ll}(1b)/Z_{ll}(0b)$ ratios are comprised of

- the statistical precision of the constant fit to the $Z_{ll}(1b)/Z_{ll}(0b)$ distribution. For the ≥ 6 jet selection, the fit uncertainties on both the constant and the slope are taken into account.
- the difference in the fit due to the background subtraction: We expect a little contribution from $t\bar{t}$ +jets events for the dileptonic selection. This contribution is subtracted using simulation and is validated in $e^{\pm}\mu^{\mp}$ data. The subtraction is varied by 100% and the difference is taken as uncertainty. This uncertainty is small.
- uncertainties due to the kinematic selection: We perform the constant fit for more exclusive selections such as $H_T \ge 750 \,\text{GeV}$ or Z boson- $p_T \ge 180 \,\text{GeV}$, and the differences observed contribute to the uncertainties for the medium and high H_T or the low H_T selection, respectively.
- the uncertainty on the average jet multiplicity for the ≥6 jets region, which determines the scaling factor. The average number of jets in data has been found to be 6.12 ± 0.06.
- the statistical precision for the ≥ 6 jets selection, expected if the $Z_{ll}(1b)/Z_{ll}(0b)$ ratio would have been fitted as a function of M_{T2} .

Table 7.3 summarizes the scaling factors and their uncertainties, obtained from the fits on the $Z_{ll}(1b)/Z_{ll}(0b)$ ratios.

Prediction for signal regions with multiple b jets: The hybrid method, as described above, cannot be applied for events with ≥ 2 b jets. The main reason

	Fitted $Z_{ll}(1b)/Z_{ll}$	(0b) ratios	
Jet multiplicity	Low H _T	Medium H _T	High H _T
2 jets	0.093 ± 0.022	0.093 ± 0.050	0.093 ± 0.060
3-5 jets	0.162 ± 0.024	0.162 ± 0.018	0.162 ± 0.030
≥6 jets	0.269 ± 0.168	0.269 ± 0.143	0.269 ± 0.201
The feeters are used	to cools the out jets activ	note from the 0 h jet to	1 h jet selection For the 2 jet

Table 7.3 Factors from fits to the $Z_{ll}(1b)/Z_{ll}(0b)$ ratios and their uncertainties

The factors are used to scale the γ +jets estimate from the 0 b-jet to 1 b-jet selection. For the 2 jet selection, 1 b jet implicitly means \geq 1 b jets

is that the contribution of $t\bar{t}$ +jets events becomes dominant for the dileptonic event selection. Furthermore, the statistical power is very weak for a selection with at least 2 b jets. The $Z(\nu\bar{\nu})$ +jets background is predicted using simulation. The uncertainty is set to 100%. As the $Z(\nu\bar{\nu})$ +jets contribution is small compared to $t\bar{t}$ +jets for events with ≥ 2 b jets, the choice of the uncertainty has no measurable influence. It has been tested that changing the uncertainty by a factor 3 does not affect the interpretations, presented in Sect. 7.8.2. We validate the Z+jets simulation by comparing data and simulation in $e^+e^-/\mu^+\mu^-+$ jets events for a selection of $H_T \geq 450$ GeV, ≥ 2 jets, and ≥ 2 b jets. We see an overall data-simulation agreement within the statistical precision for the M_{T2} and M_U distributions, shown in Fig. 7.33.

Summary of the Estimation Methods for the $Z(\nu \overline{\nu})$ +Jets Background

For events with 0 b jets, the $Z(\nu\overline{\nu})+{\rm jets}$ background is predicted using $\gamma+{\rm jets}$ data. The $Z(\nu\overline{\nu})/\gamma$ ratio is obtained from simulation. The simulation is validated using the $Z(ll)/\gamma$ ratios in data and simulation. The prompt photon purity of the photon selection is obtained by a template fit to the $\gamma+{\rm jets}$ data in the σ_{inin} distribution.

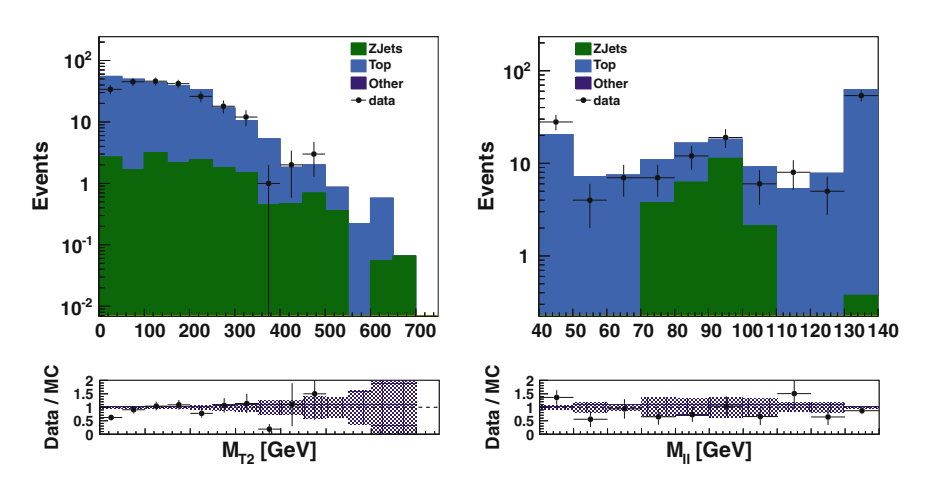


Fig. 7.33 The M_{T2} distribution (*left*) and the M_{ll} distribution after $M_{T2} > 100 \,\text{GeV}$ (*right*) in data and simulation events containing a $\mu^+\mu^-$ or e^+e^- pair, ≥ 2 b jets, and $H_T \geq 450 \,\text{GeV}$

A hybrid method is applied for events containing one b jet. The above method is applied, with the exception that still zero b jets are required. The predicted yield is then scaled by values obtained from the $Z_{ll}(1b)/Z_{ll}(0b)$ ratios. The ratios are obtained in data using the numbers of events containing Z boson decays into e^+e^- or $\mu^+\mu^-$, as well as 0 b jets and 1 b jet, respectively. The stability of this ratio is tested against the signal region variables. It has been found that the $Z_{ll}(1b)/Z_{ll}(0b)$ ratios are flat as a function of M_{T2} and H_T , but scale linearly with the number of jets. Therefore, the scaling factor is obtained inclusively in M_{T2} and H_T , but separately for the jet multiplicity regions.

The $Z(\nu\overline{\nu})+{\rm jets}$ background is taken from simulation for signal regions that require at least two b jets. The simulation is validated in data using $e^+e^-/\mu^+\mu^-+{\rm jets}$ events.

The results of the $Z(\nu \overline{\nu})$ +jets background prediction are shown in Sect. 7.7, together with the results of the other estimation methods.

7.7 Results

The background prediction methods have been described in Sects. 7.4–7.6. For each signal region, the yields of the three prediction methods are summed up and then compared to data yield. Figures 7.34, 7.35 and 7.36 show the $M_{\rm T2}$ distributions for all $H_{\rm T} \times N_{\rm j} \times N_{\rm b}$ regions in data corresponding to 19.5 fb⁻¹. The predicted yields of each background component are also shown and stacked on top of each other. The combined uncertainties are shown as shaded bands.

In Table 7.4, the combined background prediction and the data yields for all signal regions are given. The uncertainties are the quadratic sum of the uncertainties of all background estimations.

The compability of the data event counts with the results of the background estimates is tested by making the pull distributions, where the pull for each signal region (in M_{T2} , H_T , N_j , and N_b) is defined by Eq. (7.5), repeated here:

$$Pull = \frac{N_{\text{obs}} - N_{\text{pred}}}{\sqrt{\sigma_{\text{obs}}^2 + \sigma_{\text{pred}}^2}}.$$

The data yields and the associated statistical uncertainties are $N_{\rm obs}$ and $\sigma_{\rm obs}$, and $N_{\rm pred}$ denotes the results of the summed background estimates with uncertainties $\sigma_{\rm pred}$.

The pull distribution is shown in Fig. 7.37. The observed mean value of this distribution is 0.26 ± 0.07 with an r.m.s. of 0.81 ± 0.05 .

The compatibility of the data and the data-driven background predictions is studied by simulating *pseudodata*. The pseudodata are distributed in each signal region according to a Poissonian distribution with the mean being the result of the background predictions, and then smeared by a Gaussian distribution with the standard

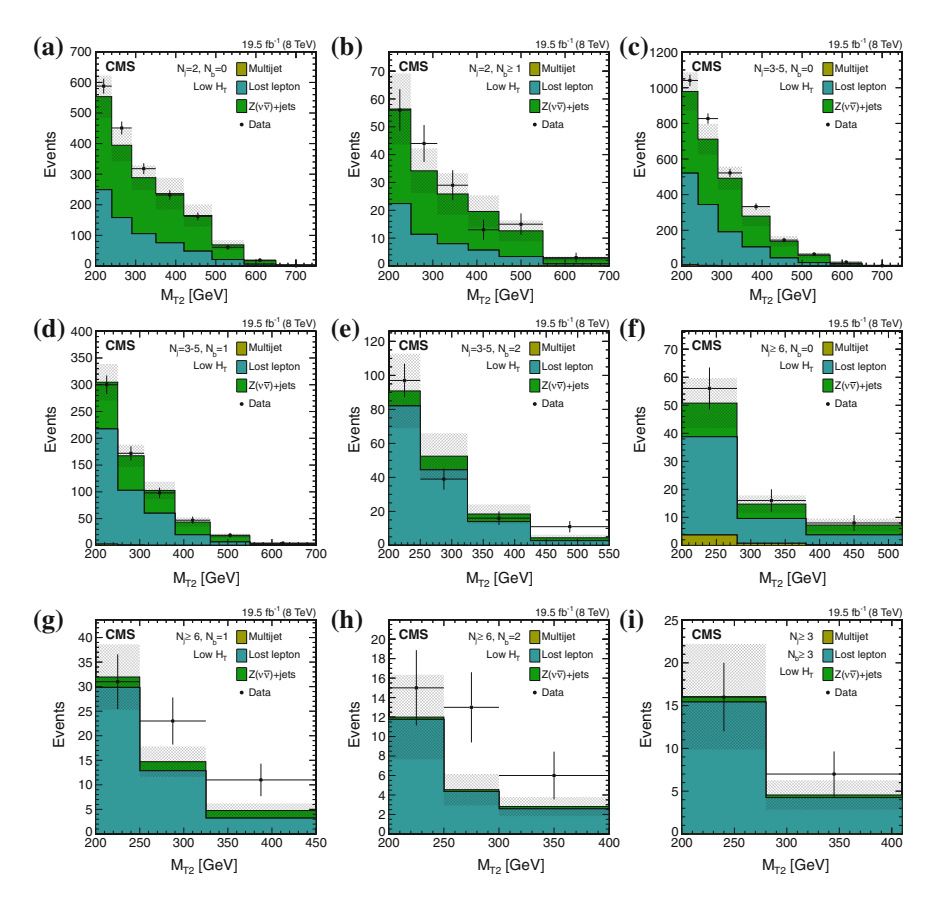


Fig. 7.34 The M_{T2} distributions in data compared to the predicted background estimates for the low H_T selection. The last bin contains the overflow. The data correspond to an integrated luminosity of 19.5 fb⁻¹. The topological regions (N_j, N_b) are given for each plot. **a** 2 jets, 0 b jets. **b** 2 jets, \geq 1 b jets. **c** 3-5 jets, 0 b jets. **d** 3-5 jets, 1 b jet. **e** 3-5 jets, 2 b jets. **f** \geq 6 jets, 0 b jets. **g** \geq 6 jets, 1 b jet. **h** \geq 6 jets, 2 b jets. **i** \geq 3 jets, \geq 3 b jets

deviation being the uncertainty associated to the background predictions. In doing so, correlations among the signal regions are kept, such as the systematic uncertainty on the $Z(\nu\bar{\nu})/\gamma$ ratio. Many *pseudoexperiments* are performed, that is we create many pull distributions for all signal regions by recreating pseudodata. We find that the probability to obtain a mean of the pull distributions of at least 0.26 (the one observed in data) is 11 %. There are three signal regions with Pull > 2. This number agrees with the expectation, which is about 2.8 regions. Therefore, it is concluded that there is satisfactory agreement between the data and the results of the background estimates, although the background estimates slightly underpredict the data. There is no hint of physics beyond the SM in this search.

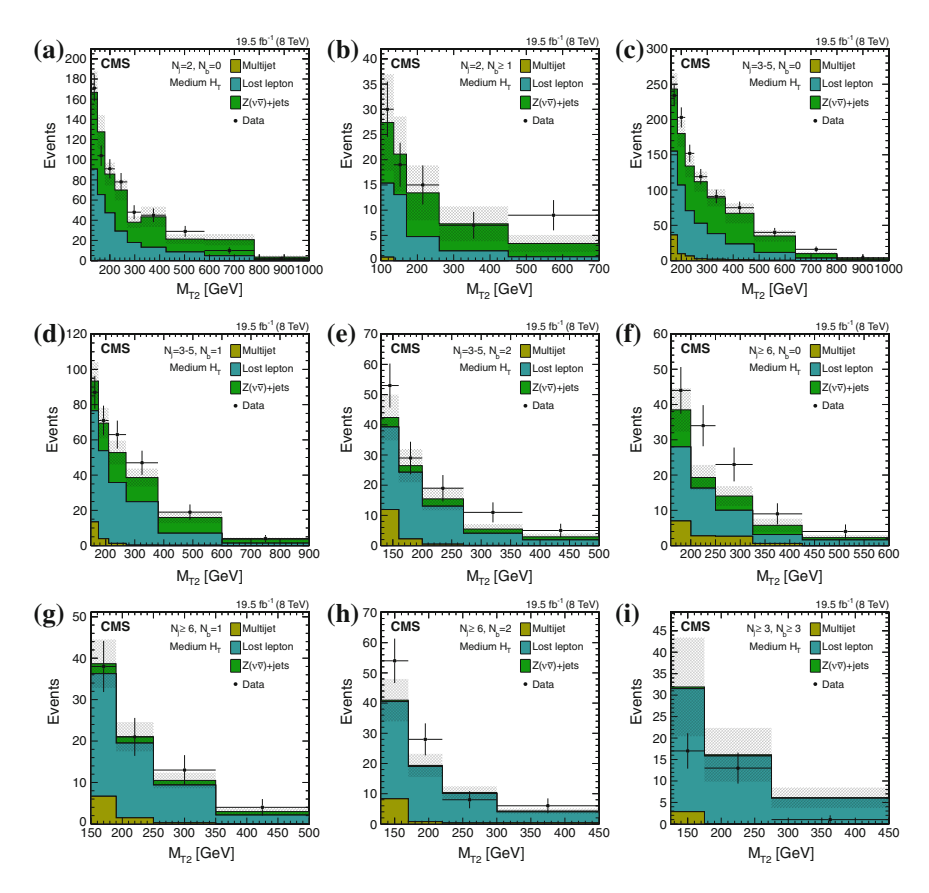


Fig. 7.35 The M_{T2} distributions in data compared to the predicted background estimates for the medium H_T selection. The last bin contains the overflow. The data correspond to an integrated luminosity of 19.5 fb⁻¹. The topological regions (N_j, N_b) are given for each plot. **a** 2 jets, 0 b jets. **b** 2 jets, \geq 1 b jets. **c** 3-5 jets, 0 b jets. **d** 3-5 jets, 1 b jet. **e** 3-5 jets, 2 b jets. **f** \geq 6 jets, 0 b jets. **g** \geq 6 jets, 1 b jet. **h** \geq 6 jets, 2 b jets. **i** \geq 3 jets, \geq 3 b jets

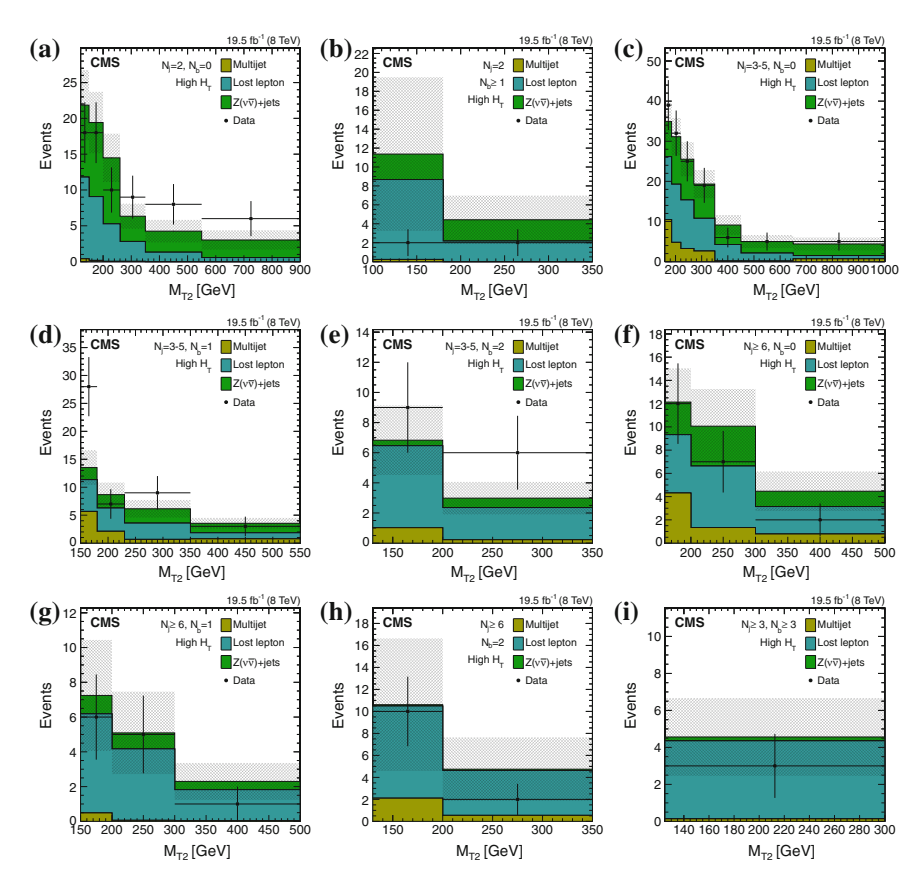


Fig. 7.36 The M_{T2} distributions in data compared to the predicted background estimates for the high H_T selection. The last bin contains the overflow. The data correspond to an integrated luminosity of 19.5 fb⁻¹. The topological regions (N_j, N_b) are given for each plot. **a** 2 jets, 0 b jets. **b** 2 jets, \geq 1 b jets. **c** 3-5 jets, 0 b jets. **d** 3-5 jets, 1 b jet. **e** 3-5 jets, 2 b jets. **f** \geq 6 jets, 0 b jets. **g** \geq 6 jets, 1 b jet. **h** \geq 6 jets, 2 b jets. **i** \geq 3 jets, \geq 3 b jets

Table 7.4 Estimated background event and data yields in all signal regions

	Low H _T region	n u		Medium H _T region	gion		High H _T region	nc	
	M _{T2} (GeV)	Prediction	Data	M _{T2} (GeV)	Prediction	Data	M _{T2} (GeV) Prediction	Prediction	Data
2 jets, 0 b jets 200–240	200–240	553 ± 70	588	125–150	167 ± 21	171	120–150	21.9 ± 4.9	18
	240–290	395 ± 53	451	150–180	128 ± 17	104	150-200	19.4 ± 4.3	18
	290–350	288 ± 40	318	180–220	85.8 ± 11.3	91	200–260	14.5 ± 3.4	10
	350-420	236 ± 52	232	220–270	70.0 ± 10.3	78	260–350	6.3 ± 1.8	6
	420–490	165 ± 36	162	270–325	38.1 ± 5.8	48	350–550	4.3 ± 1.6	8
	490–570	68.9 ± 15.5	61	325–425	43.4 ± 10.1	45	>550	3.0 ± 1.4	9
	570-650	17.3 ± 4.3	19	425–580	21.3 ± 4.7	29			
	>650	4.1 ± 1.6	1	580–780	20.5 ± 8.6	10			
				>780	3.5 ± 1.4	2			
2 jets, ≥ 1 b jets	200–250	56.4 ± 12.8	56	100–135	27.4 ± 9.6	30	100–180	11.4 ± 8.1	2
	250-310	34.2 ± 8.1	44	135–170	21.1 ± 7.5	19	>180	4.4 ± 2.6	2
	310–380	25.9 ± 7.4	29	170–260	13.4 ± 5.4	15			
	380-450	19.9 ± 5.8	13	260-450	7.3 ± 3.5	7			
	450–550	12.6 ± 3.8	15	>450	3.4 ± 1.7	6			
	>550	2.6 ± 0.8	3						
									.,

_
7
0
me
п
Ξ
Ö
ō
Ū
↔
4
4.
e 7.4
le 7.4
ble 7.4
le 7.4
ble 7.4

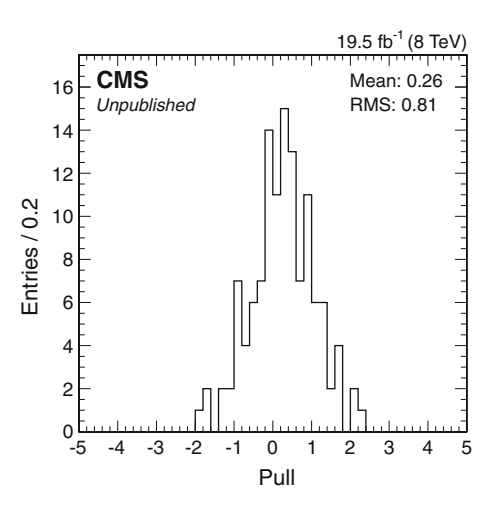
Low E	Low H _T region	uc		Medium H _T region	egion		High H _T region	lon	
	M _{T2} (GeV)	Prediction	Data	M _{T2} (GeV)	Prediction	Data	M _{T2} (GeV)	Prediction	Data
3-5 jets, 0 b jets	200–240	979 ± 108	1041	160–185	243 ± 23	234	160–185	34.9 ± 4.7	39
	240–290	711 ± 86	827	185–215	180 ± 19	203	185–220	31.1 ± 4.7	32
	290–350	492 ± 65	522	215–250	134 ± 16	152	220–270	25.5 ± 4.3	25
	350-420	280 ± 57	333	250–300	112 ± 14	119	270–350	19.3 ± 3.5	19
	420-490	138 ± 29	145	300–370	89.0 ± 12.2	91	350-450	9.1 ± 2.5	9
	490–570	60.0 ± 13.6	99	370-480	67.0 ± 14.2	75	450–650	5.0 ± 1.6	5
	570–650	13.8 ± 3.9	21	480-640	35.0 ± 8.0	40	>650	4.4 ± 1.6	5
	>650	3.6 ± 1.5	2	640–800	10.0 ± 2.7	16			
				>800	3.4 ± 1.5	4			
3-5 jets, 1 b jets	200–250	305 ± 34	300	150–175	93.4 ± 10.7	87	150–180	13.5 ± 3.1	28
·	250-310	167 ± 21	172	175–210	69.5 ± 8.7	71	180–230	8.7 ± 2.2	7
	310–380	103 ± 16	86	210–270	52.8 ± 6.8	63	230–350	6.2 ± 1.6	6
	380-460	43.6 ± 8.7	47	270–380	38.6 ± 5.1	47	>350	3.5 ± 1.0	3
	460–550	17.9 ± 4.1	19	380–600	15.9 ± 3.2	19			
	>550	4.0 ± 1.1	4	009⋜	3.6 ± 0.9	4			
3-5 jets, 2 b jets	200–250	91.1 ± 22.0	26	130–160	42.4 ± 7.5	53	130–200	6.8 ± 2.3	6
	250–325	52.7 ± 13.7	39	160–200	26.5 ± 5.5	29	>200	2.9 ± 1.1	9
	325–425	18.6 ± 5.8	16	200–270	15.4 ± 3.7	19			
	≥425	4.5 ± 1.9	11	270–370	5.5 ± 1.7	11			
				>370	2.9 ± 1.1	5			

Table 7.4 (continued)

	,								
	Low H _T region	on		Medium H _T region	region		High H _T region	on	
	<i>M</i> _{T2} (GeV)	(GeV) Prediction	Data	M _{T2} (GeV) Prediction	Prediction	Data	M _{T2} (GeV) Prediction	Prediction	Data
≥6 jets, 0 b jets	200–280	50.8 ± 8.9	56	160–200	38.5 ± 6.2	44	160–200	12.1 ± 2.9	12
	280–380	14.7 ± 3.1	16	200–250	19.3 ± 3.6	34	200–300	10.1 ± 3.2	7
	>380	7.3 ± 2.3	~	250–325	14.1 ± 2.8	23	>300	4.5 ± 1.7	2
				325-425	5.8 ± 1.9	6			
				>425	2.3 ± 0.8	4			
\geq 6 jets, 1 b jets	200–250	32.0 ± 6.7	31	150–190	38.7 ± 5.9	38	150-200	7.3 ± 3.2	9
	250–325	14.7 ± 3.1	23	190–250	21.1 ± 3.5	21	200–300	5.1 ± 2.4	5
	≥325	4.8 ± 1.5	11	250–350	10.5 ± 1.9	13	>300	2.3 ± 1.1	1
				>350	3.0 ± 0.8	4			
\geq 6 jets, 2 b jets	200-250	12.0 ± 4.3	15	130–170	41.0 ± 7.0	54	130-200	10.6 ± 6.0	10
	250–300	4.6 ± 1.6	13	170–220	19.4 ± 3.8	28	>200	4.7 ± 2.9	2
	>300	2.8 ± 1.0	9	220–300	10.4 ± 2.1	∞			
				>300	4.3 ± 0.8	9			
≥ 3 jets, ≥ 3 b jets 200–280	200-280	16.1 ± 6.2	16	125–175	31.9 ± 11.4	17	≥125	4.5 ± 2.1	3
	>280	4.6 ± 1.7	7	175–275	16.1 ± 6.3	13			
				>275	6.1 ± 2.4	1			

The uncertainties are the quadratic sums of statistical and systematic uncertainties of all background prediction methods. The data correspond to an integrated luminosity of 19.5 fb⁻¹

Fig. 7.37 The pull distribution for comparing the data with the background predictions. For each signal region there is one pull entry



7.8 Interpretation of the Results

The results of this search are interpreted in several potential signal scenarios, such as the pMSSM, cMSSM/mSUGRA, and SMS models, described in Sect. 3.3. First, I will introduce the statistical procedure used in the interpretation, and then show limits on the parameter space of the models, derived by the results of this analysis.

7.8.1 Statistical Procedure

In order to give the most complete statement for the models considered, we combine the information of multiple signal regions. Even regions with low expected signal-to-background ratio are useful, as those regions can serve as a constraint on the background predictions within their uncertainties. Hence, a multi-bin approach is used. For this, we construct a likelihood function as the product of Poisson probabilities of all signal regions:

$$\mathcal{L} = \prod_{i=1}^{N_{SR}} \frac{\lambda_i^{n_i} e^{-\lambda_i}}{n_i!}.$$
 (7.8)

Here, λ_i and n_i denote the prediction and the observed data event yield for signal region i, where i ranges from 1 up to the number of signal regions, N_{SR} . The prediction in a signal region is given as

$$\lambda_i = \mu \cdot s_i + \sum_{j=1}^{N_{\text{BS}}} b_{ij},\tag{7.9}$$

where b_{ij} is the background prediction in signal region i from background source j ($N_{\rm BS}$ is the number of background sources), and s_i is the expected signal prediction, which can be modified by the scale μ , commonly known as the *signal strength modifier*, to test also other values for the signal production cross section. In short, we will write Eq. (7.8) as $\mathcal{L}(n|\mu) = \mathrm{Poisson}(n|\mu \cdot s + b)$.

The uncertainties on the predictions are handled by nuisance parameters θ_m . For each uncertainty source m, a separate θ_m is introduced. The sources of uncertainties are considered to be fully correlated, uncorrelated, or fully anti-correlated, whichever seems to be more appropriate or more conservative. We denote $\theta = \{\theta_1, \ldots, \theta_{N_{\rm unc}}\}$ as the collection of all nuisance parameters for $N_{\rm unc}$ different uncertainty sources. In this way, we can incorporate the systematic uncertainties into the likelihood function in a clean manner:

$$\mathcal{L}(n|\mu,\theta) = \text{Poisson}(n|\mu \cdot s(\theta) + b(\theta)) \cdot p(\theta), \tag{7.10}$$

with $p(\theta)$ being the probability density function (pdf⁴) associated with a given uncertainty.

In this analysis, the pdfs are lognormal distributions:

$$p(\theta) = \frac{1}{\sqrt{2\pi} \ln \kappa} \frac{1}{\theta} \exp \left\{ -\frac{\left(\ln \left(\theta/\bar{\theta}\right)\right)^2}{2(\ln \kappa)^2} \right\},\tag{7.11}$$

where $\bar{\theta}$ is the best estimate of the nuisance parameter (usually its mean value) and κ encodes the spread in the distribution: $\kappa \equiv 1 \pm \sigma_{\theta}/\theta$ with σ_{θ} being the uncertainty of θ . Usually, $\kappa \equiv 1 + \sigma_{\theta}/\theta$ is chosen.

The estimate of the background component j in signal region i can be modeled by [57]

$$b_{ij}(\theta) = \prod_{m=0}^{N_{\text{unc}}} b_{ij}^0 \cdot (\kappa_{ijm})^{\theta_m}, \tag{7.12}$$

where b_{ij}^0 is the central prediction of background component j in signal region i, and κ_{ijm} is defined as the lognormal spread for the nuisance parameter m. In this model, θ_m is a random number generated according to a Gaussian distribution with mean = 0 and standard deviation = 1.

Using this approach, two components b_{ij} and b_{kl} (with either $i \neq k$ and/or $j \neq l$) can be modeled to be fully (anti-)correlated under source m, if $\kappa_{ijm} > 1$ and $\kappa_{klm} > 1$ ($\kappa_{klm} < 1$).

⁴The probability density function (pdf) should not be confused with the parton density function (PDF).

The compatibility of the data with the background-only and background + signal hypotheses is tested using a modified frequentist approach referred to as CL_s [58, 59]. First, we construct the test statistics q_{μ} [60]:

$$q_{\mu} = -2 \ln \left\{ \frac{\mathcal{L}(n|\mu, \hat{\theta}_{\mu})}{\mathcal{L}(n|\hat{\mu}, \hat{\theta})} \right\} \qquad \text{with } 0 \le \hat{\mu} \le \mu, \tag{7.13}$$

where n can denote observed data or pseudodata yields. In the numerator, the likelihood is maximized for a fixed μ , but floating nuisance parameters. The value, where the maximum is achieved, is $\hat{\theta}_{\mu}$. For the denominator, both the signal strength modifier and the nuisance parameters are floating, and the maximal likelihood is achieved for $\hat{\mu}$ and $\hat{\theta}$. Two contraints on $\hat{\mu}$ are imposed: first, $\hat{\mu}$ is required to be positive as the signal contribution is expected to be positive, secondly, the upper constraint results in one-sided confidence intervals. The latter constraint can be interpreted as upward fluctuations in data not being considered as evidence against the signal hypothesis. If n denotes observed data yields, the test statistics is called q_{μ}^{obs} .

Next, we define the probabilities of observing an experiment with an outcome at least as "signal-like" as the one observed in data for the background-only hypothesis, H_0 , and for the signal + background hypothesis, H_1 :

$$CL_{s+b} = P(q_{\mu} \ge q_{\mu}^{obs}|H_1),$$

 $CL_b = P(q_{\mu} \ge q_{\mu}^{obs}|H_0).$ (7.14)

Then, the CL_s value is given by the ratio of the two probabilities:

$$CL_{s} = \frac{CL_{s+b}}{CL_{b}}. (7.15)$$

This value depends on μ . In the frequentist picture, $CL_s \le \alpha$ is required in order to claim a $(1 - \alpha)$ confidence level (CL) exclusion on the considered signal.

The probabilities, Eq. (7.14), are calculated from the distribution of q_{μ} , obtained by simulated pseudoexperiments.

7.8.2 Exclusion Limits on the Production of Supersymmetric Particles

This search is interpreted in three classes of SUSY models: the pMSSM, the cMSSM/mSUGRA, and several SMS models. The key features of these models are described in Sect. 3.3. The interpretation in the pMSSM model is part of another analysis and is not described here.

The interpretation can be done in two ways:

- For a given model, we compute a 95 % CL upper limit on the signal production cross section. It is obtained by finding μ_{UL} , the signal strength modifier, for which $CL_s=0.05$. Then, the limit is simply the nominal signal production cross section times μ_{UL} . The meaning of that limit is that we exclude signal models like the given model at 95 % CL if the cross section is larger than the computed upper limit.
- The signal strength modifier is fixed to unity, $\mu=1$. A given signal model is excluded at 95% CL, if we obtain $CL_s \leq 0.05$. This procedure is performed for the observed signal region distribution (in data), as well as for the expected signal region distribution (from the background prediction). For the observed distribution, we also vary the signal production cross section by its theoretical uncertainty, and for the expected distribution, we vary the distribution by the experimental uncertainty on the signal and background.

The uncertainties on the background have been discussed in the Sects. 7.4–7.6. The following sources of systematic uncertainties on the signal yield have been considered: The uncertainty on the trigger efficiency has been measured to be $\lesssim 1\%$. The uncertainty on the integrated luminosity is 2.6% [61]. The uncertainty associated to the choice of PDFs has been evaluated following the prescription of the PDF4LHC group [62]. The dominant sources of the systematic uncertainties, that both affect the shape and the normalization of the signal region distribution, are the jet energy scale [51], the b-tagging efficiency [50], and the system recoil modeling [47]. A summary of the uncertainties, for signal and background, is given in Table 7.5.

Exclusion Limits on Simplified Model Spectra

Here, mass exclusion limits at 95% CL are given for various SMS. The concept of the SMS was given in Sect. 3.3.3. Limits are set on both the upper signal production cross section and the model itself. The SMS considered are parameterized by two mass parameters: the mass of the initially produced sparticle and the mass of the LSP. For a given SMS, not all topological signal regions are used for the interpretation. Only a subset, for which a high signal sensitivity is expected, is used. But within this subset, the information of all signal regions in H_T and M_{T2} is combined with the method described in Sect. 7.8.1.

Six topologies are studied by this analysis:

- Direct squark pair production: pp → \$\widetilde{q}\widetilde{q}^* + q \widetilde{\chi}_1^0 \widetilde{q} \widetilde{\chi}_1^0\$, where \$\widetilde{q}\$ denotes squarks of the first and second generations. For this model, the following topological regions are used: \$(N_j = 2, N_b = 0)\$, \$(N_j = 2, N_b \geq 1)\$, \$(3 \leq N_j \leq 5, N_b = 0)\$, \$(3 \leq N_j \leq 5, N_b = 1)\$, and \$(N_j \geq 6, N_b = 0)\$. The exclusion limits are shown in Fig. 7.38a. Two scenarios are shown: in the first one, all squarks of the first and second generations are degenerate; the second scenario assumes that only one squark within the first and second generations is light and accessible.
- Direct sbottom pair production: pp $\rightarrow \tilde{b}_1 \tilde{b}_1^* \rightarrow b \tilde{\chi}_1^0 \bar{b} \tilde{\chi}_1^0$. The following topological regions are used: $(N_j = 2, N_b \ge 1)$, $(3 \le N_j \le 5, N_b = 1)$, and $(3 \le N_j \le 5, N_b = 2)$. The exclusion limits are shown in Fig. 7.38b.

Process	Source/Region	Effect (%)	Shape		
Multijet	$M_{\mathrm{T2}} < 200\mathrm{GeV}$	10-50	_		
	$M_{\rm T2} \ge 200{\rm GeV}$	50-100	_		
$W(l\nu)$ +jets and $t\bar{t}$ +jets	Lost lepton method	10–65	_		
	b-tagging scale factor	_	×		
	Jet energy scale	_	×		
	Matching scale	_	×		
	Renormalization and factorization scale	-	×		
	System recoil modeling	_	×		
$Z(u\overline{ u})$ +jets	$Z(\nu\overline{\nu})/\gamma$ ratio (0-1 b jets)	20–30	_		
	$Z_{ll}(1b)/Z_{ll}(0b)$ ratio	10–75	_		
	Statistics from γ +jets data (0-1 b jet)	5–100	_		
	Simulation (≥ 2 b jets)	100	_		
Signal	Luminosity measurement	2.6	-		
	Trigger efficiency	1	_		
	Parton distribution functions	5–15	-		
	b-tagging scale factor	5–40	×		
	Jet energy scale	5–40	×		
	System recoil modeling	10–20	×		

Table 7.5 Summary of the systematic uncertainties

The column "Effect" denotes typical ranges of the effect of a systematic uncertainty on the normalization. If the \times symbol is set in the column "Shape", the shape of the signal region distribution is affected by the uncertainty

- Direct stop pair production: pp $\rightarrow \tilde{t}_1 \tilde{t}_1^* \rightarrow t \tilde{\chi}_1^0 \bar{t} \tilde{\chi}_1^0$. The following topological regions are used: $(3 \le N_{\rm j} \le 5, N_{\rm b} = 1), (3 \le N_{\rm j} \le 5, N_{\rm b} = 2), (N_{\rm j} \ge 6, N_{\rm b} = 1), (N_{\rm j} \ge 6, N_{\rm b} = 2), (N_{\rm j} \ge 3, N_{\rm b} \ge 3)$. The exclusion limits are shown in Fig. 7.38c.
- Direct gluino pair production: pp $\rightarrow \widetilde{g}\widetilde{g} \rightarrow q\overline{q}\widetilde{\chi}_1^0 q\overline{q}\widetilde{\chi}_1^0$. The following topological regions are used: $(3 \le N_j \le 5, N_b = 0)$, $(3 \le N_j \le 5, N_b = 1)$, $(N_j \ge 6, N_b = 0)$, and $(N_i \ge 6, N_b = 1)$. The exclusion limits are shown in Fig. 7.39a.
- Direct gluino pair production: pp $\rightarrow \widetilde{g}\widetilde{g} \rightarrow b\overline{b}\widetilde{\chi}_1^0b\overline{b}\widetilde{\chi}_1^0$. The following topological regions are used: $(3 \le N_{\rm j} \le 5, N_{\rm b} = 1), (3 \le N_{\rm j} \le 5, N_{\rm b} = 2), (N_{\rm j} \ge 6, N_{\rm b} = 1), (N_{\rm j} \ge 6, N_{\rm b} = 2), (N_{\rm j} \ge 3, N_{\rm b} \ge 3)$. The exclusion limits are shown in Fig. 7.39b.

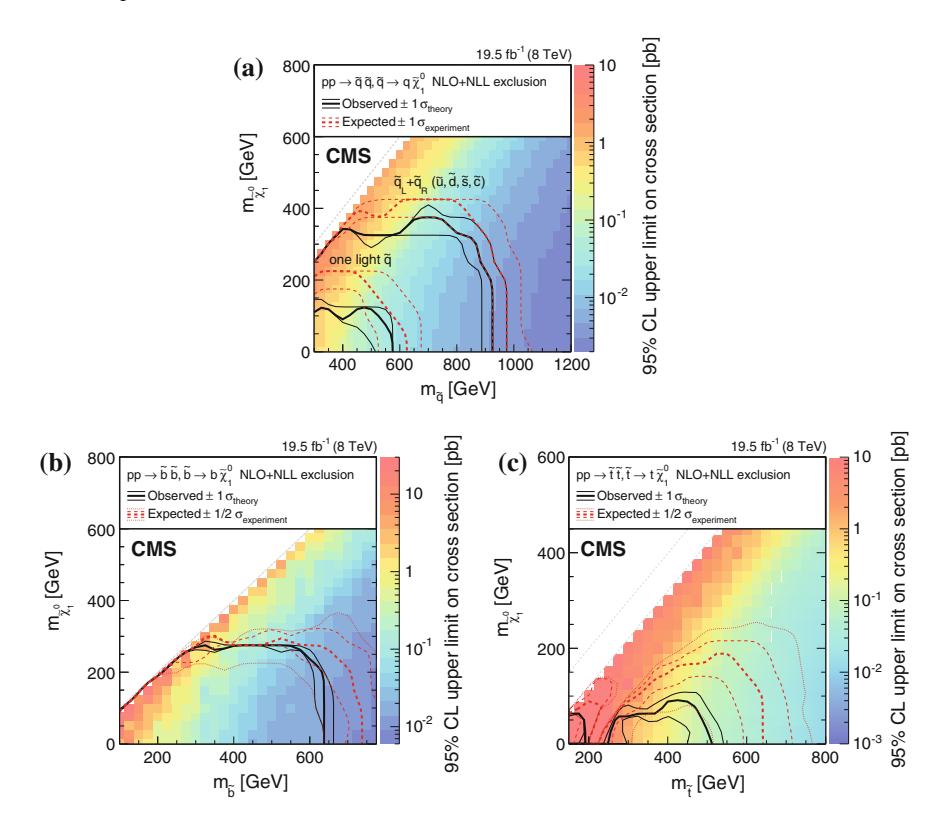
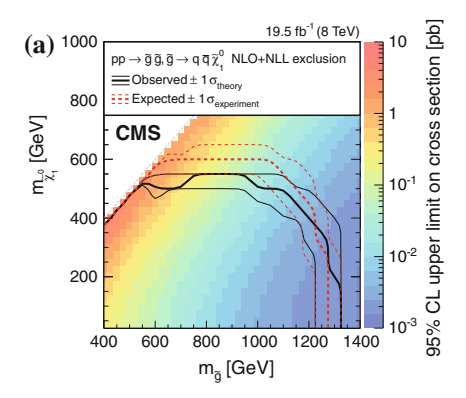


Fig. 7.38 Exclusion limits for simplified models with direct squark production. **a** pp $\to \widetilde{q}\widetilde{q}^* \to q\widetilde{\chi}_1^0 \overline{q}\widetilde{\chi}_1^0$. **b** pp $\to \widetilde{b}_1\widetilde{b}_1^* \to b\widetilde{\chi}_1^0 \overline{b}\widetilde{\chi}_1^0$. **c** pp $\to \widetilde{t}_1\widetilde{t}_1^* \to t\widetilde{\chi}_1^0 \overline{t}\widetilde{\chi}_1^0$

• Direct gluino pair production: pp $\to \widetilde{g}\widetilde{g} \to t\bar{t}\widetilde{\chi}_1^0 t\bar{t}\widetilde{\chi}_1^0$. The following topological regions are used: $(N_j \ge 6, N_b = 1), (N_j \ge 6, N_b = 2), \text{ and } (N_j \ge 3, N_b \ge 3)$. The exclusion limits are shown in Fig. 7.39c.

Except for the model of direct stop pair production, the expected and observed mass limits at 95 % CL agree within the uncertainties. The disagreement for the model of direct stop pair production has been investigated. We find that the data in the μ +jets and τ +jets control regions for events with \geq 6 jets and 1 b jet seem to underfluctuate strongly with respect to the expectation from simulation. The probability to find an underfluctuation in the leptonic control regions at least as strong as the one observed in data has been evaluated to be \sim 65 %.

The observed mass exclusion limits for the various simplified models, given at 95 % CL, are summarized in Table 7.6. We quote mass limits of the gluino or squark mass for a LSP mass of 0 GeV, the absolute mass limit on the LSP mass for any parent mass, as well as the lower limit on the difference between parent and LSP mass. The mass limits are quoted for the observed limits minus the theory uncertainty, σ_{theory} .



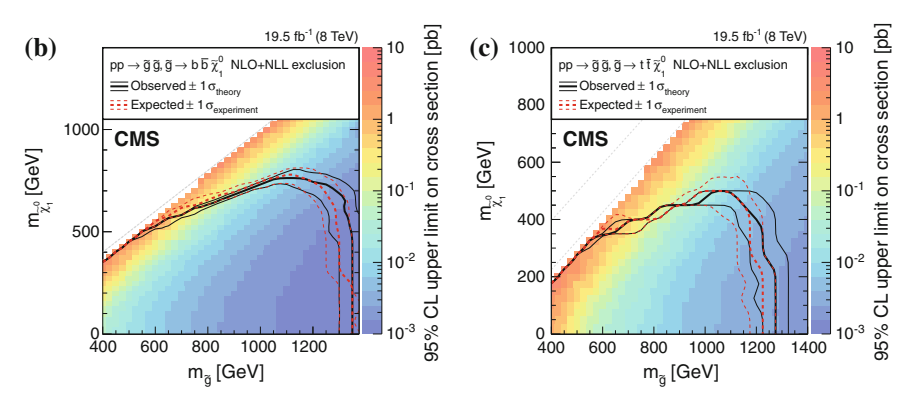


Fig. 7.39 Exclusion limits for simplified models with direct gluino production. **a** pp $\to \widetilde{g}\widetilde{g} \to q\overline{q}\widetilde{\chi}_1^0 q\overline{q}\widetilde{\chi}_1^0$. **b** pp $\to \widetilde{g}\widetilde{g} \to b\overline{b}\widetilde{\chi}_1^0 b\overline{b}\widetilde{\chi}_1^0$. **c** pp $\to \widetilde{g}\widetilde{g} \to t\overline{t}\widetilde{\chi}_1^0 t\overline{t}\widetilde{\chi}_1^0$

Exclusion Limits for a cMSSM/mSUGRA Model

The cMSSM/mSUGRA has been introduced in Sect. 3.3.2. It is, contrary to the simplified models, a full model of SUSY. The cMSSM/mSUGRA has five free parameters: $m_{1/2}$, m_0 , A_0 , $\tan \beta$, $\text{sign}(\mu)$.

These parameters need to be constrained, such that $M(h^0) \approx 125$ GeV. We choose $A_0 = -2 \max(m_0, m_{1/2})$, as mentioned before in Sect. 3.3.2.

In order to visualize the results, further choices are made: we set $\tan \beta = 30$ and $\operatorname{sign}(\mu)$ positive. Thus, we have fixed three parameters, the two free parameters are m_0 and $m_{1/2}$.

For this model, 95 % CL exclusion limits on the parameter space in the $m_0 - m_{1/2}$ plane are obtained by combining all signal regions of this search. The limits are shown in Fig. 7.40.

The limits can be directly transformed onto mass limits in the $M(\widetilde{g})$ versus $M(\widetilde{q})$ plane. Here, $M(\widetilde{q})$ is the averaged mass of all squarks of the first generation. The transformed limits are shown in Fig. 7.41.

Table 7.0 Summary of	obscived mass mints at	75 % CL for the various v	31413		
Simplified model	Limit on parent mass	Best limit on LSP	Limit on mass splitting		
	at $M(\widetilde{\chi}_1^0) = 0$ (GeV)	mass (GeV)	parent—LSP (GeV)		
Direct squark productio	n				
Single light squark	$M(\widetilde{q}) > 520$	$M(\widetilde{\chi}_1^0) > 120$	$\Delta M(\widetilde{q}, \widetilde{\chi}_1^0) < 200$		
8 degenerate light squarks	$M(\widetilde{q}) > 875$	$M(\widetilde{\chi}_1^0) > 325$	$\Delta M(\widetilde{q}, \widetilde{\chi}_1^0) < 50$		
Direct sbottom production	$M(\widetilde{b}) > 640$	$M(\widetilde{\chi}_1^0) > 275$	$\Delta M(\widetilde{b}, \widetilde{\chi}_1^0) < 10$		
Direct stop production					
$M(\widetilde{t}) > M(t) + M(\widetilde{\chi}_1^0)$	$M(\widetilde{t}) > 450$	$M(\widetilde{\chi}_1^0) > 60$	$\Delta M(\widetilde{t}, \widetilde{\chi}_1^0) < 230$		
$M(\widetilde{t}) > M(t) + M(\widetilde{\chi}_1^0)$	$M(\widetilde{t}) > 175$	$M(\widetilde{\chi}_1^0) > 60$	$\Delta M(\widetilde{t}, \widetilde{\chi}_1^0) < 90$		
Direct gluino production	n				
$\widetilde{g} \to q \overline{q} \widetilde{\chi}_1^0$	$M(\widetilde{g}) > 1225$	$M(\widetilde{\chi}_1^0) > 510$	$\Delta M(\widetilde{g}, \widetilde{\chi}_1^0) < 25$		
$\widetilde{g} \to b \overline{b} \widetilde{\chi}_1^0$	$M(\widetilde{g}) > 1300$	$M(\widetilde{\chi}_1^0) > 740$	$\Delta M(\widetilde{g}, \widetilde{\chi}_1^0) < 50$		
$\widetilde{g} \to t \overline{t} \widetilde{\chi}_1^0$	$M(\widetilde{g}) > 1225$	$M(\widetilde{\chi}_1^0) > 450$	$\Delta M(\widetilde{g}, \widetilde{\chi}_1^0) < 225$		

Table 7.6 Summary of observed mass limits at 95 % CL for the various SMS

The limits quoted are the observed limits minus the theory uncertainty, σ_{theory} . The limit on the mass of the intially produced particle is quoted for $M(\widetilde{\chi}_1^0)=0$, the limit on the LSP mass is taken as the best limit. The limit on the mass splitting of squark/gluino and LSP is taken, where it is the smallest

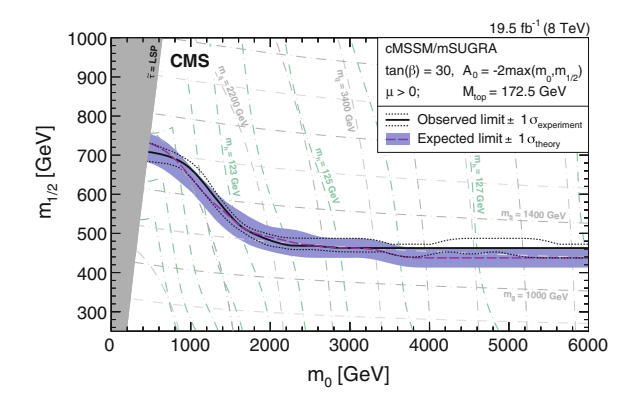


Fig. 7.40 The 95% CL exclusion limits as a function of m_0 and $m_{1/2}$ for the cMSSM/mSUGRA model with $\tan \beta = 30$, $A_0 = -2 \max(m_0, m_{1/2})$, and $\mu > 0$. Here, $m(\widetilde{q})$ is the average mass for the first generation squarks. The isomass lines for the lightest Higgs boson, the gluino and squarks are shown. The $\widetilde{\tau} = \text{LSP}$ region indicates the region, where the $\widetilde{\tau}$ is the LSP. This case is disfavored by cosmology

For the parameter choice as done here $(A_0 = -2 \max(m_0, m_{1/2}), \tan \beta = 30, \text{ and } \mu > 0)$, we obtain, at 95 % CL, an absolute gluino mass limit of $M(\widetilde{g}) < 1150 \,\text{GeV}$, and an absolute squark mass limit of $M(\widetilde{q}) < 1450 \,\text{GeV}$. For the special case of $M(\widetilde{g}) = M(\widetilde{q})$, the mass limit is $M(\widetilde{g}, \widetilde{q}) < 1550 \,\text{GeV}$. All these limits correspond to the observed limits minus the theory uncertainty, σ_{theory} .

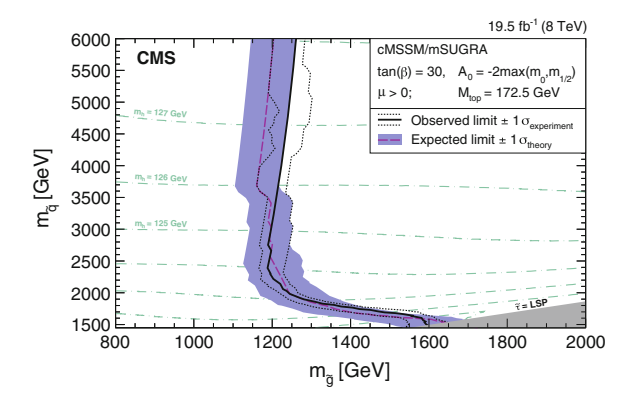


Fig. 7.41 The 95% CL exclusion limits as a function of $m_{\text{squark}} \equiv M(\widetilde{q})$ and $m_{\text{gluino}} \equiv M(\widetilde{g})$ for the cMSSM/mSUGRA model with $\tan \beta = 30$, $A_0 = -2 \max(m_0, m_{1/2})$, and $\mu > 0$. Here, $M(\widetilde{q})$ is the average mass for the first generation squarks. The isomass lines for the lightest Higgs boson are shown. The $\widetilde{\tau} = \text{LSP}$ region indicates the region, where the $\widetilde{\tau}$ is the LSP. This case is disfavored by cosmology

7.9 Comparison of the Results of the M_{T2} Analysis to Other Searches for Supersymmetry

In this section, I will compare the results of the M_{T2} analysis with other hadronic SUSY searches. The best way to do so is using the expected limit interpretations of the analyses. In CMS, there are several "inclusive" hadronic SUSY analyses: a multijet+ H_{T}^{miss} search [4], a search with b jets and E_{T}^{miss} [3], the α_{T} analysis [2], and the Razor analysis [63]. Also specific searches, targeting sbottom [64] and stop production [65, 66], have been performed. The ATLAS collaboration has a similar set of analyses: inclusive analyses searching for squark and gluino production [5, 6], as well as specific searches for sbottom [67] and stop pair production [68, 69].

Reviewing the exclusion limits in the SMS or cMSSM/mSUGRA pictures, one finds the M_{T2} analysis among the strongest hadronic analyses for any of the interpretations. In fact, each model parameter space contains regions, where the expected limit (at 95 % CL) of the M_{T2} analysis is the strongest ones of all hadronic analyses. For the comparison to CMS analyses, this can be appreciated in the examples of Fig. 7.42 or other summary plots given in [70]. The M_{T2} analysis did not interpret its results in very specific models, such as direct stop production with $\tilde{t} \to c \tilde{\chi}_1^0$. It is expected that the targeted searches are stronger for such models.

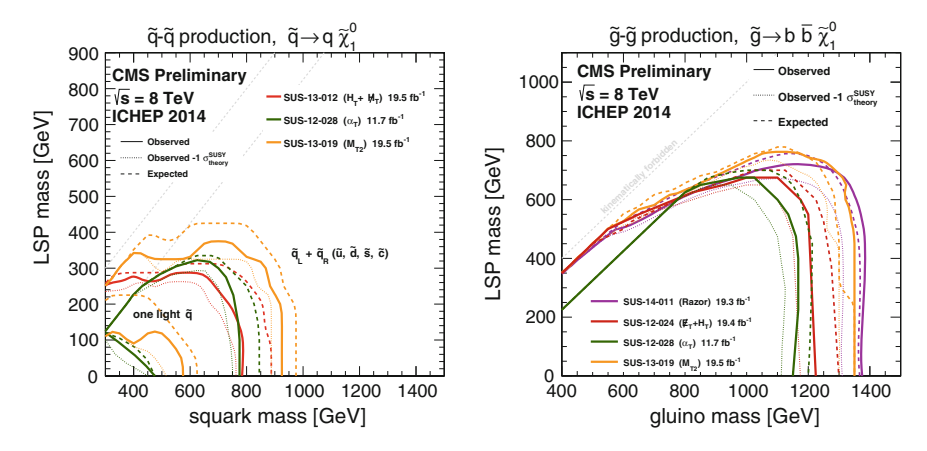


Fig. 7.42 Comparison of the observed and expected limits at 95 % CL among several CMS analyses for the simplified models of pp $\to \tilde{q}\tilde{q}^* \to q \tilde{\chi}_1^0 q \tilde{\chi}_1^0$ (left) and pp $\to \tilde{g}\tilde{g} \to b\bar{b}\tilde{\chi}_1^0 b\bar{b}\tilde{\chi}_1^0$ (right) [70]. The orange lines indicate the limits obtained with the M_{T2} analysis

7.10 Summary of the Hadronic M_{T2} Search for Supersymmetry

A search for SUSY or new physics with similar final states has been presented. The search is based on pp collision data, collected by the CMS experiment at $\sqrt{s} = 8 \text{ TeV}$ and corresponding to an integrated luminosity of 19.5 fb^{-1} . The signal has been discriminated against the SM background using the kinematic variables M_{T2} and H_{T} . It was shown that M_{T2} is small for multijet events. For events of SUSY production, M_{T2} can be large. A search selecting events with high values of M_{T2} is sensitive to SUSY signals for models with R-parity conservation.

The M_{T2} analysis is based on fully hadronic final states. Events are collected with three different trigger types. The phase space is divided into multiple exclusive search regions depending on the jet and b-jet multiplicities, H_T , and M_{T2} . By doing so, the search is sensitive to both gluino production and squark production of all three generations, and is also sensitive to a wide mass range of the initially produced sparticle.

The main SM backgrounds are predicted using data-driven estimation methods. No significant excess over the SM background prediction has been observed. The results are interpreted in several SMS scenarios, in the cMSSM/mSUGRA model, and the pMSSM model. For the cMSSM/mSUGRA models, absolute mass limits $M(\widetilde{g}) > 1150 \, \text{GeV}$ for gluinos, and $M(\widetilde{q}) > 1450 \, \text{GeV}$ for squarks are obtained at 95% CL. For simplified models, gluino mass limits between 1225 up to 1300 GeV are reached. Squark mass limits vary between 450 and 875 GeV.

The analysis is summarized in [17].

7.10.1 Prospects for the Continuation of This Search

The M_{T2} -based all hadronic search will be continued for the 13 TeV run of the LHC. The increase in the center-of-mass energy will tremendously boost the discovery reach of new physics searches. For example, the cross-section for gluino pair production at $M(\tilde{g}) = 1$ (1.5) TeV increases by a factor ≈ 20 (55) for $\sqrt{s} = 14$ TeV compared to $\sqrt{s} = 8$ TeV, see Fig. 7.43.

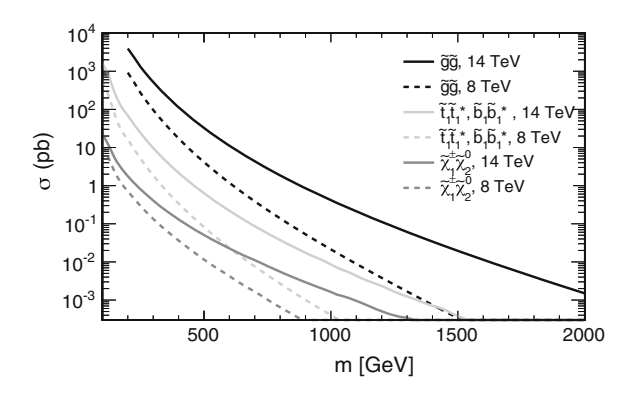
However, the analysis needs to be consolidated: The expected rise in instantaneous luminosity will also strongly increase the amount of pileup interactions per bunch-crossing. In order to keep the influence of pileup small, new object definitions might be needed. Another challenge might be the trigger definition. The overall trigger rate is expected to increase due to the higher center-of mass energy and the higher instantaneous luminosity. Therefore, trigger thresholds might become tighter.

In case of no discovery, the analysis might, on the one hand, be pushed to more extreme selections in order to boost the sensitivity for sparticles with very large masses. Another direction might be to try to access difficult regions in phase space, such as compressed mass spectra, for which the current search has only limited reach.

If an excess is observed in the signal regions of this search, the main effort will be the classification of the new physics involved. This includes mass and spin measurements. The $M_{\rm T2}$ variable is very well suited for this. Endpoints can be used for mass determination. The LSP mass could be determined using the $M_{\rm T2}$ kink method [72–75], for example. Also, spin measurements could be made with a $M_{\rm T2}$ -based search [76, 77].

The M_{T2} variable can be generalized to the 3+1 dimensional variable M_2 [78–80], where the full momenta of the LSPs are estimated (instead of only their transverse momenta). While a search based on M_2 does not improve the discovery reach compared to a M_{T2} -based general SUSY search, it will result in sharper endpoints for subsystems, and therefore lead to more accurate mass measurements for sparticles within the decay chain of the initial sparticles. Furthermore, M_2 might help to discriminate between event topologies, for example between pp $\rightarrow \widetilde{g}\widetilde{g} \rightarrow q\overline{q}\widetilde{\chi}_1^0 q\overline{q}\widetilde{\chi}_1^0$ (three-body decay of the gluino) and pp $\rightarrow \widetilde{g}\widetilde{g} \rightarrow \widetilde{q}q\widetilde{q}q \rightarrow q\overline{q}\widetilde{\chi}_1^0 q\overline{q}\widetilde{\chi}_1^0$ (two-body decay of the gluino via a squark).

Fig. 7.43 Cross sections for the pair production of sparticles as a function of the sparticle mass for $\sqrt{s} = 14 \text{ TeV}$ and $\sqrt{s} = 8 \text{ TeV}$, computed with Prospino. Plot taken from [71]



References

- CMS Collaboration, Search for supersymmetry in hadronic final states using M_{T2} in pp collisions at √s = 7 TeV. JHEP 10, 018 (2012). doi:10.1007/JHEP10(2012)018. arXiv:1207.1798
- 2. CMS Collaboration, Search for supersymmetry in hadronic final states with missing transverse energy using the variables $\alpha_{\rm T}$ and b-quark multiplicity in pp collisions at 8 TeV. Eur. Phys. J. C **73**, 2568 (2013). doi:10.1140/epjc/s10052-013-2568-6. arXiv:1303.2985
- 3. CMS Collaboration, Search for gluino mediated bottom- and top-squark production in multijet final states in pp collisions at 8 TeV. Phys. Lett. B **725**, 243 (2013). doi:10.1016/j.physletb. 2013.06.058. arXiv:1305.2390
- 4. CMS Collaboration, Search for new physics in the multijet and missing transverse momentum final state in proton-proton collisions at $\sqrt{s}=8$ TeV. JHEP **06**, 055 (2014). doi:10.1007/ JHEP06(2014)055. arXiv:1402.4770
- 5. ATLAS Collaboration, Search for new phenomena in final states with large jet multiplicities and missing transverse momentum at $\sqrt{s} = 8$ TeV proton-proton collisions using the ATLAS experiment. JHEP **10**, 130 (2013). doi:10.1007/JHEP10(2013)130. arXiv:1308.1841
- 6. ATLAS Collaboration, Search for squarks and gluinos with the ATLAS detector in final states with jets and missing transverse momentum using $\sqrt{s} = 8$ TeV proton-proton collision data. JHEP **09**, 176 (2014), doi:10.1007/JHEP09(2014)176. arXiv:1405.7875
- CDF Collaboration, Measurement of the top quark mass in the dilepton channel using m_{T2} at CDF, Phys. Rev. D 81, 031102 (2010). doi:10.1103/PhysRevD.81.031102. arXiv:0911.2956
- 8. ATLAS Collaboration, Search for direct slepton and gaugino production in final states with two leptons and missing transverse momentum with the ATLAS detector in pp collisions at $\sqrt{s} = 7$ TeV. Phys. Lett. B **718**, 879 (2013). doi:10.1016/j.physletb.2012.11.058. arXiv:1208.2884
- ATLAS Collaboration, Search for a heavy top-quark partner in final states with two leptons with the ATLAS detector at the LHC. JHEP 11, 094 (2012). doi:10.1007/JHEP11(2012)094. arXiv:1209.4186
- 10. CMS Collaboration, Measurement of masses in the $t\bar{t}$ system by kinematic endpoints in pp collisions at \sqrt{s} = 7 TeV, Eur. Phys. J. C **73**, 2494 (2013). doi:10.1140/epjc/s10052-013-2494-7. arXiv:1304.5783
- 11. ATLAS Collaboration, Search for direct production of charginos and neutralinos in events with three leptons and missing transverse momentum in $\sqrt{s} = 8$ TeV pp collisions with the ATLAS detector. JHEP **04**, 169 (2014). doi:10.1007/JHEP04(2014)169. arXiv:1402.7029
- 12. ATLAS Collaboration, Search for direct top-squark pair production in final states with two leptons in pp collisions at $\sqrt{s}=8$ TeV with the ATLAS detector. JHEP **06**, 124 (2014). doi:10. 1007/JHEP06(2014)124. arXiv:1403.4853
- 13. ATLAS Collaboration, Search for direct production of charginos, neutralinos and sleptons in final states with two leptons and missing transverse momentum in pp collisions at $\sqrt{s} = 8$ TeV with the ATLAS detector. JHEP **05**, 071 (2014). doi:10.1007/JHEP05(2014)071. arXiv:1403.5294
- 14. ATLAS Collaboration, Search for the direct production of charginos, neutralinos and staus in final states with at least two hadronically decaying taus and missing transverse momentum in pp collisions at $\sqrt{s} = 8$ TeV with the ATLAS detector. JHEP 10, 96 (2014). doi:10.1007/JHEP10(2014)096. arXiv:1407.0350
- 15. ATLAS Collaboration, Search for top squark pair production in final states with one isolated lepton, jets, and missing transverse momentum in $\sqrt{s} = 8$ TeV pp collisions with the ATLAS detector. Submitted to JHEP 11, 118 (2014). arXiv:1407.0583
- CMS Collaboration, Searches for electroweak neutralino and chargino production in channels with Higgs, Z, and W bosons in pp collisions at 8 TeV. Phys. Rev. D. arXiv:1409.3168
- 17. CMS Collaboration, Search for supersymmetry in hadronic final states using $M_{\rm T2}$ with the CMS detector at \sqrt{s} = 8 TeV, CMS-PAS SUS-13-019 (2014). http://inspirehep.net/record/1345027/export/hx
- T. Sjöstrand, S. Mrenna, P.Z. Skands, PYTHIA 6.4 physics and manual. JHEP 05, 026 (2006). doi:10.1088/1126-6708/2006/05/026. arXiv:hep-ph/0603175

- 19. S. Alioli et al., NLO single-top production matched with shower in POWHEG: *s* and *t*-channel contributions. JHEP **09**, 111 (2009). doi:10.1088/1126-6708/2009/09/111. arXiv:0907.4076. An erratum has been published in JHEP **02**, 011 (2010)
- E. Re, Single-top Wt-channel production matched with parton showers using the POWHEG method. Eur. Phys. J. C 71, 1547 (2011). doi:10.1140/epjc/s10052-011-1547-z. arXiv:1009.2450
- J. Alwall et al., MadGraph 5: Going Beyond. JHEP 06, 128 (2011). doi:10.1007/ JHEP06(2011)128. arXiv:1106.0522
- J. Pumplin et al., New generation of parton distributions with uncertainties from global QCD analysis. JHEP 07, 012 (2002). doi:10.1088/1126-6708/2002/07/012. arXiv:hep-ph/0201195
- 23. CMS Collaboration, Study of the underlying event at forward rapidity in pp collisions at \sqrt{s} = 0.9, 2.76, and 7 TeV. JHEP **04**, 072 (2013). doi:10.1007/JHEP04(2013)072. arXiv:1302.2394
- 24. CMS Collaboration, Study of the underlying event, b-quark fragmentation and hadronization properties in tt events, CMS-PAS TOP-13-007 (2013)
- 25. S. Jadach et al., The τ decay library TAUOLA, version 2.4. Comput. Phys. Commun. **76**, 361 (1993). doi:10.1016/0010-4655(93)90061-G
- GEANT4 Collaboration, GEANT4—a Simulation toolkit. Nucl. Instrum. Methods A 506, 250 (2003). doi:10.1016/S0168-9002(03)01368-8
- 27. R. Rahmat, R. Kroeger, A. Giammanco, The fast simulation of the CMS experiment. J. Phys. Conf. Ser. 396, 062016 (2012). doi:10.1088/1742-6596/396/6/062016. See also other proceedings, for example by D. Orbaker or S. Jain
- B. Allanach, SOFTSUSY: a program for calculating supersymmetric spectra. Comput. Phys. Commun. 143, 305 (2002). doi:10.1016/S0010-4655(01)00460-X. arXiv:hep-ph/0104145
- M. Mühlleitner, A. Djouadi, Y. Mambrini, SDECAY: a fortran code for the decays of the supersymmetric particles in the MSSM. Comput. Phys. Commun. 168, 46 (2005). doi:10. 1016/j.cpc.2005.01.012. arXiv:hep-ph/0311167
- A. Djouadi, M. Mühlleitner, M. Spira, Decays of supersymmetric particles: the program SUSY-HIT (SUspect-SdecaY-Hdecay-InTerface). Acta Physica Polonica B 38, 635 (2007). arXiv:hep-ph/0609292
- 31. A. Djouadi, J. Kalinowski, M. Spira, HDECAY: a program for Higgs boson decays in the standard model and its supersymmetric extension. Comput. Phys. Commun. **108**, 56 (1998). doi:10.1016/S0010-4655(97)00123-9. arXiv:hep-ph/9704448
- 32. W. Beenakker, R. Höpker, M. Spira, PROSPINO: a program for the production of supersymmetric particles in next-to-leading order QCD. arXiv:hep-ph/9611232
- 33. W. Beenakker et al., Squark and gluino production at hadron colliders. Nucl. Phys. B **492**, 51 (1997). doi:10.1016/S0550-3213(97)80027-2. arXiv:hep-ph/9610490
- 34. W. Beenakker et al., Stop production at hadron colliders. Nucl. Phys. B **515**, 3 (1998). doi:10. 1016/S0550-3213(98)00014-5. arXiv:hep-ph/9710451
- W. Beenakker et al., The production of charginos/neutralinos and sleptons at hadron colliders. Phys. Rev. Lett. 83, 3780 (1999). doi:10.1103/PhysRevLett.83.3780. arXiv:hep-ph/9906298. An erratum was published under. Phys. Rev. Lett. 100, 029901 (2008)
- A. Kulesza, L. Motyka, Threshold resummation for squark-antisquark and gluino-pair production at the LHC, Phys. Rev. Lett. 102, 111802 (2009). doi:10.1103/PhysRevLett.102.111802. arXiv:0807.2405
- A. Kulesza, L. Motyka, Soft gluon resummation for the production of gluino-gluino and squarkantisquark pairs at the LHC. Phys. Rev. D 80, 095004 (2009). doi:10.1103/PhysRevD.80. 095004. arXiv:0905.4749
- W. Beenakker et al., Soft-gluon resummation for squark and gluino hadroproduction. JHEP 12, 041 (2009). doi:10.1088/1126-6708/2009/12/041. arXiv:0909.4418
- W. Beenakker et al., Squark and gluino hadroproduction. Int. J. Mod. Phys. A 26, 2637 (2011). doi:10.1142/S0217751X11053560. arXiv:1105.1110
- 40. https://twiki.cern.ch/twiki/bin/view/CMSPublic/LumiPublicResults
- 41. CMS Collaboration, Performance of the missing transverse energy reconstruction by the CMS experiment in $\sqrt{s} = 8$ TeV pp data. JINST **10**, P02006 (2015) arXiv:1411.0511

References 145

 I. Azhgirey et al., Machine-induced background in the near-beam detectors (IR1/IR5). LHC-PROJECT NOTE-414 (2008)

- 43. H. Liu, Private communication
- 44. CMS Collaboration, Jet performance in pp collisions at $\sqrt{s}=7$ TeV. CMS-PAS JME-10-003 (2010)
- 45. CMS Collaboration, Search for new physics in events with same-sign dileptons and jets in pp collisions at $\sqrt{s} = 8$ TeV. JHEP **01**, 163 (2014). doi:10.1007/JHEP01(2014)163. arXiv:1311.6736
- 46. CMS Collaboration, Tau ID performance plots. CMS **DP-2014-015** (2014)
- 47. CMS Collaboration, Search for top-squark pair production in the single-lepton final state in pp collisions at $\sqrt{s} = 8$ TeV. Eur. Phys. J. C **73**, 2677 (2013). doi:10.1140/epjc/s10052-013-2677-2. arXiv:1308.1586
- 48. N. Kidonakis, Differential and total cross sections for top pair and single top production, in *Proceedings of the 20th International Workshop on Deep-Inelastic Scattering and Related Subjects (DIS 2012)*, p. 831 (2012). doi:10.3204/DESY-PROC-2012-02/251. arXiv:1205.3453
- 49. CMS Collaboration, Measurement of inclusive W and Z boson production cross sections in pp collisions at $\sqrt{s} = 8$ TeV. Phys. Rev. Lett. **112**, 191802 (2014). doi:10.1103/PhysRevLett. 112.191802. arXiv:1402.0923
- CMS Collaboration, Identification of b-quark jets with the CMS experiment. JINST 8, P04013 (2013). doi:10.1088/1748-0221/8/04/P04013. arXiv:1211.4462
- CMS Collaboration, Determination of jet energy calibration and transverse momentum resolution in CMS. JINST 6, P11002 (2011). doi:10.1088/1748-0221/6/11/P11002. arXiv:1107.4277
- 52. S. Ask et al., Using γ + jets production to calibrate the standard model $Z(\rightarrow \nu\bar{\nu})$ + jets background to new physics processes at the LHC. JHEP **10**, 058 (2011). doi:10.1007/ JHEP10(2011)058. arXiv:1107.2803
- 53. C. Kuo et al., Private communication
- 54. CMS Collaboration, Measurement of the ratio of the $Z/\gamma*+jets$ and photon+jets cross section in pp collisions at $\sqrt{s}=8$ TeV. CMS-PAS SMP-14-005 (2014)
- 55. CMS Collaboration, Measurement of the Z/γ^* +b-jet cross section in pp collisions at 7 TeV. JHEP **06**, 126 (2012). doi:10.1007/JHEP06(2012)126. arXiv:1204.1643
- ATLAS Collaboration, Measurement of differential production cross-sections for a Z boson in association with b-jets in 7 TeV proton-proton collisions with the ATLAS detector. JHEP 10, 141 (2014). arXiv:1407.3643
- 57. ATLAS and CMS Collaborations, Procedure for the LHC Higgs boson search combination in summer 2011. ATL-PHYS-PUB-2011-011, CMS-NOTE-2011-005 (2011)
- A.L. Read, Modified frequentist analysis of search results (The CL_s method). Workshop on confidence limits, CERN, Geneva, Switzerland, 17–18 Jan 2000, in *Proceedings OPEN-2000-005*, p. 81 (2000). doi:10.5170/CERN-2000-005.81
- 59. A.L. Read, Presentation of search results: the CL_s technique. J. Phys. G **28**, 2693 (2002). doi:10.1088/0954-3899/28/10/313
- G. Cowan et al., Asymptotic formulae for likelihood-based tests of new physics. Eur. Phys. J. C 71, 1554 (2011). doi:10.1140/epic/s10052-011-1554-0. arXiv:1007.1727
- CMS Collaboration, CMS luminosity based on pixel cluster counting—summer 2013 update. CMS-PAS LUM-13-001 (2013)
- 62. M. Botje et al., The PDF4LHC working group interim recommendations. arXiv:1101.0538
- 63. CMS Collaboration, Search for supersymmetry using razor variables in events with b-jets in pp collisions at 8 TeV. Phys. Rev. D **91**, 052018 (2015) CMS-PAS SUS-13-004 (2013)
- 64. CMS Collaboration, Search for direct production of bottom squark pairs. CMS-PAS SUS-13-018 (2014). Publication under preparation
- CMS Collaboration, Search for top squarks decaying to a charm quark and a neutralino in events with a jet and missing transverse momentum. CMS-PAS SUS-13-009 (2014). Publication under preparation
- 66. CMS Collaboration, Search for top squarks in multijet events with large missing momentum in proton-proton collisions at $\sqrt{s}=8$ TeV. CMS-PAS SUS-13-015 (2013). Publication under preparation

- 67. ATLAS Collaboration, Search for direct third-generation squark pair production in final states with missing transverse momentum and two *b*-jets in $\sqrt{s} = 8$ TeV *pp* collisions with the ATLAS detector. JHEP **10**, 189 (2013). doi:10.1007/JHEP10(2013)189. arXiv:1308.2631
- 68. ATLAS Collaboration, Search for direct pair production of the top squark in all-hadronic final states in proton-proton collisions at $\sqrt{s}=8$ TeV with the ATLAS detector. JHEP **09**, 015 (2014). doi:10.1007/JHEP09(2014)015. arXiv:1406.1122
- 69. ATLAS Collaboration, Search for pair-produced third-generation squarks decaying via charm quarks or in compressed supersymmetric scenarios in pp collisions at √s = 8TeV with the ATLAS detector. Phys. Rev. D 90, 052008 (2014). doi:10.1103/PhysRevD.90.052008. arXiv:1407.0608
- 70. https://twiki.cern.ch/twiki/bin/view/CMSPublic/PhysicsResultsSUS
- CMS Collaboration, Projected performance of an upgraded CMS detector at the LHC and HL-LHC: contribution to the snowmass process. arXiv:1307.7135
- W.S. Cho et al., Transverse mass for pairs of gluinos. Phys. Rev. Lett. 100, 171801 (2008). doi:10.1103/PhysRevLett.100.171801. arXiv:0709.0288
- 73. B. Gripaios, Transverse observables and mass determination at hadron colliders. JHEP **02**, 053 (2008). doi:10.1088/1126-6708/2008/02/053. arXiv:0709.2740
- A.J. Barr, B. Gripaios, C.G. Lester, Weighing wimps with kinks at colliders: invisible particle mass measurements from endpoints. JHEP 02, 014 (2008). doi:10.1088/1126-6708/2008/02/ 014. arXiv:0711.4008
- 75. W.S. Cho et al., Measuring superparticle masses at hadron collider using the transverse mass kink. JHEP **02**, 035 (2008). doi:10.1088/1126-6708/2008/02/035. arXiv:0711.4526
- W.S. Cho et al., M_{T2}-assisted on-shell reconstruction of missing momenta and its application to spin measurement at the LHC. Phys. Rev. D 79, 031701 (2009). doi:10.1103/PhysRevD.79. 031701. arXiv:0810.4853
- 77. W.S. Cho et al., Mass and spin measurement with M_{T2} and MAOS momentum. Nucl. Phys. B (Proc. Suppl.) 200, 103 (2010). doi:10.1016/j.nuclphysbps.2010.02.072. arXiv:0909.4853
- 78. A. Barr et al., Guide to transverse projections and mass-constraining variables. Phys. Rev. D 84, 095031 (2011). doi:10.1103/PhysRevD.84.095031. arXiv:1105.2977
- 79. R. Mahbubani, K.T. Matchev, M. Park, Re-interpreting the Oxbridge stransverse mass variable M_{T2} in general cases. JHEP **03**, 134 (2013). doi:10.1007/JHEP03(2013)134. arXiv:1212.1720
- 80. W.S. Cho et al., On-shell constrained M_2 variables with applications to mass measurements and topology disambiguation. JHEP **08**, 070 (2014). doi:10.1007/JHEP08(2014)070. arXiv:1401.1449

Chapter 8

Assessment of a Search for Stop Pair Production in Dileptonic Events

It has been mentioned in Sect. 2.3 that the lighter stop is the lightest squark for many SUSY scenarios. It could be the only accessible strongly produced sparticle at the LHC. Therefore, a large effort by both the CMS [1] and ATLAS [2–6] collaborations is invested on searches for direct stop production.

In R-parity conserving SUSY, stop pair production usually leads to similar final states as $t\bar{t}$ production. The stop likely decays via

$$\widetilde{t}_1 \to t\widetilde{\chi}_1^0$$
 and/or $\widetilde{t}_1 \to b\widetilde{\chi}_1^+ \to bW^+\widetilde{\chi}_1^0$.

However, other possible decays exist: stop decays could involve the $\widetilde{\chi}^0_2$ instead of $\widetilde{\chi}^0_1$, furthermore, the $\widetilde{\chi}^\pm_1$ could decay via other sparticles like $\widetilde{l}\nu$ or $\widetilde{\nu}l$. Also multibody decays (like $\widetilde{t}_1 \to bqq'\widetilde{\chi}^0_1$), and decays involving CKM matrix elements and loops (like $\widetilde{t}_1 \to c\widetilde{\chi}^0_1$) might be possible.

In most cases, the numbers and nature of the visible final state particles are the same as for $t\bar{t}$ events: one possible final state is composed out of events with two charged leptons (*dileptonic* events) and two b-quark jets plus particles from ISR/FSR, and $E_{\rm T}^{\rm miss}$ because of the neutrinos and LSPs.

This chapter describes a study testing the discrimination power between a signal from stop pair production and SM background for several variables in this final state. Most variables are based on the M_{T2} definition, Eq. (6.2), but also a different kind of variable is introduced. The study presented here is not a full analysis. No attempt on predicting the SM background or similar was done. It assesses only the usage of search variables to discriminate between the stop production signal and the SM background. The study has been presented within the CMS collaboration, however, no public documentation exists.

8.1 Basic Event Selection and Signal Models

The final state of the signal of interest contains at least two differently charged leptons and two b-quark jets. As the purity of taus is not high enough, we consider only events with a $\mu^+\mu^-$, e^+e^- or $\mu^\pm e^\mp$ pair. An event containing a third charged lepton is rejected. Leptons are required to have $p_T > 20\,(10)\,\text{GeV}$ for the leading (trailing) lepton and $|\eta| < 2.4$. For events with same-flavor leptons $(\mu^+\mu^-/e^+e^-)$, we additionally require $|M_{ll}-M(Z)|>10\,\text{GeV}$. Thus, the SM background due to Z+jets events is heavily reduced. The event is required to contain at least two b jets. Since b jets can also originate from ISR/FSR, no veto on events with more than two b jets is applied. The b jets are required to pass $p_T > 40\,\text{GeV}$ and $|\eta| < 2.4$. In principle, one could also require a certain amount of E_T^{miss} . However, a selection on E_T^{miss} will be applied implicitly via the search variables. Finally, events affected by electronic noises, dead detector regions, misreconstructions, or physics noises are rejected. The definitions of the objects used are given in Chap. 5.

The SM simulation used in this study is the same as described in Sect. 7.1. The signal models shown here are produced with the PYTHIA 6.4 generator, the sparticle decay branching fractions are calculated with SDECAY. The generated signal events are processed with the fast simulation of the CMS detector response. The considered signal models contain the following stop decay modes:

• $\widetilde{t}_1 \to t\widetilde{\chi}_1^0 \to bW^+\widetilde{\chi}_1^0 \to bl^+\nu_l\widetilde{\chi}_1^0$ ("via t"), • $\widetilde{t}_1 \to b\widetilde{\chi}_1^+ \to bW^+\widetilde{\chi}_1^0 \to bl^+\nu_l\widetilde{\chi}_1^0$ ("via $\widetilde{\chi}_1^\pm$ "), • $\widetilde{t}_1 \to b\widetilde{\chi}_1^+ \to b\nu\widetilde{l}^+ \to bl^+\nu_l\widetilde{\chi}_1^0$ ("via \widetilde{l} "), • $\widetilde{t}_1 \to b\widetilde{\chi}_1^+ \to bl^+\widetilde{\nu}$ ("via $\widetilde{\nu}$ ").

As the $\widetilde{\nu}$ decay is usually fully invisible ($\nu\widetilde{\chi}_1^0$), the sneutrino can effectively be treated as LSP. In the simulation, the latter two decays are modeled within one sample with 50% branching ratio for each decay chain. The label in parentheses is used as the identifier of the decay chain.

8.2 M_{T2} -based Search Variables

The M_{T2} variable has been discussed in detail in Sects. 6.1 and 6.3. Dileptonic stop searches are ideal for a M_{T2} -based search, as the two stop decays are often identical. We can define three variants of M_{T2} :

- $M_{T2}(lb)$: each visible system is composed out of one charged lepton and one b jet.
- $M_{T2}(b)$: each visible system is composed out of one b jet. As the leptons are downstream, the \vec{E}_{T}^{miss} is replaced by $\vec{E}_{T}^{miss} + \vec{p}_{T}(l^{+}l^{-})$ when calculating $M_{T2}(b)$.
- $M_{T2}(l)$: each visible system is composed out of one lepton. As the b jets are upstream of the W boson or $\tilde{\chi}_1^{\pm}$ decay, they are considered as UTM.

Each of these M_{T2} definitions will have different endpoints depending on the process. The endpoints are given in Table 8.1 for the case of no ISR and correct

Decay	$M_{\text{T2}}(lb)$	$M_{\text{T2}}(b)$	$M_{\text{T2}}(l)$
Via t	$M(\widetilde{t}_1)$	$M(\widetilde{t}_1)$	×
Via $\tilde{\chi}_1^{\pm}$	$M(\widetilde{t}_1)$	$M(\widetilde{t}_1) \left(1 - \frac{M^2(\widetilde{\chi}_1^{\pm})}{M^2(\widetilde{t}_1)}\right)$	$\sim M(\widetilde{\chi}_1^{\pm})$
Via \tilde{l}	$M(\widetilde{t}_1)$	$M(\widetilde{t_1}) \left(1 - \frac{M^2(\widetilde{\chi}_1^{\pm})}{M^2(\widetilde{t_1})}\right)$	$\sim M(\widetilde{\chi}_1^{\pm})$
Via $\tilde{\nu}$	$M(\widetilde{t}_1)\left(1-\frac{M^2(\widetilde{\nu})}{M^2(\widetilde{t}_1)}\right)$	$M(\widetilde{t}_1) \left(1 - \frac{M^2(\widetilde{\chi}_1^{\pm})}{M^2(\widetilde{t}_1)}\right)$	
Top quark	M(t)	$M(t)\left(1-\frac{M^2(W)}{M^2(t)}\right)$	M(W)

Table 8.1 M_{T2} endpoints for different stop decay modes and for $t\bar{t}$ events in case of no UTM and correct testmass

The endpoint of $M_{\rm T2}(l)$ is not available for the stop decays via top quarks, as the leptons and $E_{\rm T}^{\rm miss}$ do not form a complete decay chain of an (intermediate) particle

testmass. Several endpoints for $M_{T2}(lb)$ and $M_{T2}(l)$ are approximations. They are not analytical due to the presence of unseen particles of different nature, except for the stop decay via $\tilde{\nu}$ and the top quark decay. The endpoints of $M_{T2}(l)$ should be taken with care, as the event always contains UTM because of the two b jets.

Hereafter, we will consider only one model point for plotting: $\tilde{t}_1 \to b \tilde{\chi}_1^+ \to b W^+ \tilde{\chi}_1^0 \to b l^+ \nu_l \tilde{\chi}_1^0$ with $M(\tilde{t}_1) = 400 \, \text{GeV}$, $M(\tilde{\chi}_1^\pm) = 300 \, \text{GeV}$, and $M(\tilde{\chi}_1^0) = 100 \, \text{GeV}$. As only few model points were studied, no exact numbers will be stated, the discussion is kept generic. The conclusions are the same for all tested models, although the exact discrimination strength depends on the model.

8.2.1 Search with $M_{T2}(lb)$

The $M_{T2}(lb)$ variable cannot be constructed straight away: there are two combinations of forming the lb pairs out of the two leptons and the two b jets. If more than two b jets are available, more combinations are possible. Going to a simple parton level simulation of $t\bar{t}$ production, we find that for the correct combination of lb pair (that is each lepton—b-quark pair originates from the same top quark decay), $M_{T2}(lb)$ has an endpoint at the top quark mass, while the wrong combination can yield values above the top quark mass, see Fig. 8.1.

We cannot know the correct pairing. Therefore, we calculate M_{T2} for all combinations of lepton-b-jet pairing, and take the smallest value of M_{T2} as the $M_{T2}(lb)$ value of the event.

Unfortunately, we find a large contribution of $t\bar{t}$ +jets events at high $M_{T2}(lb)$, see Fig. 8.2. The tail is due to events, where at least one of the selected b jets does not come from a top quark decay, see Fig. 8.3. There are two reasons for that: The first one is the b-quark jet tagging efficiency, which is about 70 %. The other one is the jet acceptance. In both cases, instead of picking the correct b-quark jet, a b-tagged ISR jet is used in the $M_{T2}(lb)$ calculation. Another contribution in the tail of the $M_{T2}(lb)$ distribution is tW+jets production with a b-tagged ISR jet.

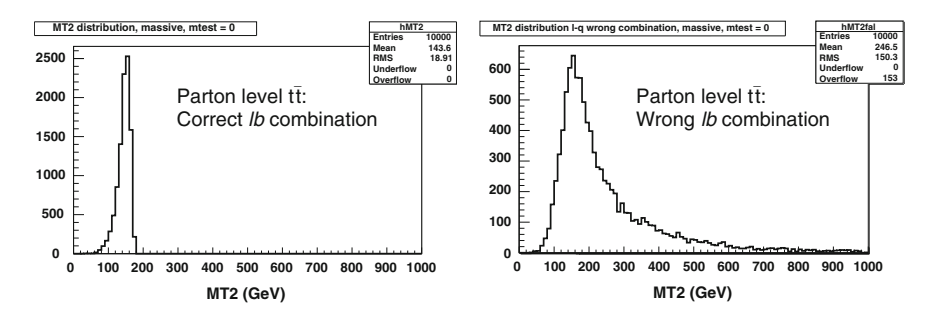
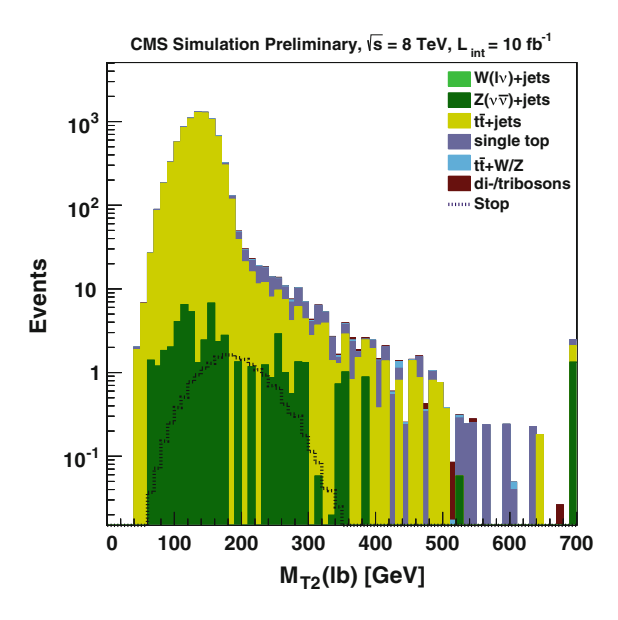


Fig. 8.1 The $M_{T2}(lb)$ distribution for $t\bar{t}$ events at parton level. *Left* correct pairing of the lepton–b-quark system. *Right* wrong pairing of the lepton–b-quark system

Fig. 8.2 The $M_{T2}(lb)$ distribution for simulated signal and SM background events. The simulation is normalized to an integrated luminosity of 10 fb⁻¹



We can suppress the contribution of those events with another variable: M_{lb} , the invariant lepton–b-jet mass. For top quark decays, $M_{lb} \leq M(t) \sqrt{1 - \frac{M^2(W)}{M^2(t)}} = 153 \, \text{GeV}$. For all the considered stop decay modes except the one via t, the M_{lb} variable is not constrained to such low values. The M_{lb} distribution for signal and SM background is shown in Fig. 8.4a. If we apply a selection on this variable, $M_{lb} < 180 \, \text{GeV}$ for both lepton–b-jet pairs, we significantly clean up the tail in the $M_{T2}(lb)$ distribution for the SM background, because the M_{lb} variable can exceed 180 GeV for lepton–b-jet pairs with a b-tagged ISR jet. Therefore, we strongly enhance the discrimination power of this variable, see Fig. 8.4b, even though we might remove some good signal events.

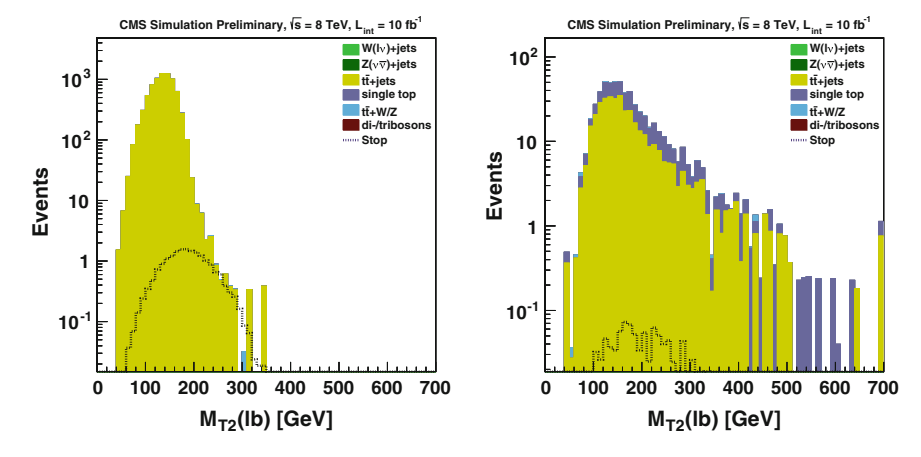


Fig. 8.3 The $M_{T2}(lb)$ distribution for simulated signal and SM background events. The simulation is normalized to an integrated luminosity of 10 fb^{-1} . *Left* both b jets originate from a stop or top quark decay. *Right* one of the two b jets does not originate from a stop or top quark decay

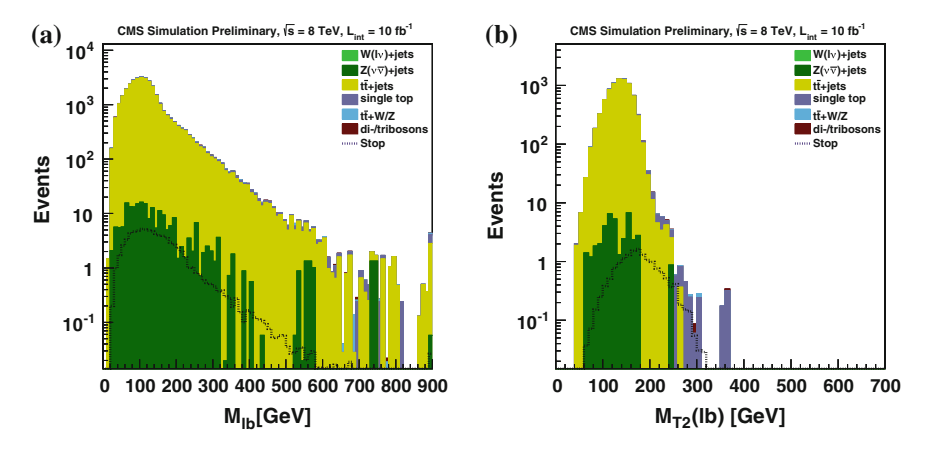


Fig. 8.4 Effect of the M_{lb} selection on the $M_{T2}(lb)$ distribution. **a** The M_{lb} distribution for all possible lepton–b-jet pairs. **b** The $M_{T2}(lb)$ distribution after requiring that the lepton–b-jet pairs pass $M_{lb} < 180 \,\text{GeV}$

8.2.2 Search with $M_{T2}(b)$

The $M_{T2}(b)$ variable does not consider the leptons as visible objects, the dilepton- \vec{p}_T is added to the \vec{E}_T^{miss} . Then, $M_{T2}(b)$ is calculated for all choices of two b jets as visible systems. We take the smallest one as the $M_{T2}(b)$ value of the event.

Because of events with a b-tagged ISR jet and a missed b-quark jet from the top quark decay, the $M_{T2}(b)$ variable shows no discrimination power, the tail is dominated by $t\bar{t}$ +jets events as shown in Fig. 8.5a. We disregard this variable as signal selection variable.

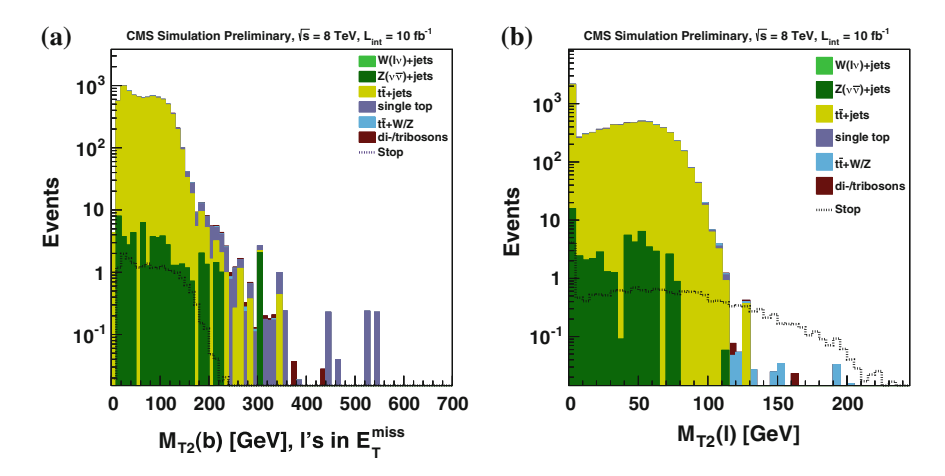


Fig. 8.5 The $M_{T2}(b)$ (**a**) and $M_{T2}(l)$ (**b**) distributions for simulated signal and SM background events. The simulation is normalized to an integrated luminosity of 10 fb⁻¹

8.2.3 Search with $M_{T2}(l)$

The third variant of M_{T2} is $M_{T2}(l)$. This variable is purely constructed out of the two charged leptons and E_T^{miss} . Hence, it does not suffer from the problem that a b jet from the top quark decay was missed and an ISR jet was used in the calculation of M_{T2} . In Fig. 8.5b, the $M_{T2}(l)$ distribution is shown. We find strong discrimination power for $M_{T2}(l) \gtrsim 120$ GeV, a signal-over-background ratio of $\gtrsim 1$ is achieved for the shown SUSY model.

As the discrimination power is very good for this variable, one can try to select a larger phase space. An obvious choice is allowing also events with 1 b jet, as the b jets are not required for the $M_{\rm T2}(l)$ calculation. Still, two jets are required. Thus, we also collect those events, where one b-quark jet from the stop decay was not tagged as a b jet. We find, that $M_{\rm T2}(l)$ still leads to a strong discrimination between signal and background events. This can be appreciated from Fig. 8.6a. One can try to do the same for $M_{\rm T2}(lb)$. Here, the second "b" for finding the lepton—"b-jet" pairs is obtained from the list of all jets. For the $M_{\rm T2}(lb)$ distribution, the discrimination power is extremely small, as can be seen from Fig. 8.6b.

8.2.4 Search Using Multiple Variants of M_{T2}

We found so far that $M_{T2}(l)$ has a very good signal sensitivity, $M_{T2}(lb)$ has only little signal discrimination power against the SM background, while $M_{T2}(b)$ shows no sensitivity for signal discrimination. For $M_{T2}(l) \lesssim 120 \,\text{GeV}$, the $M_{T2}(l)$ variable itself is not powerful enough. We can combine the information of $M_{T2}(l)$ and

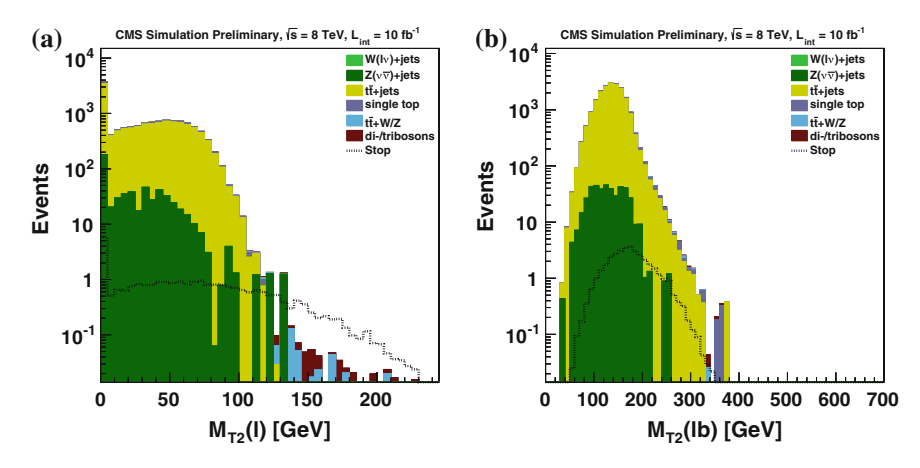


Fig. 8.6 The $M_{\rm T2}(l)$ (**a**) and $M_{\rm T2}(lb)$ (**b**) distributions for events with one b jet for signal and SM background simulation. The simulation is normalized to an integrated luminosity of 10 fb⁻¹. For the $M_{\rm T2}(lb)$ distribution both lepton–jet pairs need to pass $M_{lb} < 180 \, {\rm GeV}$

 $M_{\rm T2}(lb)$ to increase the signal sensitivity for this region. A loose cut on $M_{\rm T2}(l)$, for example $M_{\rm T2}(l) \geq 85$ GeV, already rejects a lot of SM background events. Then, the $M_{\rm T2}(lb)$ distribution can be used to discriminate the signal. In Fig. 8.7, the $M_{\rm T2}(lb)$ distributions for ≥ 2 b jets (left) and 1 b jet (right) are shown after requiring $M_{lb} < 180$ GeV for both lepton–jet pairs and $M_{\rm T2}(l) \geq 85$ GeV. The region with $M_{\rm T2}(lb) \gtrsim 220$ GeV shows a nice signal-to-background ratio.

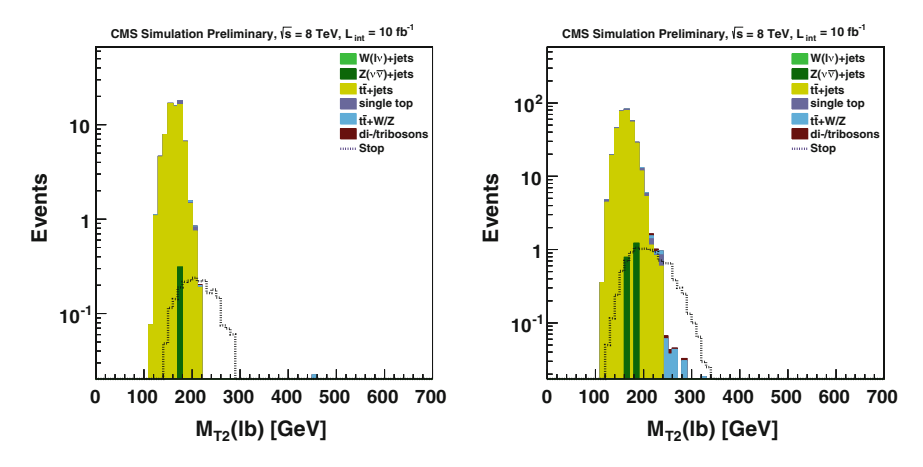


Fig. 8.7 The $M_{T2}(lb)$ distributions for simulated signal and SM background events with ≥ 2 b jets (*left*) and 1 b jet (*right*) after requiring $M_{lb} < 180$ GeV for both lepton–jet pairs, and $M_{T2}(l) \geq 85$ GeV. The simulation is normalized to an integrated luminosity of 10 fb⁻¹

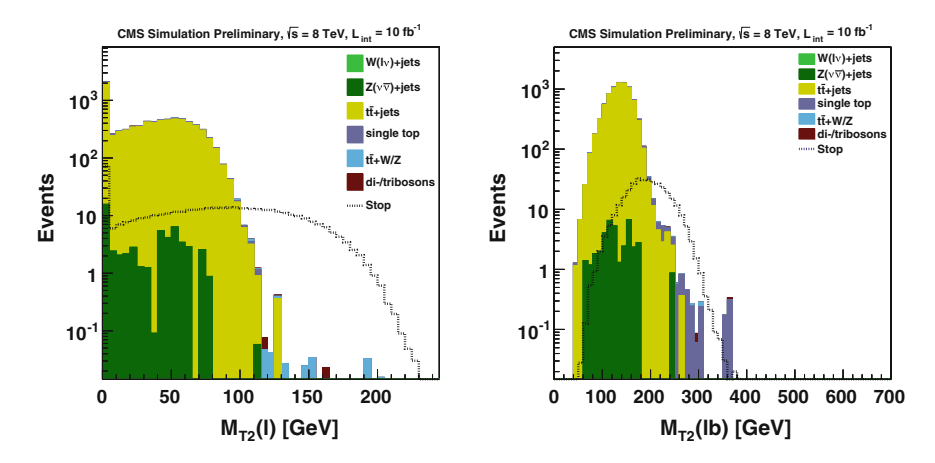


Fig. 8.8 The $M_{\rm T2}(l)$ (*left*) and $M_{\rm T2}(lb)$ (*right*) distributions for simulated signal and SM background events with at least two b jets. The simulation is normalized to an integrated luminosity of $10~{\rm fb^{-1}}$. For the $M_{\rm T2}(lb)$ distribution, both lepton–b-jet pairs need to pass $M_{lb} < 180~{\rm GeV}$. In this signal, the stop decays via sleptons or sneutrinos

8.2.5 Comment on the Stop Decays via Sleptons or Sneutrinos

It has been mentioned before that the general features observed above are valid for all considered signal models. However, out of the four stop decay modes mentioned above, the ones labeled as "via \tilde{l} " or "via $\tilde{\nu}$ " always lead to a final state containing two charged leptons, while for the other two decay modes, the branching ratio to a final state with two charged leptons (e or μ only) is roughly 4% due to the W boson branching ratio into electrons and muons. Therefore, for the stop decay modes via sleptons or sneutrinos, we expect an effective dileptonic stop production cross section that is roughly 20 times larger than the one of the other stop decay modes. To demonstrate this, we define a signal model with a mixture of $\tilde{t}_1 \to b\tilde{\chi}_1^+ \to b\nu\tilde{l}^+ \to bl^+\nu_l\tilde{\chi}_1^0$ and $\tilde{t}_1 \to b\tilde{\chi}_1^+ \to bl^+\tilde{\nu}$ with branching ratio of 50% for each decay mode, and $M(\tilde{t}_1) = 400\,\text{GeV}$, $M(\tilde{\chi}_1^\pm) = 300\,\text{GeV}$, $M(\tilde{l}) = M(\tilde{\nu}) = 200\,\text{GeV}$ and $M(\tilde{\chi}_1^0) = 100\,\text{GeV}$. We observe in Fig. 8.8 the tremendous dominance of signal events over SM background events for high values of M_{T2} for both the $M_{T2}(l)$ and $M_{T2}(lb)$ distributions.

8.3 Distinguishing Direct Stop Pair Production from $t\bar{t}$ +jets Production Using the Event Kinematics

We know that the kinematics of $t\bar{t}$ events are constrained by the properties of the top quarks and W bosons. Let us denote

$$t_i \to b_i W_i^+ \to b_i l_i^+ \nu_i \text{ with } i = 1, 2.$$

The momenta of the b quarks and the charged leptons can be measured. In total, there are six unknowns, the momenta of the two neutrinos. However, we can impose four mass constraints (the top quark and W boson masses for both decays) and two momentum constraints from $\vec{E}_{\rm T}^{\rm miss}$. These six constraints should allow to determine the neutrino momenta.

The constraints lead to a fourth-order equation [7] that can be solved. A test on simulated $t\bar{t}$ events shows that, for perfect detector resolution, the solution is found in 99.8% of all cases. However, if the $t\bar{t}$ signal is smeared with the experimental resolution, the efficiency of finding the solution drops to 72.2%. It is expected to further decrease if ISR is present.

Therefore, a discriminant has been developed to quantify how " $t\bar{t}$ -like" an event is. First, let us state the constraints:

$$M^{2}(t) = (p_{b_{1}} + p_{l_{1}} + q_{1})^{2} = (p_{b_{2}} + p_{l_{2}} + q_{2})^{2},$$

$$M^{2}(W) = (p_{l_{1}} + q_{1})^{2} = (p_{l_{2}} + q_{2})^{2},$$

$$\vec{E}_{T}^{\text{miss}} = \vec{q}_{T,1} + \vec{q}_{T,2}.$$
(8.1)

The four-momenta of the neutrinos, b quarks and charged leptons are denoted by q_i , p_{b_i} and p_{l_i} , respectively. Instead of solving this system of equations, we parameterize it by two parameters, for example $q_{z,1}$ and $q_{z,2}$. For notation purposes, we define auxiliary variables

$$\begin{split} A_i &= \frac{1}{2} \left(\frac{M^2(t)}{|\vec{p}_{b_i}|} - \frac{M^2(W)}{|\vec{p}_{l_i}|} \right), \qquad \qquad c_1 = \frac{M_{l_1b_1}^2 + M_{W_1}^2}{2|\vec{p}_{b_1}|} - A_1, \\ \vec{w}_i &= \frac{\vec{p}_{b_i}}{|\vec{p}_{b_i}|} - \frac{\vec{p}_{l_i}}{|\vec{p}_{l_i}|}, \qquad \qquad c_2 = \frac{M_{l_2b_2}^2 + M_{W_2}^2}{2|\vec{p}_{b_2}|} - A_2 - \vec{w}_2 \cdot \vec{E}_{\mathrm{T}}^{\mathrm{miss}}. \end{split}$$

In these expressions, $M_{l_ib_i}$ is the invariant mass of the charged lepton-b-quark pair l_ib_i , and M_{W_i} the invariant mass of the charged lepton-neutrino pair $l_i\nu_i$. Similar, we define M_{t_i} as the invariant mass of the charged lepton-neutrino-b-quark triplet $l_i\nu_ib_i$. For correct \vec{q}_i , we should obtain $M_{W_i}=M(W)$ and $M_{t_i}=M(t)$ for a $t\bar{t}$ event

Using these auxiliary variables and assuming the b quarks and the charged leptons to be massless, we arrive at two constrained equations

$$-\vec{w}_i \cdot \vec{q}_i + c_i = 0, \quad i = 1, 2.$$

Thus, we can parameterize the transverse momenta of the neutrinos by $q_{z,1}$ and $q_{z,2}$:

$$q_{x,1} = \frac{w_{y,2}(w_{z,1}q_{z,1} - c_1) + w_{y,1}(w_{z,2}q_{z,2} - c_2)}{w_{y,1}w_{x,2} - w_{x,1}w_{y,2}}, \qquad q_{x,2} = (E_{\mathrm{T}}^{\mathrm{miss}})_x - q_{x,1},$$

$$q_{y,1} = \frac{w_{x,2}(w_{z,1}q_{z,1} - c_1) + w_{x,1}(w_{z,2}q_{z,2} - c_2)}{w_{x,1}w_{y,2} - w_{y,1}w_{x,2}}, \qquad q_{y,2} = (E_{\mathrm{T}}^{\mathrm{miss}})_y - q_{y,1}.$$

$$(8.2)$$

Within the 2D plane $(q_{z,1}, q_{z,2})$, we should be able to find a point such that $M_{W_i} \approx M(W)$ and $M_{t_i} \approx M(t)$ for a $t\bar{t}$ event. But this does not have to be true for events of direct stop pair production because of the presence of the two LSPs. This allows us to define a discriminator

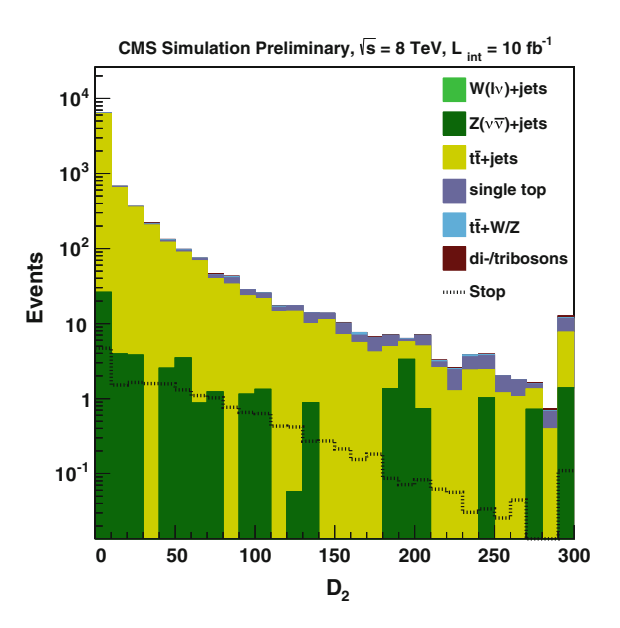
$$D_{2} = \frac{1}{2} \min_{q_{z,1}, q_{z,2}} \left([M_{W_{1}} - M(W)]^{2} + [M_{W_{2}} - M(W)]^{2} + [M_{t_{1}} - M(t)]^{2} + [M_{t_{2}} - M(t)]^{2} \right)^{1/2}.$$
(8.3)

A value of D_2 compatible with zero should reflect that the event is $t\bar{t}$ -like, whereas for a $\tilde{t}_1\tilde{t}_1^*$ event, D_2 can have large values.

Note that the auxiliary variables c_i depend on M_{W_i} . This introduces a loop in the calculation of D_2 , as we need M_{W_i} in order to calculate $q_{x,i}$ and $q_{y,i}$. We, therefore, approximate the calculation of D_2 by replacing M_{W_i} by the true value M(W) in the calculation of c_i .

The D_2 distribution is obtained as follows: First, we test if the fourth-order equation [7] can be solved for an event. If the event kinematics solves the equation, we set $D_2 = 0$. Otherwise, we obtain D_2 by finding the values of $q_{z,1}$ and $q_{z,2}$, for which the minimum in Eq. (8.3) is reached. We test all combinations of lepton-b-jet pairing lb, and choose the smallest value of Eq. (8.3) as the D_2 value for the event.

Fig. 8.9 The D_2 distribution for simulated signal and SM background events. The simulation is normalized to an integrated luminosity of 10 fb^{-1}



The distribution of D_2 in simulated signal and SM background events is shown in Fig. 8.9. Unfortunately, we do not observe any signal-background discrimination for any selection on D_2 . It appears that misreconstruction (not selecting all b-quark jets from top quark decays) and detector resolution enlargen the contribution of $t\bar{t}$ +jets events for high values of D_2 , such that the variable does not discriminate between the signal and the SM background. Also, often small D_2 values are obtained for the stop signal events.

8.4 Summary

The ability of discriminating a signal from stop pair production against SM background processes has been tested for several search variables in events containing at least two charged leptons. It was found that $M_{T2}(l)$, the M_{T2} variable calculated with the two charged leptons as visible systems, is very well suited as search variable: for the main background of $t\bar{t}$ +jets production, we expect $M_{T2}(l) \lesssim M(W)$, while this bound does not hold for the signal because of the momenta of the two LSPs present in a $\tilde{t}_1\tilde{t}_1^*$ +jets event.

Another variant of the M_{T2} variable, $M_{T2}(lb)$, calculated with one b jet and one charged lepton for each visible system, was found to provide only small discrimination power: the $M_{T2}(lb)$ variable in $t\bar{t}$ +jets events can reach high values, when a b-quark jet, originating from a top quark decay, has not been reconstructed as a b jet. However, using a loose selection on $M_{T2}(l)$ increases the discrimination power of $M_{T2}(lb)$.

Another variant of M_{T2} has been tested using only b jets as visible systems. Also a discriminant based on kinematic constraints has been developed. Both variables have been found to not discriminate between signal events from stop pair production and SM background events.

References

- 1. CMS Collaboration, Search for top-squark pair production in the single-lepton final state in pp collisions at $\sqrt{s} = 8$ TeV. Eur. Phys. J. C **73**, 2677 (2013). doi:10.1140/epjc/s10052-013-2677-2. arXiv:1308.1586
- 2. ATLAS Collaboration, Search for pair-produced third-generation squarks decaying via charm quarks or in compressed supersymmetric scenarios in pp collisions at $\sqrt{s}=8$ TeV with the ATLAS detector. Phys. Rev. D **90**, 052008 (2014). doi:10.1103/PhysRevD.90.052008. arXiv:1407.0608
- 3. ATLAS Collaboration, Search for top squark pair production in final states with one isolated lepton, jets, and missing transverse momentum in $\sqrt{s} = 8$ TeV pp collisions with the ATLAS detector. JHEP 11, 118 (2014). arXiv:1407.0583
- 4. ATLAS Collaboration, Search for direct pair production of the top squark in all-hadronic final states in proton-proton collisions at $\sqrt{s} = 8$ TeV with the ATLAS detector, JHEP **09**, 015 (2014). doi:10.1007/JHEP09(2014)015. arXiv:1406.1122

- 5. ATLAS Collaboration, Search for direct top-squark pair production in final states with two leptons in pp collisions at $\sqrt{s} = 8$ TeV with the ATLAS detector, JHEP **06**, 124(2014). doi:10. 1007/JHEP06(2014)124. arXiv:1403.4853
- 6. ATLAS Collaboration, Search for direct third-generation squark pair production in final states with missing transverse momentum and two b-jets in $\sqrt{s} = 8$ TeV pp collisions with the ATLAS detector, JHEP 10, 189(2013). doi:10.1007/JHEP10(2013)189. arXiv:1308.2631
- L. Sonnenschein, Analytical solution of tt dilepton equations. Phys. Rev. D 73, 054015 (2006). doi:10.1103/PhysRevD.73.054015. arXiv:hep-ph/0603011. An erratum has been published in Phys. Rev. D 78, 079902 (2008)

Part III Studies for the Upgrade Program of the Compact Muon Solenoid Detector

Chapter 9 Upgrade Efforts for the Compact Muon Solenoid Detector

The third part of this dissertation contains two studies related to the upgrade efforts for the CMS detector. This chapter serves as an introduction. The reasons and general ideas for future detector upgrades of the CMS experiment are summarized.

The performance of the LHC has been extraordinary. Already in the first years of operation, the performance has reached or even exceeded the design values for various parameters. This can be appreciated from Table 4.1.

The high luminosities provided by the LHC to the experiments can create issues related to the performance of the experiments [1]: A high instantaneous luminosity leads to high numbers of pileup interactions. The trigger must be able to discriminate bunch-crossings with a hard interaction against bunch-crossings with many soft interactions, such that the trigger performance is not biased by pileup interactions. Also, the experiments must be able to reconstruct a hard-collision event and reduce the influence of pileup interactions to the event kinematics.

The second issue is radiation damage: high doses of radiation will damage the materials of several CMS detector components. For some subdetectors, which are exposed to high radiation doses, the damage becomes severe and their capability of detecting particles decreases strongly.

Other, minor issues can also degrade the performance of the CMS experiment [1]. Already during the long shutdown of the LHC in 2014, parts of the CMS experiment have been upgraded, such as the CSC and RPC systems [2]. These upgrades were not addressing the degradation of the detector performance, but are rather improvements of the muon detection capability at high $|\eta|$.

The first major upgrade, the *Phase-I* upgrade, is anticipated for 2016–2018. The pixel detector, the electronics of the HCAL, and the L1 trigger system will be modified or replaced.

The pixel detector is the innermost subdetector of the CMS experiment. Therefore, it is exposed to high radiation doses. The induced damage to the read-out chips of the pixel modules will lead to significant data losses. In order to avoid this, the complete pixel detector will be replaced. The new detector is expected to be more insensitive to radiation, but also be able to increase the performance of reconstructing charged

particles. The design of the upgraded pixel detector will be introduced in Chap. 10, a detailed discussion can be found in [3].

The electronics of the HCAL subdetector will be replaced both in the forward and barrel parts. The PMTs, currently used in the HF subdetector, will be replaced by multi-anode tubes. The new read-out electronics are less affected by anomalous signals, and they are also able to act as time-to-digital converters. The electronics of the HB, HE and HO components, the HPDs, will be replaced by multipixel Geigermode APDs, which are silicon photomultipliers (SiPMs). The HPDs are affected by the appearances of electric discharges when high voltages are applied. This problem does not occur for the SiPMs. Another advantage of the SiPMs is their fine segmentation. This allows for a better reconstruction of particle showers in the HCAL subdetector. A detailed description of the HCAL Phase-I upgrade is given in [4].

The L1 trigger system is the third system that will be upgraded. The upgrade will happen already for 2015/2016. The bandwidth of the optical links will be increased, the trigger logic will be implemented on field programmable gate arrays, and the electronics will be implemented in the standard μ TCA. These changes allow for more flexibility in the trigger logic such as defining isolation criteria at the L1 trigger. Also, subdetector information can be combined: for example, the information of all three muon subsystems will be combined in order to increase the efficiency of reconstructing muons at L1 trigger. The upgrade of the L1 trigger system is discussed in more detail in [5].

It is foreseen that the LHC will provide about 300 fb⁻¹ integrated luminosity of pp collision data at $\sqrt{s} = 13$ –14 TeV until 2022. After this phase (*Phase-II*), the LHC will be upgraded to the High-Luminosity LHC (HL-LHC) [6]. The HL-LHC is expected to reach an instantaneous luminosity of about 10^{35} cm⁻² s⁻¹, a value, which is ten times higher than the design value of the LHC. With this upgrade, the HL-LHC is expected to provide much more pp collision data to its experiments than initially planned. For the ATLAS and CMS experiments, the data amount will correspond to an integrated luminosity of about 3000 fb⁻¹.

In order to cope with the new conditions because of the higher instantaneous luminosity of the HL-LHC, several components of the CMS detector need to be upgraded. A general discussion about challenges for the detectors after the HL-LHC upgrade can be found in [7]. The current upgrade strategy of the CMS collaboration is not fully defined yet, as studies for the possible upgrade are still ongoing. However, it is clear that parts of the tracker system and the calorimeters of the CMS detector will need to be replaced in order to keep a high detector performance under the radiation dose rates expected at the HL-LHC.

In the following chapters, two studies are presented: The first one focuses on the physics performance of the CMS experiment after the upgrade of the pixel detector, foreseen for 2017. It is documented in Chap. 10. The other study is more general. The long-term evolution of the signals measured by the ECAL endcap crystals is presented in Chap. 11. This study can bring valuable information for decisions on a future upgrade of the ECAL endcaps, needed for the HL-LHC.

References 163

References

 CMS Collaboration, Technical proposal for the upgrade of the CMS detector through 2020. CERN LHCC-2011-006 (2011)

- M.S. Kim, The CMS RPC system detector performance and upgrade. PoS EPS-HEP2013 123
 (2014). For more details on CSCs see also I. Suarez, Cathode Strip Chamber Upgrade for the
 CMS Endcap at the HL-LHC, talk given at 2013 Meeting of the APS Division of Particles and
 Fields
- CMS Collaboration, CMS Technical design report for the pixel detector upgrade. CERN LHCC-2012-016 (2012)
- 4. CMS Collaboration, CMS Technical design report for the phase 1 upgrade of the hadron calorimeter. CERN LHCC-2012-015 (2012)
- CMS Collaboration, CMS Technical design report for the level-1 trigger upgrade. CERN LHCC-2013-011 (2013)
- 6. L. Rossi and O. Brüning, High luminosity large hadron collider a description for the european strategy preparatory group. CERN ATS-2012-236 (2012)
- 7. F. Gianotti et al., Physics potential and experimental challenges of the LHC luminosity upgrade. Eur. Phys. J. C 39, 293 (2005). doi:10.1140/epjc/s2004-02061-6. arXiv:hep-ph/0204087

Chapter 10 Physics Performance Study for the Pixel Detector Phase-I Upgrade

This chapter describes a study that has been conducted to show the physics performance of the CMS detector after replacing the current pixel detector with a new design. This replacement is foreseen for 2017 and is known as the pixel phase-1 upgrade.

After a short introduction of the need of the upgrade and the design of the new pixel detector in Sects. 10.1 and 10.2, the actual study will be shown in Sect. 10.3.

10.1 The Need of a Pixel Detector Upgrade

There are several reasons, why the pixel detector needs to be replaced:

- The pixel detector is the innermost part of the CMS experiment. It is exposed to the full radiation generated in the *pp* collisions. The radiation damages both the pixel sensors and the readout electronics, the performance degrades with integrated luminosity. The excellent performance of the LHC machine has led to the estimate that instantaneous peak luminosities of twice the design luminosities will be reached. Due to the higher radiation an intermediate replacement during the year 2017 is needed. A replacement of the pixel detector had been foreseen already in the initial technical design report [1].
- The increased estimate of the LHC luminosity will also inflate the hit occupancy.
 This will lead to unwanted data losses, as the buffer size and the readout bandwidth are limited.
- A higher luminosity also means higher rate of tracks needed to be reconstructed.
 The CPU time will grow, and the rate of wrongly reconstructed and fake tracks increases.

10.2 The Design of the Upgraded Phase-1 Pixel Detector

The current design of the pixel detector has been mentioned in Sect. 4.2.1: three cylindrical layers in the barrel, and two discs on each end hold in total about 66 million pixels.

The new design will have four layers in the barrel and three disks on each end, the number of pixels increases to approximately 124 million pixels. In this design, the innermost barrel layer will be closer to the beam line with a distance r=3.0 cm instead of 4.4 cm. The new fourth layer will be at a radius r=16.0 cm. Furthermore, the arrangement of modules within the disks has been changed to have a better pixel hit coverage for a single track. The new layout is compared with the current one in Fig. 10.1.

The new geometrical design will enhance the physics performance: the better pixel coverage will increase the purity of the tracking algorithm, as a single track will be composed out of more pixel hits. Also the primary and secondary vertex reconstruction is enhanced, as the innermost layer is closer at the *pp* collision point.

Besides the geometrical differences, also the electronics and supporting structures will be upgraded:

The readout chips will be replaced to decrease the latency, increase the buffer size, and thus minimize data losses. The new chip has roughly double buffer size for data and timp stamps. Its readout has been changed from a 40 MHz analog readout to an 8 bit digitized readout with 160 Mbits/s. Furthermore, the operational charge threshold can be decreased. The tracking efficiency loss will be less than $0.5\,\%$ instead of $8.6\,\%$ in the current design for tracks from muons.

Moreover, the material budget will decrease. First, the new readout chip will be smaller in its transverse dimension (75 μ m instead of 175 μ m). Second, the cooling system is changed. The current cooling, using liquid C_6F_{14} , will be replaced by two-phase CO_2 cooling. Besides the lighter element, also the cooling structures, such as tubes, can be reduced in size and thickness in the new system. The third aspect is a lighter support structure. The reduced material budget has several advantages: the

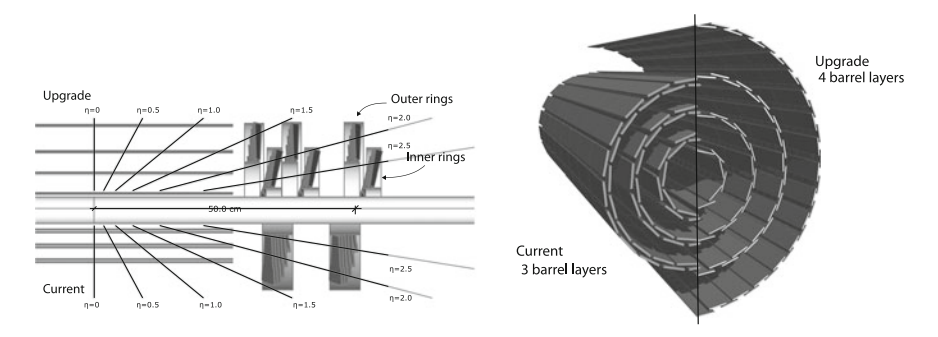


Fig. 10.1 Comparison between the layout of the current and the upgraded pixel detector. Left the rz view. Right the transverse-oblique view. Taken from [2]

number of unwanted interactions between particles and the pixel detector (that is interactions that are not with the pixel sensor) are decreased. This, on the one hand, increases the resolution of low $p_{\rm T}$ track measurements itself, but also can boost the performance of downstream detectors, such as the ECAL: a photon hitting the pixel detector might convert into a e^+e^- pair. If the material budget is reduced, such conversions happen less often, thus a better discrimination for photons coming from the hard interaction can be achieved. The total reduction of the material is 20% at $\eta=0$ and over one half in the endcap part.

A detailed description of the pixel phase-1 detector and its expected performance can be found in [2].

10.3 The 2011 $M_{T2}b$ Analysis as a Performance Study of the Pixel Phase-1 Upgrade

The pixel detector phase-1 upgrade should improve the capability of identifying jets originating from b-hadron decays as b jets. This needs to be verified. Therefore, the 2011 $M_{T2}b$ analysis, as summarized in Sect. 6.4, is used as an example analysis. The only objective of the analysis described here, is a test, how the new detector geometry influences the b-tagging capability of the CMS detector, and thus, how the signal efficiency is modified for SUSY signal events containing primarily b quarks in the final state. This is the reason, why the analysis is based on the selection of the 2011 $M_{T2}b$ search, but does not contain all aspects of a search such as background estimation methods. The study presented here has been documented in [2].

Let me recall the key selection of the $M_{\rm T2}b$ analysis: Data were selected with a $H_{\rm T}$ trigger. Therefore, events needed to pass $H_{\rm T} > 750\,{\rm GeV}$. At least four jets were selected, out of which one needed to be tagged as a b jet. In order to reduce the multijet contribution to the signal region, an event was required to pass $\Delta\phi$ (four leading jets, $E_{\rm T}^{\rm miss}) > 0.3$ and $|\vec{E}_{\rm T}^{\rm miss} - \vec{H}_{\rm T}^{\rm miss}| < 70\,{\rm GeV}$. Events containing an electron or muon, as well as anomalous signatures like electronic noises were rejected. In total, eight signal regions had been defined as a function of $H_{\rm T}$ and $M_{\rm T2}$. The lowest requirement on $M_{\rm T2}$ was $M_{\rm T2} > 125\,{\rm GeV}$.

The same selection is used for this study with three modifications: The b tagging relies on the CSV tagger rather than a simple secondary vertex tagger. This reason for this change is that b-tagging performance studies are the primary object of this analysis. However, it is important to note that the algorithm of the CSV tagger has not been optimized for either the new detector designs nor the conditions expected for 2017 data taking. It has been taken as the one used for analyses of the 7 TeV pp collision data. Furthermore, the jet- p_T threshold was increased from $p_T > 20 \, \text{GeV}$ to $p_T > 30 \, \text{GeV}$, and the isolation criteria on leptons were relaxed. These two modifications have been made to decrease the influence of pileup interactions, as the number of pileup interactions is expected to increase for 2017 data taking.

The study has been performed for $\sqrt{s} = 14 \text{ TeV}$. Two processes were considered: as SM background, only the dominant contribution of $t\bar{t}$ +jets events has been

Benchmark	m_0	$m_{1/2}$	$\tan \beta$	A_0	$sign(\mu)$., .,		M(u, d)
point	(GeV)	(GeV)		(GeV)		(GeV)	(GeV)	(GeV)	(GeV)
LM9	1450	175	50	0	+	507	66	870	1481
considered. Its cross-section is 874 pb [3] for $\sqrt{s} = 14 \text{TeV}$. The signal model is									
called I MQ. This model is defined in the context of the cMSSM (see Sect 3.3.2)									

Table 10.1 Definition of the benchmark point LM9 [4]

considered. Its cross-section is 874 pb [3] for $\sqrt{s} = 14$ TeV. The signal model is called LM9. This model is defined in the context of the cMSSM (see Sect. 3.3.2). The parameters for this model can be found in Table 10.1, together with the values of some sparticle masses. The cross-section for this signal model at $\sqrt{s} = 14$ TeV is 39.8 pb [4]. One should note that the $M_{\rm T2}b$ search performed with 7 TeV pp collision data, collected during 2011, already excluded, at 95 % CL, this signal model.

For each process, two samples are produced. Samples denoted by "StdGeom2" describe events being reconstructed with the current detector design. Events reconstructed by the CMS detector with the new proposed pixel detector are denoted by "Phase1".

We expect to find mainly one $b\overline{b}$ pair inside a $t\overline{t}+$ jets event. Additional b quarks can come from gluon splitting, $g \to b\overline{b}$. Events of the LM9 signal model can have different b-quark content: for roughly 10% of the events, no b quark is produced, there is one $b\overline{b}$ pair in 40% of the events, else the event contains two $b\overline{b}$ pairs. The primary

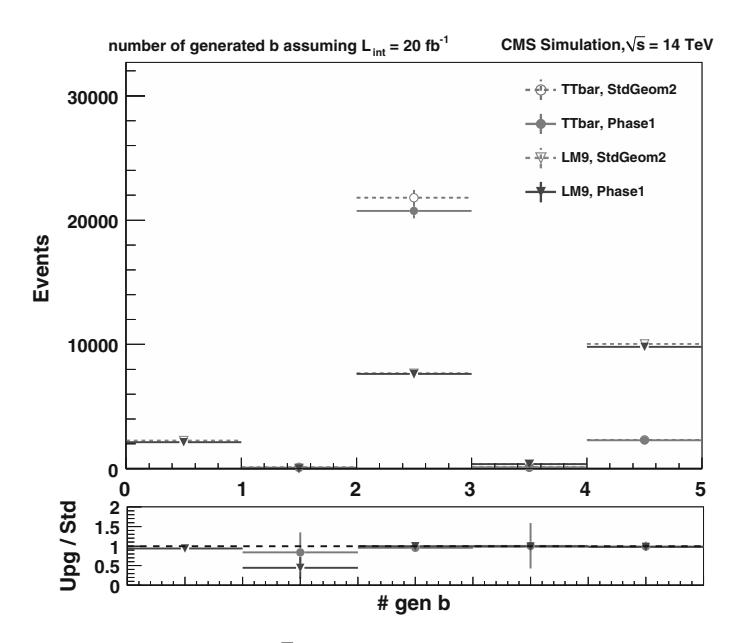


Fig. 10.2 Number of generated b and \bar{b} quarks within detector acceptance ($p_T > 30$ GeV, $|\eta| < 2.4$) for both signal and background events. The difference of the yields for 2 b quarks for the $t\bar{t}$ +jets samples is not understood. The ratio plot shows the ratio of event yields of the "Phase1" and "StdGeom2" samples. The simulations are normalized to an integrated luminosity of 20 fb⁻¹

source of $b\bar{b}$ pairs inside the signal events are three-body decays of the gluino. The number of generated b (and \bar{b}) quarks within detector acceptance ($p_T > 30 \,\text{GeV}$, $|\eta| < 2.4$) for both signal and background events is shown in Fig. 10.2.

If the b-tagging performance of the CMS detector improves, the selection efficiency for signal events containing several b quarks can be increased substantially. We compare the b-tagging efficiency for b-quark jets versus the b-tagging efficiency of non-b-quark jets within the event selection. The correlations between these two

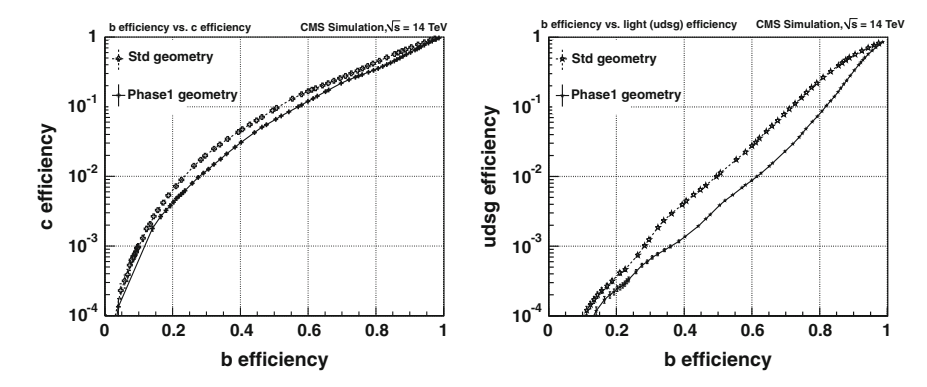


Fig. 10.3 The b-tagging efficiency for b-quark jets versus the b-tagging efficiency for c-quark jets (*left*) and u, d, s-quark or gluon jets (*right*). The efficiencies have been calculated for $t\bar{t}$ +jets events. The correlations have been obtained by varying the selection on the CSV discriminant

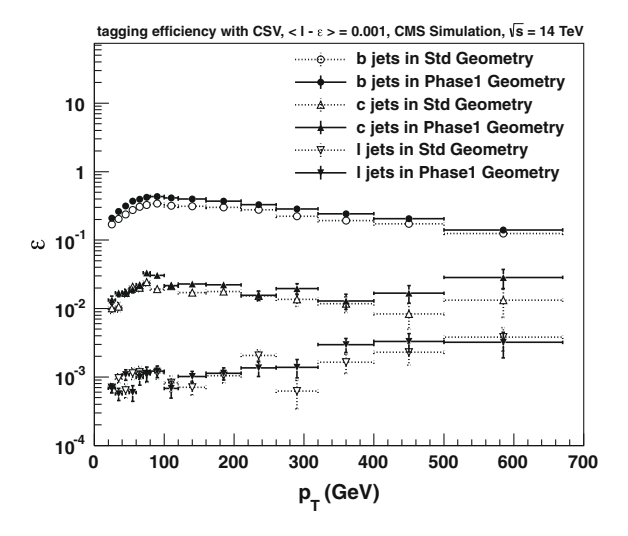


Fig. 10.4 The b-tagging efficiency for b-quark jets, c-quark jets and light (u, d, s-quark and gluon) jets as a function of jet- p_T for a CSV working point yielding an overall 0.1% mistagging rate on light jets

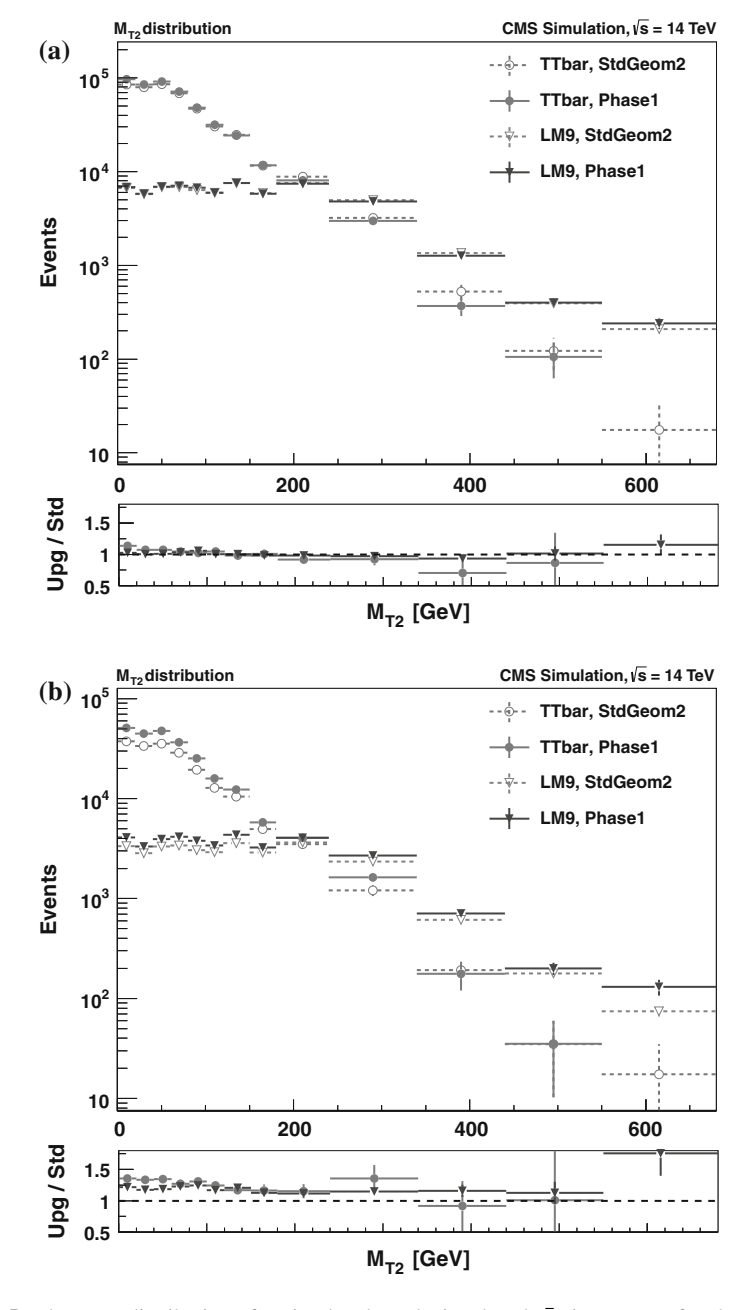


Fig. 10.5 The M_{T2} distributions for simulated LM9 signal and $t\bar{t}$ +jets events for the two detector geometries. a M_{T2} distribution with no b-jet requirement. b M_{T2} distribution for events with \geq 1b jets. The ratio plots show the ratios of event yields of the "Phase1" and "StdGeom2" samples. The simulations are normalized to an integrated luminosity of 20 fb⁻¹

efficiencies is illustrated in Fig. 10.3 for $t\bar{t}$ +jets events. We find that for any mistagging rate of non-b-quark jets as b jets, the detector design using the new pixel detector instead of the current one yields a higher b-tagging efficiency for b-quark jets.

A working point that has the same mistagging rate as the one used in the 7 TeV search is chosen: We require a mistagging rate of 0.1% for jets originating from u-, d-, s-quark or gluon hadronization. For this choice, the b-tagging efficiency for b-quark jets improves from 28% in the current detector geometry to about 36% for the geometry with the proposed new pixel detector layout. The b-tagging efficiency as a function of jet- p_T is shown in Fig. 10.4.

We are now ready to evaluate the improvement of the b-tagging efficiency for the $M_{T2}b$ analysis.

First, events are selected using the $M_{T2}b$ event selection with no requirement on b jets. It is verified that the selection efficiency for both the current and the upgraded geometry are the same. This can be appreciated from the ratio plot of Fig. 10.5a.

Next, the requirement of at least one b jet is added to the event selection. One can observe, Fig. 10.5b, that the signal selection efficiency is improved by roughly 20% for a selection on $M_{T2} > 200$ GeV.

Conclusion

It has been shown, using the selection of the 7 TeV $M_{T2}b$ analysis, that the CMS detector design with the new proposed pixel detector enhances the b-tagging performance, leading to an increase of the signal selection efficiency of 20% (for the tested signal model) without substantial effort of optimizing the analysis.

Since the time this study had been performed, the $M_{\rm T2}$ analysis itself has progressed a lot. With the b-jet multiplicity binning introduced (see Sect. 7.3), the gain of the selection efficiency for signal events involving third generation squarks can be expected to be even higher. Additionally, reoptimizing the b-tagging discriminant for the new detector design might further improve the b-tagging performance. Overall, one can conclude that the new pixel detector design will improve analyses, which use b-tagging variables.

References

- 1. CMS Collaboration, CMS: Tracker. Technical design report. CERN LHCC-98-06 (1998)
- CMS Collaboration, CMS Technical Design Report for the Pixel Detector Upgrade. CERN LHCC-2012-016 (2012)
- U. Langenfeld, S. Moch, P. Uwer, Measuring the running top-quark mass. Phys. Rev. D 80, 054009 (2009). doi:10.1103/PhysRevD.80.054009. arXiv:0906.5273
- CMS Collaboration, CMS physics technical design report, volume II: physics performance. J. Phys. G 34, 995 (2007). doi:10.1088/0954-3899/34/6/S01

Chapter 11 Evolution Studies of the CMS Electromagnetic Calorimeter Endcap Signals

The study presented in this chapter has been performed to disentangle various contributions to the ECAL endcap signal modulations during 2011 and 2012 data taking. It has been known that there are different sources of radiation damages decreasing the light transparency observed by the crystal readout. While models of these sources exist, based on laboratory measurements performed prior to the ECAL assembly, no study has been done for observing the different sources in-situ previous to this one. However, a good knowledge of the different components changing the signal transparency is needed in order to understand the longterm evolution of the ECAL signals. Since the radiation doses are much higher in the forward region of the detector, this study focuses on the ECAL endcap readout.

Measurements on crystal and VPT properties have been used. These were determined during quality assurance tests prior to the built-up of the CMS detector. The measurements have been correlated with in-situ data of the ECAL light monitoring system.

This chapter introduces the sources to signal losses, the characteristic variables used in this analysis, and the light monitoring systems in Sects. 11.1–11.3. This introduction is based on [1]. The general layout of the ECAL has already been presented in Sect. 4.2.2. The actual study is shown in Sects. 11.4–11.7. It has been documented in a CMS note, which is not accessible publicly.

11.1 Signal Losses Within the Electromagnetic Calorimeter Endcaps

The ECAL endcaps are exposed to radiation degrading the performance of the crystals and the on-detector electronics, mainly the VPTs. The predicted dose rates hitting the ECAL for the design luminosity of 10^{34} cm⁻²s⁻¹ are shown in Fig. 11.1.

Extensive studies had been done to identify how radiation damages the crystals and readout electronics, and what are the underlying mechanisms. For the PbWO₄ crystals, the source of the main mechanism has been found to be ionizing radiation

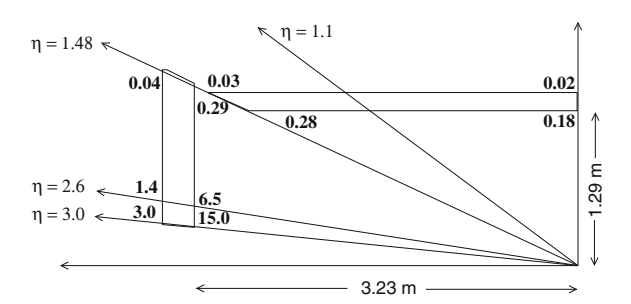


Fig. 11.1 Predicted dose rates in Gy/h at various places of the ECAL for an instantaneous luminosity of 10^{34} cm⁻²s⁻¹. The values given at the front of the ECAL are those obtained at the shower maximum, values at the end of ECAL are obtained behind the crystals. Taken from [1]

[1–6]. Oxygen vacancies are created, so-called color centers. These color centers absorb scintillation light, and thus the transparency of the crystals decreases. However, this damage to the crystals can recover spontaneously at room temperature. In fact, the transparency loss stabilizes under radiation at a dose rate-dependent level, when the color center annihilation and creation rates equalize. Both the scintillation mechanism and the uniformity of the crystal are not affected by this radiation type.

Another component of crystal damage is hadron-induced damage [7]. Nuclear interactions between incoming hadrons and the crystal material can lead to fission products like iron and zirconium. These processes can lead to displacement of lattice atoms and reduce the scintillation light transparency. The hadron-induced damage is cumulative and does not recover at the temperature of operation (18 °C). However, for high temperatures above 350 °C, full recovery of the hadron-induced damage can be achieved.

Also the VPTs are exposed to the radiation in the endcaps, although the received dose is damped by the crystals before them, as seen in Fig. 11.1. An important component is the damage to the face-plates of the VPTs. Under irradiation, color centers are formed in the glass material of the face-plates, leading to a further decrease in transparency. Transmission losses of $\sim 10\,\%$ under γ radiation for doses expected at $|\eta| \approx 2.6$ have been measured [8, 9]. For neutron irradiation up to $7\times 10^{15} \text{n/cm}^2$, light transmission losses of about $\sim 10-30\,\%$ have been measured [8]. These neutron fluences are at least an order of magnitude larger than expected at the LHC [1]. The VPTs used in CMS were required to receive small face-plate damages by requiring a transparency loss of the VPTs less than $10\,\%$, when the loss is weighted by the scintillation spectrum for a dose of $20\,\text{kGy}$ [10].

A further contribution to the VPT losses under radiation is the response loss caused by positive charge accumulation on the photo cathode, mainly due to the scintillation light showers within the photo tube [9]. This can happen if, for example, the scintillation light hits residual gas in the photo tube leading to ion collection on the photo cathode. This contribution is sometimes called VPT conditioning.

A third component to the VPT damage could be ingress of Helium to the photo tube, deteriorating the vacuum. However, it has been concluded in tests that this effect has no significant influence for CMS operation at conditions expected at the LHC [11].

Damages to the photo tube or due to crystal shower leakages have been tested and estimated to be negligible [1].

11.2 Characteristic Variables Describing the Radiation Hardness of Detector Components

Most of the components leading to decreasing transparency because of radiation have been known prior to the construction of the CMS ECAL. Therefore, many measurements have been performed to test the radiation hardness of the used materials for each radiation component.

The damage to the crystals due to ionizing radiation had been studied with great detail [1–6]. The variable characterizing the ionizing damage is the induced absorption coefficient $\mu_{\text{IND}}(\lambda)$, derived from the Beer-Lambert law and defined as

$$\mu_{\rm IND}(\lambda) = \frac{1}{\ell} \cdot \ln \frac{LT_0(\lambda)}{LT(\lambda)}, \tag{11.1}$$

where LT_0 (LT) is the longitudinal light transmission measured before (after) irradiation through the length ℓ of the crystal.

The hadron-induced absorption does not correlate with the μ_{IND} variable [7].

The crystals from the two producers (BTCP and SIC) behave differently due to the distinct production mechanism, see Sect. 4.2.2. A fraction of the PbWO₄ crystals of the CMS ECAL had been tested for radiation hardness to the ionizing radiation component under a standardized irradiation condition. Two different irradiation conditions, optimized for each set of crystals from the two producers, were designed. The crystals were exposed to photons from a ⁶⁰Co source. The BTCP crystals were exposed to 350 Gy/h for 1 h at the Geneva hospital, and μ_{IND} was measured at CERN, Geneva roughly 1 h after the irradiation. The SIC crystals were exposed to 30 Gy/h for 24h at the Calliope source, Rome, and μ_{IND} was measured directly following the irradiation. More details on the radiation damage and the procedure to measure μ_{IND} can be found in [12]. Although the two methods are very different, the resulting absorption coefficients measured are in good agreement, as shown in Fig. 11.2. Still, as the crystals from the two producers have different properties, the samples will be studied separately. The induced absorption coefficient measured under these standardized irradiation conditions is called μ_{std} hereafter. Maps of the μ_{std} values for the ECAL endcaps (EE+ and EE-1) are shown in Fig. 11.3. Only 6.6% of all PbWO₄ crystals were tested under these conditions. The SIC measured also $\mu_{\rm IND}$ privately for their production and provided their measurements to CMS. These measurements will be called μ_{SIC} .

 $^{^{1}}$ The sign indicates the sign along the z axis.

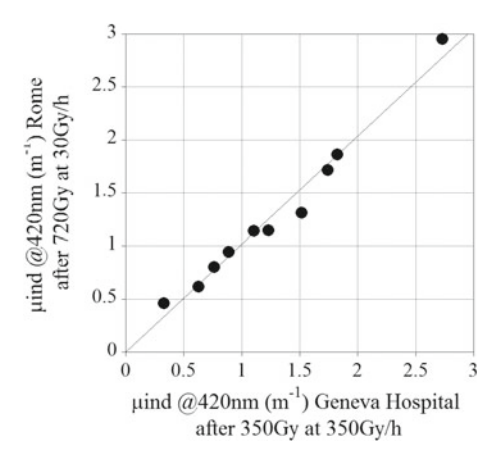


Fig. 11.2 Correlation between the $\mu_{\rm IND}$ values obtaind in irradiation tests performed at CERN and in Rome [12]

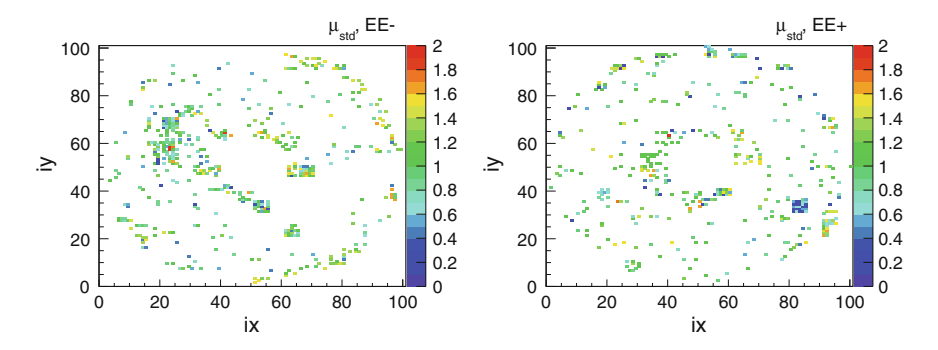


Fig. 11.3 Maps of $\mu_{\rm std}$ (given in m⁻¹) for the ECAL endcaps EE- (*left*) and EE+ (*right*). The crystals are identified by their location indices *ix* and *iy* for each endcap, going from 1 to 100

A characteristic variable also exists for the VPT damage component. The variable used in this study is the burn-in ratio, or short burn-in. It is obtained in accelerated ageing tests as described in [11]: The VPTs are exposed to a high constant current by illuminating them uniformly with LED light. The anode response is then measured using a second pulsing LED. The ratio of the initial current and the final current after illumination is the relative anode response loss. An example of the response loss of a VPT anode during the LED illumination is given in Fig. 11.4.

For CMS, a standardized illumination [13] was defined as follows: Each VPT will be initially illuminated uniformly by a LED producing an initial photocurrent of $100 \,\mathrm{nA}$ for 2 h under normal VPT operation. Then, the illumination is readjusted to produce again a photocurrent of $100 \,\mathrm{nA}$ and the initial anode current, I_0 , is recorded. After a 4 h uniform illumination period the final anode current, I_f , is recorded. The burn-in is defined as the relative anode response loss,

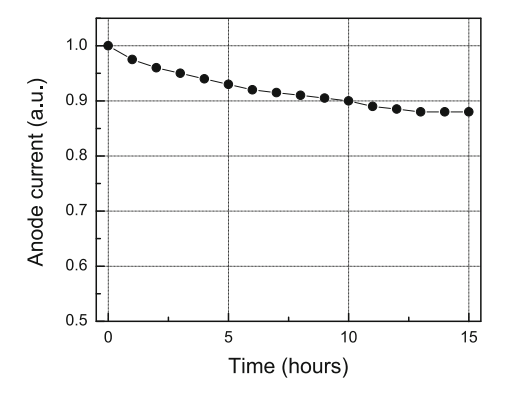


Fig. 11.4 Relative VPT anode current as a function of time under LED illumination producing an initial photocurrent of 200 nA [9]

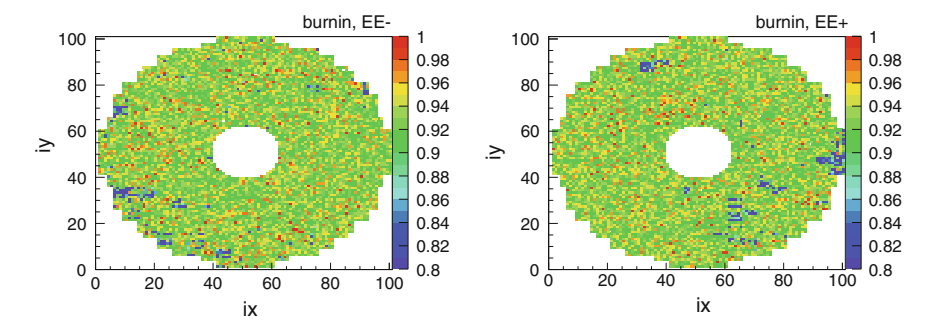


Fig. 11.5 Maps of the burn-in values for the ECAL endcaps EE- (left) and EE+ (right). The VPTs are identified by the location indices ix, iy

$$burn-in = \frac{I_f}{I_0}.$$
 (11.2)

In CMS, the burn-in has been used to reject VPTs with inferior vacua. Except for the preproduction batch of 500 VPTs, all VPTs were required to pass burn-in \geq 0.9 [13]. Maps of the burn-in values for the ECAL endcaps are shown in Fig. 11.5. All of the VPTs have been tested under these conditions.

11.3 The Monitoring System of the Electromagnetic Calorimeter

The reasons for the transparency losses in the ECAL subdetector under the radiation expected during LHC operation have been discussed. The loss of transparency leads to energy measurements being smaller than the true signals. In order to be able to reconstruct the correct energy of a particle in the calorimeter, a laser monitoring

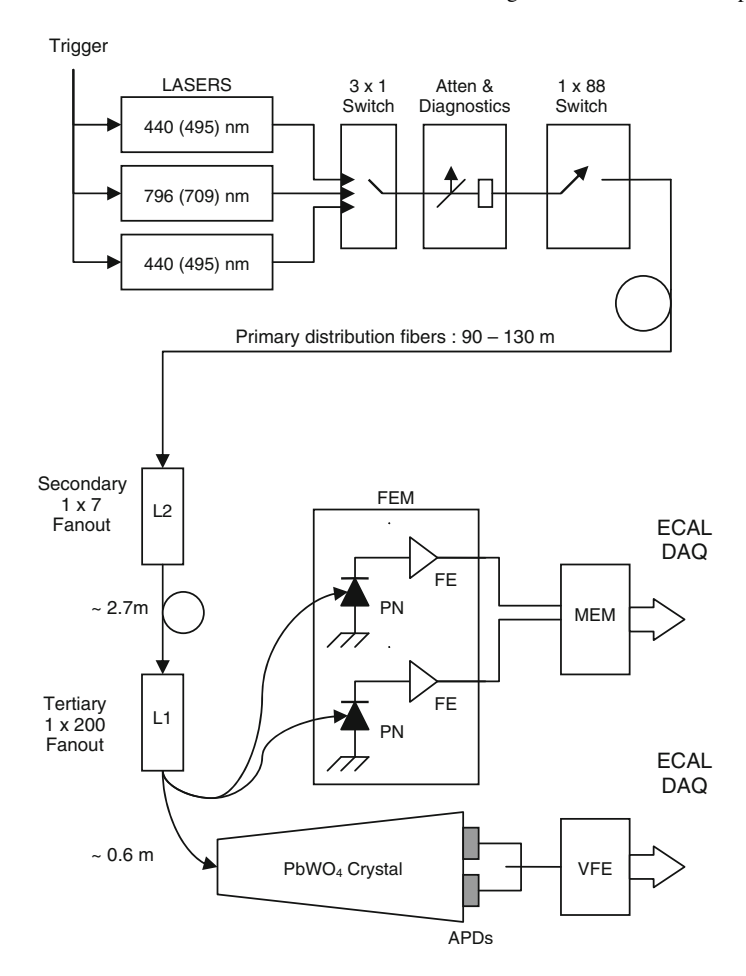


Fig. 11.6 Sketch of the components of the laser monitoring system for a barrel crystal [10]. The laser chain is identical for endcap crystals that have a VPT instead of two APDs attached to it

system has been built to measure the relative transparency changes of the crystal and the connected readout electronics. A sketch of the monitoring system is drawn in Fig. 11.6.

Blue light with $\lambda=440$ nm is produced by a light source of a Nd:YLF pump laser and a tunable Ti:Sapphire laser. There exists a second blue laser system as backup to ensure constant availability of laser pulses at $\lambda=440$ nm, as well as an infrared laser system producing pulses at $\lambda=796$ nm. The light is sent to multiple crystals at the same time, one out of 88 calorimeter regions is monitored at once. The light is injected to the crystals during $\sim 1\,\%$ of the LHC beam abort gaps, a 3.17 μs period at the end of every 88.924 μs LHC beam cycle. Thus, the light does not interfere with the collision data taking. The monitoring of the full ECAL detector takes about $40\,\mathrm{min}$ [14].

The same blue laser light is sent to control silicon PN photodiodes outside the detector. This PN diode is not subject to the radiation inside CMS, thus the relative response of APD/PN or VPT/PN is a measure of the relative crystal transparency. Here APD (VPT) denotes the laser light signal produced in the crystal and readout by the APD (VPT), and PN denotes the laser light signal produced in the PN photodiode. This ratio is stable against many systematics like laser light intensity, and therefore is chosen rather than the direct signal from the APDs and VPTs. The APD/PN and VPT/PN values have been normalized to unity at the beginning of 2011 *pp* collision data taking.

The optical paths and the spectra are not equal between the laser light and the scintillation light produced in the crystals during collision data recording; the changes in response are not the same. The relation between the response changes can be written as

$$\frac{S}{S_0} = \left(\frac{R}{R_0}\right)^{\alpha},\tag{11.3}$$

where $R_0(S_0)$ is the APD/PN or VPT/PN ratio for the laser (scintillation) light signals before irradiation, and R(S) are the same ratios after irradiation. The variable α is a characteristic value for the crystal and has been defined as $\alpha \approx 1.53$ for BTCP crystals and $\alpha \approx 1.0$ for SIC crystals. This correction is needed to correctly reconstruct the true energy of a particle in the electromagnetic calorimeter.

Between the data taking periods in 2011 and 2012, the laser monitoring system of the CMS ECAL has been upgraded. The reason was the discontinuation of the production of Nd:YLF pump lasers by the supplier. A diode-pumped solid state laser was installed. This new laser is much more stable in operation and has consistent response compared to the Nd:YLF laser-pumped Ti:Sapphire laser. More information on this new laser can be found in [15].

In the studies presented hereafter, we will only consider the data obtained by the blue lasers at $\lambda = 440$ nm.

11.4 Correlation Between Light Monitoring Signals and μ_{std}

The first set of studies examines the correlation between the laser monitoring data and the measurements of $\mu_{\rm std}$. As introduction, we consider only a fixed time period for the study. The correlation for this time period is shown and the parameters related to it are defined.

We have seen the geometrical dependence of the radiation exposure of the ECAL crystals in Fig. 11.1. Hence, the correlation will be investigated as a function of $|\eta|$.

Then, the time evolution of the previous observations is studied. Finally, the results are compared to simulation.

²Recent measurements determine $\alpha \approx 1.12$ for BTCP crystals in the endcaps, effectively correcting for VPT response variation [14].

11.4.1 Study of the Correlation for a Fixed Time Period

For this initial study, we considered monitoring data taken in autumn 2011 and corresponding to a delivered integrated luminosity of approximately 2 fb⁻¹. The chosen period provided two objectives:

The crystals had been irradiated for a long time, but the time period began just after a technical stop of the LHC, which had been about two weeks long. The crystals had time to recover from the expected damage due to ionizing radiation. On the other hand, a component due to permanent hadron-induced damage could still be present. The other reason was that pp collision data were taken without major interruptions during the chosen time period.

As an example, the correlation between the maximal VPT/PN signal change and $\mu_{\rm std}$ for crystals within 2.6 $\leq |\eta| < 2.8$ and produced by the SIC is shown in Fig. 11.7. Each entry corresponds to an individual crystal, for which a $\mu_{\rm std}$ measurement was performed.

As expected, a correlation is observed between the in-situ measurement and $\mu_{\rm std}$: if the measured value of $\mu_{\rm std}$ is large, meaning that the crystal was sensitive to ionizing damage during the laboratory classification tests, the crystal should be equally sensitive within the detector. Thus, a large change in the VPT/PN signal is expected. For small values of $\mu_{\rm std}$, small changes in VPT/PN are anticipated.

The correlation seems to be linear, therefore, a linear fit on the correlation is performed. The fit parameters are a " μ -slope" and a " μ -intercept". The μ -slope characterizes the contribution to the VPT/PN change correlating with the crystal resistance to ionizing radiation. The μ -intercept corresponds to the contributions unrelated to $\mu_{\rm std}$. It contains other components, like those from hadron-induced damage or VPT damage.

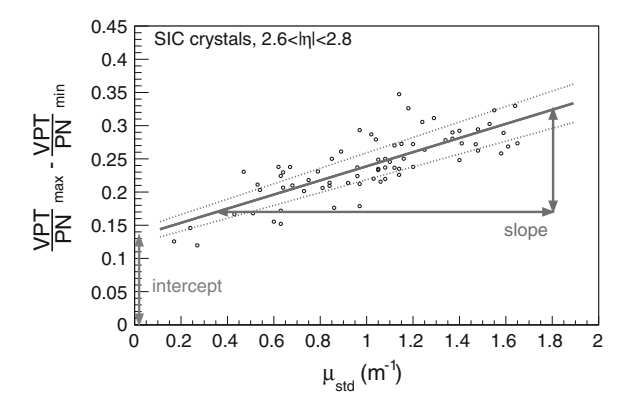


Fig. 11.7 Correlation between the maximal VPT/PN change and $\mu_{\rm std}$ for crystals within 2.6 \leq $|\eta| < 2.8$ and produced by the SIC. Each entry corresponds to a single crystal. The correlation is fitted with a *straight line*. The two *dotted lines* indicate the uncertainty on the fit: Both fit parameters are scaled up or down at the same time

Using this correlation, we are able to disentangle the damage component of crystals due to ionizing radiation.

As both parameters are not compatible with zero, we observe, in this example, components related and not related to ionizing radiation contributing to the transparency loss observed by the light monitoring system.

The amount of radiation, the crystals are exposed to, depends on the inclination of the crystal position, thus on $|\eta|$. The correlation is investigated for various bins of $|\eta|$ of size $\Delta \eta = 0.2$. In addition, the BTCP and SIC crystals are studied separately.

We perform linear fits for the correlations between the maximal VPT/PN signal change and μ_{std} for all groups of crystals, as done in the example of Fig. 11.7. The results of those fits are reported in Figs. 11.8 and 11.9 for the μ -slopes and μ -intercepts, respectively. The BTCP crystals do not populate the most inner region of the ECAL endcaps (closest to the beampipe). Therefore, no correlation results are available for $|\eta| \geq 2.6$.

The μ -slopes increase with $|\eta|$, the correlation fits become steeper. This is expected: the ionizing dose rate also increases towards higher $|\eta|$ values, thus causing a larger damage amplitude for crystals of same $\mu_{\rm std}$. It is also observed, for a given $|\eta|$ bin, that the μ -slope values between crystals of the SIC and BTCP are consistent despite the differences in the way $\mu_{\rm std}$ was obtained for the two production sets (see Sect. 11.2).

We observe a similar behavior for the μ -intercepts: they increase for higher $|\eta|$. Hence, it can be assumed that the underlying causes, responsible for the presence of the intercepts, depend on the radiation exposure. This is true for hadron-induced damage, which scales with the radiation dose. Also, the VPT damage is dependent on the radiation dose.

For a given $|\eta|$ bin, the μ -intercept values for SIC and BTCP crystals are consistent, although the μ -intercepts for SIC crystals seem to be a bit higher. The comparison can be made only up to $|\eta| < 2.6$ because BTCP crystals do not populate the inner ECAL endcap regions.

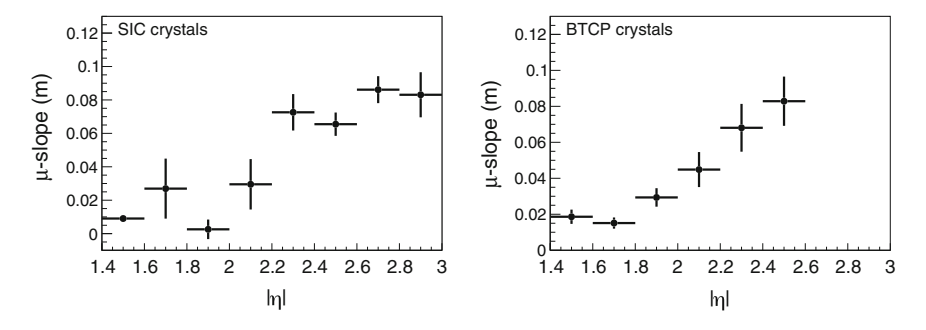


Fig. 11.8 The μ -slopes, obtained from the linear fits to the correlations between the VPT/PN change and $\mu_{\rm std}$, as a function of $|\eta|$. The uncertainties in the μ -slopes are the fit uncertainties while the *horizontal* bars simply correspond to the η coverage of the bins. *Left* for crystals produced by the SIC. *Right* for crystals produced by the BTCP

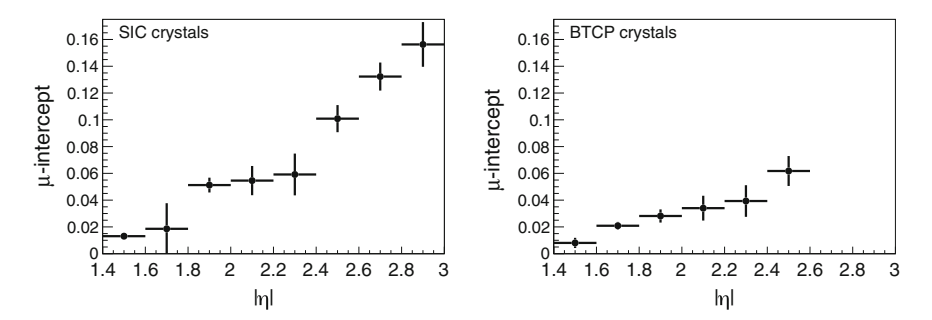


Fig. 11.9 The μ -intercepts, obtained from the linear fits to the correlations between the VPT/PN change and $\mu_{\rm std}$, as a function of $|\eta|$. The uncertainties in the μ -intercepts are the fit uncertainties while the *horizontal* bars simply correspond to the η coverage of the bins. *Left* for crystals produced by the SIC. *Right* for crystals produced by the BTCP

11.4.2 Time Evolution of the Correlations

So far, we have studied the correlation between the VPT/PN change and μ_{std} as a function of $|\eta|$, but for a fixed time period. However, the goal of this analysis is to observe the long-term signal evolution of the ECAL signals.

Therefore, we want to study the correlation as a function of time. For this, the approach of calculating the correlations is slightly modified. We do not use the maximal change in VPT/PN, but define

$$\Delta\left(\frac{\text{VPT}}{\text{PN}}(t)\right) = 1 - \frac{\text{VPT}}{\text{PN}}(t). \tag{11.4}$$

This formula expresses the change of VPT/PN with respect to the beginning of *pp* collision data taking in 2011. Note, that the VPT/PN values were normalized to unity for this beginning of data taking in 2011. The VPT/PN values are chosen as daily averages, that is one VPT/PN value per day.

First, we test if the correlation between $\Delta(\text{VPT/PN})$ and μ_{std} is observed over a large span of time. We define the correlation coefficient

$$\rho_{\mu} = \frac{\sum_{i=1}^{n} \left\{ \left(\mu_{\text{std},i} - \langle \mu_{\text{std}} \rangle \right) \left(\Delta \left(\frac{\text{VPT}}{\text{PN}} \right)_{i} - \langle \Delta \frac{\text{VPT}}{\text{PN}} \rangle \right) \right\}}{\sqrt{\sum_{i=1}^{n} \left(\mu_{\text{std},i} - \langle \mu_{\text{std}} \rangle \right)^{2}} \sqrt{\sum_{i=1}^{n} \left(\Delta \left(\frac{\text{VPT}}{\text{PN}} \right)_{i} - \langle \Delta \frac{\text{VPT}}{\text{PN}} \rangle \right)^{2}}},$$
(11.5)

where i denotes the ith crystal within n crystals contributing to the correlation. The values within $\langle \ \rangle$ are the averaged values for all n crystals. This coefficient is calculated for each $|\eta|$ bin and the two producer groups. The uncertainty on ρ_{μ} is given by $\sigma(\rho_{\mu})=(1-\rho_{\mu}^2)/\sqrt{n-3}$.

The time evolution of the correlation coefficients is shown in Fig. 11.10. The correlation builds up very quickly, the correlation coefficients reach roughly stable values

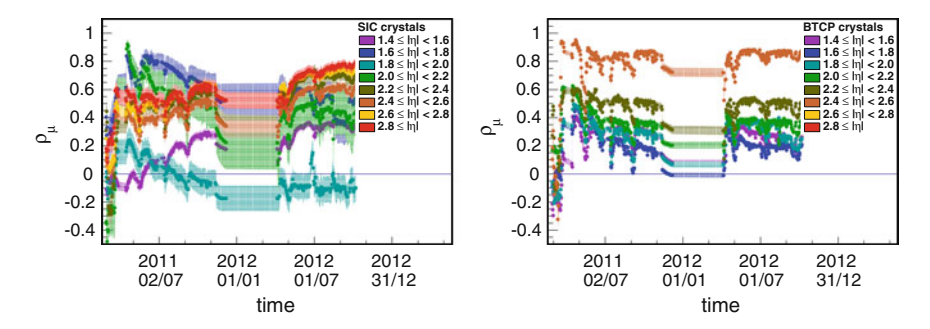


Fig. 11.10 The correlation coefficient as a function of time for crystals in various $|\eta|$ bins and produced by the SIC (left) and the BTCP (right). The anomalous behavior of ρ_{μ} for the SIC crystals between $1.8 \le |\eta| < 2.0$ is not understood. See the corresponding discussion in Sect. 11.5

of about 0.3–0.8, depending on the crystal producer and $|\eta|$ region. Furthermore, we see that the correlation coefficient decreases in periods where no pp collisions were provided by the LHC. This could be due to different time constants for color center creation and annihilation because of ionizing radiation: If crystals with similar $\mu_{\rm std}$ have different annihilation time constants, the spread in $\Delta({\rm VPT/PN})$ increases, reducing the value of ρ_{μ} .

We have observed the correlation to be reasonably large. Therefore, linear fits to the correlations are performed. For each day, the correlation between $\Delta(\text{VPT/PN})$ and μ_{std} is formed and fitted, μ -slopes and μ -intercepts are obtained in each $|\eta|$ bin and for the two crystal producer groups.

The time evolution of the μ -slopes is shown in Fig. 11.11. The μ -slopes increase over time. This is expected because of the increasing instantaneous luminosity (see corresponding figures in [16]) and thus an increasing ionizing dose rate. We also observe the $|\eta|$ dependence, as has been observed before in Fig. 11.8. A different

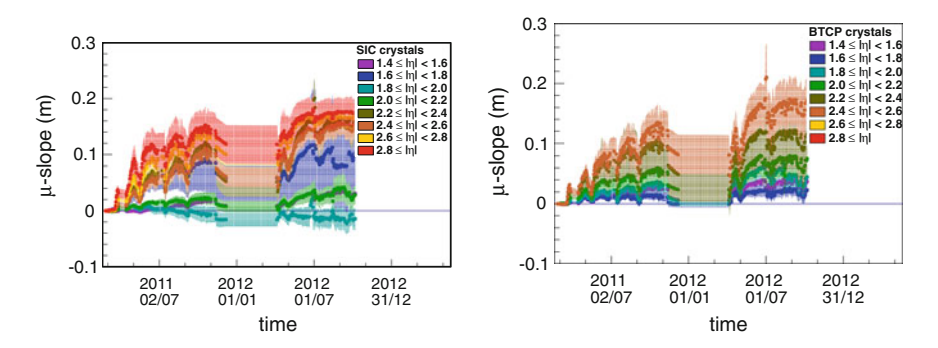


Fig. 11.11 The μ -slopes as a function of time for crystals in various $|\eta|$ bins and produced by the SIC (left) and the BTCP (right). The anomalous behavior of the μ -slopes for the SIC crystals between $1.8 \le |\eta| < 2.0$ is not understood. See the corresponding discussion in Sect. 11.5

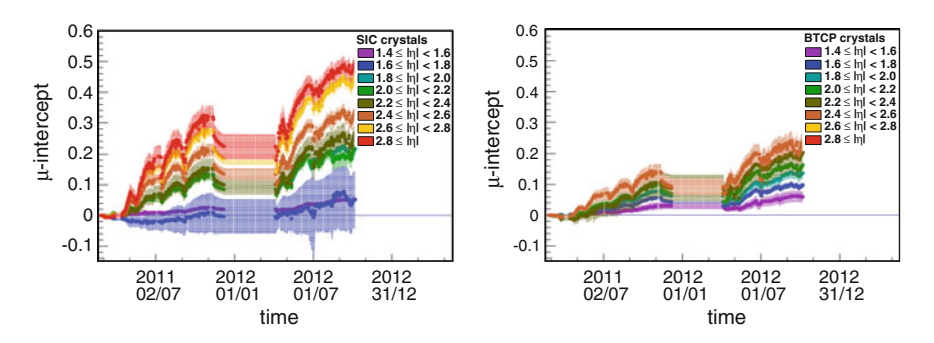


Fig. 11.12 The μ -intercepts as a function of time for crystals in various $|\eta|$ bins and produced by the SIC (left) and the BTCP (right)

behavior seems to be present for the SIC crystals within $1.8 \le |\eta| < 2.0$ and is not understood. A corresponding discussion can be found in Sect. 11.5.

During 2012, the μ -slope values approach a stable level, the transparency loss due to irradiation and the spontaneous recovery level out. In this period, the averaged instantaneous luminosity had been roughly constant. This behavior had already been observed in laboratory measurements for damages from ionizing radiation. Another observation is the increase of the μ -slope values as a function of $|\eta|$. This was already shown in Fig. 11.8.

One notices further that the μ -slope values decrease during beam-off periods, that are periods, where LHC did not provide pp collisions: this is expected, since the damage from ionizing radiation recovers spontaneously at room temperature.

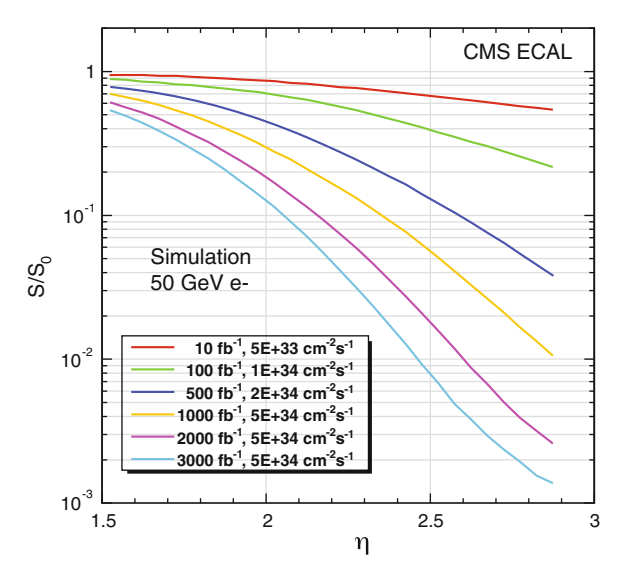
Next, the time evolution of the μ -intercepts is inspected. It is shown in Fig. 11.12. As for the μ -slopes, we see an increase over time, albeit the behavior of the increase is different: μ -intercept values do not reach a plateau value, they seem to grow steadily. This might hint to a cumulative damage component, dependent on the dose (or integrated luminosity) rather than the dose rate (or instantaneous luminosity). Such a behavior is predicted for the hadron-induced damage, for example.

The μ -intercepts also have a recovering component. This component might be of different origin than the annealing from ionizing damage. For example, the VPT response might exhibit some recovery [17]. Another reason might be that, due to the difference between the creation and annihilation rates for color centers, the recovery for μ -intercepts could partially come from the connection between μ -slopes and μ -intercepts in the fitting procedure.

11.4.3 Comparison of the Correlation Results with Simulation

Using the results obtained in the previous section, we want to perform a comparison with simulation. Given the complexity of the exact understanding of the transparency loss in the ECAL readout chain, and given the simple ansatz of the present analysis,

Fig. 11.13 Relative loss of ECAL endcap response for electrons with an energy of 50 GeV as a function of $|\eta|$ and for various values of integrated luminosity, as obtained from simulations. Taken from [21]



we do not aim to give a quantitive statement of the agreement between data and simulation. Rather, a qualitative corroboration of the predictions from simulation is given.

We make the reasonable assumption that the time, for which we had the largest recovery of the ionizing damage, is prior to the 2012 pp collision running. The μ -intercepts from the fits of the $\Delta(\text{VPT/PN})$ -versus- μ_{std} correlations are compared to predictions from simulation. In Fig. 11.13, the expected loss of ECAL endcap response for electrons with an energy of 50 GeV as a function of $|\eta|$ and for various values of integrated luminosities is shown.

Inputs to the simulation are:

- The fluence of charged hadrons in CMS based on MARS simulations [18], and measured μ_{IND} values for hadron damage [7].
- The ionizing dose, based on MARS simulations and measured $\mu_{\rm IND}$ values of the ionizing damage, assuming a simple model for the equilibrium between darkening and recovery [19]. A maximum value of $\mu_{\rm IND} = 2\,{\rm m}^{-1}$ is permitted in the simulation.
- The integrated charge Q of photoelectrons from the VPT cathode as well as the resulting VPT conditioning VPT(Q), based on the average behavior of about ten VPTs, tested by the CMS ECAL collaboration [20].

As stated above, the comparison between the μ -intercepts and the prediction from simulation is only a qualitative statement. No studies on varying the fit model have been performed. Furthermore, no uncertainty on the VPT/PN measurement is considered beyond the statistical spread of the population. This is the reason, why no uncertainties in the comparison are quoted, such that the impression of a precise measurement is avoided.

non-recovering Levil endeap signar ross					
$ \eta $ bin	$ \eta \simeq 2.1$	$ \eta \simeq 2.3$	$ \eta \simeq 2.5$	$ \eta \simeq 2.7$	$ \eta \simeq 2.9$
Prediction	0.11	0.14	0.20	0.25	0.29
Observation	0.10(0.08)	0.08(0.14)	0.14(0.07)	0.19(-)	0.23 (-)

Table 11.1 Comparison between predictions and observations for the SIC (BTCP) crystals of the non-recovering ECAL endcap signal loss

The values of the μ -intercepts at the beginning of 2012 pp collision data taking are chosen as the observed values. In order to avoid the impression of a precise measurement, no uncertainties in the comparison are quoted

The comparison between the μ -intercepts and the prediction from simulation is shown in Table 11.1. The predictions match the order of magnitude of the measurements. This suggest that the prediction model of the ECAL transparency loss as a function of $|\eta|$ and integrated luminosity is correct to an acceptable level.

11.5 Correlations Between Light Monitoring Signals and μ_{SIC} , a Validation

The SIC measured the $\mu_{\rm IND}$ values for all of its crystals by itself. In order to distinguish it from $\mu_{\rm IND}$ of Eq. (11.1), the measured variable is called $\mu_{\rm SIC}$. Figure 11.14 illustrates the $\mu_{\rm SIC}$ values for both endcaps. Also, the comparison of the $\mu_{\rm std}$ and $\mu_{\rm SIC}$ values for crystals, where a measurement of $\mu_{\rm std}$ had been performed, is shown in Fig. 11.15. The correlation is wide spread.

We repeat the studies presented in Sect. 11.4.2 for the SIC crystals using $\mu_{\rm SIC}$. Using Eq. (11.4), we form the correlation between $\Delta({\rm VPT/PN})$ and $\mu_{\rm SIC}$, and fit it to obtain μ -slopes and μ -intercepts. The correlation coefficient is shown in Fig. 11.16. We make three general observations with respect to the correlation between $\Delta({\rm VPT/PN})$ and $\mu_{\rm std}$, Fig. 11.10, left:

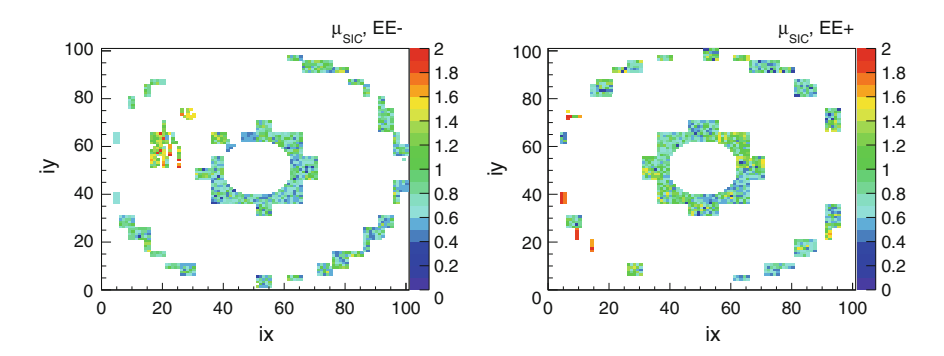


Fig. 11.14 Maps of $\mu_{\rm SIC}$ (given in m⁻¹) for the ECAL endcaps EE- (*left*) and EE+ (*right*) for all crystals produced by the SIC. The crystals are identified by their location indices ix and iy for each endcap, going from 1 to 100

Fig. 11.15 Correlation between μ_{std} (x axis) and μ_{SIC} (y axis). The *dashed line* indicates $\mu_{\text{std}} = \mu_{\text{SIC}}$

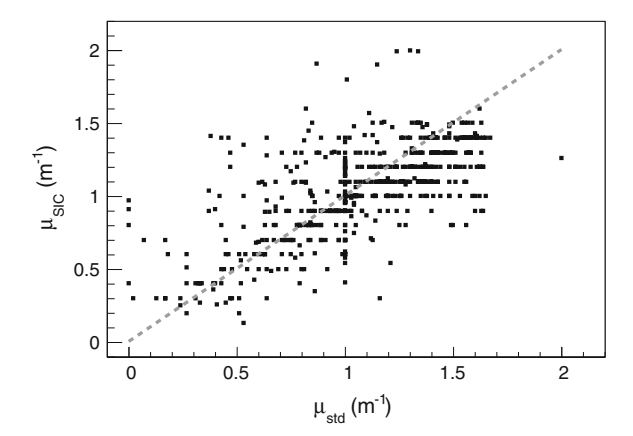
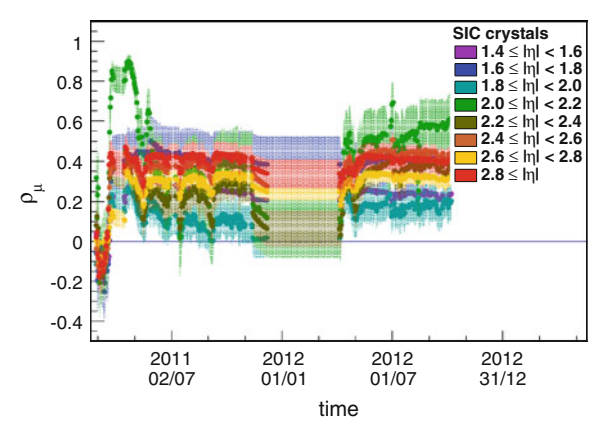


Fig. 11.16 The correlation coefficient as a function of time for the SIC crystals in various $|\eta|$ bins



- The anomalous behavior for the SIC crystals within $1.8 \le |\eta| < 2.0$ is not observed when using $\mu_{\rm SIC}$. However, the observation from Fig. 11.10 is not due to fluctuations in the $\mu_{\rm std}$ measurements, because the anomalous behavior is also observed for correlations with burn-in, see Sect. 11.6.1. The non-observation in Fig. 11.16 does not give any hint for the underlying reason of the anomalous behavior in Figs. 11.10 and 11.11.
- The correlations seem to build up quicker than presented in Fig. 11.10. A reason might be that all SIC crystals contribute to the correlation and fits. The correlation might be visible even for small changes in VPT/PN, while for the correlation between $\Delta(\text{VPT/PN})$ and μ_{std} we need stronger changes, as less crystals contribute and statistical fluctuations have larger impact.
- The correlation seems weaker. For the correlation between $\Delta(\text{VPT/PN})$ and μ_{std} , we had values of about 0.3–0.8. Now, values between 0.2–0.6 are reached. We might find the reason for this difference in Fig. 11.15: most of the μ_{SIC} values are given in steps of 0.1. Furthermore, the difference between μ_{std} and μ_{SIC} is quite large for some crystals. If the μ_{SIC} measurements have a larger uncertainty than the measurements of μ_{std} , a lower ρ_{μ} is expected.

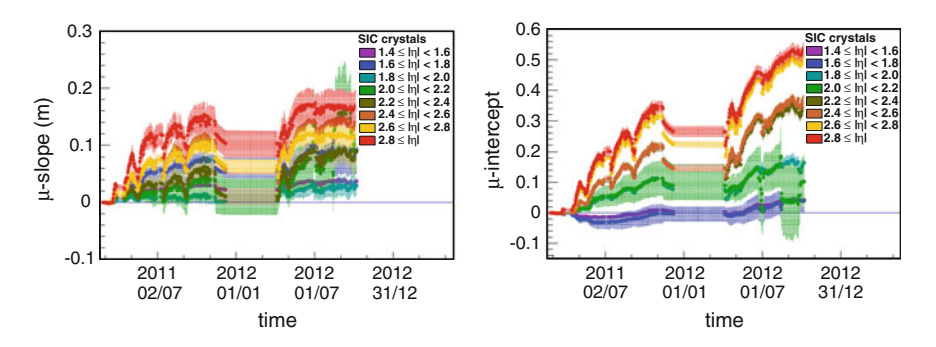


Fig. 11.17 The μ -slopes (*left*) and μ -intercepts (*right*) for the SIC crystals in various $|\eta|$ bins as a function of time

Figure 11.17 shows both the μ -slopes and μ -intercepts obtained from the fits of the correlations between $\Delta(\text{VPT/PN})$ and μ_{SIC} .

The general behavior of the previous results as a function of time or $|\eta|$ is reproduced in the correlations between $\Delta(\text{VPT/PN})$ with μ_{SIC} compared to the correlations with μ_{std} . However, the absolute strengths of the μ -slopes and μ -intercepts for the regions $1.8 \leq |\eta| < 2.4$ are a bit different from those of the correlations using μ_{std} . Only few crystals contribute in that region, see Fig. 11.14. Therefore, this observation could be due to statistical fluctuations.

Another strange behavior is observed for the μ -slopes and μ -intercepts for September/October 2012 and $2.0 \le |\eta| < 2.2$: the μ -slopes suddenly increase strongly, while the μ -intercepts decrease in a similar strong manner. Maybe, statistical fluctuations lead to different fit conditions in that period.

Besides these observations, the general observations made previously in Sect. 11.4.2 also hold for the correlations using μ_{SIC} .

11.6 Correlations Between Light Monitoring Signals and the Burn-In

In the previous sections, we studied the correlations between the laser monitoring data and the laboratory measurements of $\mu_{\rm std}$ ($\mu_{\rm SIC}$). We interpreted the observed linear correlations as follows: The slopes must be mostly because of the transparency change of the crystals due to ionizing radiation. We attributed every other damage component to the intercepts. Among those could be a component due to radiation damages to the on-detector readout electronics.

In this section, we will investigate damages to the VPTs more closely. We use the same approach as before: the laser monitoring data are correlated with laboratory measurements, this time with a variable describing the VPT quality. We have introduced the burn-in in Sect. 11.2. It is the ratio of the anode currents measured before and after LED illumination.

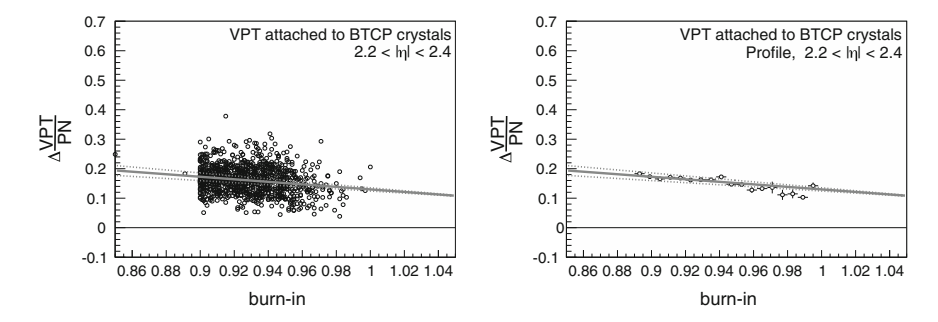


Fig. 11.18 Left Correlation between $\Delta(\text{VPT/PN})$ and burn-in for VPTs attached to BTCP crystals within $2.0 \leq |\eta| < 2.2$. A linear fit to the correlation is shown with uncertainties indicated by dotted lines. Right Corresponding profile of the $\Delta(\text{VPT/PN})$ as a function of burn-in. The linear fit function (solid line) is the one on the correlation in the left-hand side plot

First, we want to review the correlation itself. For this, we consider the same fixed period as we did in Sect. 11.4.1, obtain the $\Delta(\text{VPT/PN})$ for each VPT (connected to a crystal) and correlate it with the measurements of the burn-in. An example of the correlation for VPTs attached to BTCP crystals within $2.0 \leq |\eta| < 2.2$ is shown in Fig. 11.18, left. We observe a linear anti-correlation. The anti-correlation is much weaker than the correlations observed between $\Delta(\text{VPT/PN})$ and μ_{std} , but its existence is nicely illustrated by the profile shown in Fig. 11.18, right. We fit this anti-correlation with a linear function. We obtain a negative "burn-in slope" and the value of burn-in at unity ("burn-in = 1").

The burn-in is purely a VPT quantity. Therefore, the burn-in slope contains information about the VPT component of the transparency changes due to radiation damages. On the other hand, burn-in = 1 contains all components not related to VPTs.

11.6.1 Time Evolution of the Anti-correlations

Similar to the study presented in Sect. 11.4.2, we define $\Delta(\text{VPT/PN})$ values as in Eq. (11.4), correlate them with the burn-in values, and fit the correlations to obtain burn-in slopes and burn-in = 1 values. But first, we test the strengths of the anti-correlations by studying the correlation coefficient ρ_{burnin} , defined in a similar manner as Eq. (11.5), as a function of time and various bins in $|\eta|$. The study is done separately for VPTs attached to SIC or BTCP crystals, as we do not want to introduce any bias due to the crystal properties. The time evolution of the correlation coefficient is shown in Fig. 11.19.

The anti-correlation is very weak, but builds up quickly within few months. The ρ_{burnin} values are roughly between -0.1 and -0.25, but for the most outer ring $(1.4 \le |\eta| < 1.6)$, the correlation is positive for a large fraction of 2011 pp collision

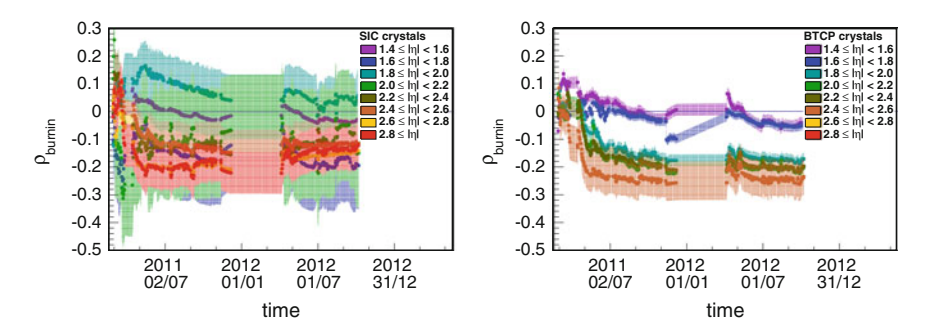


Fig. 11.19 The correlation coefficient ρ_{burnin} as a function of time for VPTs attached to crystals produced by the SIC (*left*) and the BTCP (*right*) for various $|\eta|$ bins. The anomalous behavior of ρ_{burnin} for VPTs attached to SIC crystals between $1.8 \le |\eta| < 2.0$ is not understood. It is related to the observations of Figs. 11.10 and 11.11

data taking. The statistical uncertainties on the correlation coefficients for VPTs attached to SIC crystals are very large in most $|\eta|$ regions because of the limited numbers of VPTs within those regions. We observe an anomalous behavior of ρ_{burnin} for VPTs attached to SIC crystals between $1.8 \leq |\eta| < 2.0$. This behavior is related to the anomalous behavior observed previously in Sect. 11.4. The reason for it is not understood. Possible wrong associations of crystals and VPTs with either the laser monitoring data output or the laboratory measurements of μ_{std} and burn-in have been discarded after discussion with experts [20].

Next, we investigate the evolution of the burn-in = 1 values as a function of time in Fig. 11.20. We expect no new information from these values, as they encode the time evolution behavior not related to the VPT quality, which was also studied in the correlations between Δ (VPT/PN) and μ_{std} in Sect. 11.4.

We observe a steady increase of the burn-in = 1 values during collisions that seems to become flatter with time (or instantaneous luminosity), and a rapid decrease of

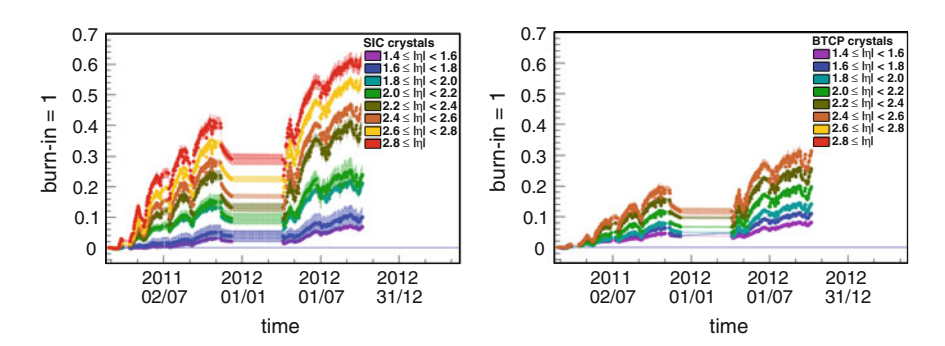


Fig. 11.20 The burn-in = 1 values as a function of time for VPTs attached to crystals produced by the SIC (*left*) and the BTCP (*right*) in various $|\eta|$ bins

burn-in = 1 values during periods, where no pp collisions were provided to CMS by the LHC. The rapid decrease is mainly due to the recovery of crystal transparency losses from ionizing damage. The tendency of the increase in burn-in = 1 values to be small during stable running conditions reflects the equilibrium between creation and annihilation rates for color centers in crystals because of ionizing radiation. However, a plateau is not reached. This is expected because of permanent damage components like hadron damage to crystals.

The more interesting observation is the evolution of the burn-in slopes as a function of time and $|\eta|$. It is shown in Fig. 11.21. The burn-in slopes get steeper over time. Such a behavior is expected for damages to the VPTs. Since the integrated luminosity, and with it also the dose, has been increasing over time, also the damage to the VPTs could increase. The dependence on the radiation exposure of VPT damage is also reflected in the dependence of burn-in slopes with $|\eta|$.

The initial drop of the burn-in slope values over time is most likely coming from the initial rapid VPT conditioning rate, which had already been observed in dedicated laboratory tests and can be seen in the example of Fig. 11.4. In Fig. 11.21, one also notices that the burn-in slopes reach a plateau, suggesting that the VPT response loss stabilizes at a constant value in 2012. A similar behaviour was found in laboratory tests, see Fig. 11.4.

In general, for both the burn-in slopes and burn-in = 1 amplitudes, one observes values that are slightly larger in channels with SIC crystals than in channels with BTCP crystals. A possible explanation might be that, on average, SIC crystals produce 50% more light than BTCP crystals. Thus, the integrated photocurrent for VPTs reading out SIC crystals is on average 50% larger than that for BTCP channels, causing correspondingly larger losses through VPT conditioning.

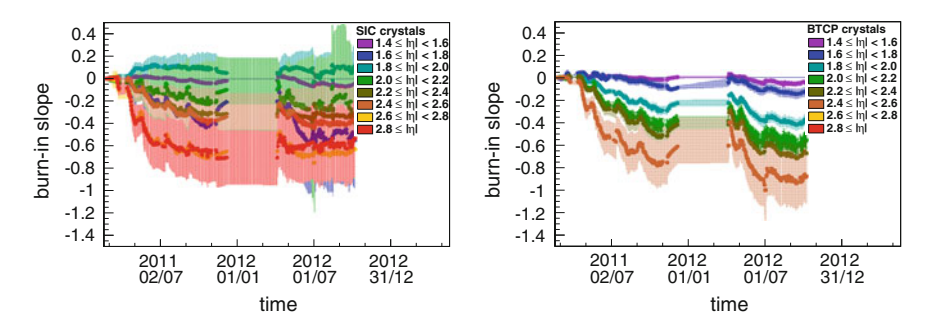


Fig. 11.21 The burn-in slopes as a function of time for VPTs attached to the SIC (*left*) and the BTCP (*right*) crystals in various $|\eta|$ bins. The anomalous behavior of burn-in slopes for VPTs attached to SIC crystals between $1.8 < |\eta| < 2.0$ is not understood

11.7 Summary

The evolution of the signals measured in the CMS ECAL endcaps was studied. The change in light signals obtained by the laser monitoring system of the ECAL, $\Delta(VPT/PN)$, was compared to several quality parameters of ECAL on-detector components.

The first quality parameter considered was μ_{std} , the absorption coefficient of ionizing radiation measured for the PbWO₄ crystals of the ECAL under standardized conditions. The comparison is done for both crystal producers separately and for various regions in $|\eta|$ because of the dose (rate) dependence on $|\eta|$. We have observed a linear correlation between the laser monitoring data and the laboratory measurements of μ_{std} . The correlation has been fitted with a linear function. Encoded in the slope of the linear fit, this correlation has allowed to disentangle the component of ionizing radiation to the crystal transparency change. The same results have been found when μ_{SIC} , the absorption coefficient as measured by the SIC for its crystals, was considered in the correlation.

The μ -slopes reached a stable value during 2012 pp collision data taking, indicating that the amount of ionizing radiation damage to the crystals was compensated by the recovery rate of the same damage component.

Within the extrapolation of the correlation to $\mu_{std}=0$, the average crystal transparency change not related to ionizing radiation, was found. Non-vanishing values of the μ -intercepts indicated the presence of contributions to the signal loss uncorrelated with crystal resistance to ionizing radiation. The μ -intercepts kept growing throughout 2011 and 2012, as expected for a cumulative damage like hadron damage to the crystals or VPT damage. The comparison between the μ -intercepts and the prediction from simulation support the validity of the long-term EE performance predictions that are needed for informed decisions on the upgrade needs for HL-LHC conditions.

The other quality parameter that has been studied is the burn-in, a quality parameter for the VPTs in the ECAL endcaps. The burn-in is the ratio of VPT anode currents before and after an illumination with standardized conditions. We have observed a linear anti-correlation between the signal changes of the laser monitoring system, $\Delta(\text{VPT/PN})$, and the burn-in values. The strength of this anti-correlation has been weaker than the correlation between $\Delta(\text{VPT/PN})$ and μ_{std} . This shows that the contribution of the crystal damage to the ECAL transparency is dominant over the contribution of the VPTs. The slopes of the linear fit to the anti-correlation between $\Delta(\text{VPT/PN})$ and burn-in can be used to partly disentangle the photodetector contribution of the transparency loss.

These measurements provide the first evidence with in-situ data for a cumulative damage component and a component to the transparency loss related to the readout electronics within the CMS ECAL.

With the availability of more data after the long shutdown from 2015 onwards, these studies can be extended to further establish the evolution of various contributions to the signal changes in the ECAL endcaps. One might also gain more significant evidence of the observations made in this study.

References

- CMS Collaboration, CMS: the electromagnetic calorimeter. Technical design report, CERN LHCC-97-33(1997)
- X. Qu, L. Zhang, R. Zhu, Radiation induced color centers and light monitoring for lead tungstate crystals. IEEE Trans. Nucl. Sci. 47, 1741 (2000). doi:10.1109/TNS.2000.914439
- A. Annenkov, M. Korzhik, P. Lecoq, Lead tungstate scintillation material. Nucl. Instrum. Methods A 490, 30 (2002). doi:10.1016/S0168-9002(02)00916-6
- Crystal Clear Collaboration, Ten years of lead tungstate development. Nucl. Instrum. Methods A537, 15 (2005). doi:10.1016/j.nima.2004.07.223
- H. Chen et al., Radiation damage measurements of undoped lead tungstate crystals for the CMS electromagnetic calorimeter at LHC. Nucl. Instrum. Methods A 414, 149 (1998). doi:10. 1016/S0168-9002(98)00573-7
- H. Hofer, P. Lecomte, F. Nessi-Tedaldi, Afterglow measurements of lead tungstate crystals. Nucl. Instrum. Methods A 433, 630 (1999). doi:10.1016/S0168-9002(99)00398-8
- M. Huhtinen et al., High-energy proton induced damage in PbWO₄ calorimeter crystals. Nucl. Instrum. Methods A 545, 63 (2005). doi:10.1016/j.nima.2005.01.304
- 8. Y. Blinnikov et al., Radiation hardness, excess noise factor and short-term gain instability of vacuum phototriodes for the operation in pseudorapidity range $1.5 \le \eta \le 3.0$ at CMS ECAL. Nucl. Instrum. Methods A **504**, 228 (2003). doi:10.1016/S0168-9002(03)00795-2
- 9. Y. Gusev et al., Super radiation hard vacuum phototriodes for the CMS endcap ECAL. Nucl. Instrum. Methods A 535, 511 (2004), doi:10.1016/j.nima.2004.07.181
- CMS Collaboration, The CMS experiment at the CERN LHC. JINST 3, S08004 (2008). doi:10. 1088/1748-0221/3/08/S08004
- K.W. Bell et al., The development of vacuum phototriodes for the CMS electromagnetic calorimeter. Nucl. Instrum. Methods A 469, 29 (2001). doi:10.1016/S0168-9002(01)00700-8
- CMS Electromagnetic Calorimeter Group Collaboration, Radiation hardness qualification of PbWO₄ scintillation crystals for the CMS Electromagnetic Calorimeter. JINST 5, P03010 (2010). doi:10.1088/1748-0221/5/03/P03010. arXiv:0912.4300
- 13. H. Rykaczewski, R. Brown, I. Vasilyev, Private communication
- F. Ferri, Monitoring and correcting for response changes in the CMS lead-tungstate electromagnetic calorimeter. J. Phys. Conf. Ser. 404, 012041 (2012). doi:10.1088/1742-6596/404/1/012041
- L. Zhang, On behalf of the CMS ECAL Collaboration, a diode-pumped solid state blue laser for monitoring the CMS lead tungstate crystal calorimeter at the LHC. J. Phys. Conf. Ser. 404, 012042 (2012)
- 16. https://twiki.cern.ch/twiki/bin/view/CMSPublic/LumiPublicResults
- P.R. Hobson, On behalf of the CMS Collaboration, the stability of vacuum phototriodes to varying light pulse loads and long term changes in response. PoS PhotoDet2012, 064(2012)
- CMS Collaboration, MARS15 Simulation Studies in the CMS Detector of Some LHC Beam Accident Scenarios, CMS NOTE-2009-019 (2009)
- 19. R. Zhu, Precision crystal calorimetry in future high energy colliders. IEEE Trans. Nucl. Sci. 44, 468 (1997). doi:10.1109/23.603693
- 20. D. Cockerill, Private communication
- A. Martelli, On behalf of the CMS Collaboration, Evolution of the response of the CMS ECAL and possible design options for electromagnetic calorimetry at the HL-LHC. JINST 9, C04017 (2014). doi:10.1088/1748-0221/9/04/C04017

Chapter 12 **Summary**

The successful operation of the LHC and the associated experiments during the first run of data taking from 2010 to 2012 has resulted in remarkable results. The highlight has certainly been the observation of a boson at a mass of about 125 GeV by the ATLAS and CMS collaborations. This boson seems to be compatible with the predicted Higgs boson, and therefore its observation has resulted in the adwarding of the Nobel Prize in Physics to François Englert and Peter Higgs in 2013.

Among the rich physics program of the two general-purpose experiments, the ATLAS and CMS experiments, large efforts have been put into direct searches for physics beyond the SM. Several indications exist that the SM is not the final theory of particle physics, and that new physics signatures might be accessible at the energy scale of the LHC.

One of the new physics models is SUSY. Several "problems" of the SM can be solved: SUSY offers a natural explanation of the hierarchy problem, can provide a dark matter particle candidate, and might even open the door for a more complete theory including gravity. Therefore, SUSY is one of the most popular theories of physics beyond the SM. As the masses of the supersymmetric particles are expected to be around the TeV scale, SUSY signatures should be observable by the LHC experiments.

In this dissertation, a search for SUSY has been presented. The search analyzed pp collision data collected by the CMS experiment at $\sqrt{s} = 8$ TeV. Events resulting in hadronic final states were selected.

In order to surpress the SM background of the QCD production of multijet events, a selection on M_{T2} was deployed. The variable M_{T2} and its kinematical properties were reviewed, as well as the search for SUSY performed with pp collision data collected at $\sqrt{s} = 7$ TeV, which also had been based on a selection on M_{T2} .

The search made use of multiple signal regions defined by selections on $M_{\rm T2}$, $H_{\rm T}$, the number of jets, and the b-jet multiplicity. This multibin approach allowed for a high sensitivity to several SUSY scenarios. A dedicated dijet selection was designed for squark pair production signals, while the multijet regions were sensitive to gluino production. The division of search regions along the b-jet multiplicity allowed to search for any kind of squark flavor, either in the direct production or within gluino

196 12 Summary

decays. A wide range of masses of supersymmetric particles was made accessible by the selection criteria on M_{T2} and H_T .

The background due to SM processes was estimated by the means of data-driven estimation methods. No significant excess beyond the expectation from SM processes was observed. The results were interpreted in various models of SUSY. Within the framework of simplified models, gluino masses below 1225 GeV have been excluded at 95 % CL, independent of the considered decay modes. In models of direct squark pair production, squark masses up to 450–875 GeV have been excluded at 95 % CL, depending on the flavor and number of the accessible squarks. The best limits at 95 % CL on the LSP mass have been between 450 and 740 GeV for gluino-initiated LSP production, while the limits have been 60–325 GeV for squark-initiated LSP production. In a cMSSM/mSUGRA model with tan $\beta=30$, $A_0=-2$ max(m_0 , $m_{1/2}$), and $\mu>0$, the absolute mass limits on the gluino and first generation squarks at 95 % CL have been determined to be 1150 and 1450 GeV, respectively. The established exclusion limits belong to the strongest limits obtained for hadronic SUSY signatures.

Another strategy for a search for supersymmetric particle production was presented. This strategy was focused specifically on the direct production of stop pairs using events containing two charged leptons. The discrimination power for signal events from stop production against background events from the production of $t\bar{t}$ +jets was investigated for several variables. Most of them were based on the M_{T2} variable. It was found that M_{T2} constructed with the two charged leptons as visible systems and E_{T}^{miss} provides the best discrimination power. Small signal sensitivity was observed for M_{T2} constructed with two visible systems, each one composed of a charged lepton and one b jet, and E_{T}^{miss} for events, where the invariant masses of the lepton—b-jet systems were below 180 GeV. The usage of another variant of M_{T2} , using only the b jets as visible systems, did not enhance the discrimination for signal events. In addition to M_{T2} variables, a discriminant based on fitting the event kinematics to mass constraints from top quarks and W bosons was developed. However, this discriminant was not able to distinguish between signal and background events.

Even though the first run of data taking at the LHC at $\sqrt{s}=7$ –8 TeV did not reveal any clear hint of new physics, a large phase space for new physics signatures is still uncovered. For the second run of the LHC, the center of mass energy will be increased to 13–14 TeV. This will boost the sensitivity for many new physics models, where the new physics particles have masses above 1 TeV. Furthermore, the validity of the SM will be probed at higher energies, and the properties of the Higgs boson will be studied.

Nevertheless, new physics signatures might still "hide" at lower energies: For instance, SUSY scenarios where the masses of the initially produced particle and the LSP are very close, the so-called compressed scenarios, are not constrained by most of the searches performed. In order to clearly observe a signal in those models, searches might need to study a very large data set, especially when only sparticles produced in electroweak processes are accessible at the energies provided by the LHC. This is one of several reasons for the decision to upgrade the LHC machine for the HL-LHC.

12 Summary 197

The upgrade program of the CMS experiment has already been started. In 2014, the coverage of the CSC and RPC detectors in the muon subsystem has been extended to higher $|\eta|$. The next step involves major upgrades of the L1 trigger system, the HCAL electronics, and the pixel detector.

The pixel detector will be replaced by a newly designed detector during the yearly shutdown between 2016 and 2017. Instead of three layers in the barrel part of the detector and two disks in each endcap, the new design will be composed of four barrel layers and three disks per endcap. At the same time, the material budget will be decreased. The overall tracking and vertexing performance is expected to increase. In order to evaluate the physics performance of this upgrade in the context of SUSY searches, a study was performed using the event selection of the $M_{T2}b$ analysis, which had been performed with pp collision data collected at $\sqrt{s}=7$ TeV. A special focus was set on the capability of identifying jets originating from b-quark hadronization. For the tested model, the signal selection efficiency increased by 20% for the CMS detector design with the new pixel detector compared to the current design. This increase was found for a constant rate of misidentifying light-flavor quark and gluon jets as b jets.

For the HL-LHC upgrade, also other parts of the CMS detector will need to be upgraded. Among them will be the (partial) replacement of the ECAL endcaps. The radiation exposure in the forward part of the CMS detector leads to a decrease of the energies measured by the ECAL system. For the HL-LHC, the radiation will be too strong to be sustained by the ECAL endcaps.

Several reasons for the decrease in signals are known: ionizing radiation will create color centers in the crystals of the ECAL, thus reducing the transparency of the crystals. Also, hadron-induced damage is diminishing the transparency of the crystals. Moreover, several sources are known to damage the VPTs. In a study presented in this dissertation, the long-term evolution of the signals produced in the ECAL endcaps was investigated.

The objective of the study was to disentangle various contributions to the signal decrease. For this purpose, response changes in data, obtained by the ECAL light monitoring system, were compared to measurements of quality parameters of the different ECAL on-detector components. The absorption coefficient μ_{std} , measured under standardized conditions, describes the resistance of the PbWO₄ crystals to ionizing radiation. Linear correlations between the values of μ_{std} and the changes in the in-situ data measurements were observed. The slopes of the correlations can be contributed to damages because of ionizing radiation. The values of those slopes stabilized during 2012 pp collision data taking, indicating that the annihilation and creation rate for color centers had leveled out. The linear correlations also showed the existence of non-zero intercepts, indicating the presence of a damage component not related to ionizing radiation. The values of the intercepts kept growing throughout data taking, as expected for cumulative damage, for example because of hadron radiation. The values of the intercepts were compared with predictions of the signal decrease due to the cumulative damage to the ECAL. The comparison acts as a validation of the prediction model used in studies performed for the ECAL upgrade. 198 12 Summary

A similar study was done for a VPT quality parameter, the burn-in. The burn-in is the ratio of the measured anode current before and after LED illumination. Linear correlations with non-zero slopes were observed between the burn-in values and the changes in monitoring data. Therefore, for the first time with in-situ data, a contribution to the ECAL signal changes could be attributed to the readout chain.

The coming years will be very interesting in the field of high energy physics. The jump in the center of mass energy of the LHC will allow to test the validity of the SM at high energies, allow to probe the Higgs sector and determine the properties of the new boson, and allow to search for new physics signatures. Regardless if new physics is found or only null results are obtained, the impact of searches to our understanding of particle physics will be substantial.

Appendix A Alternatives to the Hemisphere Algorithm Used in the 7 and 8 TeV Searches

The hemisphere algorithm, described in Sect. 6.2, has been studied in great detail and the choice of the hemisphere for the 7 and 8 TeV searches, as described in Sect. 6.4 and Chap. 7, was driven by a high efficiency for correct jet assignment to the hemispheres.

The studies presented in this subsection are twofold: first, a study of the input to the hemisphere algorithm for stronger background rejection for multijet background. Here, the idea is not driven by the correct jet assignment, but rather by the sensitivity of M_{T2} to discriminate signal versus background. The second part of the studies is of different nature. When the hemisphere algorithm was introduced, no fast calculation of an iterative jet clustering algorithm had been available. Now, with the FASTJET package [1, 2], k_T -type jet finding algorithms could be used as an alternative to the hemisphere algorithm. It should be noted by the reader that these studies where done after the 8 TeV SUSY search had been performed.

In these studies, the performance of M_{T2} , using as visible systems the pseudojets as defined in Sect. 6.2, is compared to a "modified M_{T2} ", short m M_{T2} , where the input for the pseudojet calculation has been changed. The comparison is performed using simulation samples of QCD multijet production, an electroweak sample, mainly consisting of simulated events of $W(l\nu)$ +jets and $Z(\nu\overline{\nu})$ +jets, and a SUSY benchmark signal of direct stop pair production with decay $\widetilde{t} \to t\widetilde{\chi}_1^0$ and masses $M(\widetilde{t}) = 400 \, \text{GeV}$, $M(\widetilde{\chi}_1^0) = 0 \, \text{GeV}$, see also Sect. 7.1. The samples are normalized to 19.5 fb⁻¹ and generated at $\sqrt{s} = 8 \, \text{TeV}$. The events selected for this study have $H_T > 750 \, \text{GeV}$ and at least three jets. This is a relaxed selection compared to Sect. 7.2.

The first set of studies is targeting stronger multijet background rejection. One ansatz is using transverse objects already in the seeding. The reasoning behind that is the following: M_{T2} is sensitive to the p_T of the two hemispheres, however the seeding and clustering uses the full momenta of the visible objects. The two hemispheres could be seeded by two hard forward ISR jets, but not by the hard process, which is expected to by more central. Therefore the event might be asymmetric in the transverse plane. One possibility is to use the transverse dijet mass instead of the invariant dijet mass for selecting jets in the seeding of the algorithm. Figure A.1 shows

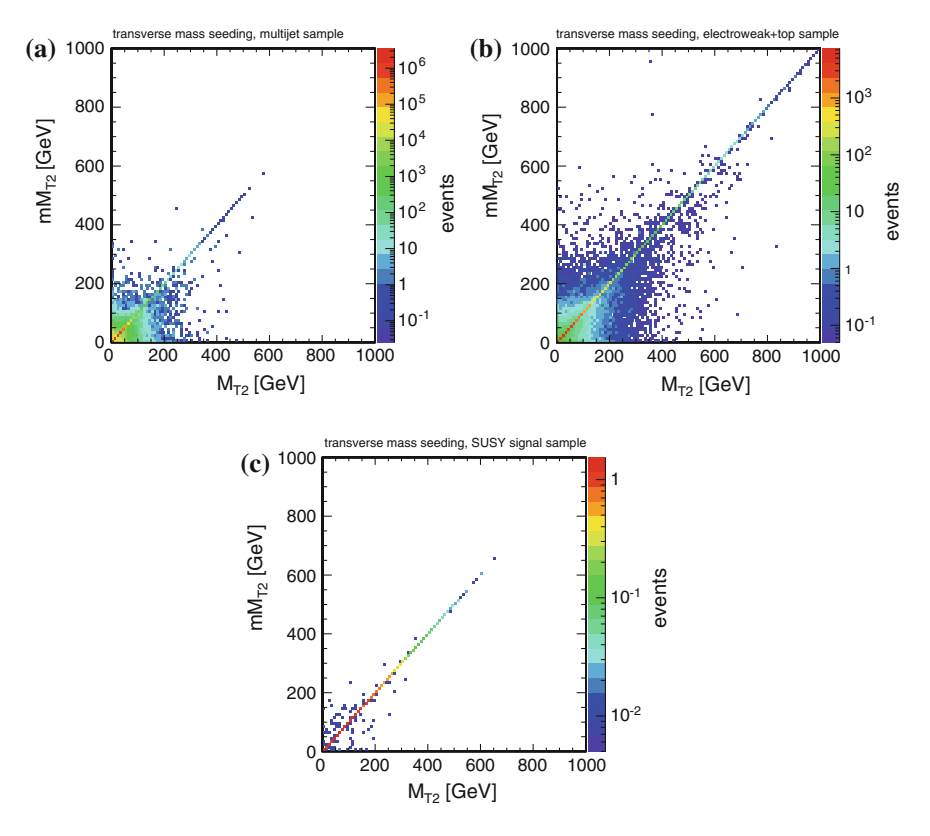


Fig. A.1 Correlation between M_{T2} , seeded by the invariant dijet mass (x axis), and m M_{T2} , seeded by the transverse dijet mass (y axis), for events with ≥ 3 jets. **a** for multijets, **b** for electroweak production, **c** for a SUSY model

the correlations between M_{T2} and m M_{T2} with the modified seeding. For most events, the different seeding method does not change the M_{T2} value, only a fraction of events obtain a different value. In order to better visualize the effect on the M_{T2} variable, the M_{T2} distributions with and without modified seeding are shown in Fig. A.2. The multijet background at high M_{T2} is suppressed substantially by $\sim 20\,\%$, while the electroweak background and the SUSY signal benchmark models are not affected within the statistical precision.

An attempt to quantify this result is the metric

$$M(X) = \frac{N_{+}(X) - N_{-}(X)}{N_{+}(X) + N_{-}(X)}$$
(A.1)

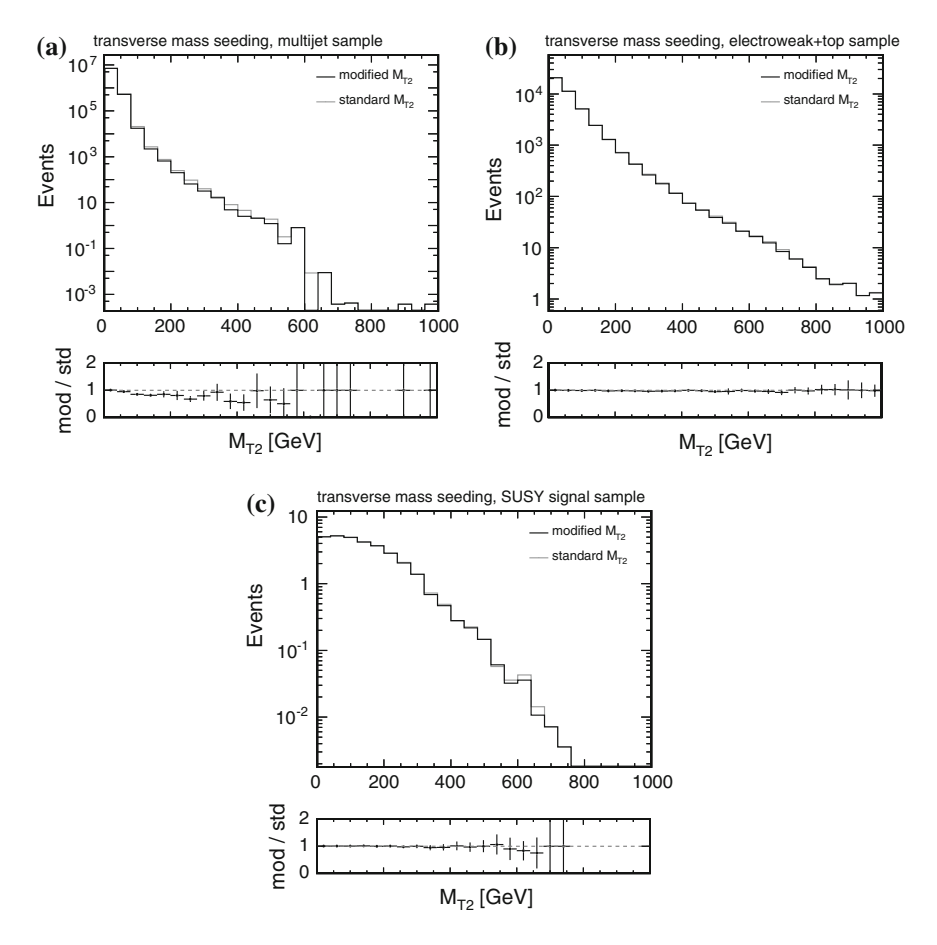


Fig. A.2 Comparison and ratio between M_{T2} distribution for events with ≥ 3 jets for M_{T2} , seeded by the invariant dijet mass (*gray* distribution), and m M_{T2} , seeded by the transverse dijet mass (*black* distribution). **a** for multijets, **b** for electroweak production, **c** for a SUSY model

with

$$N_+(X)$$
 = number of events with $\{(M_{T2} - mM_{T2}) > +X\}$
 $N_-(X)$ = number of events with $\{(M_{T2} - mM_{T2}) < -X\}$.

The idea is the following: if M(X) > 0 holds for multijet events, but not for SUSY signal events (and electroweak events, which behave SUSY-like as explained in Sect. 6.3), then the new implementation might perform better, while for M(X) < 0 it does not. This statement, of course, depends on the cut value X and also the SUSY model under consideration, and therefore is not very strict.

If X = 20 GeV (100 GeV), this metric yields $M = 0.23 \pm 0.01$ (0.68 \pm 0.03) for the multijet sample, while $M = 0.06 \pm 0.03$ (0.24 \pm 0.06) for the SUSY benchmark model. This metric confirms the observation of Fig. A.2.

Further studies have been performed, changing the seeding or clustering algorithm, as well as changing the object selection for the pseudojets calculation. However, none of the other studies showed such an improvement as the one presented here. Therefore, those figures are omitted.

The second set of the studies examines, whether the hemisphere algorithm can be replaced by a $k_{\rm T}$ -type clustering algorithm. Three algorithms have been tested: the $k_{\rm T}$, the Cambridge-Aachen [6], and the anti- $k_{\rm T}$ algorithms. The $k_{\rm T}$ algorithm uses 2 instead of -2 as exponent of Eq. (5.1), the Cambride-Aachen algorithm uses 0. The algorithm is slightly modified with respect to the one presented in Sect. 5.7: The starting point is the list of jets. The reason for using jets over individual PF particles is that the energy corrections applied to the jets (Sect. 5.7) are already included. The clustering is performed in the same manner as in Sect. 5.7, but instead of removing an object i when d_i is smaller than any d_{ij} , the clustering is continued, using the minimum d_{ij} , until exactly two objects are left.

As for the first study, the M_{T2} variable is called M_{T2} if the hemisphere algorithm was used, while the name will be mM_{T2} if a k_T -type clustering has been used.

In Figs. A.3 and A.4, the correlation between $M_{\rm T2}$ and m $M_{\rm T2}$ are shown for using the $k_{\rm T}$ and anti- $k_{\rm T}$ algorithms, respectively. While the $M_{\rm T2}$ value does not change for a large fraction of events, meaning that both the hemisphere and $k_{\rm T}$ -type algorithm yield the same pseudojets, there are significant differences between $M_{\rm T2}$ and m $M_{\rm T2}$ for the other fraction of events. The difference tends to yield, on average, lower m $M_{\rm T2}$ values compared to $M_{\rm T2}$, especially for the anti- $k_{\rm T}$ algorithm. For better comparisons, the $M_{\rm T2}$ distributions for both $M_{\rm T2}$ and m $M_{\rm T2}$ are drawn in Figs. A.5 and A.6 for using the $k_{\rm T}$ algorithm or the anti- $k_{\rm T}$ algorithm, respectively. The studies using the Cambridge-Aachen algorithm are not shown, because the shapes of the distributions are between the ones using the anti- $k_{\rm T}$ and $k_{\rm T}$ algorithms.

The first observation is that the M_{T2} distributions obtained using the k_T clustering algorithm are very close to the ones using hemisphere algorithm, the correlations are fairly symmetric with respect to the diagonal $M_{T2} = mM_{T2}$.

Let us apply the metric from above, Eq.(A.1): if $X=20\,\mathrm{GeV}$ (100 GeV), the metric is $M=0.33\pm0.01$ (0.82 ±0.03) for multijets event, while it is $M=-0.02\pm0.02$ (0.10 ±0.05) for the chosen SUSY model. The results lead to the conclusion that the hemisphere algorithm can be replaced with the k_T clustering algorithm.

The picture is different for the comparison between M_{T2} , computed using the hemisphere algorithm, and mM_{T2} , using the anti- k_T clustering algorithm. Many events are populating the region of $M_{T2} > mM_{T2}$, the tail of the mM_{T2} distribution

¹Considered changes involve all proposals of [3], as well as clustering algorithms used by other analyses [4, 5].

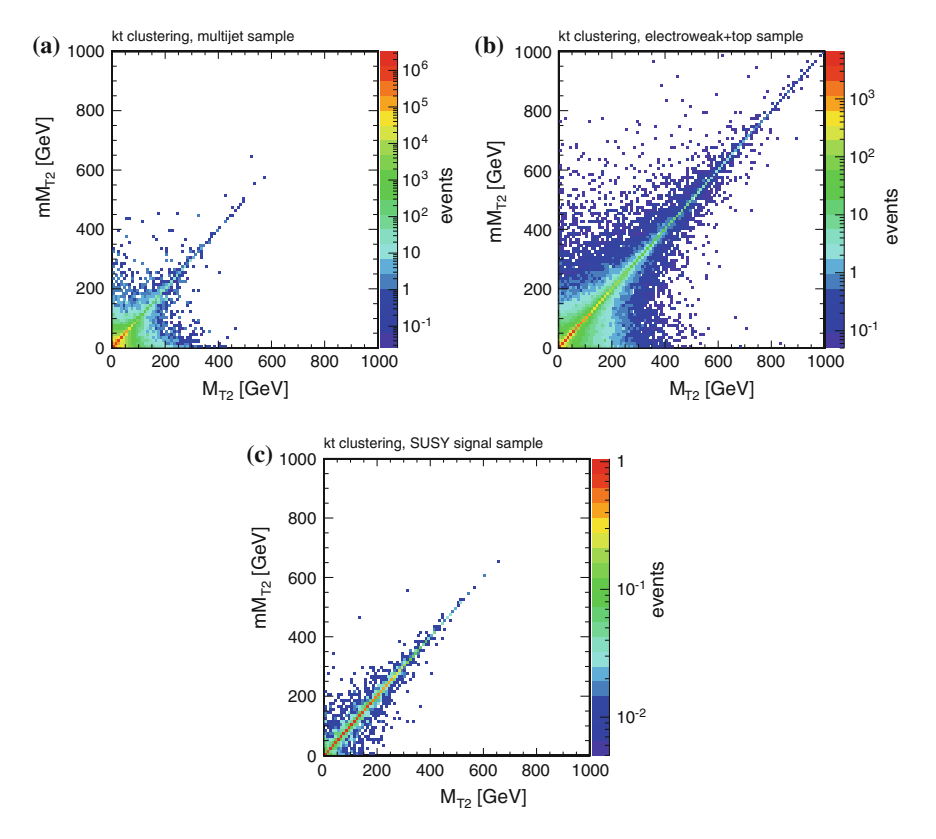


Fig. A.3 Correlation between M_{T2} , using the hemisphere algorithm (x axis), and mM_{T2} , using the k_T algorithm (y axis), for events with ≥ 3 jets. **a** for multijets, **b** for electroweak production, and **c** for a SUSY model

is depleted with respect to the $M_{\rm T2}$ distribution. This feature is not wanted for a search: The multijet background is already strongly suppressed for $M_{\rm T2} \gtrsim 200\,{\rm GeV}$ for $M_{\rm T2}$ using the hemisphere. This limits the phase space for the sensitive region in a search using $M_{\rm T2}$. At high $M_{\rm T2}$, the m $M_{\rm T2}$ distributions are shifted to lower values by $\sim 150-200\,{\rm GeV}$ with respect to $M_{\rm T2}$. Thus, the sensitive region of phase space is largely reduced.

The source for this dramatic change for mM_T using the anti- k_T algorithm has been investigated. It lies within the algorithm itself: the anti- k_T algorithm clusters, to leading order, first the hard objects. When the anti- k_T algorithm is applied on a collection of jets, the hardest jet is usually clustered with a softer jet close to it. As the new clustered object becomes harder than the initial hard jet, it is likely that the new object will be clustered next, and so on. Therefore, one can obtain very asymmetric

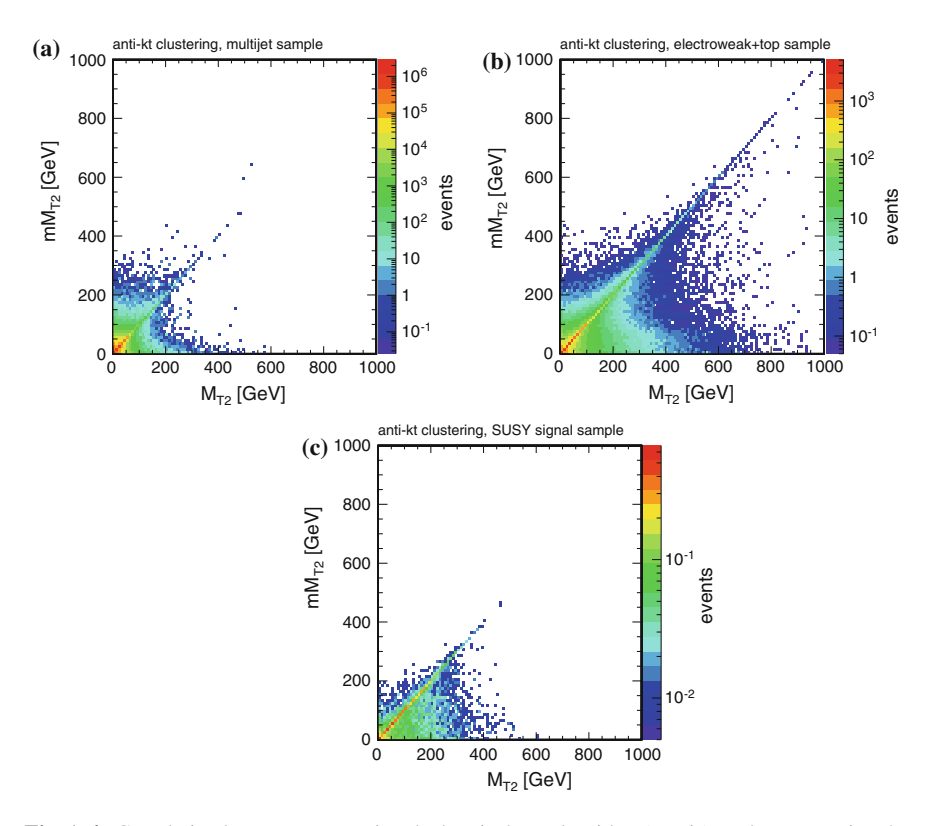


Fig. A.4 Correlation between M_{T2} , using the hemisphere algorithm (x axis), and mM_{T2} , using the anti- k_T algorithm (y axis), for events with ≥ 3 jets. **a** for multijets, **b** for electroweak production, and **c** for a SUSY model

numbers of jets between the pseudojets. This reasoning is confirmed in Fig. A.7. In this figure, the events of the SUSY signal model are investigated closer. A cluster asymmetry is defined as

cluster asymmetry =
$$\left| \frac{\{N_{\text{jets}} \text{ in pseudojet } 1\} - \{N_{\text{jets}} \text{ in pseudojet } 2\}}{N_{\text{jets}} \text{ in the event}} \right|$$
, (A.2)

where $N_{\rm jets}$ stands for number of jets. While this asymmetry is small for pseudojets constructed with the hemisphere algorithm, the $k_{\rm T}$ algorithm, and the Cambridge-Aachen algorithm, the pseudojets from the anti- $k_{\rm T}$ algorithm can yield a very large asymmetry.

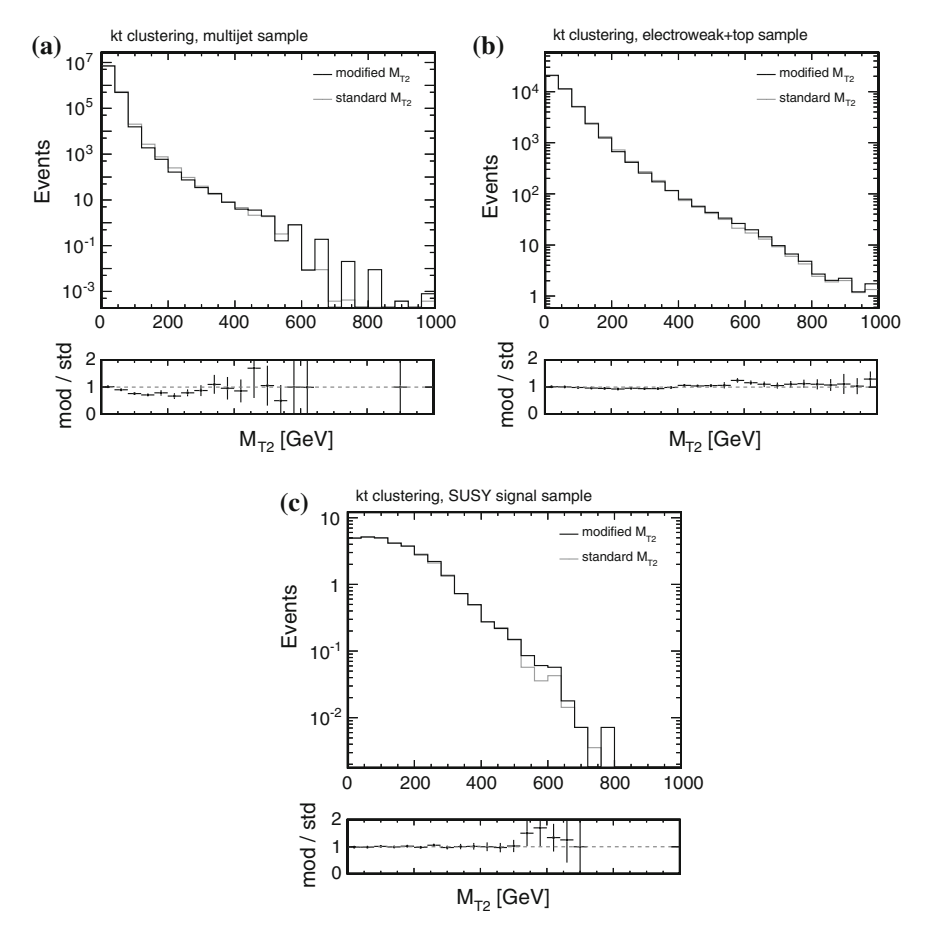


Fig. A.5 Comparison and ratio between the M_{T2} distribution for events with ≥ 3 jets for M_{T2} , using the hemisphere algorithm (*gray* distribution), and mM_{T2} , using the k_T algorithm (*black* distribution). **a** for multijets, **b** for electroweak production, and **c** for a SUSY model

The result of this is that, in many events, one of the pseudojets is soft while the other one is hard and contains most of the jets inside an event. It is easy to see, for example using Eq. (6.8) that the M_{T2} value for such a configuration can be significantly lower than for a symmetric distribution of jets into the pseudojets.

This set of studies shows that indeed the hemisphere algorithm can be replaced by a $k_{\rm T}$ -type algorithm. The tested algorithm, resembling closest the distributions of $M_{\rm T2}$ using the hemisphere algorithm, is the $k_{\rm T}$ clustering algorithm. The anti- $k_{\rm T}$ algorithm, used for jet clustering in CMS, is not optimal for the construction of the two pseudojets.

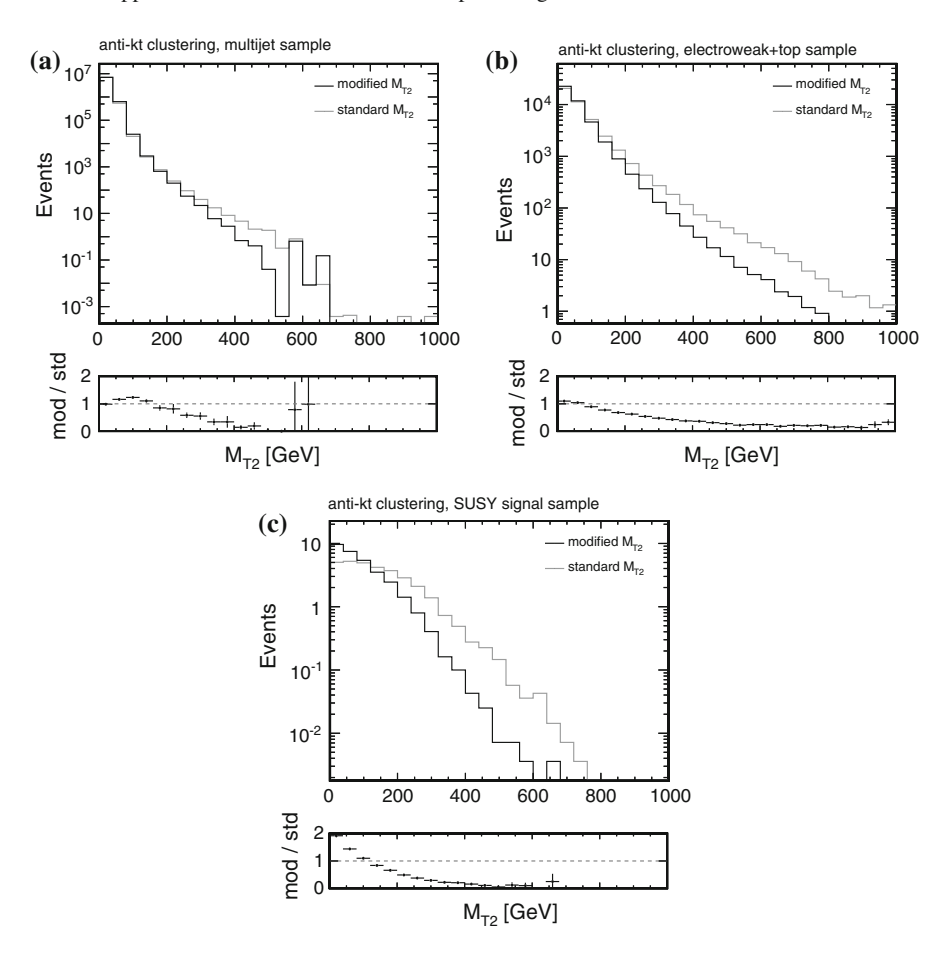
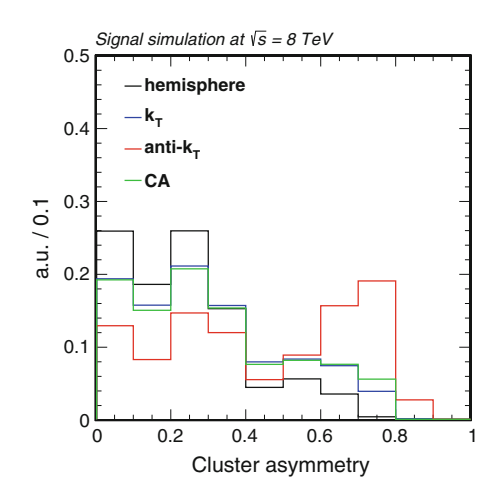


Fig. A.6 Comparison and ratio between M_{T2} distribution for events with ≥ 3 jets for M_{T2} , using the hemisphere algorithm (*gray* distribution), and mM_{T2} , using the anti- k_T algorithm (*black* distribution). a for multijets, b for electroweak production, and c for a SUSY model

Both studies presented in this section show that there is flexibility in the definition of the pseudojets. There is some room of improvement on the hemisphere algorithm itself, however, the settings used for the hadronic search (Chap. 7) are close to optimal. Another option of replacing the hemisphere algorithm with a $k_{\rm T}$ -type clustering algorithm has been investigated and was shown to be a valid alternative, but the choice of the clustering algorithm is very important. While $M_{\rm T2}$ using the $k_{\rm T}$ algorithm

Fig. A.7 Cluster asymmetry, as defined in Eq. (A.2), for SUSY events, for pseudojets constructed with the hemisphere algorithm (black) described in Sect. 6.2, the $k_{\rm T}$ algorithm (blue), the anti- $k_{\rm T}$ algorithm (red), and the Cambridge-Aachen algorithm (green)



seems to result in a similar distribution compared to M_{T2} using hemispheres, the anti- k_T algorithm yields very asymmetric pseudojets and therefore a much softer M_{T2} distribution.

References

- 1. M. Cacciari, G.P. Salam, Dispelling the N^3 myth for the k_t jet-finder. Phys. Lett. B **641**, 57 (2006). doi:10.1016/j.physletb.2006.08.037. arXiv:hep-ph/0512210
- 2. M. Cacciari, G.P. Salam, G. Soyez, FastJet user manual. Eur. Phys. J. C **72**, 1896 (2012). doi:10.1140/epjc/s10052-012-1896-2. arXiv:1111.6097
- 3. CMS Collaboration, CMS physics technical design report, volume II: physics performance. J. Phys. G **34**, 995 (2007). doi:10.1088/0954-3899/34/6/S01
- 4. CMS Collaboration, Search for supersymmetry in pp collisions at 7 TeV in events with jets and missing transverse energy. Phys. Lett. B **698**, 196 (2011). doi:10. 1016/j.physletb.2011.03.021. arXiv:1101.1628
- 5. CMS Collaboration, Inclusive search for squarks and gluinos in pp collisions at $\sqrt{s}=7$ TeV. Phys. Rev. D **85**, 012004 (2012). doi:10.1103/PhysRevD.85. 012004. arXiv:1107.1279
- 6. Y.L. Dokshitzer et al., Better jet clustering algorithms. JHEP **08**, 001 (1997). doi:10.1088/1126-6708/1997/08/001. arXiv:hep-ph/9707323

Curriculum Vitae

Name Hannsjörg Artur Weber

Address Professional

Fermilab PO Box 500

Batavia, IL 60510-5011 United States of America

Date of birth August 15, 1986

Place of birth Waldshut-Tiengen, Germany

Citizenship German

Languages German (mother tongue), English



Career

2015-present Research Associate,

Fermi Research Alliance, LLC (FRA, Fermilab),

Batavia, IL, United States of America

2011–2015 Scientific Assistant,

ETH Zürich,

Zürich, Switzerland

Education

2011–2015 Doctor of Sciences

ETH Zürich, Switzerland

Supervision: Prof. Günther Dissertori

210 Curriculum Vitae

PhD Thesis:

Search for Supersymmetry in Hadronic Final States using M_{T2} in pp collisions at $\sqrt{s}=8\, {\rm TeV}$ and

Evolution Studies of the CMS Electromagnetic Calorimeter Endcap Signals

2009–2011 Master of Science (mit Auszeichnung (with distinction))

ETH Zürich, Switzerland Field of studies: Physics

Master Thesis:

SUSY searches at the LHC in the b+MET final state,

Supervision: Prof. Günther Dissertori

2006–2009 Bachelor of Science (mit Auszeichnung (with distinction))

ETH Zürich, Switzerland Field of studies: Physics

1997–2006 Abitur (high school graduation diploma)

Klettgau-Gymnasium Tiengen, Waldshut-Tiengen, Germany

Awards

September 2011 Award for "Most pedagogic poster" for the poster

Search for BSM physics in hadronic final states with M_{T2}

at the CMS Physics Week, Bruxelles, Belgium

Seminars and Outreach Activities

August 2013 Search for SUSY in hadronic final states using M_{T2} at CMS

Talk given at the Ph.D. Seminar for students of the particle physics

institutes of ETH Zürich and University of Zurich

ETH Zürich, Switzerland

May 2013 An example of Research at the Institute of Particle Physics: Search

for SuperSymmetry

Talk given to first year students of physics in an information event of the AMP (Akademischer Mittelbau am Physikdepartment) and

VMP (Verein der Mathematik- und Physikstudierenden)

ETH Zürich, Switzerland

March 2013 Assistant for 9th International Masterclasses: Hands on Particle

Physics, at University of Zurich (jointly with ETH Zürich)

Curriculum Vitae 211

August 2012 Search for supersymmetry in hadronic final states with M_{T2} at the CMS experiment

Talk given at the Ph.D. Seminar for students of the particle physics institutes of ETH Zürich and University of Zurich

University of Zurich, Switzerland

Talks and Posters at Conferences

June 2014 Third generation SUSY searches at the CMS experiment

Talk at the Large Hadron Collider Physics conference (LHCP

2014)

New York, USA

September 2013 Search for SUSY in hadronic final states using M_{T2} at the CMS

experiment

Talk at the Joint Annual Meeting of the Austrian and Swiss Phys-

ical Societies (APS/SPS 2013)

Linz, Austria

June 2012 Search for Supersymmetry in hadronic final states using M_{T2} with

the CMS detector

Talk at the Annual Meeting of the Swiss Physical Society (SPS

2012)

Zürich, Switzerland

May 2012 Search for third generation squarks at the LHC

Talk at the 24th Rencontres de Blois, Particle Physics and Cos-

mology

Blois, France

November 2011 Search for supersymmetry in hadronic final states with M_{T2}

Poster at the Hadron Collider Physics Symposium (HCP 2011)

Paris, France

List of Publications

(with major contribution)

• The CMS Collaboration

Searches for supersymmetry using the M_{T2} variable in hadronic events produced in pp collisions at $8\,\mathrm{TeV}$

arXiv:1502.04358 JHEP 05 (2015) 078, published

• The CMS Collaboration

Search for supersymmetry in hadronic final states using M_{T2} in pp collisions at $\sqrt{s} = 7 \,\text{TeV}$

JHEP 10 (2012) 018 (2012), doi:10.1007/JHEP10 (2012) 018

• The CMS Collaboration

CMS Technical Design Report for the Pixel Detector Upgrade CERN-LHCC-2012-016, CMS-TDR-11 (2012), unpublished

• H. Weber for the ATLAS and CMS Collaborations

Search for third generation squarks at the LHC (status of light stop and sbottom searches)

Presented at Blois2012: 24th Rencontres de Blois, Particle Physics and Cosmology (September 2012)

L. Celnikier, J. Dumarchez, B. Klima, J.T.T. Vân (editors), *Particle Physics and Cosmology, Proceedings of the XXIVth Rencontres de Blois* (2013) Thế Giói Publisher, also CMS CR-2012/184

H. Weber on behalf of the CMS Collaboration
 Search for supersymmetry in hadronic final states with M_{T2}
 Presented at the 2011 Hadron Collider Physics symposium, Paris, France (June 2012)

EPJ Web of Conferences 28, 12021 (2012), doi:10.1051/epjconf/20122812021

• The CMS Collaboration

Search for supersymmetry in hadronic final states using M_{T2} in 7 TeV pp collisions at the LHC

CMS PAS SUS-11-005 (August 2011), unpublished

The full list of publications can be found in the link below: http://inspirehep.net/search?p=exactauthor%3AH.A.Weber.1+

[©] Springer International Publishing Switzerland 2015 H. Weber, *Search for Supersymmetry in Hadronic Final States*, Springer Theses, DOI 10.1007/978-3-319-19956-6